DISS. ETH NO. 25335

Carbon partitioning in the Early Earth

A dissertation submitted to attain the degree of

Doctor of Sciences of ETH Zürich

(Dr. sc. ETH Zürich)

presented by

Carolin Eva Fichtner

Master of Science in Geosciences

Goethe Universität Frankfurt am Main

born on January 4, 1988

citizen of Germany

accepted on the recommendation of

Prof. Dr. Max W. Schmidt

Dr. Christian Liebske

Prof. Dr. Michael J. Walter

Für Elfi

Ich kann,
weil ich will,
was ich muss.

Immanuel Kant

Kurzfassung

Im Frühstadium der Akkretion der Erde, als noch ein Magmaozean ohne darüber liegende Erdkruste die obersten hunderte von Kilometern der Erde bildete, war Kohlenstoff zwischen metallischer und silikatischer Schmelze, sowie einer heißen, möglicherweise dichten Atmosphäre verteilt. Kohlenstoff partitionierte zwischen beiden Schmelzen während sich die kernbildende Metallschmelze gravitationsbedingt zum Erdmittelpunkt bewegte. Diese Kohlenstoffpartitionierung lässt sich durch den Kohlenstoffpartitionierungskoeffizienten, $D_C^{metal/silicate}$, ausdrücken, der durch den Kohlenstoffmassenanteil der Metallschmelze, dividiert durch den Kohlenstoffmassenanteil der Silikatschmelze berechnet wird. $D_C^{metal/silicate}$ wird in dieser Studie experimentell mit dem Ziel bestimmt, die Größe der Kohlenstoffreservoire des Erdkerns und der Gesamterde zu ermitteln. Des Weiteren spielt $D_C^{metal/silicate}$ eine wichtige Rolle bei der Frage nach der Herkunft von Kohlenstoff in der Erde und der initialen Kohlenstoffverteilung zwischen Erdkern und Erdmantel während der Akkretion.

Die vorliegende Studie basiert auf Hochdruck- und Hochtemperaturexperimenten, die bei 1,5, 3,5 und 6,0 GPa und zwischen 1300 und 2000°C durchgeführt wurden. Ziel der Experimente war es, die Einflüsse von Druck, Temperatur, Sauerstofffugazität (fO_2), Depolymerisierungsgrad der Silikatschmelze (NBO/T) und Zusammensetzung der Metallschmelze (X_{Ni}, X_{Si}) auf $D_C^{metal/silicate}$ zu untersuchen. Um einen großen Bereich der obigen Parameter abzudecken und um deren jeweiligen Einfluss auf die Kohlenstofffraktionierung zu bestimmen, wurden drei Reihen von Experimenten untersucht. Die erste Reihe von Experimenten wurde in kohlenstofffreien Kapseln aus San-Carlos-Olivin durchgeführt, um systematisch den Einfluss des Depolymerisierungsgrades der Silikatschmelze (NBO/T) auf $D_C^{metal/silicate}$ zu bestimmen. Die zweite Reihe von Experimenten wurde in Graphitkapseln durchgeführt, um den Druck- und Temperaturbereich zu höheren Bedingungen erweitern zu können (Druck > 3,5 GPa und Temperatur > 1750°C). Metallisches Nickel und Silizium wurden dem Startmaterial zugefügt, um einen großen Bereich von Sauerstofffugazitäten zu ermöglichen. Die Sauerstofffugazität, die in San-Carlos-Olivinkapseln erreicht werden kann, liegt bei etwa ΔIW -1,5. Um noch reduzierendere fO_2-Bedingungen bis zu ΔIW -4,8 zu erreichen, wurde eine dritte Reihe von Experimenten in kohlenstofffreien Forsteritkapseln durchgeführt.

Kohlenstoffkonzentrationen der Metall- und Silikatschmelzen wurden *in-situ* mit einem Sekundärionen-Massenspektrometer (SIMS) und einer Elektronenstrahlmikrosonde (EPMA) gemessen. Der Gesamtkohlenstoffgehalt von ausgewählten Proben wurde zusätzlich mit einem

elementaren Kohlenstoff-Analysator (EA) bestimmt. Mithilfe der Ramanspektroskopie wurden die in der Silikatschmelze gelösten Kohlenstoffspezies festgestellt. Während die Kohlenstoffkonzentrationen der Metallschmelze unabhängig von den experimentellen Bedingungen nahezu konstant 5,6 ± 0,7 wt.% betragen, variieren die Kohlenstoffkonzentrationen der Silikatschmelze deutlich (0,010 ± 0,001 bis 0,97 ± 0,01 wt.%). Dadurch, dass die Menge gelösten Kohlenstoffs in der Metallschmelze in allen Experimenten ähnlich ist, lässt sich schlussfolgern, dass $D_C^{metal/silicate}$ hauptsächlich von der Menge gelösten Kohlenstoffs in der Silikatschmelze abhängt. Letzteres wird überwiegend durch die Einflüsse von NBO/T, Temperatur und fO_2 bestimmt. Druck hingegen scheint einen untergeordneten Effekt auf $D_C^{metal/silicate}$ zu haben. Die in dieser Studie experimentell bestimmten Werte für $D_C^{metal/silicate}$ variieren zwischen 0,035 ± 0,004 und 640 ± 49 und werden kleiner mit steigender Temperatur, zunehmendem NBO/T und zunehmender fO_2. Der Effekt von fO_2 wird durch die Ramanspektren der Silikatgläser verdeutlicht, die die Veränderung der dominanten Kohlenstoffspezies von Karbonatkomplexen zu Methylgruppen mit abnehmender Sauerstofffugazität zeigen. Diese Speziesänderung führt zu einer deutlichen Reduktion der Kohlenstoffmenge, die in der Silikatschmelze gelöst werden kann.

Basierend auf den Daten der vorliegenden Studie wurde eine Parametrisierung vorgenommen, die den Kohlenstoffpartitionierungskoeffizienten bei Bedingungen ermittelt, die während der Akkretion der Erde geherrscht haben. Kombiniert man die Parametrisierung mit gängigen Kernbildungsmodellen aus der Literatur, ermöglicht dies die Bestimmung von $D_C^{metal/silicate}$ und damit eine Abschätzung der Kohlenstoffkonzentration des Erdkerns und der Gesamterde bei bekannter Kohlenstoffkonzentration der Silikaterde. Die Ergebnisse zeigen, dass die $D_C^{metal/silicate}$ Werte für die Erde zwischen 3 und 30 variieren, für Bedingungen am Boden des Magmaozeans von 3 – 90 GPa, 1800 – 4200°C, ΔIW -5 bis ΔIW -2, einem konstanten NBO/T Wert von 2,6 und einem Ni- und Si-Gehalt von 5, beziehungsweise 4,5 wt.%. Normiert man die gefundenen Kohlenstoffkonzentrationen der Silikaterde auf die heutigen Werte von ~ 100 bis ~ 500 ppm, lässt sich ein Kohlenstoffgehalt des Erdkerns von 0,17 bis 1,30 wt.% abschätzen. Der resultierende Kohlenstoffgehalt für die Gesamterde beträgt 0,06 bis 0,47 wt.%. Diese Ergebnisse sind größtenteils unabhängig von den gewählten Kernbildungsmodellen, und werden vielmehr von dem Kohlenstoffgehalt der planetaren Körper beeinflusst, die die Erde gebildet haben. Die hier vorliegende Doktorarbeit zeigt, dass sich während der Akkretion der Erde Kohlenstoff wahrscheinlich weniger siderophil verhielt, als von früheren Studien vorgeschlagen. Dadurch ist ein volatilreiches „late veneer"-Ereignis im Endstadium der Akkretion nicht erforderlich, um den heutigen Kohlenstoffgehalt des Erdmantels zu erklären. Folglich dürfte sich das Kohlenstoffreservoir des Erdmantels bereits während der Erdkernbildung und Differenzierung der Erde eingestellt haben.

Abstract

During the early accretion of the Earth, when a lid-less magma ocean is thought to have covered the upper hundreds of kilometres of the Earth, carbon (C) was distributed between metallic and silicate melts, and a hot, potentially dense atmosphere. The metal segregated gravitationally from the magma ocean ultimately forming the core, and carbon partitioned between the two melts. This carbon partitioning is expressed by the carbon partition coefficient, $D_C^{metal/silicate}$, which is determined through the mass fraction of carbon in the metallic melt in wt.% divided by the mass fraction of carbon in the silicate melt. $D_C^{metal/silicate}$ is experimentally investigated in this study to constrain the size of the Earth's core and bulk carbon reservoirs. Further, $D_C^{metal/silicate}$ plays an important role in order to determine the origin and the initial distribution of carbon between the core and the mantle during Earth's accretion.

In this study, high-pressure and temperature experiments have been performed at 1.5, 3.5, and 6.0 GPa and between 1300 and 2000°C to investigate the effect of pressure, temperature, oxygen fugacity (fO_2), silicate melt depolymerisation (NBO/T), and metallic melt composition (X_{Ni}, X_{Si}) on $D_C^{metal/silicate}$. Several sets of experiments were conducted to cover a large variation of the above-mentioned parameters, and to determine their effects on carbon partitioning. The first set of experiments was performed in C-free capsules of San Carlos olivine to systematically investigate the effect of melt depolymerisation (NBO/T) on $D_C^{metal/silicate}$. A second set of experiments was performed in graphite capsules to expand the experimental conditions to higher pressures (> 3.5 GPa) and temperatures (> 1750°C). To cover a large range of oxygen fugacities prevailing in the experiments, metallic Ni and Si were added to the starting material. Since San Carlos olivine capsules mainly yield oxygen fugacities of ~ ΔIW -1.5, a third set of experiments was conducted in C-free synthetic forsterite capsules, which allow for more reducing fO_2 conditions down to ΔIW -4.8.

Carbon concentrations of metallic and silicate melts were analysed *in-situ* by secondary ionisation mass spectrometry (SIMS) and electron probe microanalysis (EPMA). The bulk carbon content of selected samples was determined by an elemental carbon analyser (EA). Raman spectroscopic analyses were conducted for all silicate melts to identify the C-bearing species. While the carbon concentration in the metallic melt is nearly constant throughout the range of conditions covered, being 5.6 ± 0.7 wt.% C in all experiments, the carbon content in the silicate melt strongly varies (0.010 ± 0.001 to 0.97 ± 0.01 wt.%). Consequently, since the amount of C dissolved in the metallic melt is similar in all experiments, $D_C^{metal/silicate}$ mainly depends on the C content of the silicate melt, which is mostly controlled by NBO/T, temperature and fO_2. Pressure, however, appears to have little

effect. The experimentally determined $D_C^{metal/silicate}$ of this study ranges from 0.035 ± 0.004 to 640 ± 49 and decreases with increasing temperature, increasing NBO/T, and increasing fO_2. The latter effect is supported by Raman spectra of silicate glasses showing that the dominant C species changes from carbonate complexes to methyl groups while fO_2 decreases, which strongly reduces the amount of C dissolved in the silicate melt.

First, the carbon partition coefficient during Earth's accretion is determined based on the experimental result that $D_C^{metal/silicate}$ is mainly controlled by NBO/T, which is assumed to be at a constant value of 2.6 through the period of accretion. Derived $D_C^{metal/silicate}$ values are in the range of 25 to 43 during the time of core formation. Extending the experimental set to reveal and quantify the effects of P, T and fO_2 on carbon partitioning, enables the development of a parameterisation based on our experimental data. This parameterisation constrains the carbon partition coefficient at conditions of Earth's accretion in a more comprehensive way, taking all above describe parameters into account, as well as the Si and Ni content of the metal melt. Combining the parameterisation with core formation scenarios from the literature, $D_C^{metal/silicate}$ during core-mantle segregation can be inferred to range between 3 to 30. These values are nearly independent of the core formation scenario that was applied. Further, our results show that the Earth's carbon inventory mainly depends on the C concentration of the impactors. Assuming different types of chondrites as Earth building blocks mainly results in estimated C concentrations of the magma ocean that are 1 – 2 orders of magnitude higher than the present–day BSE C content. Thus, severe carbon loss, perhaps caused by the escape of the Earth's proto–atmosphere, may have occurred. Alternatively, the Earth may have formed solely from C-depleted enstatite chondrites. Normalising the estimated BSE C concentrations to present-day values of ~ 100 to ~ 500 ppm results in core C concentrations of ~ 0.17 to ~ 1.30 wt.%, and bulk Earth C concentrations of ~ 0.06 to ~ 0.47 wt.%. In conclusion, there is no need for a post-accretion delivery process like a volatile-rich "late veneer" to explain C abundances of the Earth's mantle. Instead, the mantle C reservoir may have been set during core formation and differentiation.

Table of Contents

1. Introduction

This doctoral thesis focusses on the experimental investigation of the partitioning behaviour of carbon between core-forming metallic melt and mantle-forming silicate melt during Earth's accretion. The results help to enhance our understanding of the origin and distribution of carbon in the Earth and deliver new constraints on the amount of carbon stored in the core and mantle after accretion.

1.1 Core formation and magma ocean

The general concept of core formation involves a massive reorganisation of the Earth's interior, where a core-forming metallic liquid segregated from a mantle-forming silicate melt (Ringwood, 1966; Walter & Trønnes, 2004), probably within a deep magma ocean (Melosh, 1990; Tonks & Melosh, 1993; Canup, 2004). Thus, the Earth, and various other planetary bodies, have a metallic core because liquid iron and iron-bearing alloys are denser than silicates, so that the most stable arrangement of a rotating planet is an oblate spheroid with dense iron in the centre. The details of this broad picture of the present configuration of the Earth depend on what material was added to the Earth, at what times, under which conditions, and how this material evolved over time.

The most important iron source contributing to the growth of the Earth during accretion are probably planetesimals. Whether the planetesimals had already segregated Fe-rich cores or not, depends primarily on their size but also on the Earth's feeding zone during accretion. Pre-existing metal cores may strongly influence the extent of chemical equilibration between the core-forming metallic melt and the mantle-forming silicate melt in the Earth's magma ocean. Generally, differentiation of planetesimals is thought to have occurred within the first few million years of the evolution of the solar system (Kleine et al., 2005; Scherstén et al., 2006; Kruijer et al., 2014). In the case of an undifferentiated planetesimal, the impact would have probably resulted in a finely dispersed mixture of molten target and projectile material. In this scenario, iron likely existed as small dispersed droplets ($0.8 - 1.1$ cm) that continuously equilibrated with the surrounding material (Rubie et al., 2003). If a planetesimal was already differentiated, containing a large metal mass of possibly 50 - 500 km in diameter, its core is still likely to have experienced emulsification and at least partial equilibration with the target silicate magma ocean (Rubie et al., 2003; Rubie et al., 2007). However, the cores of larger impacting bodies, i.e., of the size of Mars, probably remained intact as discrete masses or large metal droplets and may have merged rapidly with the Earth's core (Rubie et al., 2003; Canup, 2004; Rubie et al., 2007). Equilibration in this latter scenario is very unlikely, because the timescales required to

chemically equilibrate large metal droplets (e.g., metre or more in diameter) with the silicate melt (40 000 – 150 000 years) are two to three orders of magnitude longer than the magma ocean may have needed to crystallise (40 – 165 years) (Rubie et al., 2003; Rubie et al., 2007). Even the slightly longer estimate of the magma ocean lifetime of 1 000 years based on fluid dynamic calculations (Solomatov, 2000), is not sufficient to ensure chemical equilibrium between the metallic and the silicate melt. However, the above estimates of magma ocean survival times are based on the absence of both an early thick atmosphere and an insulating proto-crust. If those had already developed, the lifetime of a magma ocean may be extended to 10^8 years (Spohn & Schubert, 1991; Abe, 1997), which would allow large metal droplets to equilibrate with the silicate magma ocean.

Alternatively, parts of the giant impactor's core could have been ejected during the collision, and large iron fragments could have fallen back onto the mostly molten Earth (Cameron, 2000). These fragments would probably also have emulsified and rapidly equilibrated with the silicate melt on their way to the core.

The actual process of metal-silicate separation depends strongly on the thermal state of the Earth. Three sources of energy can be distinguished to produce partial melting, essential for the segregation of the core. First, the decay of short-lived radioactive nuclides, such as ^{26}Al (half-time ($t_{1/2}$) = 0.74 Ma) and ^{60}Fe ($t_{1/2}$ = 1.5 Ma), was an important energy source directly after the birth of the solar system and hence at the early stage of accretion. Second, the kinetic energy delivered by the impacts constituted the main energy source especially during the late stage of accretion (10 – 100 Ma after the formation of the solar system) (Wetherill & Stewart, 1994). Finally, the process of differentiation itself released an appreciable amount of heat due to the reduction of gravitational potential energy of the Earth during the redistribution of mass (Rubie et al., 2007). Physical models show that impacts of Moon-sized and larger bodies could have delivered sufficient energy to form one or more global

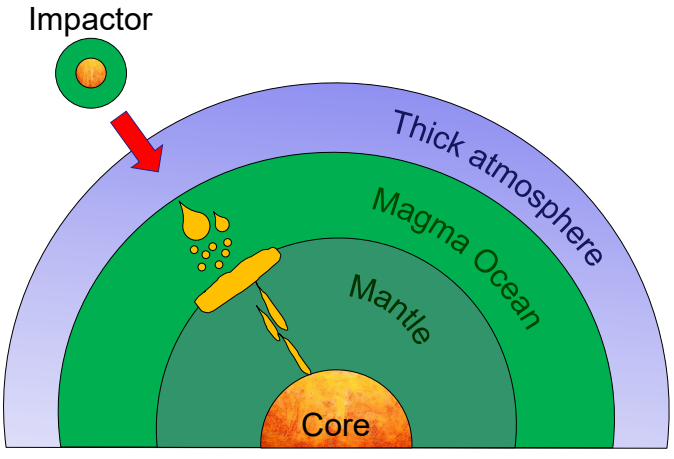

Figure 1.1. During Earth accretion impactors brought silicate and metal to the Earth. After collision, the impactor's core (if any) burst apart and the Fe-rich metal segregated from a magma ocean, possibly as small dispersed droplets. These droplets may have ponded at the ocean floor and equilibrated isobarically with the surrounding silicate melt. Further movement towards the core occurred in large diapirs due to gravitational instability (Stevenson, 1990; Taylor & Norman, 1990; Righter et al., 1997).

magma oceans at a late stage of accretion (~ 30 Ma, Boyet & Carlson, 2005), when a proto-core in the Earth's centre already existed (Melosh, 1990; Tonks & Melosh, 1992). The depth of the magma ocean mainly depended on the impactor/target mass ratio, the impact velocity and the initial temperature of the impacting planetary objects (Tonks & Melosh, 1993). Further, the effective base of the magma ocean was likely located above the core-mantle boundary because the solidus probably crossed the geotherm at shallower depth (Rubie et al., 2003; Walter & Trønnes, 2004). Therefore, the descending iron droplets may have ponded at the interface between the magma ocean and the underlying solid mantle and may have equilibrated with the surrounding silicate melt at conditions of around 3300 − 3600 K, 27 − 33 GPa and ΔIW -1 − ΔIW -3.5 (McDonough & Sun, 1995; Righter, 2011; Rubie et al., 2011). The resulting iron layer would still have been denser than the solid mantle underneath, such that gravitational instabilities permitted a discontinuous transport of metal towards the core in the form of large, negatively buoyant diapirs without further chemical equilibration, as illustrated in Fig. 1.1 (Stevenson, 1990; Taylor & Norman, 1990).

Core formation can only be a single event if a last giant impact (e.g., the collision between the Earth and Theia, which led to the formation of the Moon) reorganised our entire planet due to efficient large-scale melting, mixing of material, and extensive re-equilibration (e.g., Stevenson, 2008; Righter, 2011). However, fluid dynamics simulations of Davies (1985), Tonks & Melosh (1993) and Solomatov (2000) suggest that even giant impacts would probably not have resulted in a global melting event. Therefore, core formation may have more likely occurred continuously over a 30 to 50 Ma time period (Halliday, 2004; Kleine et al., 2005) through a series of events and under a range of progressively changing pressure, temperature and oxygen fugacity conditions (O'Neill, 1991; Wade and Wood, 2005; Wood et al., 2006; Corgne et al., 2008; Wood et al., 2008; Siebert et al., 2011). Consequently, it is crucial to find a progressive set of conditions that can account for the observed mantle abundances of siderophile elements regarding their metal-silicate partitioning behaviour (Walter et al., 2000; Righter, 2003; Wood et al., 2006). The widely accepted concept is that siderophile elements partitioned preferentially into the Fe-rich core such that the abundance of these elements in the mantle resulted from their partitioning behaviour and therefore provide a record of the physical conditions of core formation, assuming that metal and silicate were in equilibrium (e.g., Ertel et al., 2006; Cottrell et al., 2009).

In order to gain information about the timing of core formation and chemical differentiation processes within planetary bodies, the radioactive decay of short-lived isotopes is a particularly powerful tool. Thereby, fractionation of the parent element from the daughter element is used to date the chemical

event of isotopic closure. Meaningful timescales can only be derived, if the isotopic system was in equilibrium prior the fractionation event, and if no perturbation of the isotopic system has occured after the fractionation event. The ^{182}Hf-^{182}W chronometer is the most useful isotopic system to investigate the timing of core formation (Kleine et al., 2002; Halliday, 2004; Burkhardt et al., 2008), thanks to the refractory character of both elements, the precise knowledge of the Hf and W isotope composition at the beginning of the solar system (known from Ca-Al-rich inclusions in meteorites) and the half-life of ^{182}Hf, which is comparable to the timescales of planet formation ($t_{1/2}$ = 8.9 Ma). The ^{182}Hf-^{182}W chronometer is based on the decay of the lithophile parent isotope ^{182}Hf to the stable, siderophile daughter isotope ^{182}W. If the Earth's core formed after all the ^{182}Hf had decayed, the ^{182}W would be depleted in the mantle, because all ^{182}W would have been extracted into the core. If the core formation occurred when ^{182}Hf was still present, the mantle would be enriched in ^{182}W. Since excess ^{182}W exists in the terrestrial mantle, the ^{182}Hf-^{182}W chronometer indicates that core formation was largely complete 50 Ma after the formation of the solar system (Halliday, 2004; Kleine et al., 2005).

The main goal of this study is to investigate the partitioning of carbon between metallic core and silicate magma ocean material, model the distribution of carbon for plausible sets of core material segregation conditions, and to draw conclusions concerning the Earth’s core formation and carbon content.

1.2 Carbon in the Earth

Carbon is, after hydrogen, helium, and oxygen, the most abundant element in the solar system (Anders & Grevesse, 1989), and significantly affects several important chemical and physical processes and properties of the Earth’s atmosphere, mantle and core (e.g. Wyllie & Huang, 1976; Fallon & Green, 1989; Sleep & Zahnle, 2001; Dasgupta & Hirschmann, 2006; Dasgupta & Walker, 2008; Stanley et al., 2011). Still, C belongs to the volatile elements which are, with respect to chondrites, depleted in the silicate Earth, either as a result of core formation (Fig. 5.1.), accretion (Ringwood, 1966), or due to prior nebula fractionation (Anders, 1968). Wood (1993), however, shows that the volatility of carbon is strongly pressure-dependent, suggesting that carbon is in fact not volatile under pressure conditions that prevailed during planetary accretion and differentiation. Further, the volatility of carbon depends on carbon speciation, e.g., carbides, graphite and diamond are among the most refractory minerals in the Earth. The bulk composition of the silicate Earth (BSE) is often approximated by the composition of C1 carbonaceous chondrites that match well the Earth's volatile depletion trend (Allègre et al., 2001; Palme & O’Neill, 2003). These carbonaceous chondrites represent pristine material from the

Table 1.1
Summary of terrestrial carbon reservoirs described in the text.

Reference	Reservoir	C content in ppm	Method
Saal et al., 2002	MORB	20 ± 5	CO_2/Nb
Salters & Stracke, 2004	MORB	14 ± 7	CO_2/Nb
Cartigny et al., 2008	MORB	44	CO_2/Nb
Marty, 2012	MORB	20 ± 8	weighted above estimates
Hirschmann & Dasgupta, 2009	most depleted MORB	16 ± 9	H/C
Hirschmann & Dasgupta, 2009	enriched OIB	33-500	H/C
Sleep & Zahnle, 2001	Mantle without crust	21-54	model of the modern CO_2 cycle
Dasgupta & Hirschmann, 2010	MORB	20-300	Extrapolations of magmatic CO_2 to mantle concentrations
Dasgupta & Hirschmann, 2010	depleted MORB	20-30	Extrapolations of magmatic CO_2 to mantle concentrations
Dasgupta & Hirschmann, 2010	enriched MORB or OIB	300-1300	Extrapolations of magmatic CO_2 to mantle concentrations
Trull et al., 1993	upper mantle	50-250	C/He
Pineau et al., 2004	depleted MORB	20-119	C directly measured from glassy samples of volcanoclastic deposits
Pineau et al., 2004	enriched MORB	343-15677	C directly measured from glassy samples of volcanoclastic deposits
Marty & Zimmermann, 1999	BSE	580 ± 380	C/N
Marty, 2012	BSE	1164 ± 544	combination of C/He and He/Ar
Marty, 2012	BSE	765 ± 300	weighted the two approaches above
Sleep & Zahnle, 2001	BSE	42-75	model of the modern CO_2 cycle
McDonough & Sun, 1995	BSE	120	abundances of non-lithophile and non-refractory elements in the silicate Earth
McDonough, 2003	BSE	120	compositional model based on the absolute abundances of refractory elements in the Earth and the planetary signature of the volatile elements depletion pattern
Dasgupta & Hirschmann, 2010	BSE	20-30	if MORB-source mantle (10-30 ppm C) applies to the entire mantle
Dasgupta & Hirschmann, 2010	BSE	68-313	if the whole mantle is a mixture of depleted (40 % by mass) and enriched mantle source (50-500 ppm C)
Marty, 2012	Bulk Earth	526 ± 206	normalising the BSE value (765 ± 300 ppm C) to the total mass of the Earth
McDonough, 2003	Bulk Earth	730	extending the depletion pattern for the abundances of non-refractory, non-lithophile elements to the entire Earth

early state of the solar system and are thought to be essential building blocks of the Earth (Allègre et al., 1995; McDonough & Sun, 1995; O'Neill & Palme, 1998). In recent years, however, several observations like the superchondritic abundances of some element ratios (e.g., H/C; Mg/Si, Ca/Al) and the different isotopic signature of the Earth in comparison to C1 chondrites (e.g., ^{48}Ca, ^{50}Ti, ^{62}Ni) give reason to assume a non-C1-chondritic composition of the bulk Earth (O'Neill & Palme, 2008; Dauphas, 2017). Possible explanations include (1) a loss of crust during accretion caused by large impactor collisions that modified the original chondritic composition (Caro et al., 2008; Bonsor et al., 2015; Carter et al., 2015), (2) a "hidden" reservoir in the deep Earth (Boyet & Carlson, 2005; Labrosse et al., 2007; Hirschmann & Dasgupta, 2009), (3) enstatite chondrites composing a large fraction of the accreting material (Dauphas, 2017; Liebske & Khan, 2018) or (4) a fractionation process like mantle differentiation of ultra-high pressure mantle phases such as perovskite and ferropericlase (Walter et al., 2004; Walter, 2014) which would then require a stratified mantle.

In chondrites, carbon is mainly stored either as solid graphite or as carbides. The amount of carbon in chondrites is estimated to be ~ 35 000 ppm C (Anders & Grevesse, 1989; Palme, 1988; Lodders, 2003), corresponding to 3.5 wt.% C. In comparison to chondrites, the BSE carbon concentration is expected to be at least one order of magnitude lower (Table 1.1). Direct measurements of the mantle carbon inventory are difficult, because samples might not represent the original C concentrations of the primary magma due to CO_2 degassing (e.g., Wallace, 2005). Still, many studies exist on estimates of the mantle C content based on CO_2 concentrations in melt inclusions trapped in olivine combined with measurements of incompatible element concentrations, e.g., CO_2/He (Trull et al., 1993) or CO_2/Nb (Saal et al., 2002; Salters & Stracke, 2004; Cartigny, 2008). These studies are all based on the assumption that the CO_2/incompatible element ratio does not significantly scatter within the mantle, and that the concentration of the incompatible element is relatively well constrained. For these approaches, the C content of the depleted mid-ocean ridge basalt (MORB)-source mantle varies from 14 ± 7 ppm (Salters & Stracke, 2004) to 44 ppm (Cartigny, 2008). Trull et al. (1993), however, analysed the C and He abundances of fluid inclusions in xenoliths from oceanic hotspot volcanos and estimated higher values of 50 – 250 ppm C for a more enriched mantle. Hirschmann & Dasgupta (2009) based their estimates on the H/C ratio of the mantle and found values of 16 ± 9 ppm C for a MORB-source and 33 – 500 ppm C for an enriched ocean island basalt (OIB)-source mantle. Dasgupta & Hirschmann (2010) used all of the above magmatic CO_2 concentrations, including the direct measurements of Pineau et al. (2004) from Mid-Atlantic Ridge volcanoclastic deposits, which yield 20 to 119 ppm C for a depleted MORB and 343 to 15 677 ppm C for an enriched MORB, to extrapolate these C values to mantle concentrations. Taking into account the effects of partial melting,

crystal fractionation, and degassing, their results suggest values of 20 – 300 ppm C for MORB-source and 300 – 1300 ppm C for an enriched MORB or OIB-source mantle. Alternatively, Sleep & Zahnle (2001) based their estimates of the Earth's C reservoirs on data about fluxes coupled with knowledge about plate tectonics to construct a model of the modern CO_2 cycle. Their estimates for the present-day mantle (without the crust) include 21 – 25 ppm C and are similar to the values presented above for depleted MORB-source mantle regions. Including today's C content of the crust into the budget of the mantle, a bulk silicate Earth C content of 42 – 75 ppm can be derived. These values are similar to those suggested by Dasgupta & Hirschmann (2010) of 20 – 30 ppm C, assuming that a MORB-source mantle applies to the entire mantle. Dasgupta & Hirschmann (2010) estimated an alternative BSE C content of 68 – 313 ppm for a scenario, where the mantle comprises a mixture of 40 % (by mass) depleted MORB-source and 60 % enriched OIB-source mantle. Marty & Zimmermann (1999) used the C/N ratio of both MORB type and OIB type reservoirs, yielding a BSE C content of 580 ± 380 ppm. Using a combination of He/Ar and C/He stable isotope ratios (Marty, 2012), the estimated bulk silicate C inventory results in even higher values of 1164 ± 544 ppm. Marty (2012) weighted the two approaches above in terms of their uncertainties and suggests a preferred BSE C content of 765 ± 300 ppm. This estimate is significantly higher in comparison to the results of the compositional model of McDonough & Sun (1995) of 120 ppm C, based on the relative abundances of non-lithophile and non-refractory elements in the Earth. Taking these element abundances and extending the model with knowledge of the iron content of the mantle and the core, establishes a bulk Earth compositional model, yielding 730 ppm C (McDonough, 2003). Marty (2012) normalised his estimate of the BSE C content (765 ± 300 ppm) to the total mass of the Earth (5.98×10^{27} g) and suggested a similar bulk Earth C content of 526 ± 206 ppm, assuming that there is no C sequestered into the core. The sizes of different terrestrial C reservoirs described above are summarised in Table 1.1. Since the estimated mantle C contents vary significantly between studies (14 ± 7 ppm C to 343 − 15 677 ppm C; Salters & Stracke (2004) and Pineau et al. (2004), respectively), and the proportions of depleted and enriched mantle regions are not well constrained, the resulting estimates for the bulk silicate Earth show a variation by an order of magnitude (42 − 75 ppm C to 765 ± 300 ppm C; Sleep & Zahnle (2001); and Marty (2012), respectively).

The amount of carbon possibly stored in the Earth’s core strongly depends on both the initial amount of carbon available and the metal affinity of carbon at core-forming conditions. Several experimental studies investigated C partitioning between iron-rich metallic melt and silicate melt during the last decade (e.g. Dasgupta et al., 2013; Chi et al., 2014; Stanley et al., 2014; Li et al., 2015; Li et al., 2016; Dalou et al., 2017). All of these studies revealed that carbon behaves as a siderophile

element ($D_C^{metal/silicate}$ >> 100 – 1000) at conditions assumed to have prevailed during Earth accretion. Consequently, some (or most) carbon from the magma ocean was lost to the core. Therefore, these authors strongly favour a post-accretion C-delivery event like a "late veneer", which refers to the late addition of chondritic or cometary material to terrestrial planets after core formation. The late veneer hypothesis was originally proposed by Chou (1978) and Jagoutz et al. (1979) who found that highly siderophile elements (HSEs, e.g., platinum group elements, Re and Au) are more abundant in the mantle than expected. Based on their metal-silicate partitioning behaviour (Ringwood, 1979), these elements should have been effectively extracted from the mantle into the core during core formation. Therefore, a late veneer has to be added to the Earth after core formation has completed (i.e., after the giant impact event) to account for the observed, roughly chondritic HSE abundances of the Earth's mantle (Wänke & Dreibus, 1988; Newsom, 1990; Palme & O'Neill, 2003). The mass of the late veneer is considered to be ~ 1 % of the mass of the entire mantle, based on the excess of mantle HSE abundances (Chou, 1978). Tungsten isotopic measurements (Halliday, 2008), however, suggest that the amount of material added after core formation is limited to 0.3 – 0.5 % of the mass of the mantle. In terms of post-accretion carbon-delivery, not only the amount of material, but also the type of material added to the Earth is decisive. For example, C1 carbonaceous chondrites of 3.5 wt.% C content (McDonough & Sun, 1995; Palme, 1988) would raise the mantle carbon inventory by 105 to 350 ppm corresponding to 0.3 or 1 % mass of the late veneer, respectively. Carbon-poor ordinary H3 chondrites (0.27 wt.% C, Jarosewich, 1990), however, would only result in an additional C mantle content of 8 (0.3 % mass of the late veneer) or 27 ppm (1 % mass of the late veneer). Most likely, a combination of both C1 carbonaceous chondrites and ordinary chondrites (and even other chondrite types or cometary materials) may have been involved in the late veneer to explain the HSE and volatile abundances of the mantle (Halliday, 2008). Based on stable and noble gas isotopes, Marty (2012) found high carbon (and H_2O) contents of the bulk Earth of 526 ± 206 ppm C, suggesting that C was mainly delivered by wet planetesimals during the main stage of accretion, rather than contributed by a late veneer.

An alternative scenario to raise the HSE concentrations to the observed mantle values is inefficient core formation. Jones & Drake (1986) proposed that small amounts of metallic Fe were trapped within the mantle during Earth's accretion. There is evidence from the oxidation state of the mantle that indeed core segregation may have been incomplete. Frost et al. (2004) argue that the crystallisation of silicate perovskite (dominant lower mantle phase) involves the production of metallic Fe, which might then be lost to the core, resulting in an increase in the oxygen fugacity of the mantle (Wood & Halliday, 2005; Wood, 2006). Since the observed oxidation state of the mantle is less oxidised than

expected if all metal produced by the crystallisation of perovskite had been stripped by the core, several authors suggest that there exists a "hidden" reservoir of metallic melt in the mantle, including refractory siderophile elements (e.g., Jones & Drake, 1986; Newsom & Sims, 1991).

One might think that the experimental investigation of the carbon content of the Earth's core is not possible, due to the high P-T conditions that are difficult or even impossible to simulate in a laboratory. Stevenson (1981), however, argues that the present-day Earth's core is not considered to be in chemical equilibrium with the mantle, because of the boundary layer dynamics, which preclude chemical equilibrium (see Holzapfel et al., 2005). Therefore, the partitioning behaviour of carbon (or any other light element) between metal- and silicate melt at the present-day core-mantle boundary (CMB) is not necessarily required for the carbon concentration in the core. Instead, it is likely that the content of carbon in the core has been set during core formation, where much lower pressure and temperature conditions have prevailed.

In this doctoral thesis, a new experimental approach was established, where metallic and silicate melt pairs were equilibrated in C-free San Carlos olivine capsules or synthetic forsterite capsules. This is in contrast to previous studies that mainly used graphite capsules as exclusive C source. Based on these experiments, this study finds that the C sequestration to the core has likely been much less pronounced than previously reported. Therefore, this thesis provides important new constraints on the distribution of C between the core and the mantle. Most importantly, it suggests an alternative scenario, where a post-core formation process like a volatile-rich "late veneer" is not needed to explain the mantle carbon inventory of the Earth.

1.3 Outline of the thesis

The scientific results of this thesis are presented in two main chapters (Chapters 3 and 4) that describe the experimental investigation of carbon partitioning under varying temperatures, pressures, and oxygen fugacities, which control the distribution of carbon between liquid metal and liquid silicate during Earth's accretion and differentiation.

The involved analytical and experimental methodologies are described in detail in Chapter 2 including information about different capsule materials tested and the synthesis of the analytical standards.

In Chapter 3, the effects of temperature, pressure, and chemical composition of the silicate melt on carbon partitioning are systematically investigated. The experimental set consists of a single

starting material containing a silicate and a metal component that are equilibrated at high pressure and temperature in a piston cylinder press or a multi-anvil apparatus. Experiments are performed in either San Carlos olivine (1.5 GPa, 1300 − 1750°C) or graphite capsules (1.5, 3.5, and 6 GPa, 1500 − 2000°C), depending on experimental conditions. The prevailing oxygen fugacity in the experiments varied between ΔIW -0.9 and ΔIW -1.9. The results enable us to constrain the potential amount of carbon stored in the core and the bulk Earth, and also give hints on the C inventroy of the Mars. This Chapter is about to be submitted for publication and is referred to as Fichtner et al. (2018a) in this thesis.

Chapter 4 focuses on the effects of oxygen fugacity and metallic melt composition on carbon partitioning, which is experimentally investigated. Experimental charges consist of several starting compositions in order to cover a large range of oxygen fugacity conditions. Two experimental sets are performed, the first one in San Carlos olivine capsules (~ ΔIW -1.5), and the second one in synthetic forsterite capsules (~ ΔIW -4). Experiments are equilibrated in a static and a centrifuging piston cylinder press at 1.5 GPa and 1400 – 1500°C. The results of these experiments and those reported in Chapter 3 are incorporated in a parameterisation that allows to constrain the carbon inventory of the Earth's mantle and core during Earth's accretion, and deliver new implications for the origin of terrestrial carbon.

In Chapter 5 the main conclusions of this doctoral thesis are summarised, and an outlook on other light elements, besides carbon, possibly stored in the Earth's core is presented.

Appendix A consists of back-scattered electron images of all experiments, Appendix B shows supplement figures to Chapter 4, Appendix C contains details about the parameterisation described in Chapter 4, and Appendix D describes the core formation scenarios employed in Chapters 3 and 4 in more detail and gives mathematical background information.

2. Methodology

The experimental approach of this doctoral study was to produce homogeneous silicate glass in equilibrium with metallic melt in a piston cylinder and a multi-anvil apparatus to investigate the carbon partitioning between these two materials at P-T-fO_2-conditions varying from 1300 to 2000°C, 1.5 to 6 GPa, and ΔIW +2.2 to ΔIW -4.8, respectively. Most experiments were conducted in a carbon-free sample container made of either single crystal San Carlos olivine or synthetic forsterite. Carbon concentrations in both, silicate glass and metal alloy were measured by SIMS at the University of Lausanne, and by a conventional elemental analyser (LECO) at ETH Zurich. The carbon content of some metal melts was additionally analysed by EPMA at the University of Frankfurt. For identifying the prevailing C species, Raman spectra were collected at ETH Zurich.

In this chapter all experimental and analytical techniques are described in detail, including the synthesis of analytical standards and unsuccessfull approaches.

2.1 Experimental methods

2.1.1 Finding appropriate starting compositions

The challenge of performing experiments in olivine capsules is to find a starting composition that results in a quenchable homogeneous glass. This is difficult, because the olivine capsule reacts with the experimental charge during the experiment and shifts its composition towards higher MgO and lower SiO_2 contents (see Fig. 3.2). Therefore, many starting compositions that were tested, showed, instead of large areas of homogeneous glass, the crystallisation of olivine, ortho- and clinopyroxene, and occasionally garnet, meaning that starting compositions had to be adjusted after each experiment.

Our initial starting composition was based on the CO_2-free primitive basaltic glass as described by Melson et al. (1976). The run product of this experiment showed homogeneous glass with a slightly modified composition (Table 2.1). Thus, a new starting mixture was prepared based on the composition of this glass, and 2 wt.% CO_2 were added through $CaCO_3$. The experimental product yielded a homogeneous glass, but additionally ~ 500 µm large ortho- and clinopyroxene crystals were present. In order to avoid the growth of any crystals, which would cause difficulties for centrifugation and analytical measurements (especially for SIMS and bulk analysis, where large glassy pools are required), we iteratively adjusted the starting composition as described above, i.e., using the composition of the present silicate melt as starting composition for the next experiment. As soon as

we found a composition that generated extensive homogeneous glass without any crystals, we used this glass as analytical standard (see also section 2.1.5) and added a metal component to the starting mix. Since the composition of the metal (Fe ± Ni ± Si) influences the redox conditions within the experimental charge, which again may lead to the crystallisation of olivine, ortho- and clinopyroxene, further iterative adjustment of the silicate starting composition was required.

We repeated the above-described procedure for a starting mixture based on the primitive (here Fe-free) high-alumina basalt from Giant Crater Lava Field, Medicine Lake Volcano, California (Donnelly-Nolan et al., 1991) in order to study the effect of chemical composition of the silicate melt on carbon partitioning, and to allow higher CO_2 concentrations of 3.9 wt.%. This starting mixture was chosen to be initially Fe-free for two reasons. First, to enable the usage of metal capsules (iridium, platinum) for the synthesis of standards. Second, to reduce the redox work in experiments at very low oxygen fugacities, where all iron would be present in its metallic form and migrate into the metallic melt.

The final experimental charge is composed of 70 - 80 wt.% silicate powder and 20 - 30 wt.% metal powder. The metal powder was composed of Fe-C, Fe-Ni-C or Fe-Si-C mixtures (Table 2.2). Carbon was added through $CaCO_3$ and pure synthetic graphite powder to the silicate and metal mixes, respectively. All components were pre-dried, spectroscopically pure oxides (SiO_2, TiO_2, Al_2O_3, MgO, NiO), silicates (Fe_2SiO_4, $CaSiO_3$, Na_2SiO_3, $NaAlSi_3O_8$, $KAlSi_2O_6$), or metals (Fe, Ni, Si) and mixed in an agate mortar in ethanol for 45 minutes. After mixing, the starting materials were stored at 110°C for ≥ 24 h to remove any moisture and ethanol remnants.

The full set of starting materials tested, is displayed in Tables 2.1 and 2.2. Additionally, the final set of starting compositions is presented in Table 4.1, and the resulting compositions of the silicate glasses and metallic alloys are shown in Tables 3.3 and 4.3.

2.1.2 Testing different capsule materials

Studying the partitioning of carbon between a metal and a silicate melt requires capsule materials that do not influence the carbon partitioning behaviour, but allow for the generation of homogeneous silicate glass without loosing the metal melt.

At first, metallic capsule materials such as iridium, rhenium and $Au^{50}Pd^{50}$ alloy were tested, but excessive iron loss occurred due to alloy formation (Fig. 2.1). Consequently, no meaningful partition coefficients could be measured from these experiments as continuous reaction of Fe^0 with the metal

Table 2.1
Experimental conditions, quantitative analyses and results of different starting compositions.

Run #	**1-S-2**		**2-S-6**		**3-S-7**		**4-S-9**		**5-SM-15**		**6-S-16**		**7-SM-18**		**8-S-19**	
Temperature (°C)	1350		1400		1400		1400		1450		1400		1450		1450	
Pressure (GPa)	2		3		3		3		3		3		3		3	
Duration (h)	72		70		28		27.5		2.5		2		2		5.5	
Capsule type	Olivine		Olivine		Olivine		Olivine		Olivine		$Au^{50}Pd^{50}$		Olivine		$Au^{50}Pd^{50}$	
Silicate mix (wt.%)	**PB1S**		**PB2S**		**PB3**		**PB4**		**PB5**		**PB6**		**PB7**		**PB8**	
SiO_2	50.9		49.9		44.4		42.4		44.6		50.2		42.3		48.0	
TiO_2	1.5		1.5		1.5		1.5		1.5		1.5		1.4		1.4	
Al_2O_3	15.7		15.4		11.1		11.1		8.6		9.7		8.2		9.3	
FeO	9.9		9.7		11.0		11.0		11.7		2.0		11.1		1.9	
MgO	7.7		7.6		18.3		18.3		21.1		23.7		20.0		22.7	
CaO	11.5		11.3		9.0		9.0		5.7		5.7		5.4		5.5	
NiO	-		-		-		-		-		-		0.0		-	
Na_2O	2.7		2.6		2.6		3.6		3.6		4.1		6.6		7.1	
K_2O	0.2		0.2		0.2		0.2		0.2		0.2		2.2		2.2	
CO_2	0.0		2.0		2.0		3.0		3.0		3.0		2.8		2.0	
Total	100		100		100		100		100		100		100		100	
Silicate melt (wt.%)	average	1 σ	average	1 σ	average	1 σ	average	1 σ	average	1 σ	average	1 σ	average	1 σ	average	1 σ
SiO_2	48.80	0.23	44.4	0.2	43.0	0.2	43.5	0.6	49.24	0.13	48.4	0.9	43.19	0.88	50.68	0.04
TiO_2	1.62	0.05	1.4	0.1	2.0	0.1	2.0	0.2	3.30	0.01	4.9	0.6	2.18	0.08	1.72	0.03
Al_2O_3	13.50	0.08	11.1	0.1	10.5	0.2	12.1	1.0	18.20	0.25	16.7	0.9	13.43	0.55	11.00	0.03
FeO	10.40	0.13	11.0	0.2	12.1	0.4	11.7	0.2	10.69	0.08	3.1	0.2	12.38	0.50	0.77	0.05
MgO	12.38	0.09	18.3	0.1	17.3	0.5	13.9	2.6	3.79	0.09	8.3	0.9	3.55	0.20	16.17	0.03
CaO	9.93	0.11	9.5	0.1	9.9	0.2	9.9	0.9	2.94	0.09	6.2	0.6	8.85	0.14	6.29	0.13
NiO	b.d.l.	-	b.d.l.	-	b.d.l.	-	b.d.l.	-	0.38	0.07	b.d.l.	-	1.27	1.01	0.01	0.01
Na_2O	3.02	0.03	2.3	0.1	3.1	0.1	3.8	0.6	11.41	0.04	12.5	0.4	10.69	0.09	8.89	0.06
K_2O	0.22	0.01	b.d.l.	-	b.d.l.	-	b.d.l.	-	0.74	0.03	b.d.l.	-	3.05	0.15	2.65	0.01
CO_2	n.d.	-	n.d.	-	n.d.	-	n.d.	-	n.d.	-	n.d.	-	n.d.	-	n.d.	-
Total	99.87	0.02	98.0	0.0	98	0.0	97	0.0	100.66	0.17	100.0	0.1	98.59	0.20	98.18	0.30
Phases																
Glass	+		+		+		+		+		+		+		+	
Olivine	-		-		+		+		+		-		+		+	
Opx	-		+		+		-		-		+		-		-	
Cpx	-		+		-		+		+		+		-		-	
Garnet	-		-		-		-		-		-		-		-	
Comment	*successful*		*unsuccessful*		*unsuccessful*		*unsuccessful*		*unsuccessful*		*unsuccessful*		*unsuccessful*		*unsuccessful*	
	Homogeneous, carbon-free glass.		Homogeneous glass with idiomorphic opx and cpx crystals. Not useful for centrifugation.		Large areas of quench and idiomorphic opx and olivine crystals. Not useful for C analysis.		Olivine equilibrium crystals and cpx within homogeneous glass. Not useful for C-analysis.		$Fe_{35}Ni_{65}$ was added to the silicate starting mix (ratio: 20/80). Run product consists of equilibrium olivine and cpx crystals. Interstitial melt only. Metal droplets smaller than 25 µm. Not useful for C-analysis.		Large areas of quench and idiomorphic opx and cpx crystals. Very low FeO content. Not useful for C analysis.		$Fe_{35}Ni_{65}$ was added to the silicate starting mix (ratio: 20/80). Run product consists of equilibrium olivine crystals. Interstitial melt only. Most metal droplets smaller than 10 µm. Not useful for C-analysis.		Olivine equilibrium crystals within homogeneous glass. Very low FeO content. Not useful for C-analysis.	

b.d.l. = below detection limit; n.d. = not determined; errors are given in 1 σ standard deviation based on replicate measurements using EPMA, SEM, LECO or SIMS.
Carbon was added through $CaCO_3$ to the starting mix.

Table 2.1 (continued)
Experimental conditions, quantitative analyses and results of different starting compositions.

Run #	**9-S-34**		**10-SM-31**		**11-S-70**		**12-S-64**		**1-B-35**		**1-1-B-63**		**2-B-53**	
Temperature (°C)	1450		1400		1400		1500		1500		1650		1500	
Pressure (GPa)	3		1.5		1.5		1.5		3.5		3.5		1.5	
Duration (h)	2		1.5		1.5		2		1.5		0.5		2	
Capsule type	Pt		Olivine		Olivine		Pt		Pt		Pt		Pt	
Silicate mix (wt.%)	**PB9**		**PB1**		**PB2**		**PB12**		**HAB1**		**HAB1-1**		**HAB2**	
SiO_2	52.0		45.9		47.5		46.2		50.4		42.7		52.2	
TiO_2	1.6		2.2		2.3		1.8		0.6		0.5		0.6	
Al_2O_3	8.8		7.6		7.9		10.0		19.5		16.5		20.2	
FeO	8.5		12.6		13.0		13.0		-		10.0		-	
MgO	10.0		7.9		8.1		11.8		10.8		9.2		11.2	
CaO	6.8		7.4		7.7		7.4		12.5		10.6		12.9	
NiO	-		3.9		0.3		0.6		-		-		-	
Na_2O	7.0		8.5		8.8		6.5		2.2		5.3		2.3	
K_2O	2.3		3.8		3.9		2.0		-		2.0		-	
CO_2	3.0		0.3		0.5		0.7		3.9		3.3		0.5	
Total	100		100		100		100		100		100		100	
Silicate melt (wt.%)	average	1 σ	average	1 σ	average	1 σ	average	1 σ	average	1 σ	average	1 σ	average	1 σ
SiO_2	54.5	0.1	45.46	0.27	46.31	0.30	47.6	0.3	52.23	0.11	49.2	0.3	52.9	0.3
TiO_2	1.9	0.1	1.95	0.05	2.03	0.07	2.0	0.1	0.64	0.01	0.6	0.1	0.6	0.1
Al_2O_3	7.9	0.1	6.30	0.08	6.25	0.05	9.1	0.1	17.93	0.12	17.1	0.2	19.5	0.2
FeO	7.2	0.1	11.51	0.11	12.72	0.18	13.4	0.2	b.d.l.	-	10.2	0.2	b.d.l.	-
MgO	8.9	0.1	14.77	0.19	13.88	0.15	10.3	0.1	9.07	0.04	8.2	0.1	11.0	0.1
CaO	7.3	0.1	6.58	0.08	6.50	0.11	8.0	0.1	13.32	0.05	11.9	0.2	13.2	0.1
NiO	b.d.l.	-	0.63	0.04	0.04	0.13	0.4	0.3	b.d.l.	-	b.d.l.	-	b.d.l.	-
Na_2O	7.1	0.1	6.70	0.07	7.14	0.23	7.4	0.3	2.47	0.08	2.7	0.1	2.2	0.1
K_2O	2.2	0.1	3.00	0.04	2.95	0.08	1.9	0.1	b.d.l.	-	b.d.l.	-	b.d.l.	-
CO_2	4.4	0.1	1.95	0.70	1.65	0.37	2.4	0.4	n.d.	-	2.9	0.5	0.8	0.4
Total	101.4	0.0	98.84	0.92	99.5	0.6	102.4	0.1	95.66	0.21	102.8	0.1	100.3	0.6
Phases														
Glass	+		+		+		+		+		+		+	
Olivine	-		-		-		-		-		-		-	
Opx	-		-		-		-		-		-		-	
Cpx	-		-		-		-		-		-		-	
Garnet	-		-		-		-		+		-		-	
Comment	*successful*		*successful*		*successful*		*successful*		*unsuccessful*		*successful*		*successful*	
	Homogeneous, carbon-bearing glass. C-content determined by LECO.		$Fe_{10}Ni_{90}$ was added to the silicate starting mix (ratio: 20/80). Run product consists of homogeneous, C-bearing glass and a large metal droplet (~700 µm diameter). C-content determined by SIMS.		Homogeneous, carbon-bearing glass. C-content determined by LECO.		Homogeneous, carbon-bearing glass. Fe added through Fe_2O_3 to avoid iron loss due to the Pt capsule. C-content determined by LECO.		Homogeneous, Fe-free glass with idiomorphic garnet crystals. Not useful for centrifugation.		Homogeneous, carbon-bearing glass. Fe added through Fe_2O_3 to avoid iron loss due to the Pt capsule. C-content determined by LECO.		Homogeneous, carbon-bearing, Fe-free glass. C-content determined by LECO.	

b.d.l. = below detection limit; n.d. = not determined; errors are given in 1 σ standard deviation based on replicate measurements using EPMA, SEM, LECO or SIMS.
Carbon was added through $CaCO_3$ to the starting mix.

Table 2.2
Starting compositions of the metal mixture in wt.%.

Metal mix	F1	F2	FN1	FN2	FN3	FN4	FN5	FS1	FS2	FS3	FS4	FS5
Fe	100	98	9.9	49.7	10	35	80	83	81.4	79.0	83.8	87.6
Ni	-	-	89.5	49.7	90	65	20	-	-	-	-	-
Si	-	-	-	-	-	-	-	17	16.7	16.2	11.4	7.6
C	-	2.0	0.6	0.6	-	-	-	-	1.9	4.8	4.8	4.8
Total	100	100	100	100	100	100	100	100	100	100	100	100

Carbon was added through graphite powder to the starting mix.

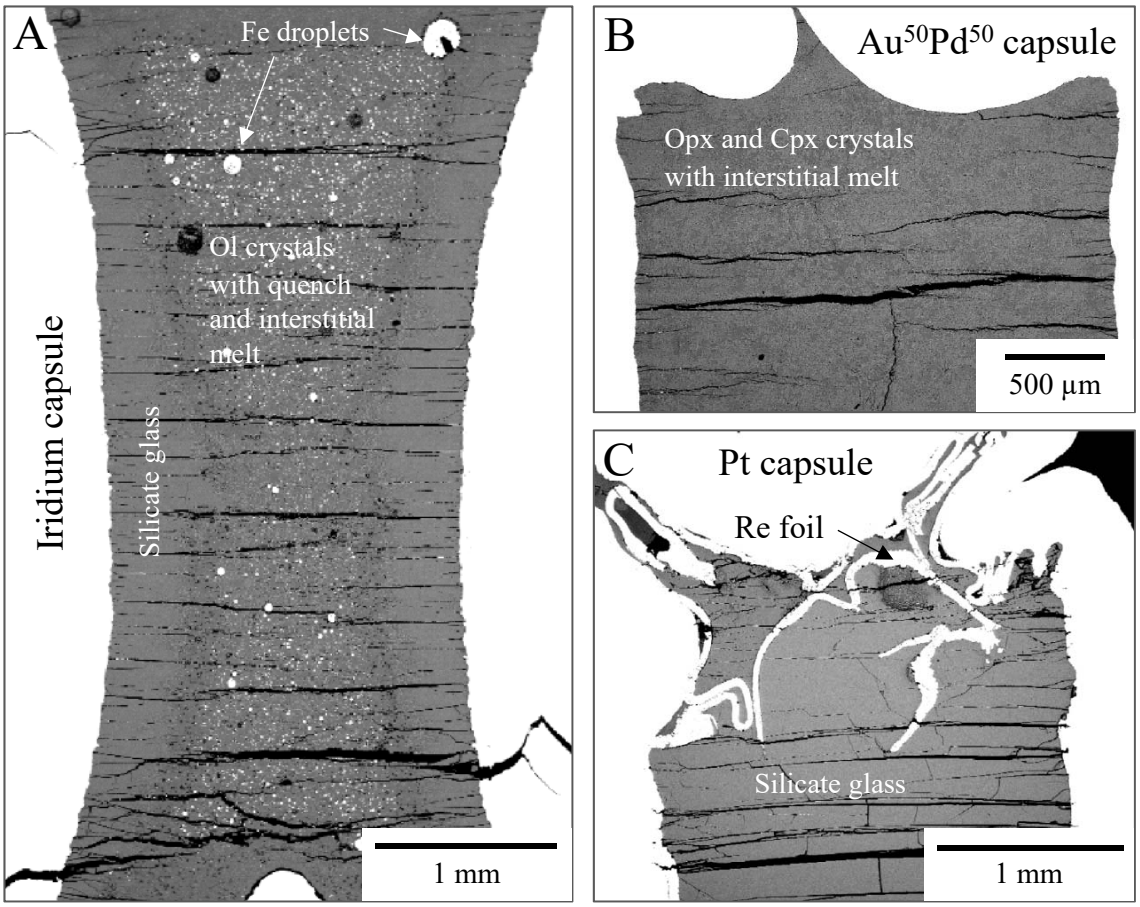

Fig. 2.1. *Back-scattered electron images of silicate melt – metal melt equilibrium experiments performed in different capsule materials at 1400 -1450°C and 3 GPa. In all samples, severe loss of the metal melt occurred.* ***A:*** *The inner part of the experimental charge consists of small metal droplets, equilibrium olivine crystals, interstitial melt and quench, whereas in the outer part the metal melt is completely detracted by the iridium capsule, leaving silicate glass behind.* ***B:*** *The metal melt is entirely absorbed by the $Au^{50}Pd^{50}$ capsule, such that the remaining experimental charge consists of opx and cpx crystals with interstitial melt.* ***C:*** *The metal melt is entirely absorbed by the rhenium foil and Pt capsule. The remaining experimental charge consists solely of silicate glass.*

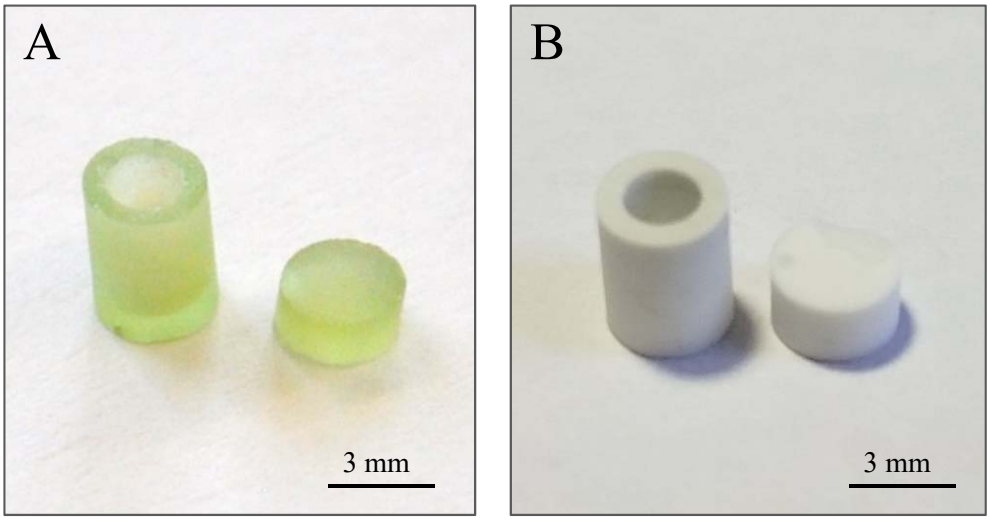

Fig. 2.2. *C-free capsule materials for silicate melt – metal melt equilibrium experiments.* ***A:*** *San Carlos olivine (fO_2-conditions of ~ ΔIW -1). San Carlos olivine (X_{Mg}=91) does mostly not allow for fO_2 < ΔIW -1 as it diminishes its fayalite component constantly supplying Fe^{2+}.* ***B:*** *Synthetic forsterite sintered in HIP (for experiments at fO_2 in the range of ~ ΔIW -2 to ~ ΔIW -5).*

alloy prevents equilibrium. In order to avoid this, we also tested dense alumina as capsule material, but the crystallisation of spinell and clinopyroxene prevented the formation of larger glass or metal pools. Further, the interstitial silicate glass contained more than 20 wt.% Al_2O_3 due to the dissolution of the capsule material, which is not representative for magma ocean compositions. Finally, we used San Carlos olivine capsules, yielding olivine-saturated silicate melts appropriate for the simulation of magma ocean melts. Almost all experiments were equilibrated at oxygen fugacities of ~ ΔIW -1.5. Lower fO_2-conditions could not be achieved, e.g., by adding metallic Si to the starting mixture, because the San Carlos olivine replenishes the Fe-poor silicate melt with FeO. To avoid this, we additionally used Fe-free synthetic forsterite capsules providing more reducing conditions in the experimental charges, down to ΔIW -4.8.

The synthetic forsterite was produced by hot hydrostatic pressing. Thereby, 1 kg of pre-dried spectroscopically pure MgO and SiO_2 were stoichiometrically mixed for more than 3 hours. Afterwards, the Mg_2SiO_4 powder was filled in a cylindrical stainless steel canister (35 mm diameter, 200 mm height, lined with molybdenum foil to avoid Fe diffusion) and uniaxially cold pressed. The canister was then sealed and hot isostatically pressed using an internally heated gas vessel (ABRA Fluid AG, Switzerland) at 1200°C and 1000 bar for 6 hours.

The sintered forsterite and the single crystal San Carlos olivine capsules consisted of a cylindrically-

shaped olivine rod of 3.4 mm in diameter and 4.0 mm in height, closed with a 2.0 mm thick olivine lid (Fig. 2.2). A borehole of 3.4 mm depth and 2.0 mm in diameter was drilled into the olivine rod using a diamond hollow drill bit to create space for the experimental charge. For the synthesis of standards, larger olivine capsules (4.4 mm capsule diameter, 3.0 mm borehole diameter) were used to increase the sample volume. All olivine capsules were placed inside an outer platinum capsule (4 or 5 mm diameter, 8 mm height) to ensure that carbon, in the form of C-H-O species, remained inside the system. In order to avoid cracks of the olivine capsule, some olivine powder (~ 10 − 12 mg) was inserted into the platinum capsule at the bottom and the top. Further, the outer diameter of the olivine capsule had to be strictly between 3.3 and 3.4 mm to enable a smooth insertion into the Pt capsule. In case the olivine capsules showed an outer diameter slightly larger than 3.4 mm, they were grinded by hand to the correct size using sandpaper.

In order to expand the experimental conditions to higher temperatures (> 1750°C) and pressures (6 GPa), some experiments were performed in graphite capsules. Using graphite as capsule material is problematic in carbon-partitioning studies, because the omnipresent graphite, either as nano-particles within the silicate melt, graphite blades or precipitates during quenching, may cause analytical difficulties.

2.1.3 Piston cylinder experiments

Experiments were carried out at ETH Zurich using a 14 mm Boyd and England type (Boyd and England, 1960) end-loaded piston cylinder apparatus. The Boyd & England piston cylinder apparatus is a high-pressure device, covering the pressure conditions of the entire crust and the uppermost mantle (pressure up to 3.8 GPa). The main constituents of the apparatus are a tungsten carbide 14 mm piston, a pressure vessel, a bottom pressure plate (bridge), a thermocouple protection plate, a top pressure plate, a hydraulic piston, a hydraulic pump, and a transformer (see Fig. 2.3A). A piston is hydraulically pressed into the pressure vessel where the sample, surrounded by a graphite heater, is placed. The transformer current delivers the power to the heater to increase the temperature at the sample. The temperature is controlled by a thermocouple, which is placed on top of the sample assembly (Fig. 2.3B).

The piston cylinder assembly consists of inner MgO cylinders and sleeves (dehydrated at 1000°C overnight) surrounded by a graphite heater and talc-Pyrex sleeves (experiments ≤ 1500°C) or talc-SiO_2-glass sleeves (experiments ≥ 1600°C). The capsule was centred at the hotspot of the assembly to

minimise temperature gradients (temperature uncertainty ± 7°C) and insulated from the thermocouple by a ruby disc. Mullite thermocouple sleeves and type B PtRh thermocouples were used for experiments at ≤ 1500°C, and type C WRe thermocouples but dense Al_2O_3 sleeves for experiments at ≥ 1600°C. Pressure calibration against the quartz-coesite transition (Bose and Ganguly, 1995) showed a friction of 10 %. Before heating the experiment, the initial piston pressure was set to ~ 0.5 GPa to ensure that all assembly parts are in contact such that the electrical circuit is closed. Subsequently, the experimental setup was heated with 50°C/min to 600°C to soften the pyrex. For experiments using SiO_2 glass instead of pyrex, the experimental setup was heated to 1000°C before the pressure was steadily and simultaneously increased with temperature to the desired run conditions. Experiments were quenched at rates of 100 – 200°C/s by switching off the electric power of the furnace.

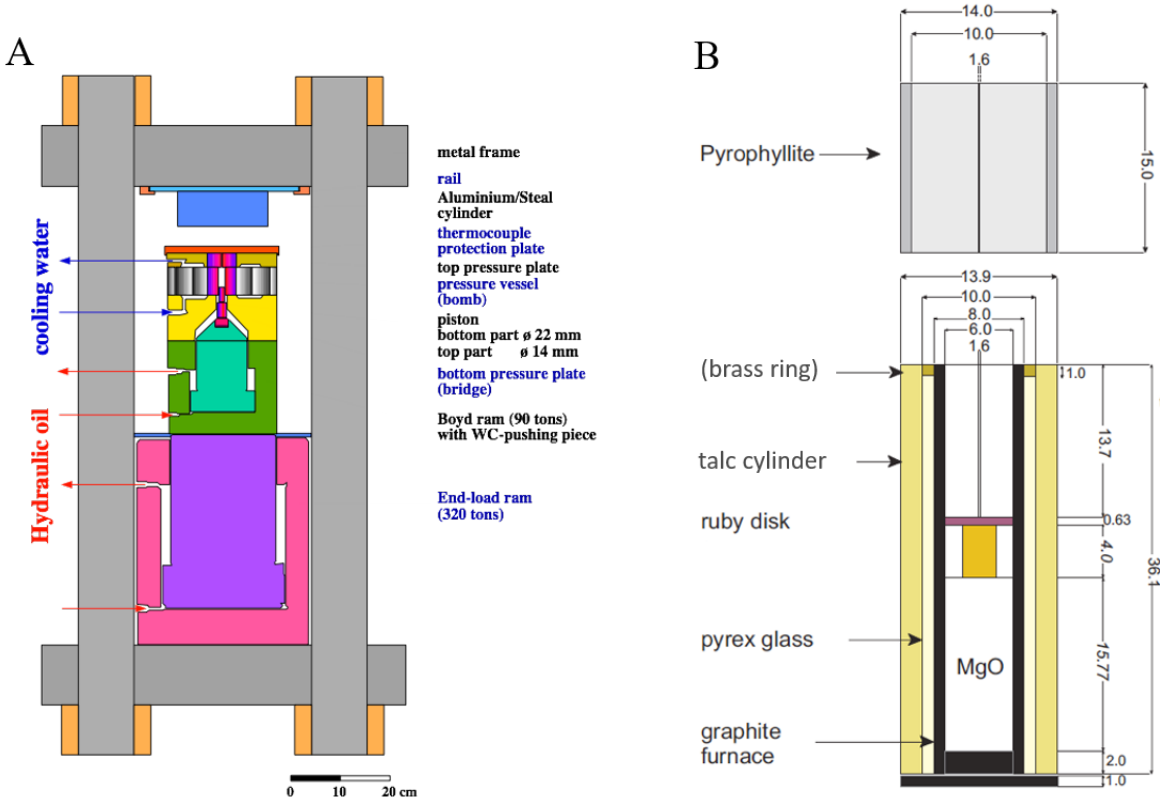

Fig. 2.3. A: *Main constituents of the piston cylinder apparatus.* ***B:*** *Sample assembly. The capsule is placed in the middle of the assembly which is essential to avoid any significant temperature gradient (temperature uncertainty ± 7°C). Thus, the capsule is surrounded by MgO spacers (6 mm diameter) that are used as electrical insulators. The upper MgO spacer and the stainless steel top plug contain a tube for the thermocouple. The MgO spacer assembly is surrounded by a graphite heater, whereas its temperature is monitored by the thermocouple. The pyrex or SiO_2 glass helps prevent talc contamination of the graphite heater which could occur as talc flows under high pressure. Talc acts as a thermal insulator and it deforms plastically to ensure near hydrostatic pressure conditions around the sample with low friction losses at around 10 %. The hardened steel plug on top of the talc sleeve conducts the electric current to the graphite heater. It is separated from the tungsten carbide pressure vessel by a pyrophyllite spacer, which is an electrical insulator with high friction, used as gasket material. At the other end of the heater (bottom), a graphite disc (14 mm) also conducts the electricity to the heater such that an electrical circuit is closed.*

In this doctoral study the piston cylinder apparatus was used to synthesise appropriate analytical standards for SIMS analyses (see section 2.1.5) and to run silicate metal melt equilibrium experiments at moderately high pressures (1.5 to 3.5 GPa) and temperatures (1300 − 1900°C), varying oxygen fugacities (ΔIW +2.2 − ΔIW -4.8) and different silicate melt compositions (NBO/T 1.0 − 3.1).

The silicate and metal melts of some experiments were gravitationally separated to create larger melt pools necessary for SIMS and bulk analyses. After pre-equilibration in the static piston cylinder, separation was reached by a centrifuging piston cylinder apparatus (Schmidt et al., 2006), which is a worldwide unique experimental apparatus only available at ETH Zurich (Fig. 2.4A). The centrifuge consists of a rotating circular table of 1.38 m in diameter and 860 kg weight. The piston cylinder mounted in the table of the centrifuge (Fig. 2.4B) can achieve pressures up to 1.8 GPa and temperatures up to 1600°C. The acceleration of the centrifuge reaches 3000 g which corresponds to 753 km/h or 2850 revolutions per minute (rpm). The centrifuging piston cylinder includes a 14 mm tungsten carbide piston and follows the same sample assembly as shown above for the Boyd & England apparatus. The capsule containing the experimental charge can have dimensions of 4 mm diameter and 6 mm length.

The experiments of this doctoral study were centrifuged at an acceleration of 800 g, which was applied for at least 30 minutes to achieve complete separation of the melt pairs (Fig. 2.5).

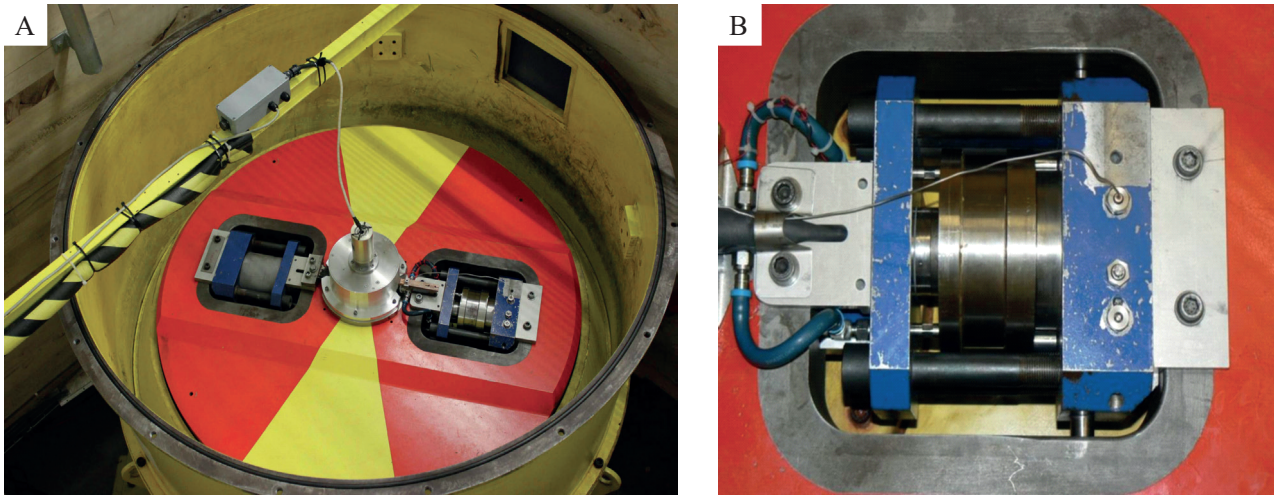

Fig. 2.4. A: *Centrifuging piston cylinder apparatus.* ***B:*** *Detailed image of the piston cylinder.*

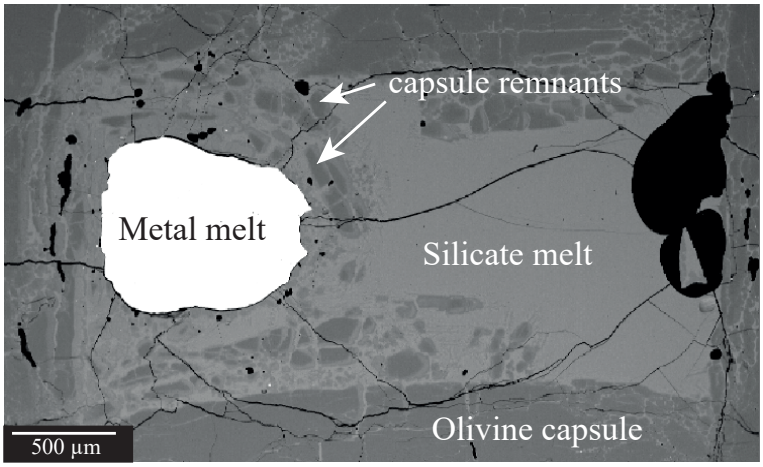

Fig. 2.5. *Back-scattered electron image of a centrifuged piston cylinder experiment. The silicate and metal melt pair is succesfully separated.*

2.1.4 Multi-anvil experiments

The multi-anvil apparatus is a solid media pressure device which is able to simulate conditions of the transition zone and the uppermost lower mantle (up to 2300°C and 24 GPa). Some experiments were performed using a 1000 tons multi-anvil device at ETH Zurich in order to constrain the effect of pressure on carbon partitioning. Experiments were conducted in graphite capsules at 6 GPa and temperatures ranging from 1650 to 2000°C. In Fig. 2.6A the mechanism of the multi-anvil apparatus is schematically illustrated. The six so-called first stage anvils press onto the faces of a cube, which is assembled from eight smaller cubes. The latter are called second stage anvils, which have a truncated corner perpendicular to a <111> direction to form an octahedral void in their centre. In this void the octahedral pressure medium is positioned, which contains the assembly shown in Fig. 2.6B. The smaller the octahedron, the higher the pressure. The octahedral pressure medium consists of MgO, doped with 5% Cr_2O_3. To monitor the temperature, a thermocouple is placed on top of the sample assembly (see Fig. 2.6B). In general, thermal gradients in multi-anvil experiments are larger compared to piston cylinder experiments due to the short furnace length (thermal gradients increase with decreasing cell volume and increasing temperature). To minimise the temperature gradient, a 3-stepped furnace of $LaCrO_3$ is used.

In this doctoral study, an 18/11 mm assembly combined with 32 mm edge length tungsten carbide anvils was used. The experimental charge was pressurised cold and then stadily heated with ~ 100°C/min. Experiments were quenched by switching off power.

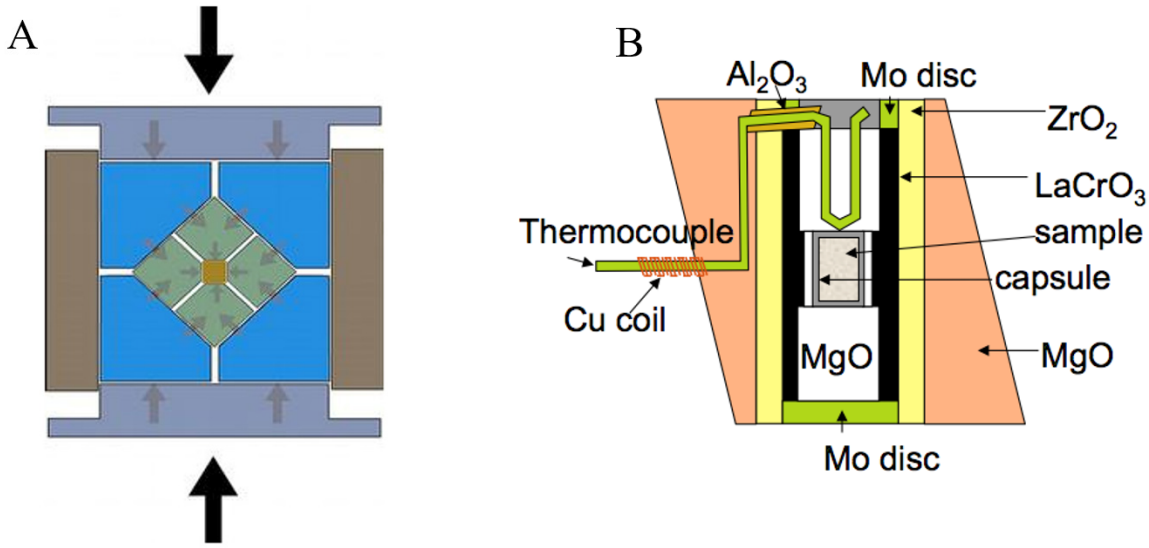

Fig. 2.6. A: *Mechanism of the multi-anvil apparatus.* ***B:*** *Sample assembly.*

2.1.5 Synthesis of analytical standards for carbon analysis

In this section, the syntheses of carbon standards for secondary ionisation mass spectrometry (SIMS) are described. To receive meaningful carbon contents determined by SIMS, it is crucial to use matrix-matching standards, due to this method's high sensitivity to matrix-effects. Therefore, it is required to synthesise analytical standards with the same major element composition and the same carbon concentration as both the silicate melt and metallic melt samples (acceptable deviations are 10 % maximum).

The synthesis of matrix-matching standards for silicate glasses is challenging, because the silicate glass samples are equilibrated at high pressure and temperature with metallic melt in olivine capsules, which leads to a compositional shift that is difficult to match. Therefore, several silicate glass standards are synthesised with different starting compositions in different capsule materials in order to receive a broad range of compositions that cover the chemistry of all experimental glass samples (Table 2.3).

For subsequent evaluations, the capsule containing the silicate glass was cut with a diamond wire saw into several pieces. One piece of silicate glass was recovered for bulk analyses (carbon content) as described in Section 2.2.3. The other glass pieces were prepared for EPMA (major element composition, see Section 2.2.1) and subsequently used as analytical carbon standard for SIMS. Fig. 2.7 shows the cross section of standard glasses, representative for each capsule material.

For SIMS analyses of carbon concentrations in metallic melt, it would also be preferrable to use matrix-matching standards. Unfortunately, it is not straightforward to synthesise a homogeneous metallic

Table 2.3
Experimental conditions of standard synthesis, starting material and composition of the run product.

Run #	**12-S-64**	**11-S-70**	**9-S-76**	**2-B-71**	**2-B-73**
Temperature (°C)	1500	1400	1450	1500	1500
Pressure (GPa)	1.5	1.5	3	1.5	1.5
Duration (h)	2	1.5	3	2.25	1.5
Capsule type	Pt	Olivine	Ir	Olivine	Pt
Silicate starting mix (wt.%)					
SiO_2	46.2	47.5	52.0	52.2	52.2
TiO_2	1.8	2.3	1.6	0.6	0.6
Al_2O_3	10.0	7.9	8.8	20.2	20.2
FeO	13.0	13.0	8.5	-	-
MgO	11.8	8.1	10.0	11.2	11.2
CaO	7.4	7.7	6.8	12.9	12.9
NiO	0.6	0.3	-	-	-
Na_2O	6.5	8.8	7.0	2.3	2.3
K_2O	2.0	3.9	2.3	-	-
CO_2	0.7	0.5	3.0	0.5	0.5
Total	100	100	100	100	100
Composition of silicate melt (wt.%)					
SiO_2	47.64 ± 0.27	46.31 ± 0.30	51.80 ± 0.29	47.47 ± 0.28	52.45 ± 0.19
TiO_2	1.95 ± 0.07	2.03 ± 0.07	1.59 ± 0.06	0.40 ± 0.05	0.64 ± 0.05
Al_2O_3	9.06 ± 0.06	6.25 ± 0.05	8.37 ± 0.13	12.20 ± 0.11	19.57 ± 0.10
FeO	13.35 ± 0.15	12.72 ± 0.18	7.60 ± 0.09	6.97 ± 0.10	0.00 ± 0.00
MgO	10.31 ± 0.08	13.88 ± 0.15	9.41 ± 0.14	22.39 ± 0.25	10.94 ± 0.05
CaO	7.99 ± 0.10	6.50 ± 0.11	6.47 ± 0.11	7.90 ± 0.05	13.03 ± 0.17
NiO	0.42 ± 0.29	0.04 ± 0.13	0.01 ± 0.01	0.00 ± 0.00	0.02 ± 0.02
Na_2O	7.38 ± 0.29	7.14 ± 0.23	6.57 ± 0.13	1.37 ± 0.05	2.27 ± 0.10
K_2O	1.90 ± 0.06	2.95 ± 0.08	2.16 ± 0.05	0.00 ± 0.00	0.01 ± 0.01
C	0.65 ± 0.12	0.45 ± 0.12	1.33 ± 0.13	0.68 ± 0.12	0.17 ± 0.02
Total	100.65	98.27	95.29	99.37	99.09

For each silicate glass, typically 10 - 15 spots were analysed by EPMA.

Carbon concentrations of silicate glasses were measured by bulk analysis (LECO). Each sample was analysed 2 - 3 times, exept run 2-B-73 that was analysed 9 times.

The standard deviation (1σ) of all elements is based on the replicate analyses.

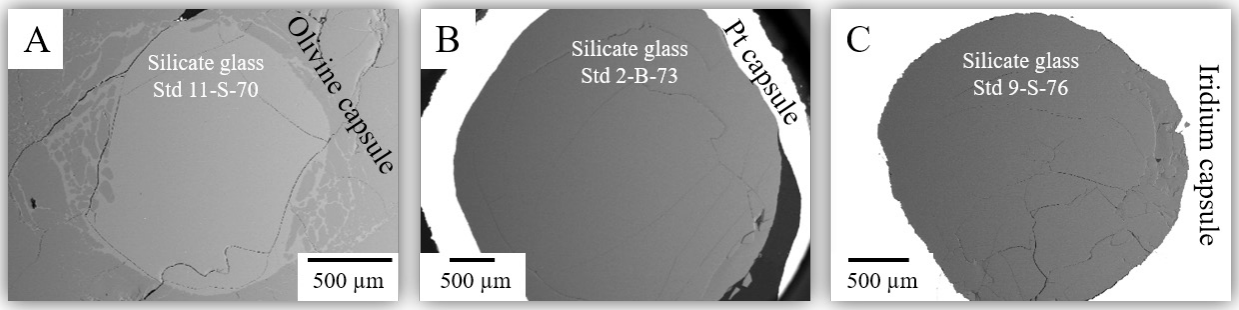

Fig. 2.7. *Back-scattered electron images of silicate glass standards performed in different capsule materials. The images demonstrate the cross section of the capsule. Experimental conditions and chemical compositions are shown in Table 2.3.* ***A:*** *Silicate glass of standard 11-S-70 conducted in San Carlos olivine.* ***B:*** *Silicate glass of standard 2-B-73 conducted in a platinum capsule.* ***C:*** *Silicate glass of standard 9-S-76 conducted in an iridium capsule.*

alloy of any desired composition, because Fe-Ni or Fe-Si alloys are not quenchable. Consequently, instead of a homogeneous alloy, the metal consists of exsolution lamellae and dendritic structures, which are problematic to use as standard material (see Appendix A). A possibility to circumvent this problem is to synthesise stoichiometric Fe-Ni carbide $(Fe,Ni)_3C$. This has the disadvantage that the carbon concentration is stoichiometrically prescribed, being 6.69 wt.%. Since our Fe-rich metal melts contain on average 5.6 ± 0.7 wt.% C in all experiments, using stoichiometric $(Fe,Ni)_3C$ appears to be appropriate. Following the procedure described in Buono et al. (2013), cohenite was crystallised from an S-rich liquid at 1100°C and 3 GPa in a MgO-Pt double capsule (Table 2.4). The dimensions of the MgO capsule were 4.4 mm diameter and 6.5 mm length with a 0.6 mm thick inner lid (2.8 mm diameter) and a 1.0 mm outer lid (4.4 mm diameter). The MgO capsule assembly was inserted into a 5.0 mm diameter Pt capsule to prevent melt escape. As shown in Fig. 2.8, the experimental run product was composed of two parts. One part contained the actual stoichiometric Fe-Ni carbide, and the other part consisted of Fe-Ni-rich dendrites embedded in an S-rich liquid. The sample material was carefully cut with a diamond wire saw at the interface of both parts and the Fe-Ni carbide was prepared for EPMA (Fe and Ni contents) analysis and subsequently used as analytical carbon standard for SIMS (see also Sections 3.2.2 and 4.2.2). All metal standards were also analysed for Pt, yielding values below the detection limit. Thus, contamination from the outer capsule material can be excluded.

In order to assure that the homogeneous phase as shown in Fig. 2.8 is indeed $(Fe,Ni)_3C$, some sample material was pulverised and analysed by X-ray powder diffraction (Bruker D8 Advance, ETH Zurich). The result is shown in Fig. 2.9 and demonstrates that our XRD pattern (red lines) is congruent with the one for cohenite available in the ICDD database (grey lines).

Table 2.4

Experimental conditions of standard synthesis, starting material and composition of the run product.

Run #	Cohenite-55	Cohenite-75	Cohenite-105
Temperature (°C)	1100	1100	1100
Pressure (GPa)	3	3	3
Duration (h)	48	48	48
Capsule type	MgO	MgO	MgO
Metal starting mix (wt.%)			
Fe	85.3	85.3	85.3
Ni	5.3	5.3	5.3
C	4.7	4.7	4.7
S	4.7	4.7	4.7
Total	100	100	100
Composition of cohenite (wt.%)			
Fe	90.75 ± 0.20	89.57 ± 0.67	89.10 ± 0.23
Ni	2.84 ± 0.04	3.06 ± 0.08	3.29 ± 0.05
C	6.69	6.69	6.69
S	b.d.l.	b.d.l.	b.d.l.
Total	100.28	99.31	99.07

For each cohenite, typically 10 spots are analysed by EPMA. The standard deviation (1σ) of Fe and Ni is based on the replicate analyses. S content of cohenite is below the detection limit (b.d.l.).

Cohenite ($(Fe,Ni)_3C$) is identified with X-ray powder diffraction.

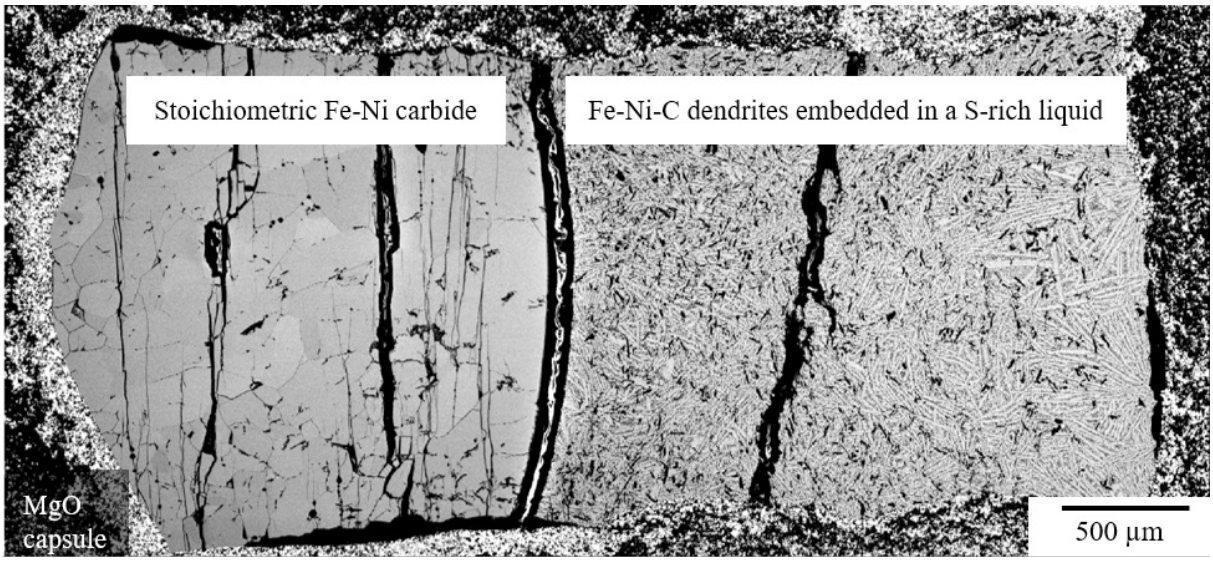

Fig. 2.8. *Back-scattered electron image of stoichiometric Fe-Ni carbide (left part) and Fe-Ni-C dendrites embedded in a S-rich liquid (right part) synthesised in a crushable MgO capsule (run Cohenite-55). The stoichiometric Fe-Ni carbide is used as metal carbon standard for SIMS analyses. Experimental conditions and chemical compositions are shown in Table 2.4.*

We also examined the synthesis of pure Fe_3C and Fe_7C_3 at different experimental conditions and assemblies (see Appendix A), but several issues occurred including iron loss, contamination of the capsule material, and heterogeneous dendritic quench structures. Using diamond powder instead of

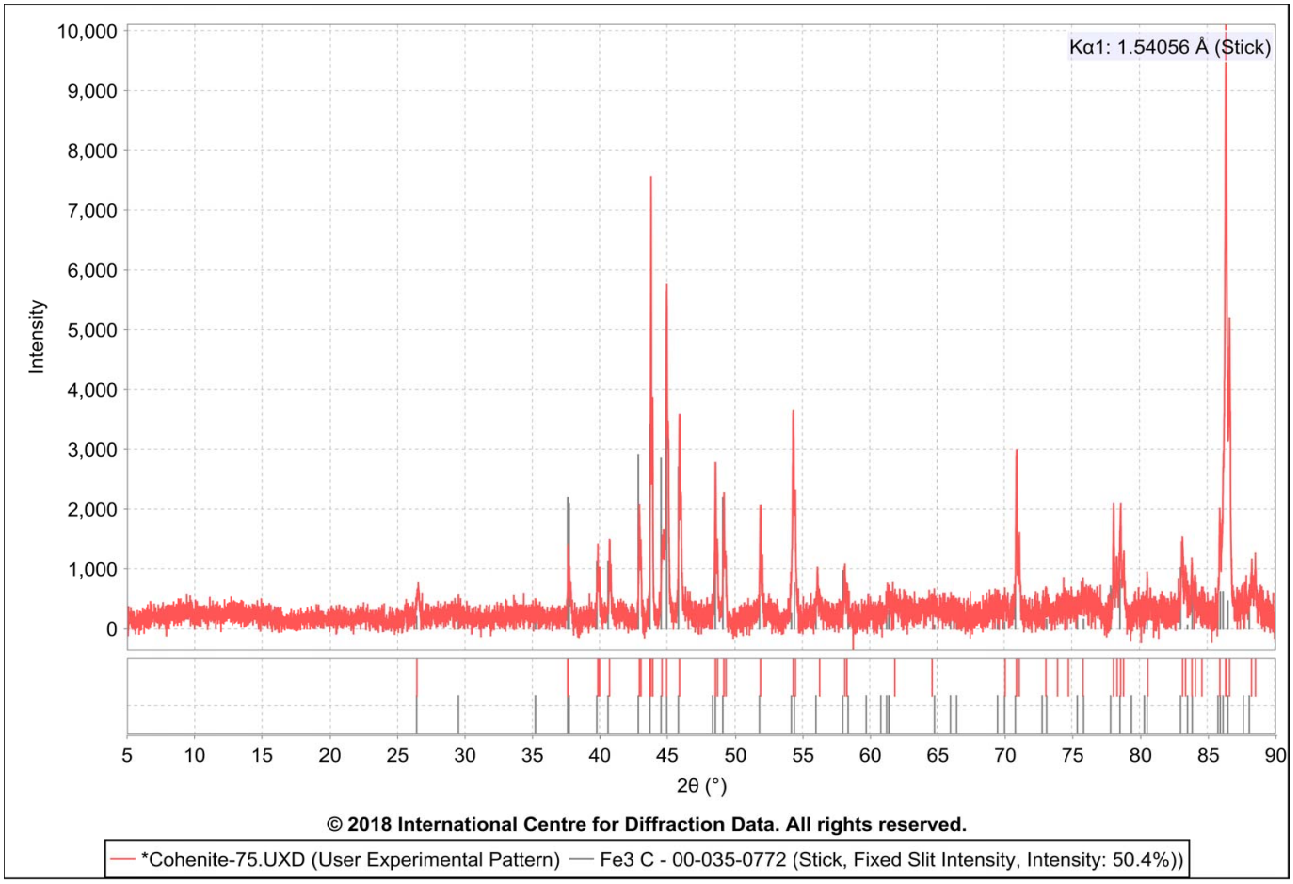

Fig. 2.9. *X-ray powder diffraction pattern of experimentally synthesised Cohenite-75 recorded by a Bruker D8 Advance XRD at ETH Zurich. Red lines represent the position of the reflection peaks of our sample, which are congruent with those reported for cohenite (Fe_3C) in the ICDD database (grey lines).*

graphite powder as carbon source was also tested, yielding useless run products that consisted of a heterogeneous mixture of Fe-carbide, graphite pockets and crystallised wüstite (FeO).

2.1.6 Sample preparation

After the experiment, the recovered capsules were embedded in methyl methacrylate epoxy resin and hand-polished with abrasive paper until the experimental charge was exposed. For fine polishing, polycrystalline diamond suspension (MetaDi™ Supreme from BUEHLER) of 3 and 1µm was employed, yielding a highly polished sample surface as required for electron microprobe analyses (EPMA), secondary ion mass spectrometry (SIMS), and Raman spectroscopy. For bulk analyses using an elemental carbon analyser (see 2.2.3), the capsules were opened with a 300 µm diamond wire saw. The quenched metal and silicate glasses were then carefully recovered in several fragments.

To ensure the purity of each sample, fragments showing any remnants of the olivine capsule or quench olivine needles in the glass were excluded from further analyses.

2.2 Analytical methods

2.2.1 Electron microscopy

Microstructural characterisation and chemical evaluation of the experimental products were first conducted using a scanning electron microscope (JEOL JSM-6390 LA SEM) at ETH Zurich. Successful experiments were then determined using a JEOL electron microprobe JXA 8900 equipped with five spectrometers at the Goethe University of Frankfurt.

All samples were carbon-coated and 10 - 15 points per glass were analysed. Analytical conditions used for silicate glasses (Si, Ti, Al, Fe, Mg, Ca, Ni, Na, K) were 15 kV accelerating voltage, 20 nA beam current, and a peak and background counting time of 20 s. For metal alloys (Fe ± Ni ± Si) the conditions were 20 kV, 30 nA and 30 s, respectively. A 30 µm diameter beam was used to obtain homogeneous analyses, especially in the heterogeneous quench textures of the metal melts. In addition to SIMS analyses (section 2.2.2), the metal melts of 11 samples were analysed for carbon contents by electron microprobe. Therefore, the previous carbon coat of the samples was carefully removed by re-polishing the samples with 1 µm corundum polishing paste. Subsequently, conductive silver paint was applied to ground the metal sample surface to the sample holder. Dissolved carbon in the metal alloy was quantitatively measured with 10 kV accelerating voltage, 120 nA beam current and 20 s peak and background counting time. To minimise the carbon blank content within the sample chamber, a decontaminant device ("cold finger") was installed, which improves the vacuum and removes any present organic hydrocarbon molecules by condensation. For the silicate melt, a NIST mineral glass (NBS K-412) was used as analytical standard. For the metal melt, pure Fe, Ni and Si metal standards from NIST were used, and for carbon measurements an experimentally-synthesised stoichiometric cohenite ($(Fe,Ni)_3C$) was used as standard (see section 2.1.5). The quantitative major element compositions of the metallic and silicate melts were determined with a precision of 1 rel. %. The detection limit of C in the metallic melt is 0.05 wt.%.

2.2.2 Secondary ionisation mass spectrometry (SIMS)

Secondary ion mass spectrometry (SIMS) is a reliable method of surface analysis using a finely focused primary ion beam under high vacuum to probe the surface of a selected sample domain.

The polished sample surface is bombarded with primary ions (Cs^+), which causes the emission of ions out of the sample. These secondary ions are analysed by a mass spectrometer due to their mass differences.

A great advantage of this method over EPMA is the higher sensitivity for light elements, including C. A challenging factor of SIMS is that the quality of the final data strongly depends on the quality of the sample preparation. Therefore, the sample must be flat (less than 1 µm topography), well-polished and largely free of scratches.

In this doctoral thesis, carbon concentration in silicate glasses and the quenched metallic alloy were measured using the IMS 1280HR ion probe at the SwissSIMS laboratory at the University of Lausanne. Samples were re-polished to remove previous C coating, and surrounding epoxy was cut off using a diamond saw. Subsequently, a 300 µm diamond wire saw was used to cut the samples at the contact between the platinum outer capsule and the olivine or graphite inner capsule. After removing all four sides of the capsule, the inner part was recovered and mounted in indium. Usually 4 to 6 samples were mounted together with the standards in one single indium mount and coated with ~ 40 nm gold.

The primary beam of $^{133}Cs^+$ was used with intensities of ~ 2 and ~ 0.2 nA for metal and silicate melts, respectively. A lower intensity for silicate melts was chosen to enable analysis of all samples with identical analytical conditions (regardless of their C content) using an electron multiplier (EM) with a field aperture of 4000 µm and an energy slit of 50 µm. Entrance slits were closed to 122 µm width and exit slits to 405 µm, resulting in a mass resolving power of ~ 3000 ($M / \Delta M$).

Prior to each analysis, pre-sputtering times of 180 s for metal and of 130 s for glass were applied, using a raster beam of 50 µm diameter to avoid any surface contamination during analyses. Automatic centring of secondary deflectors after pre-sputtering was achieved on ^{12}C and ^{28}Si for metal and glass, respectively. For the actual measurements, a raster of 30 × 30 µm was used to homogenise the signal from heterogeneous quench structures, which particularly occurred in the metal melt.

Each analysis was performed in mono-collection mode and consisted of 20 cycles of the peak-stepping sequence mass 11.8 (background: 2 s), $^{12}C^+$ (3 s, FC), $^{28}Si^+$ (1.6 s, EM), $^{56}Fe^+$ (1.8 s, EM) for metal, and 11.8 (2 s), $^{12}C^+$ (5 s, EM), $^{28}Si^+$ (3 s, FC), $^{56}Fe^+$ (1 s, FC) for silicate glasses. In order to minimise the effect of primary intensity variations, $^{28}Si^+$ and $^{56}Fe^+$ were used to normalise $^{12}C^+$ intensities in glasses and metals, respectively. Both elements were consecutively analysed during the measurements of both metals and glasses to enable a reasonable magnet stability over successive sessions of these two

materials.

Carbon standards for silicate glasses were experimentally synthesised in order to produce matrix-matching glasses (see section 2.1.5). All standards were analysed with independent methods, i.e., X-ray powder diffraction for identifying stoichiometric cohenite, and a conventional elemental analyser (LECO CS844) to determine the bulk carbon content of the standard glasses by non-dispersive infrared cells (see section 2.2.3).

Typical standard reproducibility was 1 - 6 % (standard deviation (1SD) relative) for glasses and 1 - 3 % (1SD relative) for metals. For SIMS measurements, internal errors (standard error of the mean (1SE) over the 20 cycles) were usually < 2 % for glasses and < 1 % for metals. Internal errors were larger (~ 8 %) for glasses with lower C contents, typically below 0.5 wt.%. The final uncertainty on the C content for each individual point of the analyses was computed as follows:

$$1SE_{unk}\ (wt.\%) = C_{unk}\sqrt{\left(\frac{1SE^{unk}_{SIMS}}{R^{unk}_{SIMS}}\right)^2 + \left(\frac{1SE^{std}_{SIMS}}{R^{std}_{SIMS}}\right)^2 + \left(\frac{1SE^{std}_{ref}}{C^{std}_{ref}}\right)^2}. \quad (2.1)$$

Here, $1SE_{unk}$ represents the final uncertainty in wt.% of the analysis, C_{unk} is the C content in wt.% of the analysis, $1SE^{unk}_{SIMS}$ is the standard error of the mean of the 20 cycles of a SIMS analysis, R^{unk}_{SIMS} is the ratio measured directly from the SIMS analysis (i.e. $^{12}C/^{28}Si$ for glasses and $^{12}C/^{56}Fe$ for metals), $1SE^{std}_{SIMS}$ represents the standard error of n analyses of the standard used to calibrate the SIMS measurement, R^{std}_{SIMS} is the mean of n analyses of the standard used to calibrate SIMS measurements, $1SE^{std}_{ref}$ represents the standard error of the mean of the independent C content of the standard used during the SIMS session, C^{std}_{ref} is the carbon content of the standard used to determine the C content of the unknown. The final uncertainty strongly depends on the C content of the material analysed since the $1SE^{unk}_{SIMS}$ is related to counting statistics.

2.2.3 Elemental analyser (EA)

Bulk carbon content of (1) glass standards used for SIMS measurements, and (2) silicate and metal melt pairs of two selected samples (HAB2F2-54, -72) were determined using non-dispersive infrared cells of a CS844 LECO elemental carbon analyser at ETH Zurich. Sample fragments of glass and metal ranging from 1 to 10 mg sample mass were inserted into low carbon and low sulphur ceramic crucibles (LECO Part No. 529-018), together with 1 g of copper flux to enable homogeneous

combustion by the induction furnace. Copper flux is crucial in particular for the non-conducting glass samples, but was also added to the metal samples to keep the carbon blank signal consistent. Depending on the available amount of sample material, measurements were repeated two or three times. Prior to each session, crucibles were annealed at 1000°C for at least 2 hours to minimise the carbon blank signal. The latter was determined by the combustion of 5 to 6 sintered crucibles filled with 1 g of copper flux, defining the carbon detection limit of 0.5 µg. At each analysis, the combustion area was purged with oxygen for 20 s to eliminate any atmospheric impurities. After purging, a delay time of 25 s was given to the instrument to establish a stable baseline for detection. The actual time period of analysis, where the sample carbon peaks were collected, was set to 60 s for glass and metal analyses. A sample cooling time of 5 to 10 s was applied when the analysis was completed to avoid splashing of hot material while the furnace pedestal was lowered. As shown in Fig. 2.10, calibration was made for each carbon mass range using a synthetic carbon standard (0.12 ± 0.01 wt.% C) and a high purity iron standard (0.0062 ± 0.0008 wt.% C), both LECO reference materials (Part No. 502-632 and 501-950, respectively).

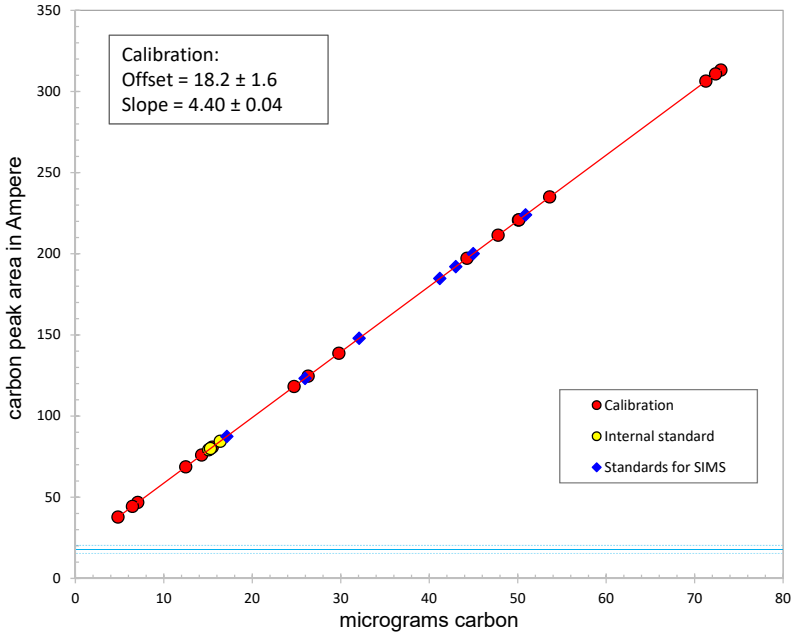

Fig. 2.10. *Calibration curve for bulk carbon analyses by a CS844 LECO elemental carbon analyser. The carbon blank signal (offset) of 18.2 A carbon peak area (solid blue line, errors in dashed blue lines) corresponds to a carbon detection limit of 0.5 µg absolute carbon content. Peak areas of measured samples correspond to 40 – 50 µg.*

As shown in Fig. 2.11, the C concentrations determined by LECO and SIMS do not match very well within uncertainties. This is most likely due to the fact that the separation of the silicate glass and the metal droplet from the olivine capsule material was very difficult. Therefore, the sample weight used for bulk analyses was probably overestimated and C concentration was consequently underestimated. To circumvent this problem, samples were mainly analysed by SIMS for C measurements. The elemental bulk analyser, however, was only used for measuring the C concentration of silicate glass standards, where the glass fragments could be easily separated from the surrounding capsule material.

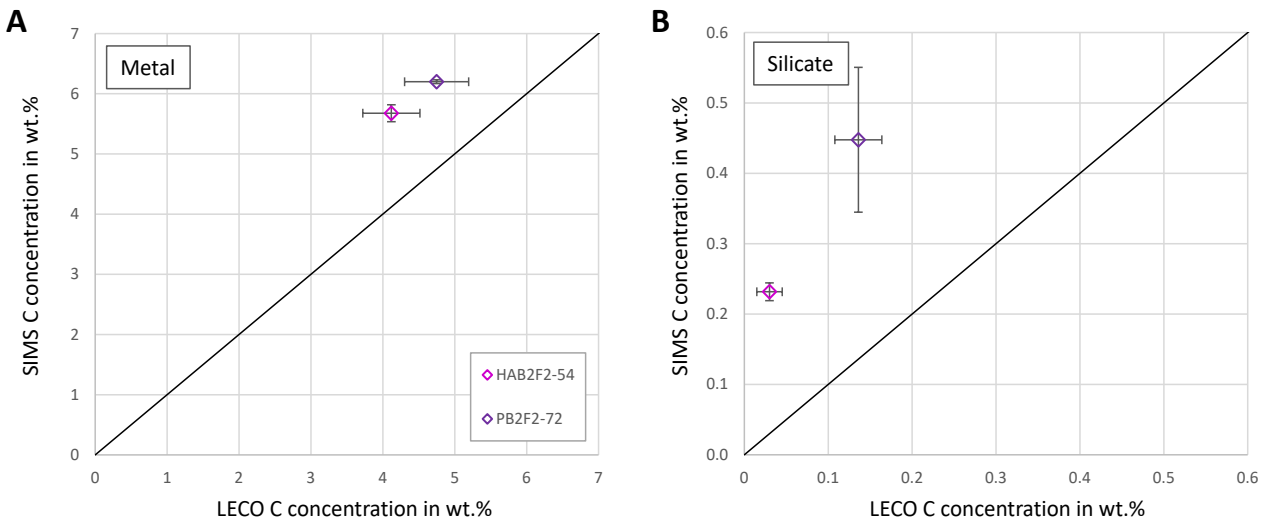

Fig. 2.11. *Comparison of C contents analysed by SIMS and a bulk elemental analyser (LECO).* ***A:*** *LECO vs. SIMS for metal alloy C content.* ***B:*** *LECO vs. SIMS for silicate melt C content. The solid line represents the 1:1 line. Errorbars represent the standard deviation (1σ) based on replicate measurements.*

2.2.4 Raman spectroscopy

Raman spectroscopy is a vibrational spectroscopy for assessing molecular motion and fingerprinting species based on inelastic scattering of a monochromatic excitation source. The technique is based on the interaction between monochromatic radiation (laser) and the irradiated material (solids, liquids, gases). The radiation generates a dipole within the irradiated substance caused by the deformation of the molecule's electron cloud and the change in energy (frequency of the radiation). This applies only if the specific material is Raman-active, thus if the polarisability of the detected species changes. The above described frequency differences correspond to characteristic energies of the unknown substance which allow for identification of the substance with the help of reference spectra.

In this doctoral study the Raman spectroscope Labram (Dilor) at ETH Zurich was used to investigate the carbon speciation of the silicate melts. The Raman system is coupled with a microscope that permits focussing a laser beam into a small sample volume and collecting the Raman signal through

the microscope objective. The spectroscope is equipped with a 532 nm laser and was used at an output power of 25 mW, yielding a power on the sample surface of 5 mW. Spectra were obtained in the wave number range of 200 - 4500 cm^{-1} with 3 cm^{-1} resolution, using a ×100 objective lens. At each point, a spectrum was accumulated three times with an exposure time of 200 s. Some glass samples could not be analysed with a 532 nm laser due to overlaying luminescence spectra. These samples were additionally analysed at the Swiss National Museum in Affoltern a. A. with a 633 and a 785 nm laser, but luminescence still occurred employing longer wavelengths.

3. Carbon partitioning between metal and silicate melts during Earth accretion

Abstract

In the accreting Earth and also in growing planetesimals, carbon was distributed between a metal melt, a silicate melt, and a hot, potentially dense atmosphere. Metal melt droplets segregating gravitationally from the magma ocean equilibrated near the base of this ocean. To understand the redistribution of carbon in this magma ocean, carbon partitioning between the two melts is experimentally investigated at 1.5 – 6.0 GPa, 1300 – 2000°C at oxygen fugacities of -0.9 to -1.9 log units below the iron-wüstite reference buffer (ΔIW). One set of experiments was performed in San Carlos olivine capsules to investigate the effect of melt depolymerisation (NBO/T), a second set in graphite capsules to expand the data set to higher pressures and temperatures. Carbon concentrations were analysed by secondary ionisation mass spectrometry (SIMS), and Raman spectra were collected to identify C species in the silicate melt.

Partition coefficients are governed by the solubility of C in the silicate melt, which varies from 0.01 to 0.6 wt.%, while metal melts contain ~ 7 wt.% C in most samples. C solubility in the silicate melt correlates strongly with NBO/T, which is at olivine saturation mostly a function of temperature, pressure having a much lesser effect. Carbon partition coefficients $D_C^{metal/silicate}$ at 1.5 GPa, 1300 – 1750°C decrease from 640 ± 49 to 14 ± 3 with NBO/T increasing from 1.04 to 3.11. For the NBO/T of the silicate Earth of 2.6, $D_C^{metal/silicate}$ is 34 ± 9. Over the limited range of oxygen fugacities appropriate for accretion of > 80% of the Earth mass, silicate melt composition hence controls carbon partitioning. Our results fundamentally differ from previous ones in that carbon concentrations in the silicate melt are comparatively higher, rendering C one order of magnitude less siderophile. This difference can be attributed to differences in the experimental protocol, which in our interpretation led to full equilibration in our experiments. Modeling present-day bulk silicate Earth values of 120 – 765 ppm C, the core would contain 0.4 – 2.6 wt.% C, yielding 0.14 – 0.9 wt.% bulk Earth carbon. These values are upper limits, considering that some of the carbon in the modern silicate Earth may have been delivered by the late veneer.

3.1 Introduction

Carbon is after H, He, and O the most abundant element in the solar system, and significantly affects chemical and physical processes and properties of the Earth's atmosphere, mantle and core (e.g., Anders & Grevesse, 1989; Fallon & Green, 1989; Sleep & Zahnle, 2001). The most popular model for core formation evokes high-energy impacts causing large-scale melting in the growing Earth or planetesimals, resulting in a magma ocean of several hundred kilometers depth. Such planetesimal's cores may have, upon impact into the proto-Earth, traversed the Earth magma ocean with partial or without equilibration. Within the magma ocean(s), carbon was distributed between disseminated metal melt and the ocean-forming silicate melt (and also a hot, potentially dense atmosphere). Metal melt droplets segregated gravitationally from the silicate melt matrix, ultimately forming the core. In order to constrain the distribution of carbon between the mantle-forming silicate melt and the core-forming metal melt, the partition coefficient of carbon between these two melts, $D_C^{metal/silicate}$, is required (Jana & Walker, 1997; Dasgupta & Walker, 2008; Dalou et al., 2017).

This partition coefficient $D_C^{metal/silicate}$ has been experimentally determined investigating a series of variables (Dasgupta et al., 2013a; Chi et al., 2014; Li et al., 2015; 2016; Dalou et al., 2017). The resulting range is large, i.e. $D_C^{metal/silicate}$ = 87 – 5370 and varies as a function of temperature (1400 – 2200°C), pressure (1 – 8 GPa), oxygen fugacity (ΔIW = -0.4 – -5.3; the difference to the reference iron-wüstite buffer in log units), silicate melt composition (NBO/T = 0.6 – 3.6; the ratio of non-bridging oxygen to tetrahedrally coordinated cations) and metal melt composition (in terms of Fe-Ni-Si-S-N). Dasgupta et al. (2013a) observed that pressure correlates positively with $D_C^{metal/silicate}$ and Chi et al. (2014) propose that pressure itself is a key variable for carbon partitioning between silicate and metal melts although the limited pressure range of 1 – 3 GPa, yielding a $D_C^{metal/silicate}$ of 3000 – 5400, makes extrapolation difficult. Li et al. (2015; 2016), however, conclude that hydration of the silicate melt and oxygen fugacity mainly govern carbon partitioning, $D_C^{metal/silicate}$ decreasing from 1300 to 820 with H_2O in the silicate melt increasing from 0.22 to 0.55 wt.% (Li et al., 2015). The effect of fO_2 on $D_C^{metal/silicate}$ seems less distinct, according to Li et al. (2016), $D_C^{metal/silicate}$ increases with fO_2 decreasing to ΔIW -1.5 and decreases at fO_2 < IW -1.5 due to an increase of methane solubility in the silicate melt. This effect was also observed by Dalou et al. (2017), but attributed to a decreasing NBO/T in the silicate melt. Dasgupta et al. (2013a) varied silicate melt compositions and found that with decreasing polymerisation (NBO/T of 0.8 to 3.6) $D_C^{metal/silicate}$ decreases from 4800 to 180.

Independent variation of the parameters investigated above is justified because it is desirable to single out the influence of each parameter. However, pressure, temperature, fO_2 and several compositional key variables of the silicate and metal melts are strongly inter-dependent in an accreting Earth and cannot be singled out. Moreover, in the accumulating Earth there is little variation in many of these parameters. Geochemical Earth models tend to agree on Ni and S contents of the core at least sufficiently well that these are not true variables. Secondly, pressure and temperature at the bottom of any magma ocean are not independent but bound to lie close to the peridotite liquidus, at least as long as the magma ocean and the solid silicate portion are roughly equal in composition (which is assumed in all models). Along the same line of arguments, NBO/T is not a variable but 2.6. Any minor direct effect of pressure is further expected to be overwhelmed by the effect of increasing temperature with a deepening magma ocean. Thirdly, oxygen fugacity and Si content of a metal as well as FeO content in the silicate melt are strictly inter-dependent. For elements, which partition coefficients do not change by several orders of magnitude as a function of fO_2, the early very reduced stage (at $fO_2 \sim \Delta$IW-5) leading to elevated Si in the core, has little influence on the bulk partitioning as only 10-20% of the Earth mass is aggregated under such conditions (e.g., Rubie et al., 2011). For the rest, fO_2 is around ΔIW-2, which yields Si contents of less than a few wt.%, too little to influence carbon partitioning.

The experiments yet available in the literature have one common denominator: carbon-free starting materials are run in graphite capsules, confiding in the ability of C^0 to saturate the silicate melt and the metal droplets therein. As there is no known C^0 solubility in silicate melt, this requires carbon to oxidise or reduce, diffuse through the silicate melt and reduce or oxidise in order to dissolve in the metal droplets (which are generally not in contact with the graphite capsule). Own previous experiments indicate that these reactions may be more sluggish than presumed and we have hence undertaken experiments without graphite capsule but carbon already present in the silicate and metal starting materials - with drastically different results. Instead of graphite, we used San Carlos olivine, which yields a strong dependence of NBO/T on temperature. At 1.5 GPa, olivine capsules in piston cylinders allow for temperatures of 1300 – 1750°C. For higher temperatures we also used graphite capsules on melts saturated in olivine at lower P-T conditions, but also in these, carbon was present both in the metal and silicate components of the starting materials. In multi-anvil experiments, double capsules with an inner olivine single crystal were not possible for space reasons, hence graphite capsules were also used at higher pressures.

3.2 Methods

To determine carbon partition coefficients, a synthetic silicate melt was equilibrated with metal melt, mostly in sample containers made of San Carlos olivine. C concentrations in both phases were measured by SIMS at the University of Lausanne and Raman spectra were used to identify the prevailing C species in the silicate melt.

3.2.1 Experimental methods

Experimental charges were composed of 80 wt.% silicate and 20 wt.% metal component (Table 3.1). The composition of the silicate mix was based on a primitive basaltic composition from Melson et al. (1976) and modified such that the silicate melt yielded a homogenous glass in a San Carlos olivine capsule. Pre-dried, spectroscopically pure oxides (SiO_2, TiO_2, Al_2O_3, MgO, NiO), silicates (Fe_2SiO_4, $CaSiO_3$, Na_2SiO_3, $KAlSi_2O_6$), or metals (Fe, Si) were used as chemicals, which were mixed in an agate mortar in ethanol for 45 minutes. Fe in the silicate component was added through synthetic fayalite, i.e. only as Fe^{2+}, and Ni as NiO, but the latter underwent complete reduction alloying with the metal phase. Carbon was added as $CaCO_3$ to the silicate component and as graphite powder to the metal mix. The homogenised silicate and metal components were mixed with each other and stored at 110°C for ≥ 24 h to remove any moisture and ethanol remnants. To avoid C saturation, the experimental charges were run in San Carlos olivine capsules, which in turn causes olivine saturation as appropriate for magma ocean melts. The olivine capsules (3.4 mm outer diameter, 6.0 mm height, 2.0 mm borehole diameter) were fabricated from San Carlos olivine single crystals by using a hollow diamond drill and closed with an olivine lid. Equilibrating silicate melt in olivine capsules shifts the silicate melt towards higher MgO with increasing temperature, and lower or higher FeO, depending on oxygen fugacity. The olivine capsules were placed in an outer welded platinum capsule ensuring that volatile species remained in the system. Melting of Fo_{91} olivine does not allow for temperatures > 1750°C (at 1.5 GPa). To expand the temperature range and to perform multi-anvil experiments at 6 GPa, some experiments were performed in graphite capsules, either with or without outer welded Pt-capsule (Table 3.1).

Experiments were carried out at ETH Zurich using a 14 mm end-loaded piston cylinder at 1.5 – 3.5 GPa, 1300 – 1900°C and a multi-anvil at 6 GPa, 1650 – 2000°C (Table 3.2). Piston cylinder assemblies consisted of inner MgO cylinders and sleeves (dehydrated at 1000°C overnight) surrounded by a graphite heater and talc-Pyrex sleeves (experiments ≤ 1500°C) or talc-SiO_2 glass sleeves (experiments

≥ 1600°C). The capsule was centered at the hotspot of the assembly to minimise temperature gradients (calculated to ± 10 – 25°C at 1300 – 1900°C) and insulated from the thermocouple by a ruby disc. Mullite thermocouple sleeves and type B PtRh thermocouples were used for experiments at ≤ 1500°C, and type C WRe thermocouples with dense Al_2O_3 sleeves for experiments at ≥ 1600°C. Pressure calibration against the quartz-coesite transition (Bose and Ganguly, 1995) showed a friction of 10 %. Experiments were quenched by switching off electric power of the furnace.

Table 3.1
Chemical composition of the starting material (in wt.%).

	Silicate mix[a]		Metal mix
SiO_2	45.9	Fe	81.4
TiO_2	2.2	Si	16.7
Al_2O_3	7.6	C	1.9
FeO	12.6	Total	100
MgO	7.9		
CaO	7.4		
NiO	3.9		
Na_2O	8.5		
K_2O	3.8		
CO_2	0.3		
Total	100		

[a] composition modified from a primitive basaltic glass described in Melson et al. (1976), such that the silicate melt quenched to a homogeneous glass in a San Carlos olivine capsule.

For space reasons, multi-anvil experiments were conducted in graphite capsules using an 18/11 mm assembly combined with 32 mm edge length tungsten carbide (WC) anvils. The assemblage contained a Cr_2O_3-doped MgO-octahedron, a zirconia insulator, a stepped $LaCrO_3$ furnace to minimise thermal gradients over the sample length, inner MgO cell parts, and a molybdenum disc and ring to separate the heater from the WC anvils. Temperature was controlled using a type C thermocouple, experiments were quenched by switching off power.

Recovered capsules were embedded in methyl methacrylate epoxy resin and polished for microprobe analyses (EPMA), secondary ion mass spectrometry (SIMS), and Raman spectroscopy.

Table 3.2
Summary of experimental conditions, carbon concentrations, and carbon partitioning between metal and silicate melt.

Sample	P (GPa)	T (°C)	Duration	inner capsule material	fO_2	Fe-Ni metal melt		Silicate melt			D_C	1 σ
					(ΔIW^a)	C SIMS (wt%)	1 σ	C SIMS (wt%)	1 σ	NBO/T[b]		
PB1FS2-84	1.5	1300	3 h	SC Olivine	-1.24	7.04	0.30	0.011	0.001	1.04	640	49
PB1FS2-57[e]	1.5	1400	2 h	SC Olivine	-1.59	4.56	0.20	0.010	0.001	1.40	460	47
PB1FS2-77	1.5	1500	1.75 h	SC Olivine	-0.93	6.65	0.73	0.022	0.001	1.73	299	34
PB1FS2-78	1.5	1600	30 min	SC Olivine	-1.07	6.87	0.68	0.07	0.03	2.23	92	34
PB1FS2-80[e]	1.5	1700	20 min	SC Olivine	-1.19	6.59	0.52	0.31	0.09	2.70	21	6
PB1FS2-87[e]	1.5	1750	2 min	SC Olivine	-1.66	6.58	0.19	0.30	0.03	2.88	22	3
PB1FS2-103[-]	1.5	1750	20 min	SC Olivine	-1.42	2.22[c]	0.20	0.16	0.03	3.11	14	3
PB1FS2-91[a,e]	1.5	1500	2 h	Graphite	-1.89	7.63	0.24	0.18	0.01	0.98	42	2
PB1FS2-89[a,e]	3.5	1900	2 min	Graphite	-1.66	7.10	0.27	0.035	0.005	0.99	202	29
PB1FS2-112[e]	6.0	1600	1 h	Graphite	-1.53	7.17	0.15	0.05	0.01	1.02	136	16
PB1FS2-102[a,e]	6.0	1650	1 h	Graphite	-1.50	7.10	0.26	0.20	0.03	1.12	35	5
PB1FS2-113	6.0	1650	1 h	Graphite	-1.22	7.01	0.12	0.10	0.05	1.07	73	36
PB1FS2-110	6.0	1700	50 min	Graphite	-1.10	7.26	0.17	0.57	0.12	1.12	13	3
PB1FS2-107	6.0	1720	30 min	Graphite	-1.08	7.59	0.29	0.30	0.05	1.20	25	4
PB1FS2-108	6.0	1810	30 min	Graphite	-1.21	7.36	0.12	0.32	0.02	1.11	23	2
PB1FS2-111	6.0	1865	20 min	Graphite	-1.21	7.19	0.36	0.10	0.01	1.04	73	6
PB1FS2-109	6.0	2000	12 min	Graphite	-1.00	7.63	0.19	0.19	0.05	1.21	40	9

[a] Non-ideal fO_2, which considers the interaction between the components in the metal and silicate melt (γFe determined by the online calculator MetalAct (http://www.earth.ox.ac.uk/~expet/metalact/, Wood, BJ; Wade, J; Norris, A, last accessed on October 18th 2017), and γFeO = 1 after Médard et al. (2008), respectively). Carbon saturation was computed in the activity calculation for experiments showing excess carbon that precipitated from the metal melt (labelled with [e] in the table).

[b] NBO refers to 2*(ΣO - 4T) with T = Si + Ti + Al.

[c] C content of metal melt was determined by EPMA instead of SIMS, because Pt from the outer capsule alloyed with the metal melt and no appropriate standard for SIMS was available. EPMA conditions for C analysis: 10 kV accelerating voltage, 120 nA beam current and 20 s peak and background counting time. To minimise the carbon blank content within the sample chamber, a decontaminant device ("cold finger") was installed, which improves the vacuum and removes any present organic hydrocarbon molecules by condensation. As analytical standard, an experimentally-synthesised cohenite ($(Fe,Ni)_3C$) was used.

[d] Experiments performed in a platinum-graphite double capsule. No Pt was detected in the metallic melt.

[e] Metal melt precipitated excess carbon.

[*] Outer platinum capsule started to melt and migrated through the sample, which resulted in a contamination of the metal droplet by 18.14 ± 0.69 wt.% Pt. Nevertheless, the silicate melt seems to be unaffected by the platinum such that this experiment was included in further considerations. The calculated oxygen fugacity, however, might not be accurate, due to a considerable amount of Pt in the metal melt and its influence on the activity of Fe, which has not been considered in the calculation. Also, Pt may negatively influence the C solubility in an Fe-rich melt, because the C content is more than 4 wt.% C less than possibly soluble at these P-T conditions.

Errors are given in 1 σ standard deviation based on replicate measurements.

3.2.2 Analytical methods

3.2.2.1 Electron probe microanalysis (EPMA)

Major and minor element concentrations of the coexisting silicate and metal melts were determined using a JEOL electron microprobe, JXA 8900, equipped with five spectrometers at the Goethe University of Frankfurt. All samples were carbon-coated and 10 – 15 points per melt were analysed. Analytical conditions for silicate glasses (Si, Ti, Al, Fe, Mg, Ca, Ni, Na, K) were 15 kV accelerating voltage, 20 nA beam current, and peak and background counting times of 20 s. For metal quench (Fe + Ni + Si) the conditions were 20 kV, 30 nA and 30 s, respectively. A 30 µm diameter beam was used to obtain homogeneous analyses, especially for the experiments where silicate melts quenched to olivine needles and interstitial glassy patches and for the coarse heterogeneous quench of the metal melts. As analytical standards, a NIST mineral glass (NBS K-412) and a natural Rockport fayalite were used for all elements in the silicate glass. For the metal quench, pure Fe, Si and Ni metal standards from NIST were used.

3.2.2.2 Secondary ionisation mass spectrometry (SIMS)

Carbon concentrations in silicate glasses and the quenched metallic melt were measured using an IMS 1280HR ion probe at the SwissSIMS laboratory at the University of Lausanne. Samples were re-polished to remove previous C coating, and surrounding epoxy was cut off using a diamond saw. Subsequently, a 300 µm diamond wire saw was used to cut the samples at the contact between the platinum and olivine capsule or through the graphite capsules. After removing all four sides of the capsule, the inner part was recovered and mounted in indium. Four to six samples were placed together with standards in one single indium mount and coated with ~ 40 nm gold.

As ion source, a primary beam of $^{133}Cs^{+}$ was used with intensities of ~ 2 and ~ 0.2 nA for metal and silicate melts, respectively. A lower intensity for silicate melts was chosen to enable analyses of all samples under identical conditions (regardless of their C content) using an electron multiplier (EM) with a field aperture of 4000 µm and an energy slit of 50 µm. The entrance and exit slits were 122 and 405 µm, resulting in a mass resolving power of ~ 3000 (M / ΔM).

To clean the sample surface, pre-sputtering times of 180 s for metal and 130 s for glass were applied, using a raster beam of 50 µm diameter. Automatic calibration on ^{12}C and ^{28}Si for metal and glass, respectively, and centring of the field aperture were made after pre-sputtering. For the actual measurements, a raster of 30 µm was used to homogenise the signal from heterogeneous quench structures as occur in the metal melt.

Each analysis consisted of 20 cycles of the peak-stepping sequence mass 11.8 (background: 2 s), $^{12}C^+$ (3 s, FC), $^{28}Si^+$ (1.6 s, EM), $^{56}Fe^+$ (1.8 s, EM) for metal, and 11.8 (2 s), $^{12}C^+$ (5 s, EM), $^{28}Si^+$ (3 s, FC), $^{56}Fe^+$ (1 s, FC) for silicate glasses. Silicon and iron were used to normalise C in the glass and the metal, respectively, and to smooth possible variations related to primary intensity variations. Both elements were analysed consecutively, which enables a more stable magnet.

Carbon standards for silicate glasses were experimentally synthesised, matrix-matched silicate melts and synthetic cohenite ($(Fe,Ni)_3C$) where large crystals were grown from a melt phase (details in section 2.1.5). The standards were analysed with an independent method, i.e., X-ray powder diffraction for identifying cohenite, and a conventional elemental analyser (LECO CS844) to determine the bulk carbon content of the standard glasses. Typical standard reproducibility was 1 – 6 % (standard deviation (1 SD) relative) for glass and 1 – 3 % (1 SD relative) for metal. Internal errors (standard error of the mean (1 SE) over the 20 cycles) were typically < 2 % for glass and < 1 % for metal but larger (up to ~ 8 %) for those glasses with C contents below 0.5 wt.%.

3.2.2.2 Raman spectroscopy

Raman spectra of the silicate glasses were collected to determine carbon speciations. A Labram Dilor Raman spectroscope equipped with a 532 nm laser at ETH Zurich was used at an output power of 25 mW, which gives a power on the sample surface of 5 mW. Spectra were collected in the frequency range of 200 − 4500 cm^{-1} with 3 cm^{-1} resolution, using a × 100 objective lens. At each point a spectrum was accumulated three times with an exposure time of 200 s.

3.2.3 Redox work in the experimental charges

The Ni/NiO, Fe/FeO, and Si/SiO_2 ratios in the starting material were chosen such that the intrinsic oxygen fugacity was relatively reducing (around ΔIW-1 to -2) as appropriate for the larger part of metal/silicate equilibration in the Earth. Oxygen fugacities of the experimental charges then result from reaction of the silicate glass components, the metal and the olivine capsule. Redox reactions that combine into a given oxygen fugacity in our charges were:

$$2\,Fe^{metal} + O_2 \leftrightarrow 2\,FeO^{silicate\ melt} \quad (3.1)$$

$$Si^{metal} + O_2 \rightarrow SiO_2{}^{silicate\ melt} \quad (3.2)$$

$$2\,Ni^{metal} + O_2 \rightarrow 2\,NiO^{silicate\ melt} \quad (3.3)$$

This results in oxygen fugacities of ΔIW -0.9 to -1.7 in San Carlos olivine capsules (see below for fO_2 calculations), which are restricted towards lower values by

$$Fe_2SiO_4^{olivine\ capsule} \leftrightarrow 2\ FeO^{silicate\ melt} + SiO_2{}^{silicate\ melt}. \quad (3.4)$$

Reaction (3.4) refurbishes FeO to the silicate melt and causes reaction (3.1) to have the by far highest buffer capacity, which in turn oxidises all Si in the metal, irrespective of its fraction in the starting mix. Single graphite capsules with the same silicate and metal starting materials yielded slightly more reducing conditions down to ΔIW -1.9.

3.3 Results

Experimental conditions, major element compositions, carbon concentrations, and carbon partition coefficients are summarised in Tables 3.2 and 3.3. In general, experimental charges are unproblematic with large metal droplets in a silicate melt which is in part quench (-olivine) modified, but leaving large unmodified patches easily measurable in all experiments. C concentrations in silicate melt vary from 0.01 to 0.3 wt.% with NBO/T increasing from 1.04 to 3.11, whereas metal melts have concentrations of about 7 wt.% C, little affected by the experimental conditions.

3.3.1 Textures and chemical equilibration

The experimental products show one or several quenched metal droplets suspended in silicate glass which in turn is surrounded by a partly dissolved San Carlos olivine capsule or an intact graphite capsule (Fig. 3.1). As commonly observed, these komatiitic melts did not fully quench to glasses (Parman et al., 1997) but to olivine quench needles and interstitial glassy patches (at ≥ 1600°C, Fig. 3.1B). Almost all NiO from the starting material was reduced to metallic Ni, the Fe-dominated metal melt imposing an oxygen fugacity of NNO -4 to -6. Experiments performed in graphite capsules resulted in MgO contents similar to those of the silicate starting material. Run PB1FS2-87 (1750°C, 1.5 GPa, ΔIW -1.7) shows slightly different results, which might be caused by the short run time of 2 minutes not enabling equilibrium, this experiment was hence repeated and held for 20 minutes (PB1FS2-103, ΔIW -1.68). For this and all other experiments the homogenous distribution of FeO, Na_2O, Al_2O_3, MgO and C within the silicate glass suggests that chemical equilibrium was attained in the experiments as shown in Fig. 3.2.

Table 3.3
Major element composition of silicate and metallic melts.

Sample No.	PB1FS2-84		PB1FS2-57		PB1FS2-77		PB1FS2-78		PB1FS2-80		PB1FS2-87		PB1FS2-103		PB1FS2-91		PB1FS2-89		PB1FS2-102		PB1FS2-112		PB1FS2-113		PB1FS2-110		PB1FS2-107		PB1FS2-108		PB1FS2-111		PB1FS2-109	
Silicate melts	Average	1 σ	Average	1 σ	Average	1 σ	Average	1 σ	Average	1 σ	Average	1 σ	Average	1 σ	Average	1 σ	Average	1 σ	Average	1 σ	Average	1 σ	Average	1 σ	Average	1 σ	Average	1 σ	Average	1 σ	Average	1 σ	Average	1 σ
SiO_2	53.86	0.13	51.13	0.31	49.33	0.49	47.05	1.02	45.58	0.72	45.88	0.82	43.22	1.13	56.60	0.09	55.73	0.27	52.77	0.20	53.28	0.11	52.71	0.30	52.40	0.88	51.67	0.17	53.25	0.23	52.97	0.38	50.42	0.24
TiO_2	2.30	0.05	1.86	0.04	1.50	0.09	1.13	0.17	0.87	0.11	0.67	0.17	0.55	0.18	2.24	0.04	2.18	0.05	2.07	0.04	2.15	0.04	2.14	0.04	2.29	0.06	2.12	0.04	2.15	0.04	2.12	0.03	2.05	0.06
Al_2O_3	7.79	0.16	5.79	0.08	5.10	0.18	3.69	0.46	3.01	0.36	2.49	0.49	2.07	0.63	7.56	0.06	7.37	0.05	7.11	0.05	7.18	0.06	7.18	0.03	7.16	0.10	7.13	0.05	7.29	0.06	7.19	0.05	6.89	0.06
FeO	9.38	0.14	10.26	0.10	13.60	0.32	14.31	0.62	15.15	1.02	9.36	1.29	13.99	2.23	6.30	0.12	7.94	0.16	10.39	0.07	9.38	0.09	10.87	0.12	11.17	0.24	11.49	0.14	10.60	0.29	10.90	0.28	13.57	0.14
MgO	8.78	0.23	14.32	0.26	19.17	1.52	26.11	3.58	31.20	2.45	37.80	4.22	36.85	5.16	8.01	0.05	8.10	0.06	7.43	0.06	7.32	0.05	7.55	0.10	6.52	0.18	7.45	0.04	7.68	0.19	7.42	0.15	7.24	0.09
CaO	5.90	0.12	6.41	0.11	5.00	0.41	3.95	0.67	2.79	0.36	2.36	0.59	1.95	0.64	7.70	0.08	8.04	0.06	7.38	0.05	7.38	0.06	6.92	0.11	6.27	0.16	7.30	0.09	7.23	0.12	7.10	0.11	6.89	0.09
NiO	0.01	0.01	0.01	0.02	0.02	0.02	0.14	0.04	0.07	0.02	0.09	0.03	0.11	0.03	0.01	0.02	0.02	0.02	0.01	0.01	0.01	0.02	0.02	0.02	0.01	0.01	0.01	0.01	0.02	0.01	0.02	0.01	0.03	0.03
Na_2O	8.49	0.13	6.30	0.10	5.08	0.31	3.45	0.56	2.79	0.39	2.24	0.61	1.85	0.66	8.00	0.06	7.99	0.09	7.69	0.09	7.45	0.05	7.26	0.11	6.88	0.17	7.56	0.07	6.71	0.16	6.59	0.19	7.13	0.04
K_2O	3.69	0.09	2.89	0.02	2.34	0.09	1.61	0.20	1.35	0.16	1.07	0.22	0.90	0.28	3.56	0.04	3.46	0.05	3.48	0.03	3.48	0.03	3.37	0.02	1.91	0.25	3.40	0.04	2.53	0.19	2.91	0.30	3.21	0.04
Total	100.20	0.15	98.97	0.28	101.1	0.51	101.43	0.64	102.80	0.42	101.96	0.21	101.50	0.37	99.98	0.18	100.81	0.29	98.32	0.26	97.64	0.20	98.02	0.46	94.61	0.98	98.12	0.31	97.46	0.33	97.22	0.63	97.43	0.20
Metallic melts	Average	1 σ	Average	1 σ	Average	1 σ	Average	1 σ	Average	1 σ	Average	1 σ	Average	1 σ	Average	1 σ	Average	1 σ	Average	1 σ	Average	1 σ	Average	1 σ	Average	1 σ	Average	1 σ	Average	1 σ	Average	1 σ	Average	1 σ
Fe	84.8	1.6	85.78	0.23	75.0	6.8	68.8	8.8	79.60	0.65	80.79	0.36	57.89	0.53	85.44	0.44	85.22	0.33	90.3	1.3	85.09	0.25	85.79	0.26	83.57	0.70	84.22	0.59	84.17	0.45	83.91	0.21	84.76	0.14
Ni	8.9	1.8	9.61	0.35	20.2	6.9	26.0	8.9	16.19	0.70	13.27	0.41	21.37	0.18	8.63	0.37	9.05	0.42	3.4	1.4	8.45	0.02	8.06	0.07	10.65	0.80	9.69	0.25	9.89	0.38	10.15	0.04	9.24	0.04
Total	93.7		95.39		95.2		94.8		95.79		94.06		79.26[a]		94.07		94.27		93.7		93.54		93.85		94.22		93.92		94.07		94.05		94.01	

Si was below the detection limit in all metal melts.

[a] Metal melt was contaminated by platinum, which migrated from the outer capsule and yield to 18.14 ± 0.69 wt.% Pt. Due to this dilution, the Fe content dropped.

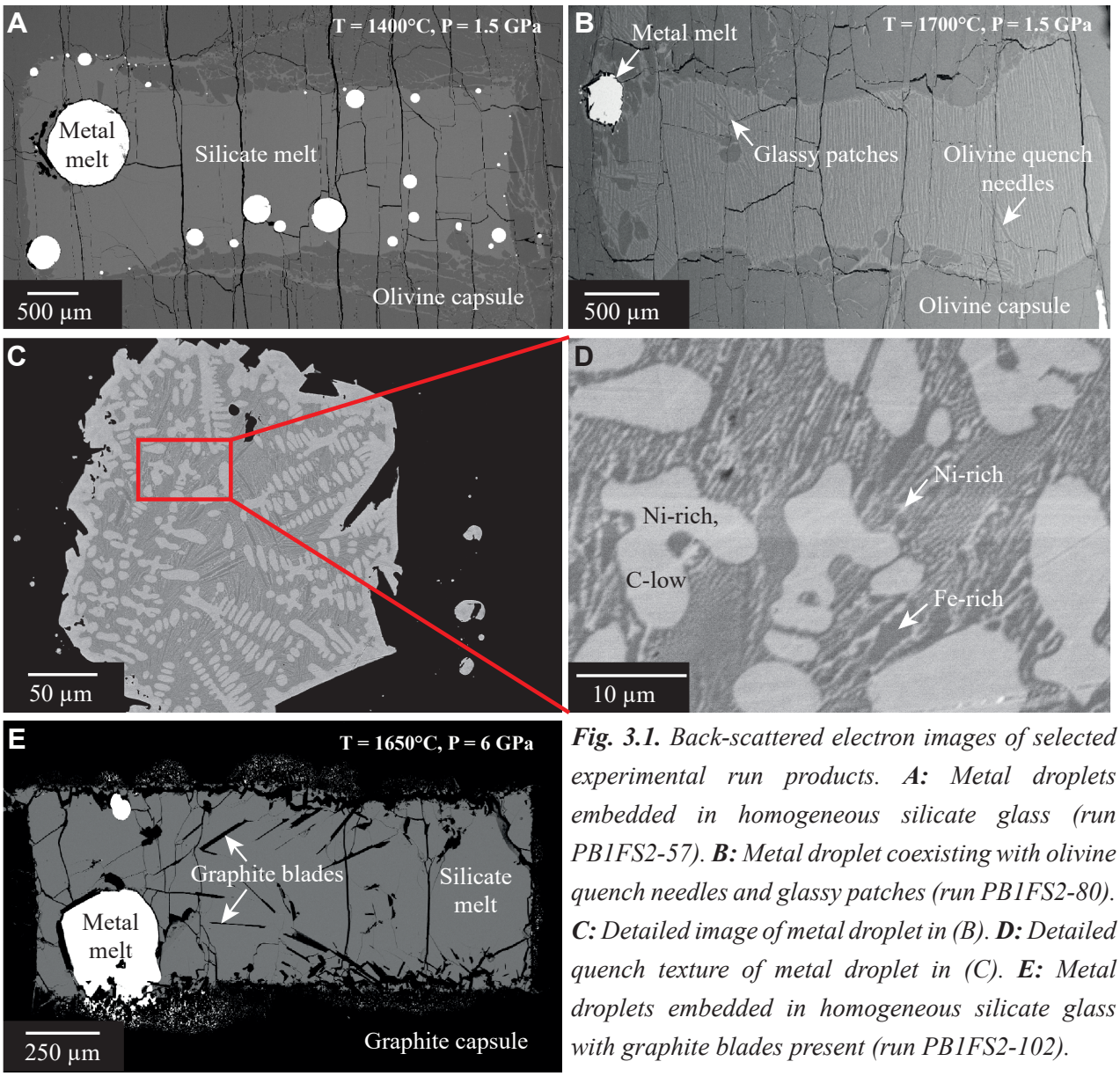

Fig. 3.1. *Back-scattered electron images of selected experimental run products.* ***A:*** *Metal droplets embedded in homogeneous silicate glass (run PB1FS2-57).* ***B:*** *Metal droplet coexisting with olivine quench needles and glassy patches (run PB1FS2-80).* ***C:*** *Detailed image of metal droplet in (B).* ***D:*** *Detailed quench texture of metal droplet in (C).* ***E:*** *Metal droplets embedded in homogeneous silicate glass with graphite blades present (run PB1FS2-102).*

Metal melt droplets quenched to Ni-rich dendrites embedded in a fine Fe-Ni alloy matrix (Fig. 3.1C+D). In some experiments, 25 – 300 µm large euhedral graphite blades are present in the silicate melt next to the metal droplets. This graphite (Fig. 3.1E) results from a bulk carbon content in the starting material higher than the proportionally combined solubilities in the silicate and metal melts, crystallised in equilibrium during the experiment and does not account towards the carbon solubility in the silicate or metal melts.

3.3.2 Major element composition of the silicate melts

The major element composition of the silicate melt varied mainly with temperature and oxygen fugacity. Experiments run in San Carlos olivine at 1.5 GPa and 1300 – 1750°C have, with increasing temperature, SiO_2 decreasing from 54 – 43 wt.% but FeO and MgO increasing from 9 – 15 and 9 –

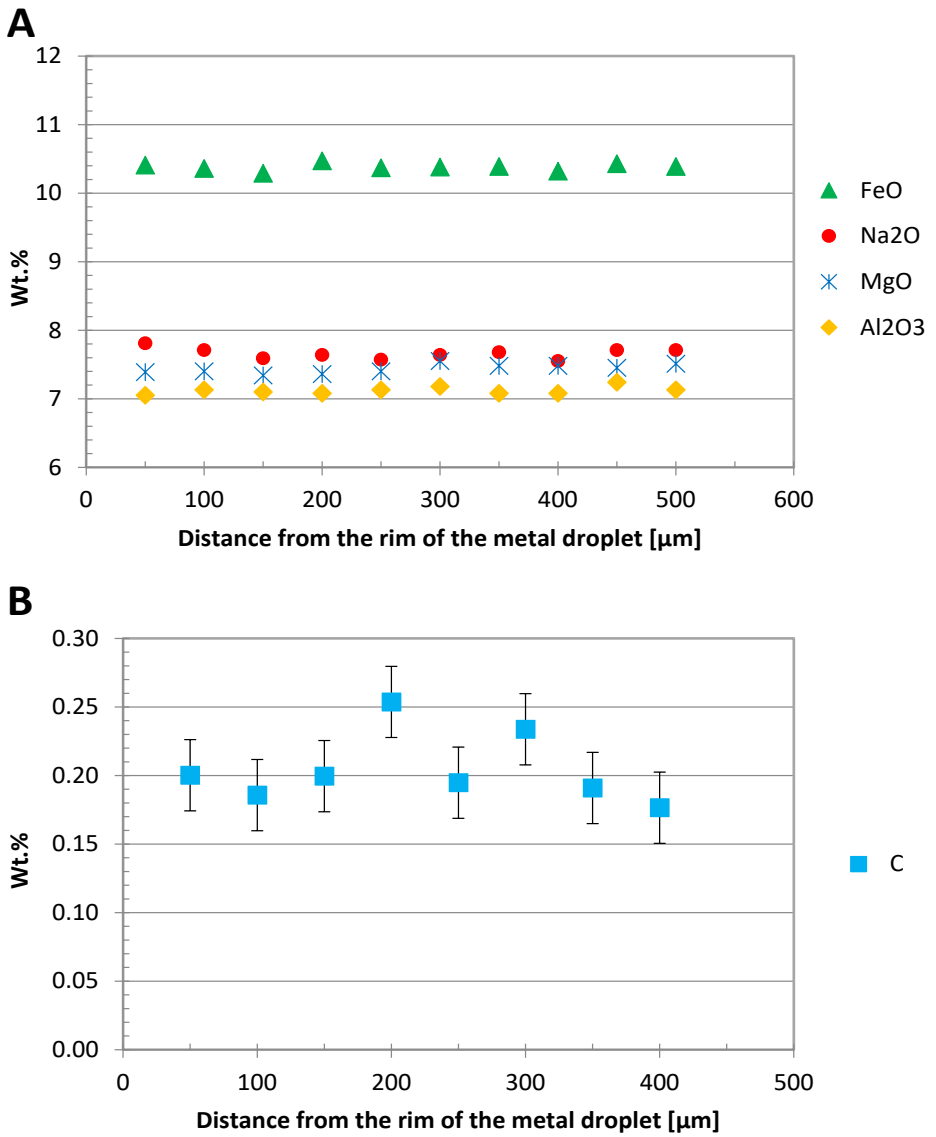

Fig. 3.2. *Concentrations of* ***A*** *FeO, Na_2O, MgO, Al_2O_3, and* ***B*** *carbon in the silicate melt across a profile, starting at the rim of a metal droplet (run PB1FS2-102).*

38 wt.%, respectively (Fig. 3.3A,B). These changes result from dissolution of and saturation in San Carlos olivine and yield NBO/T increasing from 1.0 to 3.1 at 1300 – 1750 °C. Instead, Al_2O_3, CaO, and Na_2O concentrations get diluted with increasing temperature and are 7 – 2 wt.% for Al_2O_3, from 6 – 2 wt.% for CaO, and 8 – 2 wt.% for Na_2O. It should be noted that olivine saturation is a condition fulfilled at the bottom of the magma ocean, where temperatures were necessarily at the liquidus of mantle peridotite (Wood et al., 2006).

Experiments performed in graphite capsules at 6 GPa produce glasses with much smaller variations in composition. For example, SiO_2 contents decrease from 53 – 50 wt.% with increasing temperature, mostly a result of FeO increasing from 9 – 14 wt.%, which in turn depends on the combined redox-equilibria (3.1) and (3.2). As described above, MgO and the other minor oxides remain similar to the starting mix.

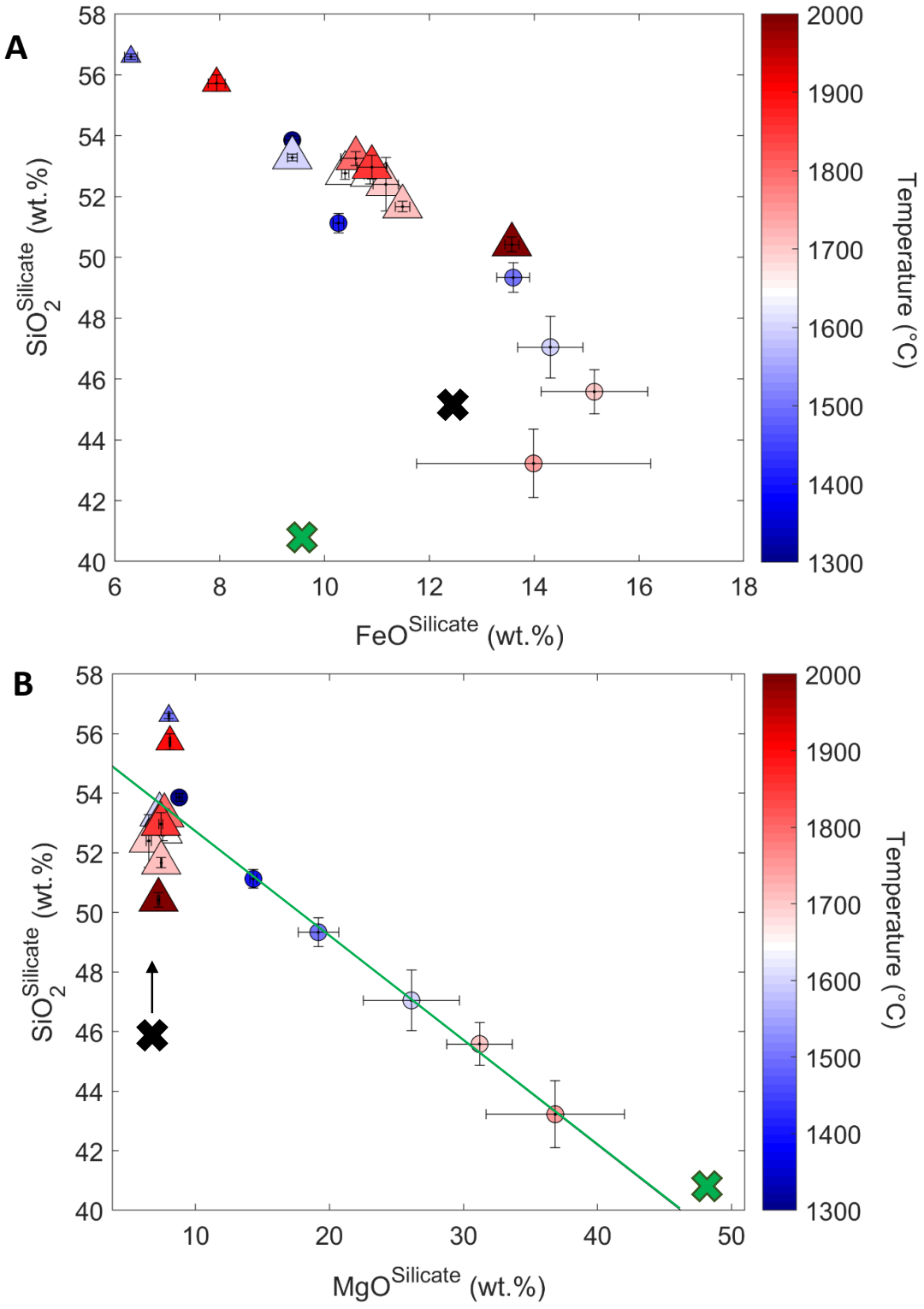

Fig. 3.3. *SiO_2 content as a function of (A) FeO content and (B) MgO content in silicate melt. Circles represent experiments performed in San Carlos olivine capsules, triangles represent experiments performed in graphite capsules. The color of the symbol corresponds to experimental temperatures, the size of the symbol refers to the experimental pressure (1.5 – 6.0 GPa). Black crosses represent the starting composition, green crosses represent the composition of the San Carlos olivine capsule.* ***A:*** *With increasing temperature, FeO content increases and SiO_2 content decreases due to several redox reactions (see text) and chemical interactions between the experimental charge and the capsule material.* ***B:*** *The black arrow demonstrates the shift in SiO_2. The green line points towards the composition of San Carlos olivine, to which the silicate melts evolve with increasing temperature.*

3.3.3 Major element composition of the metal melts

Metal melts in all experiments are Fe-dominated. Experiments performed in San Carlos olivine capsules yield Fe contents of 69 – 86 wt.%, and Ni contents of 26 – 9 wt.%. Essentially, metallic Fe is oxidised to allow for reduction of NiO and the concentration of Ni in the metal then depends on the remaining Fe^0 present. The amount of FeO in the capsule is also modified by the Si^0 present in the starting material, which becomes all oxidised, and oxygen fugacity then results from the remaining Fe^0 and the FeO dissolved in the silicate melt.

Metallic Fe in the experiments run in graphite capsules at 6 GPa is substantially higher, varying from 83 – 90 wt.%. The Ni content is accordingly lower and in the range of 3 – 11 wt.%.

The experiments with the highest concentrations of metallic Fe are the most reducing, temperature has not much effect on the chemical compostition of the metal melt. Si was analysed by EPMA, but in all metal melts, Si contents were below detection limit (~ 0.004 wt.%).

3.3.4 Oxygen fugacity

Effective oxygen fugacities during the experiments were calculated (Table 3.2) using the reaction

$$Fe^{metal} + {}^{1}/_{2}\, O_2 = FeO^{silicate\ melt}\ . \tag{3.5}$$

Oxygen fugacity relative to the iron-wüstite buffer (ΔIW) is then calculated as

$$\Delta \log fO_2\ [IW] = 2 \log\left(\frac{a_{FeO}^{silicate}}{a_{Fe}^{metal}}\right) = 2 \log\left(\frac{X_{FeO}^{silicate}}{X_{Fe}^{metal}}\right) + 2\ log\left(\frac{\gamma_{FeO}^{silicate}}{\gamma_{Fe}^{metal}}\right), \tag{3.6}$$

where $a_{FeO}^{silicate}$ and a_{Fe}^{metal} are the activities of FeO in the silicate and Fe in the metal melt, respectively. The advantage of relative oxygen fugacity is that this calculation is independent of temperature, pressure and of any thermodynamic properties other than the activity expressions. Activities are calculated from the activity coefficients ($\gamma_{FeO}^{silicate}$ and γ_{Fe}^{metal}) and mole fractions ($X_{FeO}^{silicate}$ and X_{Fe}^{metal}). Holzheid et al. (1997), with experiments at FeO contents of up to several wt.% suggested a constant activity coefficient of FeO in silicate melt ($\gamma_{FeO}^{silicate}$) of 1.7 but Médard et al. (2008) suggested that the activity coefficient would rather be unity, which we adopt in this study. Activity coefficients of Fe in metal melt were determined using the online calculator MetalAct (http://www.earth.ox.ac.uk/~expet/metalact/, Wood, BJ; Wade, J; Norris, A, [2017.10.18]), which takes non-ideal interactions between components in liquid Fe into account (Wade & Wood, 2005). The experiments showing excess carbon in form of graphite platelets were carbon-saturated, which was taken into account in the γ_{Fe}^{metal}

calculations. The effect of C saturation on γ_{Fe}^{metal} results only in differences of 0.0 – 0.3 log units in fO_2 with respect to ignoring carbon. In our experiments, oxygen fugacities result to between ΔIW -0.9 to -1.9. This range corresponds to the reigning fO_2 during the main phase of accretion (Wood et al., 2006).

3.3.5 Carbon in the silicate melt

Carbon concentrations in silicate melt generally increase with temperature and depolymerisation, and mostly range from 0.010 ± 0.001 to 0.32 ± 0.02 wt.%, but one experiment yielded 0.6 ± 0.1 wt.% (6 GPa, 1700°C, ΔIW -1.3). In olivine saturated melts, temperature and melt depolymerisation are not independent variables. At 1.5 GPa, NBO/T increases from 1.04 to 3.11 at 1300 to 1750°C (Fig. 3.4), and carbon from 0.01 to 0.3 wt.% C. For the experiments conducted in graphite capsules at 6 GPa, the silicate melt NBO/T values vary little and do not depend on temperature. The effect of pressure on carbon solubility cannot be derived directly from our data, C dissolved in the silicate melt at 6 GPa is comparable to that at 1.5 GPa for the same temperatures (e.g., 0.05 – 0.07 wt.% C at 1600°C). Over the narrow fO_2 range studied here, there is no clear effect of oxygen fugacity (Fig. 3.5).

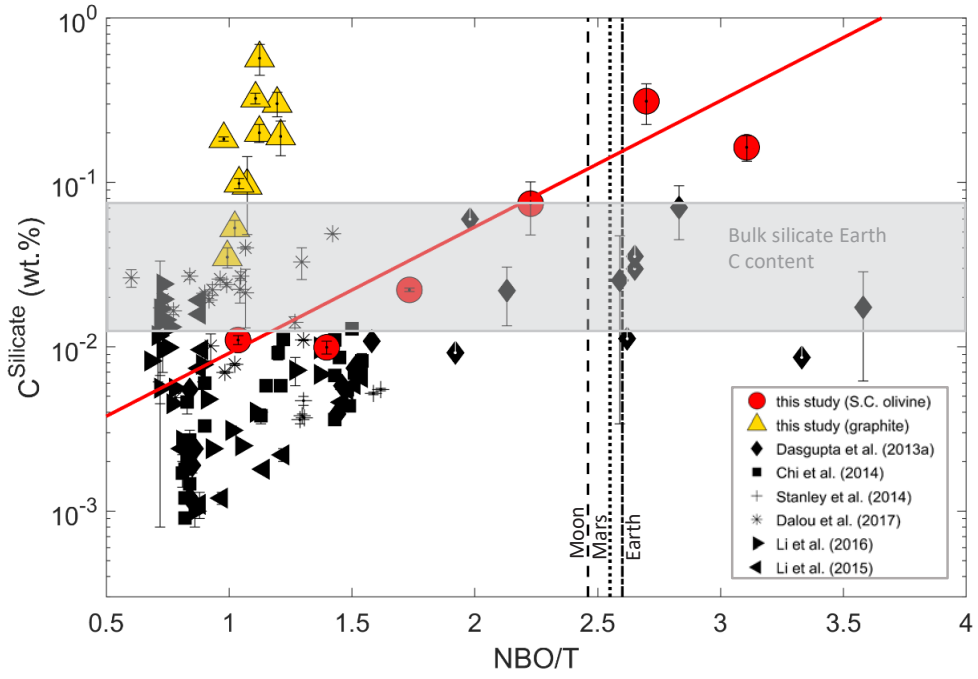

Fig. 3.4. *C content of the silicate melt versus the grade of silicate melt depolymerisation (NBO/T). C content of the silicate melt correlates positively with NBO/T. The solid red line refers to the exponential trend line fitted through the experiments performed in San Carlos (S.C.) olivine. The grey area corresponds to the bulk silicate C content of the Earth of 120 (McDonough & Sun, 1995) to 765 ppm C (Marty, 2012).*

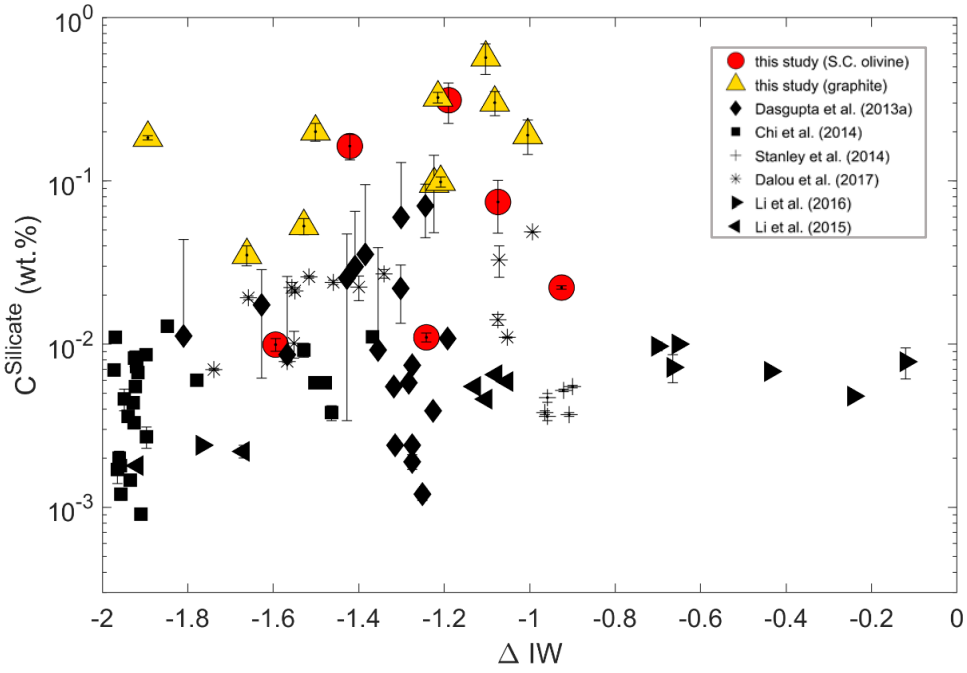

Fig. 3.5. *C content of the silicate melt as a function of oxygen fugacity (ΔIW). There is no clear correlation noticeable, between oxygen fugacity and C content of the silicate melt.*

3.3.6 Carbon in the metal melt

Carbon contents of metal melts vary from 6.6 ± 0.5 to 7.6 ± 0.2 wt.% except one experiment with 4.6 ± 0.2 wt.% (1.5 GPa, 1400°C, ΔIW -1.6), the average being around 7 wt.%. Carbon constitutes a major component in the metal melt and is only moderately affected by temperature, pressure, chemical composition and fO_2 in the range of conditions covered in this study. The metal melts run in olivine capsules show little variance in carbon with Ni increasing from 9 ± 2 wt.% to 26 ± 9 wt.% (Fig. 3.6). This trend remains somewhat controversial, since previous studies (Holzheid & Grove, 2005; Dasgupta & Walker, 2008; Dasgupta et al., 2013a) report that carbon solubility of metal melts varies inversely with Ni contents.

3.3.7 C-H-O species in the silicate melt

Raman spectra of the silicate glasses allow to constrain volatile species except for the experiments at > 1800°C that produced large areas of quench olivine and did not yield any Raman peaks of volatiles. All other sample spectra show broad bands in the low frequency range (500 – 1300 cm^{-1}) induced by the framework of the silicate glasses (Mysen, 1998; Neuville & Mysen, 1996) and occasionally sharp peaks at ~ 824 cm^{-1} and ~ 859 cm^{-1} (e.g., Weber et al., 2014) reflecting quench-olivine. Silicate glasses from temperatures of ≤ 1600°C show a broad, asymmetric band at ~ 3580 cm^{-1} (Fig. 3.7), assigned to

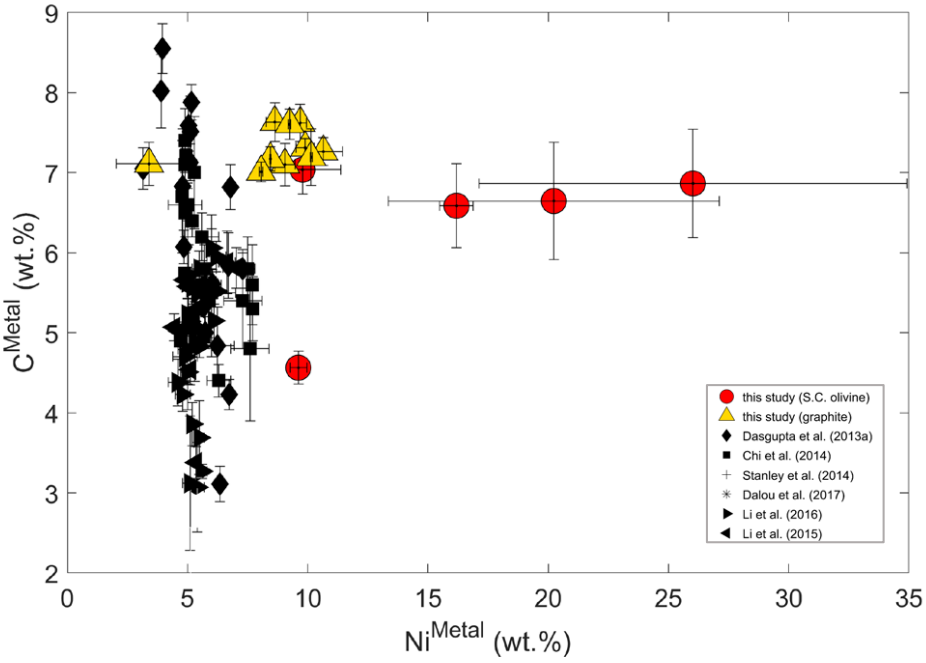

Fig. 3.6. *Metal C content as a function of Ni content of the metallic melt. C content of experiments performed in San Carlos (S.C) olivine (circles) appears to increase slightly with increasing Ni content, whereas experiments performed in graphite capsules (triangles) do not show a clear correlation.*

OH^- groups bonded to cations in the silicate network or molecular H_2O (Mysen & Virgo, 1986; Kadik et al., 2004). The presence of hydrogen is no surprise as it is difficult (and often not desirable) to conduct truly dry experiments. Nominally dry experiments gaining some H through diffusion across the Pt-capsule wall, even if all components of the assembly parts are carefully dried. The only carbon species from experiments in San Carlos olivine capsules was found at ~ 2855 cm^{-1} and ~ 2915 cm^{-1} and refers to weak C–H bonding in dissolved methane molecules that interact with the silicate network (CH_x stretching, Socrates, 2002). This doublet peak disappears from experiments above 1500°C, independent of oxygen fugacity and carbon content of the silicate glass. Further evidence for carbon related peaks is given by Debernardi et al. (1999), who suggested a carbon species with a vibrational peak at 784 cm^{-1} that can be assigned to an Si–C band. This is supported by the study of Kadik et al. (2004), whereas Mysen (1998) refers this peak to Si–OH stretching in the silicate framework. In our spectra, however, only the two experiments performed in graphite capsules at 1650°C show a slight vibrational peak at 784 cm^{-1}, the overlaying vibration band of the silicate glass framework mostly hiding this peak.

Experiments performed in graphite capsules show the broad, asymmetric OH^- or H_2O band at ~ 3580 cm^{-1}, except of one experiment at 1900°C, 3.5 GPa, and one near the lowest oxygen fugacity (ΔIW -1.2). Instead, the spectrum of this experiment shows a striking doublet peak of methane or

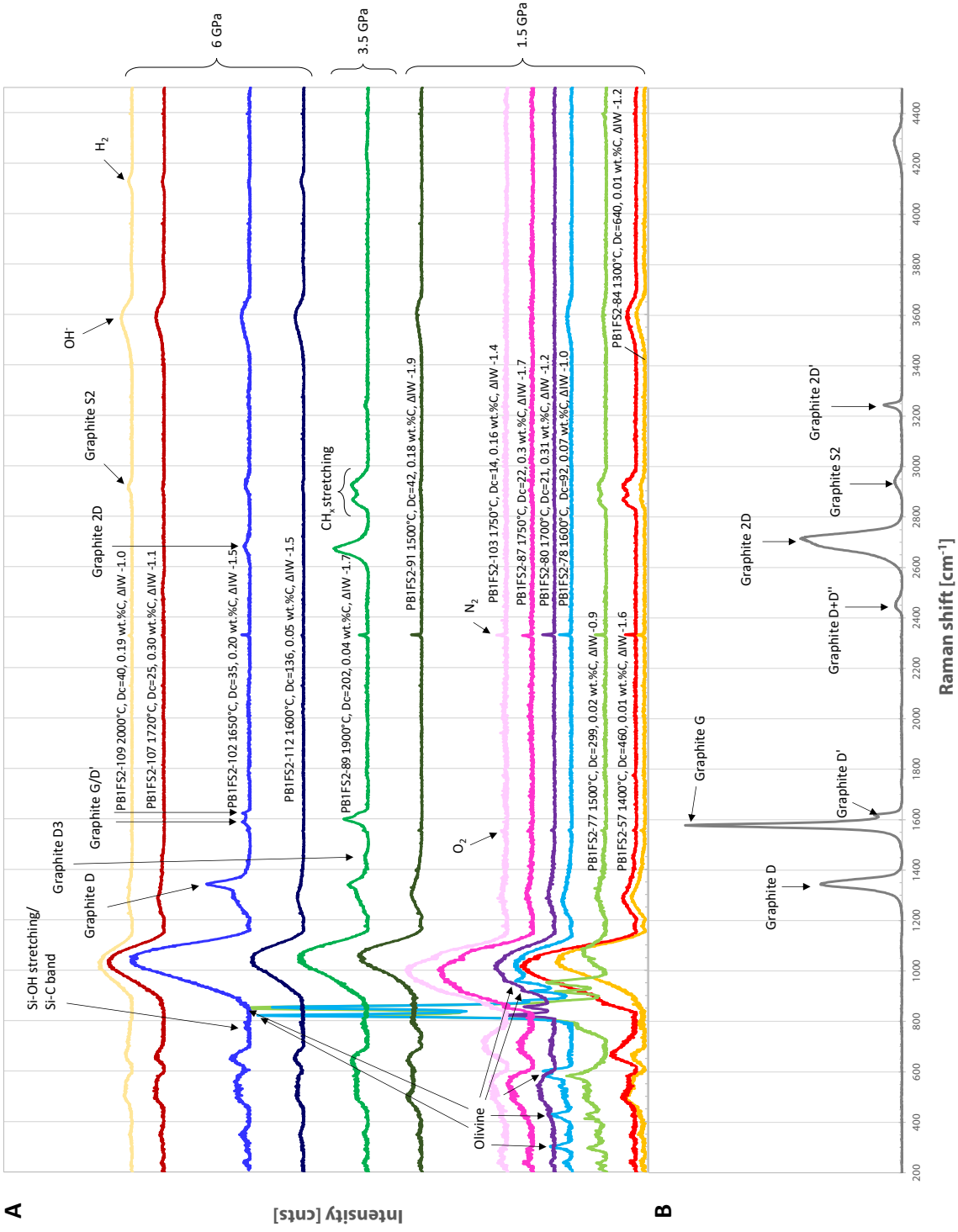

Fig. 3.7. *Raman spectra of quenched glasses (A) and a graphite blade (B) of run PB1FS2-102. Intensities are shifted to avoid overlapping spectra.*

methyl groups. In all experiments run at 6 GPa, an additional peak assigned to molecular H_2 appears at ~ 4130 cm^{-1}. Some silicate glasses produced in graphite capsules at temperatures ≥ 1650°C show several vibration peaks corresponding to poorly crystallised graphite or amorphous carbon (Tuinstra & Koenig, 1970; Beyssac et al., 2002; Kadik et al., 2004; Couzi et al., 2016; Rantitsch et al., 2016), which is best explained by badly crystallised graphite precipitating from the silicate melt during quench. Such peaks are absent in glasses from the San Carlos olivine capsules.

The main C-bearing species in reduced silicate glasses reported in previous studies are C ≡ O groups with most pronounced peaks at 2205 and 2110 cm^{-1} (Armstrong et al., 2015). There is no spectroscopic evidence for such a species in our experiments, regardless of oxygen fugacity.

3.3.8 Carbon partition coefficients

Carbon partition coefficients ($D_C^{metal/silicate}$) between metal and silicate melts were calculated based on the concentrations measured by SIMS and vary from 14 ± 3 to 640 ± 49. Experiments performed in San Carlos olivine capsules show that $D_C^{metal/silicate}$ values decrease with increasing temperature (Fig. 3.8) and silicate melt depolymerisation NBO/T (Fig. 3.9), mainly because an increase of the carbon concentration in the silicate melts (Fig. 3.10). Our experiments are within a narrow range of oxygen fugacities of ΔIW = -0.9 to -1.9, in which $D_C^{metal/silicate}$ does not correlate well with fO_2 (Fig. 3.11). Experiments conducted in graphite capsules give a slightly smaller range of $D_C^{metal/silicate}$ between 13 ± 3 to 202 ± 29. In these experiments, only the redox equilibrium (3.5) modifies starting melt compositions, hence NBO/T remains at 1.1 ± 0.1 as in the silicate starting material.

In summary, the San Carlos olivine capsule experiments show that the degree of melt depolymerisation (NBO/T) controls $D_C^{metal/silicate}$, temperature seems to have a lesser effect while pressure does not exert much of a control. Nevertheless, in an olivine-saturated magma ocean, pressure, temperature, NBO/T and to some degree oxygen fugacity are dependent variables varying much less than they can be changed in experiments.

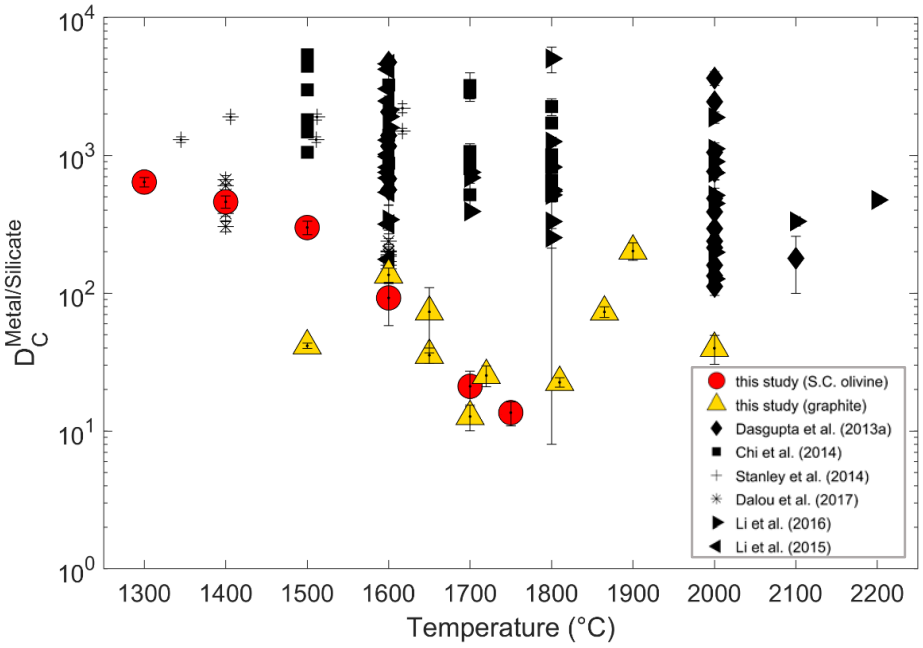

Fig. 3.8. *$D_C^{metal/silicate}$ as a function of experimental temperatures. Experiments performed in San Carlos (S.C.) olivine capsules (circles) suggest that $D_C^{metal/silicate}$ decreases with increasing temperature. In fact, this is mainly because with increasing temperature more capsule material is dissolved which results in a compositional shift towards higher NBO/T values.*

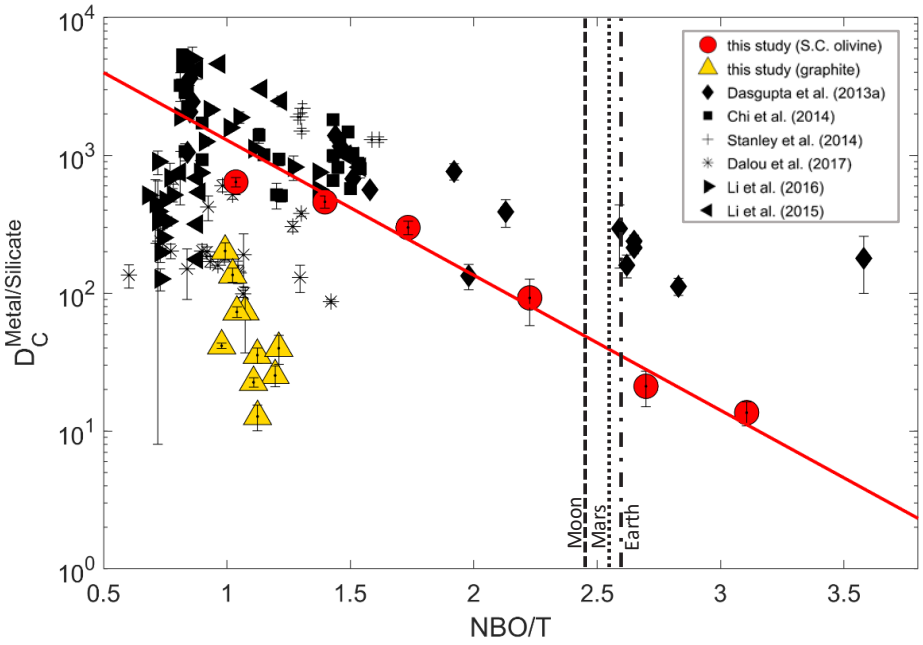

Fig. 3.9. *$D_C^{metal/silicate}$ as a function of the grade of silicate melt depolymerisation (NBO/T). With increasing temperature, the silicate melt becomes more depolymerised and the carbon partition coefficients between silicate and metal melt decreases. This is mainly due to the fact that the carbon content of the silicate melt increases with increasing NBO/T, whereas the carbon content of the metal melt remains nearly constant. The solid red line refers to the exponential trend line fitted through the experiments performed in San Carlos (S.C.) olivine, from which the $D_C^{metal/silicate}$ values of 34 ± 9, 38 ± 10, and 46 ± 11 for Earth, Mars, and Moon, respectively, can be estimated.*

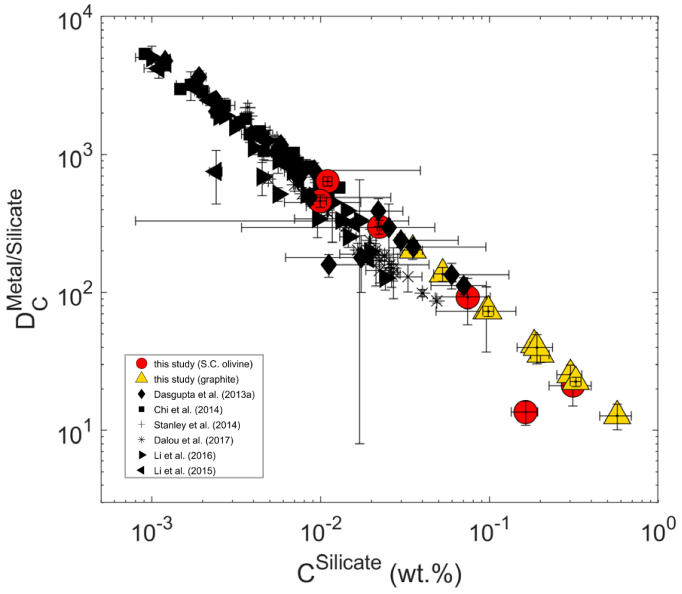

Fig. 3.10. *$D_C^{metal/silicate}$ as a function of the carbon content of the silicate melt. The carbon content in silicate melts has a strong effect on carbon partitioning. With increasing temperature and NBO/T, the carbon content of the silicate melt increases, which results in lower $D_C^{metal/silicate}$.*

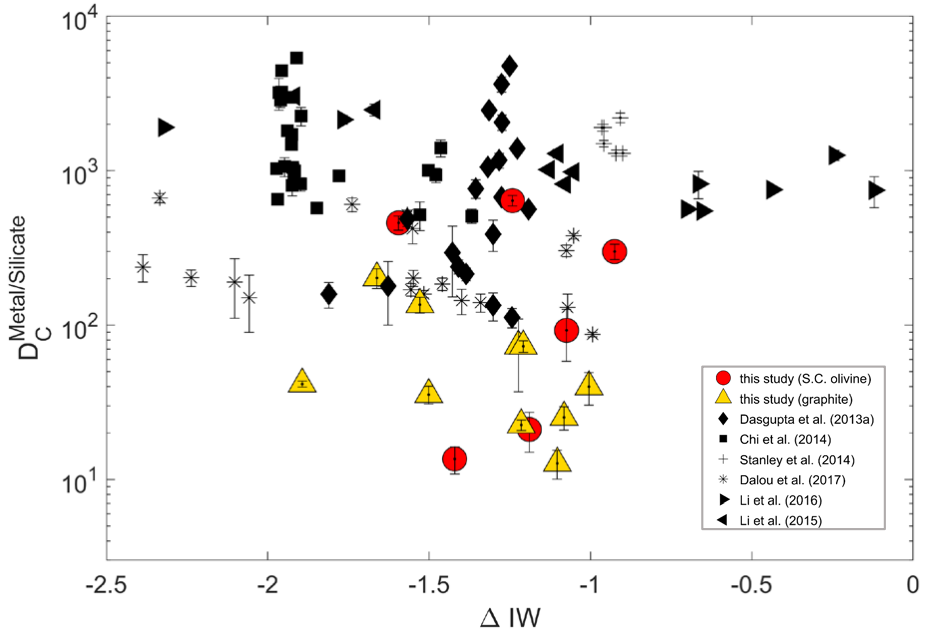

Fig. 3.11. *$D_C^{metal/silicate}$ as a function of oxygen fugacity (ΔIW). $D_C^{metal/silicate}$ seems not to correlate with fO_2 in the range of conditions covered. Whether a correlation exists at, e.g., more reducing conditions can only be determined by further experiments at an extended range of fO_2 conditions.*

3.4 Discussion

3.4.1 Carbon concentration in the silicate melt

A comparison of our carbon partition coefficients with literature data (Dasgupta et al., 2013a, Chi et al., 2014, Li et al., 2015, 2016, Dalou et al., 2017) reveals that our values are almost one order of magnitude more in favor of the silicate melt (Fig. 3.10). Specifically, we find a range from $D_C^{metal/silicate} = 14 \pm 3$ at 1750°C, 1.5 GPa, NBO/T = 3.1, ΔIW -1.2 to 640 ± 49 at 1300°C, 1.5 GPa, NBO/T = 1.0, ΔIW -1.6. For comparison, the experimental dataset with the lowest $D_C^{metal/silicate}$ in the literature yields at similar fO_2 112 ± 16 to 4757 ± 355 (2000 – 1600°C, 3 GPa, NBO/T = 2.8 – 0.8, ΔIW -1.3, Dasgupta et al. 2013a). The set with the highest $D_C^{metal/silicate}$ ranges from 510 ± 53 to 5369 ± 217 (1800 – 1500°C, 2 – 3 GPa, NBO/T = 1.2 – 0.8, ΔIW -1.9 – ΔIW-1.4, Chi et al. 2014). Since carbon concentrations in the metal melt vary only within factor two across all studies (~ 4 – 8 wt.% C), it is remarkable that carbon concentrations for a given P, T, NBO/T, fO_2 in our silicate melts are significantly higher than previously observed. Our higher C concentrations are even more surprising as all previous experiments have been performed in graphite capsules while our experimental design does not include an inherent C^0 saturation. The main difference between this study and earlier ones is that we added carbon to the silicate component as $CaCO_3$ and to the metal component as graphite powder intimately mixed into the Fe-Ni, while all previous authors used carbon-free starting materials assuming that graphite capsules would automatically lead to carbon saturation.

In an equilibrium situation, C partitioning between the silicate and metal melts should be the same at comparable experimental conditions and compositions and C concentrations should be highest under graphite saturation. This is clearly not the case (see Fig. 3.12), our C concentrations are higher in the silicate and also often in the metal melt, which leads to the interpretation that either C saturation might not have been established in some of the previous experiments or that our melts are C supersaturated. However, an in BSE images indiscernibly dispersed form of C^0 within the silicate melt, either amorphous or as badly crystallised graphite, would be observed in Raman spectra. This was not the case for experiments performed in San Carlos olivine and occurred only in two experiments run in graphite capsules (run PB1FS2-89 and run PB1FS2-102, see Fig. 3.7). Therefore, the presence of sub-microscopic C^0 can be ruled out as main reason for higher C contents in our silicate melts. The other possibility to explain the differences in C contents of silicate melts, and consequently in $D_C^{metal/silicate}$, is that experiments conducted by previous authors may not have been C-saturated. The use of graphite as capsule material may not necessarily result in carbon saturation of the sample, due to diffusion problems or non-equilibrium conditions. Further evidence for C-undersaturation in experiments run

in graphite capsules arises from the Fe-C phase diagram discussed below.

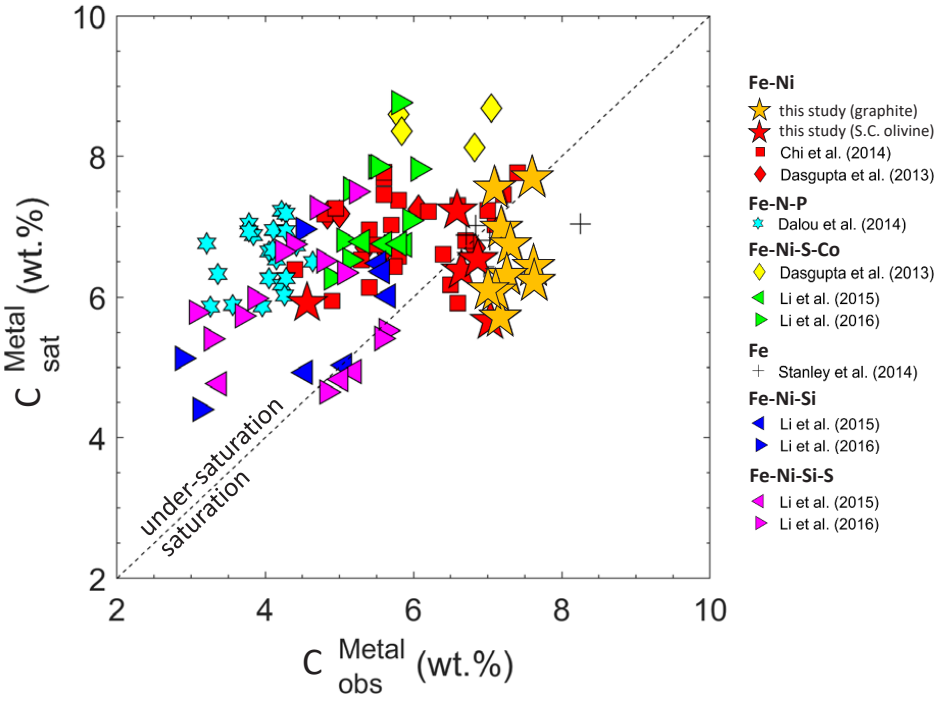

Fig. 3.12. *The calculated carbon saturation value of the metal melt versus the observed carbon content of the metal melt. The carbon saturation value was calculated from the Fe-C phase diagrams of Chipman (1972) and Nakajima et al. (2009), assuming a linear pressure-dependency of the Fe-C liquidus curve, and approximating a linear slope to this curve. Comparison of the carbon contents of the experimentally derived metallic melts with those calculated, indicates that our experiments were carbon-saturated, in contrast to most of the previous experiments from literature. The dashed line is the 1:1 line.*

3.4.2 Silicate melt polymerisation

For experiments performed in San Carlos olivine, silicate melt compositions adjust to olivine saturation. This causes with increasing temperature a strong increase of MgO in the silicate melt and decreasing SiO_2/FeO and SiO_2/MgO ratios (Fig. 3.3). Consequently, NBO/T, the ratio of non-bridging oxygen atoms to tetrahedrally coordinated cations, increases with temperature (Fig. 3.4). For experiments in graphite capsules, only the reduction of FeO changes silicate melt compositions leading to a limited compositional range of the silicate melt.

Fig. 3.9 shows the strong dependency of $D_C^{metal/silicate}$ on silicate melt depolymerisation, suggesting that NBO/T is a main factor in controlling carbon partitioning. The study of Dasgupta et al. (2013a) has also found that decreasing NBO/T from 0.8 to the value of bulk silicate Earth of 2.6 decreases $D_C^{metal/silicate}$ by about one order of magnitude. Consequently, the majority of experiments being on basaltic compositions, the $D_C^{metal/silicate}$ obtained on these compositions need to be decreased by the same amount in order to be applicable to the magma ocean. For example, the $D_C^{metal/silicate}$ values

of Li et al. (2016) at a constant NBO/T of 0.7 are mostly in the range of 100 to 1000 (temperature varying from 1600 – 2100°C) and would probably rather be in the range of 10 to 100 at magma ocean conditions (i.e., NBO/T = 2.6).

3.4.3 Carbon saturation in metal melts

Practically, carbon partitioning between silicate and metal melt is less affected by C concentrations in the metal melt than in the silicate melt, simply because there is comparatively little variability of C^{metal}, namely from ~ 4 to ~ 8 wt.% (Fig. 3.12). To rationalise C concentrations in the metal melt, we have fitted all measured concentrations with a function describing C saturation in metal. For this purpose, we used the 1 bar data from the steel literature (4.63 – 7.56 wt.% C at 1300 – 2200°C, Chipman, 1972), the 5 GPa data from Nakajima et al. (2009) (6.1 – 7.1 wt.% C at 1400 – 1700°C) and combined them with all available experiments in systems with little other ligands such as < 5 wt.% S (e.g. Dasgupta et al., 2013a; Li et al., 2015; 2016), < 4 wt.% N (e.g., Dalou et al., 2017), < 10 wt.% Si (e.g., Li et al., 2015; 2016) or < 26 wt.% Ni (e.g., Chi et al., 2014; this study). A linear pressure and temperature dependency of the C saturation curve fits the observations best and yields

$$C_{sat}^{Metal} = 0.004 \times T - 0.252 \times P + 0.521 \times \ln(fO_2) + 2.57 \times \ln(1 - X_{Ni}) + 0.142\,, \quad (3.7)$$

where the C content of the metal melt at graphite saturation (C_{sat}^{Metal}) is given in wt.%, pressure (P) in GPa, temperature (T) in K, fO_2 in IW, and X_{Ni} is the mole fraction of Ni in the metal melt. We have then compared C saturation values of the experiments on silicate/metal melt C partitioning with this fit, with deluding results: Even the data which are principally in the Fe-C system (e.g. Chi et al. 2015) yield measured C values up to 2 wt.% below saturation values (Fig. 3.12). Also those data which have additional minor elements in the metal melt (N, P, Si, S, Ni, Co, e.g., Li et al., 2015; 2016; Dasgupta et al., 2013a; Dalou et al., 2017) deviate unsystematically by similar amounts.

Part of the scatter could potentially result from a shift of the liquid-iron – graphite liquidus curve due to the influence of other elements like sulphur or nitrogen, and silicon or nickel. The effect of sulphur on C solubility in metal melt was initially found to be negligible up to 5 wt.% S (Li et al., 2015), but then Li et al. (2016) report a strong decrease in C content to less than 1 wt.% with S increasing to 5.6 wt.% or Si increasing to 7.8 wt.% in the metal melt. Corgne et al. (2008) and Dasgupta et al. (2009) reported a similar correlation between S and C solubility in metal melt for S contents of 5 – 32 wt.%. Nickel was found to diminish C solubility in metal melt (Holzheid & Grove, 2005; Dasgupta & Walker, 2008).

In summary, the available data do not yield a consistent picture. Part of the problem is most likely an overestimation of our ability to accurately determine C contents in the coarse quench of metal melts, reports of errors of 0.3 wt.% do obviously not correspond to the scatter observed. Our SIMS measurements indicate a 1σ error of up to 0.7 wt.% C, a simple result from a heterogeneity on a 30 μm scale. Secondly, reported C contents frequently below the C saturation curve and the fact that our C-undersaturated metal melts have higher C concentrations than many comparable experiments run in graphite capsules, suggest that the latter did not reach C saturation. Most of these experiments have metal droplets isolated in the silicate melt requiring redox-dissolution of C in the silicate melt, diffusion through the silicate melt and re-precipitation of C in metallic form in the metal droplet. As C solubilities in the silicate melt are low, the carbon flux through the silicate may not be sufficient to saturate the metal melt droplets. Alternatively, the highest C values in the metal may reflect supersaturation, but metal melts do precipitate excess carbon on experimental timescales (this actually happened in a few of our experiments, Table 3.2). We hence sustain that metal droplets isolated from the graphite capsule by silicate melt do not automatically reach carbon saturation and consequently the silicate melt is neither automatically carbon-saturated.

3.4.4 Implications for carbon repartitioning in Earth and Mars

The origin and distribution of Earth's carbon remains disputed (Marty, 2012). One endmember scenario has carbon delivered through chondritic materials during Earth's accretion (e.g., Morbidelli et al., 2012). The other endmember has most of the present day volatiles in the silicate Earth, including carbon, delivered after the moon-forming event by a chondritic late veneer (Chou 1978; Wänke 1981) or by comets. However, the latter hypothesis appears inconsistent in terms of isotopic composition of hydrogen and oxygen (e.g., Mandt et al., 2015).

The carbon present during accretion was fractionated between core-forming metal melt and the silicate melt that made up the magma ocean. On one hand, the carbon partition coefficient between these two melts determines the C content of the core, on the other hand, it determines how much C was present in the bulk silicate Earth (BSE) after accretion. The experimental studies of Dasgupta and coworkers (Dasgupta et al., 2013a; Chi et al., 2014; Li et al., 2015; 2016) and of Dalou et al. (2017) yield siderophile $D_C^{metal/silicate}$ values larger than 100, thus supporting that at the end of accretion carbon was mainly stored in the Earth's core. However, the BSE C content of 120 (McDonough & Sun, 1995) or 765 ppm (Marty, 2012) cannot be explained by a scenario where bulk carbon is strongly partitioned into the core, leaving behind a mostly C-free mantle. Therefore, all these authors suggest

that carbon and other volatile elements were delivered to the Earth through a post-core formation process. This could be a volatile-rich chondritic "late veneer", inefficient core formation where small batches of C-rich metal melt were trapped in the mantle (Jones & Drake, 1986; Newsom & Sims; 1991), or carbon ingassing through magma ocean – atmosphere interaction (Dasgupta et al., 2013a; Hirschmann, 2012). In this study, however, we experimentally determined $D_C^{metal/silicate}$ values that are significantly lower than previously reported and show a less siderophile character of carbon at magma ocean conditions (i.e., NBO/T = 2.6).

The correlation between $D_C^{metal/silicate}$ and NBO/T (Fig. 3.9) can be used to determine the carbon partitioning during Earth's accretion with a magma ocean equal to a peridotitic silicate Earth composition (NBO/T = 2.6, McDonough & Sun, 1995), yielding a partition coefficient of 34 ± 9. It is assumed that the chemical composition of the magma ocean has not significantly changed over time (i.e., NBO/T = 2.6 is valid throughout the accretion), such that the carbon partition coefficient may have also been constant during accretion not depending on any other accretion parameters like e.g., the depth of the magma ocean or the temperature. The only target constrain for any accretion scenario is the carbon content of BSE after accretion, which may amount to between 120 and 765 ppm (McDonough & Sun, 1995; Marty, 2012).

The homogeneous core formation scenario of Wood et al. (2006) has 99 impacts with equal masses (0.01 present-day Earth mass) that fully equilibrate in the magma ocean and always deliver the same amount of carbon. In this scenario, the above partition coefficients lead to C concentrations of the core of 0.4 ± 0.1 – 2.6 ± 0.7 wt.% and bulk Earth C contents of 0.14 ± 0.03 – 0.9 ± 0.2 wt.% (Fig. 3.13). Interestingly, the number and size of impactors does not change the final results, as after the first few impacts the C concentrations in mantle and core are already set (Fig. 3.13). These bulk Earth carbon values are relatively low in comparison to C1 carbonaceous chondrites (3.5 wt.% C, Anders & Grevesse (1989)), but similar to those of enstatite chondrites (0.42 wt.% C, Jarosewich (1990)), thought to be essential contributors to bulk Earth (e.g., Javoy, 1995). Considering a scenario where the Earth was entirely built from enstatite chondritic material and where negligible carbon would evaporate, BSE carbon would result in 260 – 460 ppm with a core containing ~1.2 wt.% C. Building the Earth only from volatile-rich C1 carbonaceous chondrites, the upper modern BSE carbon content of 765 ppm would yield a maximum of 1.6 wt.% C in the core and a bulk Earth carbon content of 0.6 wt.%, requiring 83 % of the carbon to be blown off to space during accretion.

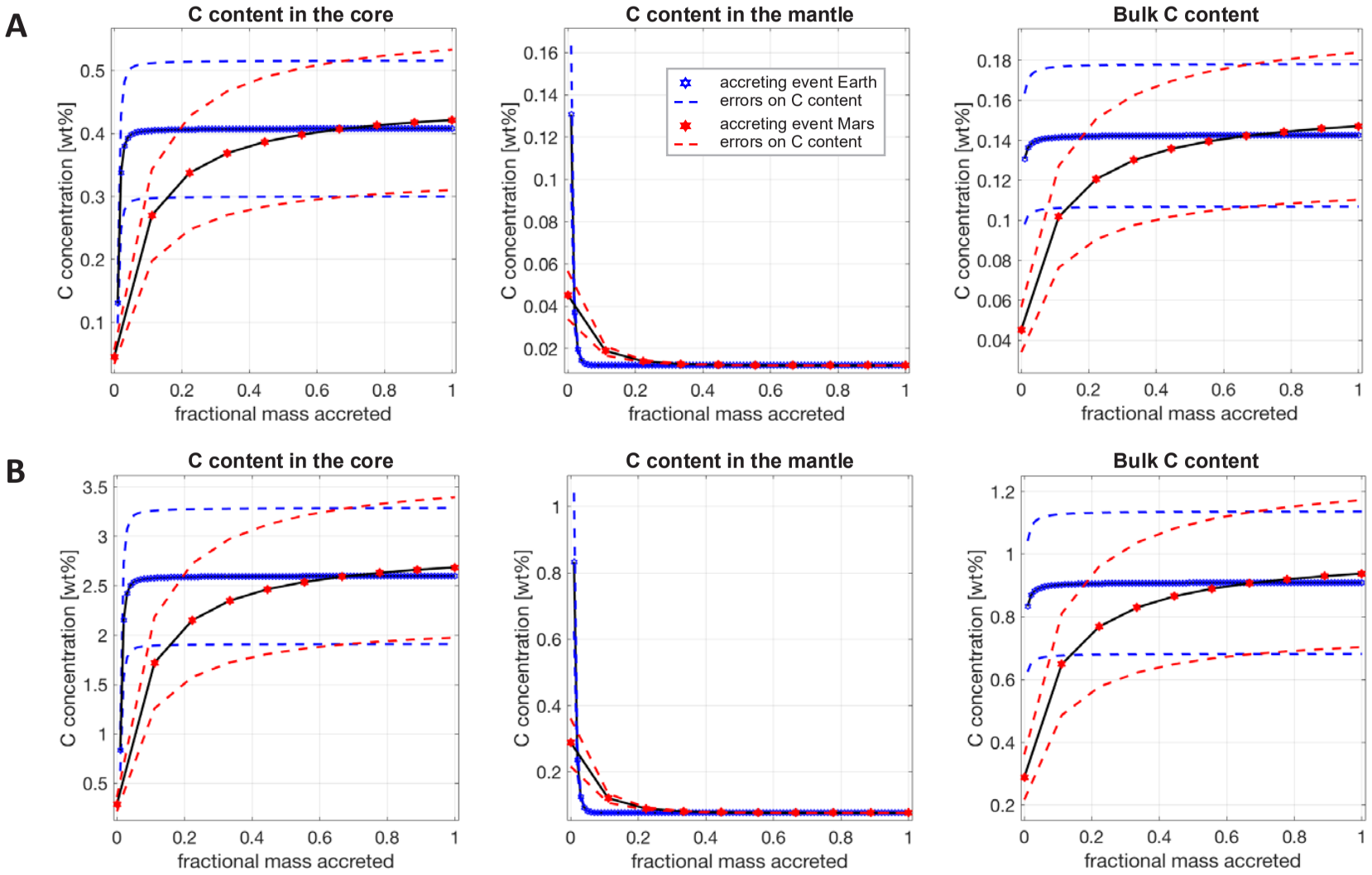

Fig. 3.13. *Carbon concentration of the core, mantle and bulk planet for the Earth and Mars. Estimations are based on a homogeneous core formation scenario after Wood et al. (2006), where 99 impactors accrete to the Earth and 9 impactors accrete to Mars. The mantle C estimations are normalised to known values for the Earth that range between 120 ppm (A) and 765 ppm (B). For Mars, the same building blocks as for the Earth are assumed. The distribution of carbon is calculated from* $D_C^{metal/silicate}$ *which is a function of NBO/T (see text and Fig. 3.9) yielding* $D_C^{metal/silicate}$ *values of* 34 ± 9 *and* 38 ± 10 *for Earth and Mars, respectively.*

Most likely, the modern BSE carbon content is not that of the mantle at the end of accretion as the abundance of highly siderophile elements in the mantle appears to require a late veneer, i.e. about 1% of Earth mass to be delivered from C1 chondritic material after completion of core formation. This late veneer would contribute around 350 ppm carbon to bulk silicate Earth, diminishing the end-of-accretion target BSE carbon. The carbon content of the core would proportionally decrease and a core of 0.3 wt% carbon would result when part of the mantle carbon was brought by an C1 chondritic late veneer.

The polymerisation of the deduced mantle composition of Mars is very similar to the Earth and has an NBO/T of 2.55 (Lodders & Fegley, 1997), suggesting a carbon partition coefficient of 38 ± 10 (Fig. 3.9). There is a complete lack of information about the C content of the Martian mantle. The mass of Mars is only 10 % of the Earth's mass, therefore, a Mars accretion scenario analogous to that of Earth requires only 9 impactors Fig. 3.13. Assuming that Mars mantle carbon contents are similar to those of Earth (i.e., 120 to 765 ppm C), this results in core concentrations of 0.4 ± 0.1 to 2.7 ± 0.7 wt.% C and inferred bulk Mars C contents of 0.15 ± 0.03 – 0.9 ± 0.2 wt.%.

The Lunar mantle is estimated to contain 44 – 64 ppm C (Wetzel et al., 2015) and may be slightly more polymerised (NBO/T = 2.46, Rai & van Westrenen (2014)). This results in a carbon partition coefficient of 46 ± 11 (Fig. 3.9). The core of Moon might be directly derived from Earth core material without equilibration, in which case partitioning on Earth is determent. If the Lunar magma ocean equilibrated with the lunar core material, an estimated 44 – 64 ppm C in the mantle result in a Lunar core content of 0.3 – 4 wt% C (Steenstra et al., 2017), also similar to the terrestrial core carbon content.

3.5 Conclusions

The experiments of this study demonstrate that carbon concentrations in the metal melt vary comparatively little, simply because carbon is a major constituent and not a trace. Instead, carbon in the silicate melt varies from 0.01 to 0.57 wt.% and carbon partition coefficients mainly correlate with melt composition (NBO/T) and range from 14 to 640. For an NBO/T of the silicate Earth (2.6), carbon is considerable less siderophile than previously thought yielding bulk $D_C^{metal/silicate}$ of 34 – 46 for the Earth, Mars and Moon. Our favorite scenario has a bulk silicate Earth carbon content at the higher end of present day estimates (~750 ppm), nevertheless, the end-of-accretion mantle has to be diminished by the carbon brought by the late veneer which accounts for 350 ppm C in silicate Earth.

We hence favor an end-of-accretion mantle with 600 ppm, which would yield about 1.3 wt.% carbon in the core as a plausible upper limit.

Finally, this study will raise some dispute about the correct experimental procedure in order to obtain true equilibrium of carbon species between silicate and metal melts. Nevertheless, we maintain that a combination of low solubilities and low diffusivities of carbon species in silicate melts prohibit diffusion to progress sufficiently on relatively short experimental time scales, hence favoring equilibration in experiments where carbon is already present in the silicate and metal starting materials.

4. Carbon partitioning between core-forming metallic and mantle-forming silicate melts – Implications for the origin and inventory of Earth's carbon

Abstract

The carbon partition coefficient between metallic and silicate melt, $D_C^{metal/silicate}$, constrains the distribution of carbon between the core and the mantle during Earth's accretion. In this study, high-pressure and -temperature experiments have been performed at 1.5 GPa and 1400 – 1500°C to investigate the effect of oxygen fugacity (fO_2), silicate melt depolymerisation (NBO/T), and metal melt composition (X_{Ni}, X_{Si}) on $D_C^{metal/silicate}$. To avoid graphite saturation and to obtain realistic melt compositions, San Carlos olivine and synthetic forsterite capsules have been used over a large range of fO_2 conditions. Raman spectroscopic analyses of silicate glasses show that the dominant C species change from carbonate complexes to methyl groups while fO_2 decreases from ΔIW +2.2 to ΔIW -4.8. This strongly reduces the amount of C dissolved in the silicate melt from 0.97 ± 0.01 to 0.07 ± 0.01 wt.%, as determined by secondary ion mass spectrometry (SIMS). The C content of the metal melts, determined by SIMS or EPMA, is hardly affected by fO_2 and amounts to 5.6 ± 0.7 wt.% in all experiments, except the Ni-rich metal melts, where the C content is 1.3 wt.% or lower. Since the amount of C dissolved in the metal melt is similar in all experiments at fO_2 < IW, $D_C^{metal/silicate}$ mainly depends on the C content of the silicate melt, which in turn is mostly controlled by fO_2. Our experimentally determined $D_C^{metal/silicate}$ ranges from 8 ± 1 to 274 ± 6 and decreases with increasing fO_2. Based on our own and on literature data, a parameterisation of the carbon partition coefficient was derived that applies to conditions of Earth's accretion. Combining the parameterisation with estimates of magma ocean conditions, the range of $D_C^{metal/silicate}$ for the Earth can be derived. The most successful core formation scenario in matching the bulk silicate Earth (BSE) carbon content of 120 – 765 ppm, involves homogeneous accretion from mostly highly reduced enstatite chondrites, yielding ~ 550 ppm C. The resulting C content of the Earth's core in this scenario would be ~ 1.15 wt.%. In general, applying our parameterisation of $D_C^{metal/silicate}$ to core formation scenarios in the literature, it is striking that the resulting C concentrations of the magma ocean are 1 – 2 orders of magnitude higher than the present–day BSE C content. Thus, severe carbon loss perhaps caused by the escape of the Earth's proto–atmosphere may have occurred. Normalising the estimated BSE C concentrations to 100 or 500 ppm results in core C concentrations of 0.17 to 0.25 and 0.85 to 1.30 wt.%, respectively. These values are nearly independent of the core formation scenario and are mainly controlled by the

C concentration of the impactors. In conclusion, there is no need for a post-accretion delivery process like a volatile-rich "late veneer" to explain C abundances of the Earth's mantle. Instead, the mantle C reservoir may have been set during core formation and differentiation.

The aim of this doctoral project was to experimentally constrain the carbon partitioning between silicate melt and metal melt at conditions that might have prevailed during Earth's accretion and differentiation. The results of this study contribute to a better understanding of the parameters determining the carbon partitioning, and they lead to important implications on the origin of carbon and its distribution between the Earth's core and mantle. In this chapter, a brief summary of the main conclusions is given, followed by an outlook about other light elements that might potentially be present in the Earth's core and may constitute the core's density deficit.

4.1 Introduction

The fate of carbon during Earth's accretion plays an important role in chemical and physical processes during the later evolution of our planet. It has therefore been the subject of several experimental studies (Dasgupta & Walker, 2008; Dasgupta et al., 2013; Chi et al., 2014; Stanley et al., 2014; Armstrong et al., 2015; Li et al., 2015; Li et al., 2016; Dalou et al., 2017; Duncan et al., 2017), which aim to shed light on (1) the incorporation mechanisms of carbon in silicate melt, (2) the storage capacity of carbon in the Earth's metallic core and the silicate mantle, and (3) the origin of the Earth's carbon, which is either some remnant fraction from accretion and/or delivered during a post-accretion event such as the "late veneer". In this context, the behaviour of carbon and other volatile elements during core-formation has been controversially discussed regarding its origin and initial distribution between a metallic core and a silicate magma ocean.

Bulk silicate Earth carbon was estimated to 120 – 765 ppm (McDonough & Sun (1995) and Marty (2012), respectively), to which the carbon stored in the crust contributes ~ 30 ppm (Sleep & Zahnle, 2001). The large range results from different methods (e.g. analogy to noble gases vs. deduction of concentrations in different mantle reservoirs from erupted magmas) and from different estimates of the various mantle type reservoir sizes. The key quantity to constrain the bulk carbon content of the Earth and its fractionation between the core-forming metallic melt and mantle-forming silicate melt is the carbon partition coefficient $D_C^{metal/silicate}$ between these two melts. Parameters controlling carbon partitioning include the depth of the magma ocean (Dasgupta et al., 2013; Chi et al., 2014), the prevailing oxygen fugacity, and possibly the available amount of H_2O in the magma ocean (Li et

al., 2015; Li et al., 2016), silicate melt polymerisation, NBO/T, (Dasgupta et al., 2013; Dalou et al., 2017; Fichtner et al., 2018a), and the C content of the silicate melt (Dalou et al., 2017; Fichtner et al., 2018a). It should be noted that in the accreting Earth, the temperature at the base of the magma ocean, which is necessarily on the liquidus of peridotitic material, is a direct function of its depth. Furthermore, oxygen fugacity and silicate melt polymerisation are somewhat dependent parameters, as oxygen fugacity controls the amount of FeO in the silicate melt.

Most of the above studies employed graphite capsules in their experiments as sole carbon source. Nevertheless, there is no evidence for dissolution of elemental carbon in silicate melts. However, carbon dissolves as carbonate or molecular CO_2, as other C≡O species, or as methyl groups (e.g., Holloway et al., 1992; King & Holloway, 2002; Mysen et al., 2009; Ardia et al., 2013). Consequently, there might be a disequilibrium in the C fractionation between the metallic and the silicate melt.

To avoid graphite saturation, Fichtner et al. (2018a) used San Carlos olivine as capsule material and added C as carbonate to the silicate fraction and as graphite powder to the metal fraction, a strategy that we further extend in this study. As the redox reaction

$$2Fe^{metal} + O_2 + {SiO_2}^{silicate\ melt} \leftrightarrow Fe_2SiO_4^{olivine\ capsule} \quad (4.1)$$

buffers oxygen fugacity, San Carlos olivine capsules only allow for a relatively limited range in fO_2 of ΔIW -1.0 – ΔIW -1.8 in this type of experiments, with IW being the oxygen fugacity defined by the iron-wüstite buffer, Fe-FeO. To reach more reducing fO_2 conditions of ΔIW -4.0, we performed experiments in synthetic forsterite capsules, thereby enabling fO_2 conditions that might have prevailed during early stages of core formation (e.g., Righter & Ghiorso, 2012; Rubie et al., 2011).

Carbon contents of 9 to 703 ppm in silicate melts found in previous studies (Dasgupta et al., 2013; Chi et al., 2014; Stanley et al., 2014; Li et al., 2015; Li et al., 2016; Dalou et al., 2017) result in relatively high carbon partition coefficients of 87 to 5369 within a wide range of conditions (pressure: 1 – 8 GPa, temperature: 1400 – 2200°C, fO_2: ΔIW -0.4 – ΔIW -5.3, NBO/T: 0.6 – 3.6, and different Fe-rich metal melt constituents: N, S, P, Si, Ni, Co). Consequently, these studies suggest that C partitioned strongly into the segregating metal that ultimately formed the core, leaving behind a mostly carbon-free mantle with only 0.04 – 4.5 ppm C (Dasgupta et al., 2013; Chi et al., 2014). These C concentrations are orders of magnitude lower than the 14 – 1300 ppm C for the present-day mantle (Saal et al., 2002; Pineau et al., 2004; Salters & Stracke, 2004; Cartigny et al., 2008). The commonly proposed addition of a volatile-rich “late veneer” after core formation would hence have to supply

the mantle C (Chou, 1978; Wänke, 1981). Inefficient core formation due to incomplete segregation and entrapment of some metal phase (subsequently oxidised, Jones & Drake, 1986; Newsom & Sims, 1991) in the mantle could also explain the observed present-day C content of the mantle. Alternatively, relatively late stage ingassing through magma ocean – proto-atmosphere interactions could have led to an enhanced C dissolution in the late magma ocean (Dasgupta et al., 2013).

In order to better understand the re-partitioning and hence bulk carbon content of the Earth, and to constrain the timing and origin of the volatile delivery process, we parameterised our new carbon partition coefficients. This is intended to quantify the effects of pressure (P), temperature (T), oxygen fugacity (fO_2), silicate melt composition (NBO/T), and metallic melt composition (X_{Ni}, X_{Si}) on $D_C^{metal/silicate}$. The parameterisation allows us to extrapolate to conditions that have prevailed during Earth's accretion and therefore constrain the carbon inventory of the Earth's mantle and core.

4.2 Methods

Carbon partition coefficients between synthetic silicate melt and Fe-rich metal melt were experimentally determined. Experiments were conducted in C-free sample containers made of either single crystal San Carlos olivine or polycrystalline synthetic forsterite. C concentrations in both silicate glass and metal alloy were measured by SIMS at the University of Lausanne, and by a conventional elemental analyser (LECO) at ETH Zurich. The C content of some metal melts were additionally analysed by EPMA at the University of Frankfurt. For identifying the prevailing C species, Raman spectra were collected at ETH Zurich.

4.2.1 Experimental methods

Experimental charges were composed of 70 – 80 wt.% silicate powder and 20 – 30 wt.% metal powder. The composition of the silicate powder is based on (1) the primitive basaltic glass described in Melson et al. (1976) or (2) a primitive (here Fe-free) high-alumina basalt from Giant Crater Lava Field, Medicine Lake Volcano, California (Donnelly-Nolan et al., 1991). Both compositions were then adjusted to our experiment's inherent olivine saturation such that a quenchable homogeneous silicate glass was obtained (Table 4.1). It was found that the olivine capsule experiments work well as long as little olivine is absorbed by the capsule charge, large amounts of olivine dissolution resulting in unwanted peritectic minerals or uncontrollable textures with, e.g., re-precipitated olivine all over the charge. The metal powder was composed of Fe-C, Fe-Ni-C or Fe-Si-C mixtures (Table 4.1).

Carbon was added through $CaCO_3$ into the silicate component and as pure synthetic graphite in the metal component. Chemicals were pre-dried, spectroscopically pure oxides (SiO_2, TiO_2, Al_2O_3, MgO, NiO), silicates (Fe_2SiO_4, $CaSiO_3$, Na_2SiO_3, $NaAlSi_3O_8$, $KAlSi_2O_6$), or metals (Fe, Ni, Si) and mixed in an agate mortar in ethanol for 45 minutes. After mixing, the starting materials were stored at 110°C for ≥ 24 h to remove any moisture and ethanol remnants.

Table 4.1
Chemical compositions of starting materials (in wt.%).

Silicate mix	Primitive basalt[a]		Fe-free, high-Al basalt[b]		
	PB1	PB2	HAB1	HAB2	
SiO_2	45.9	47.5	50.4	52.2	
TiO_2	2.2	2.3	0.6	0.6	
Al_2O_3	7.6	7.9	19.5	20.2	
FeO	12.6	13.0	–	–	
MgO	7.9	8.1	10.8	11.2	
CaO	7.4	7.7	12.5	12.9	
NiO	3.9	0.3	–	–	
Na_2O	8.5	8.8	2.2	2.3	
K_2O	3.8	3.9	–	–	
CO_2	0.3	0.5	3.9	0.5	
Total	100	100	100	100	
Metal mix	**Fe**	**Ni**	**Si**	**C**	**Total**
Fe–C					
F1	100	–	–	–	100
F2	98	–	–	2	100
Fe–Ni–C					
FN1	9.9	89.5	–	0.6	100
FN2	49.7	49.7	–	0.6	100
Fe–Si–C					
FS1	83	–	17	–	100
FS2	81.4	–	16.7	1.9	100
FS3	79.0	–	16.2	4.8	100
FS4	83.8	–	11.4	4.8	100
FS5	87.6	–	7.6	4.8	100

[a] composition modified from a primitive basaltic glass described in Melson et al. (1976), such that the silicate melt quenched to a homogeneous glass in a San Carlos olivine or synthetic forsterite capsule. PB1 and PB2 vary in NiO content.

[b] a primitive high-alumina basalt from Giant Crater Lava Field, Medicine Lake Volcano, California (Donnelly-Nolan et al., 1991). HAB1 and HAB2 vary in the amount of CO_2.

To study the effect of fO_2 on carbon partitioning between metal and silicate melt, Fe-Si and Fe-Ni ratios were varied (Table 4.1). Olivine-platinum double capsules were employed to ensure that volatile C-H-O species remained inside the system. Graphite capsules were avoided to keep control of the carbon source and to (mostly) avoid graphite saturation. Bulk Fe loss did not occur in the experimental charges loaded into San Carlos olivine (Jarosewich et al., 1980) capsules, but saturation with San Carlos olivine slightly changed bulk FeO contents. Synthetic forsterite was used for oxygen fugacities where all Fe is metallic.

The synthetic forsterite was produced by hot hydrostatic pressing. Thereby, 1 kg of pre-dried spectroscopically pure MgO and SiO_2 were stoichiometrically mixed in a large automated mortar for more than 3 hours. Afterwards, the Mg_2SiO_4 powder was filled in a cylindrical stainless steel canister (35 mm diameter, 200 mm height, lined with molybdenum foil to avoid Fe diffusion) and uniaxially cold pressed. The canister was then sealed and hot isostatically pressed using an internally heated gas vessel (ABRA Fluid AG, Switzerland) at 1200°C and 1000 bar for 6 hours. The sintered forsterite and the single crystal San Carlos olivine capsules (3.4 mm outer diameter, 2 mm inner diameter and 6.0 mm in height) were drilled using a diamond hollow drill bit.

Experiments were carried out at ETH Zurich using a static 14 mm bore end-loaded piston cylinder apparatus (Boyd and England, 1960) at mostly 1.5 GPa and 1400°C or 1500°C (Table 4.2). To create larger melt pools and to enable bulk analyses, the silicate and metal melts of five samples (experiments PB1FN1-32, -37, PB2F2-44, -72, and HAB2F2-54) were gravitationally separated using a centrifuging piston cylinder (Schmidt et al., 2006) after pre-equilibration in the static piston cylinder. The acceleration of the centrifuge reached 800 g and was applied for at least 30 minutes to achieve complete separation of the conjugate melts (Fig. 4.1). The centrifuging and the static piston cylinders have identical assemblies consisting of inner MgO cell parts (dehydrated at 1000°C) surrounded by a graphite heater and a talc-Pyrex sleeve (experiments ≤ 1500°C) or a talc-SiO_2 glass sleeve (experiment at 1900°C). The capsule was placed in the centre of the assembly to minimise temperature gradients (temperature uncertainty ± 7°C). The Pt-capsule was isolated from the thermocouple by a ruby disc. Mullite thermocouple sleeves and a type B PtRh thermocouple were used for experiments ≤ 1500°C and dense Al_2O_3 sleeves and type C WRe thermocouples for the experiment at 1900°C. The pressure calibration against the quartz-coesite transition (Bose and Ganguly, 1995) gives a friction of 10 %. Experimental runs were quenched by switching off the electric power of the furnace. The recovered capsules were embedded in methyl methacrylate epoxy resin and polished for electron probe microanalyses (EPMA), secondary ion mass spectrometry (SIMS), and Raman spectroscopy. For bulk analyses using an elemental carbon analyser (see section below), the capsules were opened with a 300 µm diamond wire saw. The quenched metal and silicate glass were then carefully recovered in several fragments. To ensure the purity of each sample, fragments showing any remnants of the olivine capsule or quench olivine needles in the glass were excluded from further analyses.

Table 4.2
Summary of experimental conditions, carbon concentrations, and carbon partitioning between metallic and silicate melt.

Sample	P (GPa)	T (°C)	Duration	inner capsule material	metal/ silicate	fO_2	Fe-Ni-Si-C metal melt				Silicate melt			D_C	1 σ
						(ΔIW^a)	C EPMA (wt.%)	1 σ	C SIMS (wt.%)	1 σ	C SIMS (wt.%)	1 σ	NBO/T[b]		
PB1FN1-31	1.5	1400	1.5 h	SC Olivine	80/20	2.20	1.30	0.02	-	-	0.53	0.18	1.81	2	1
PB1FN1-32	1.5	1400	2 h	SC Olivine	80/20	1.22	0.66	0.03	0.034	0.004	0.97	0.01	2.00	0.035	0.004
PB1FN1-37	1.5	1400	1.5 h	SC Olivine	80/20	0.89	0.81	0.09	0.12	0.04	0.44	0.05	1.87	0.27	0.09
PB1FN2-95	1.5	1400	1.5 h	SC Olivine	80/20	1.39	-	-	3.98	2.77	0.238	0.003	1.82	17	12
PB1FS2-84	*1.5*	*1300*	3 h	*SC Olivine*	*80/20*	*-1.24*	-	-	*7.04*	*0.30*	*0.011*	*0.001*	*1.04*	*640*	*49*
PB1FS2-57[c]	*1.5*	*1400*	2 h	*SC Olivine*	*80/20*	*-1.59*	*4.98*	*0.14*	*4.56*	*0.20*	*0.010*	*0.001*	*1.40*	*460*	*47*
PB1FS2-77	*1.5*	*1500*	1.75 h	*SC Olivine*	*80/20*	*-0.93*	-	-	*6.65*	*0.73*	*0.022*	*0.001*	*1.73*	*299*	*34*
PB1FS2-78	*1.5*	*1600*	30 min	*SC Olivine*	*80/20*	*-1.07*	-	-	*6.87*	*0.68*	*0.07*	*0.03*	*2.23*	*92*	*34*
PB1FS2-80[c]	*1.5*	*1700*	20 min	*SC Olivine*	*80/20*	*-1.19*	-	-	*6.59*	*0.52*	*0.31*	*0.09*	*2.70*	*21*	*6*
PB1FS2-87[c]	*1.5*	*1750*	2 min	*SC Olivine*	*80/20*	*-1.66*	-		*6.58*	*0.19*	*0.30*	*0.03*	*2.88*	*22*	*3*
PB1FS2-103	*1.5*	*1750*	20 min	*SC Olivine*	*80/20*	*-1.42*	*2.22*	*0.20*	-	-	*0.16*	*0.03*	*3.11*	*14*	*3*
PB1FS2-91[c]	*1.5*	*1500*	*2 h*	*Graphite*	*80/20*	*-1.89*	-	-	*7.63*	*0.24*	*0.18*	*0.01*	*0.98*	*42*	*2*
PB1FS2-89[c]	*3.5*	*1900*	*2 min*	*Graphite*	*80/20*	*-1.66*	-	-	*7.10*	*0.27*	*0.035*	*0.005*	*0.99*	*202*	*29*
PB1FS2-112[c]	*6.0*	*1600*	*1 h*	*Graphite*	*80/20*	*-1.53*	-	-	*7.17*	*0.15*	*0.05*	*0.01*	*1.02*	*136*	*16*
PB1FS2-102[c]	*6.0*	*1650*	*1 h*	*Graphite*	*80/20*	*-1.50*	-	-	*7.11*	*0.27*	*0.20*	*0.03*	*1.12*	*35*	*5*
PB1FS2-113	*6.0*	*1650*	*1 h*	*Graphite*	*80/20*	*-1.22*	*5.66*	*0.07*	*7.01*	*0.12*	*0.10*	*0.05*	*1.07*	*73*	*36*
PB1FS2-110	*6.0*	*1700*	*50 min*	*Graphite*	*80/20*	*-1.10*	-	-	*7.26*	*0.17*	*0.57*	*0.12*	*1.12*	*13*	*3*
PB1FS2-107	*6.0*	*1720*	*30 min*	*Graphite*	*80/20*	*-1.08*	-	-	*7.62*	*0.23*	*0.30*	*0.05*	*1.20*	*25*	*4*
PB1FS2-108	*6.0*	*1810*	*30 min*	*Graphite*	*80/20*	*-1.21*	-	-	*7.31*	*0.12*	*0.32*	*0.02*	*1.11*	*23*	*2*
PB1FS2-111	*6.0*	*1865*	*20 min*	*Graphite*	*80/20*	*-1.21*	-	-	*7.19*	*0.36*	*0.10*	*0.01*	*1.04*	*73*	*6*
PB1FS2-109	*6.0*	*2000*	*12 min*	*Graphite*	*80/20*	*-1.00*	-	-	*7.61*	*0.19*	*0.19*	*0.05*	*1.21*	*40*	*9*
PB2F2-40	1.5	1400	1.5 h	SC Olivine	80/20	-1.10	-	-	6.13	0.07	0.0224	0.0004	1.61	274	6
PB2F2-44	1.5	1400	1.5 h	SC Olivine	70/30	-1.14	4.96	0.09	4.88	0.10	0.18	0.06	1.92	27	8
PB2F2-72[c]	1.5	1400	1.5 h	SC Olivine	70/30	-0.97	4.89	0.15	6.20	0.03	0.45	0.10	2.04	14	3
HAB1F2-46[c]	1.5	1500	2 h	SC Olivine	70/30	-1.38	5.24	0.12	6.17	0.08	0.47	0.15	1.79	13	4
HAB2F1-92	1.5	1500	2 h	SC Olivine	70/30	-1.75	-	-	4.69	0.53	0.30	0.12	1.53	16	6
HAB2F2-49	1.5	1500	2 h	SC Olivine	70/30	-1.83	5.08	0.08	4.82	0.09	0.04	0.01	1.39	128	34
HAB2F2-52	1.5	1500	2 h	SC Olivine	70/30	-1.33	4.85	0.10	6.23	0.21	0.25	0.04	1.23	25	4
HAB2F2-54	1.5	1500	2 h	SC Olivine	70/30	-1.53	-	-	5.68	0.14	0.23	0.01	1.35	25	1
HAB2FS1-97	1.5	1500	2 h	SC Olivine	80/20	-3.80	-	-	4.78	0.64	0.048	0.004	1.17	101	16
HAB2FS1-96	1.5	1500	2 h	Forsterite	80/20	-4.36	-	-	4.48	0.25	0.07	0.01	1.40	65	10
HAB2FS3-83[c]	1.5	1500	2 h	Forsterite	80/20	-4.47	-	-	6.02	0.41	0.12	0.03	1.24	52	12
HAB2FS3-88[c]	3.5	1900	2 min	Forsterite	80/20	-4.03	-	-	6.18	0.23	0.13	0.01	2.15	49	3
HAB2FS4-85[c]	1.5	1500	2 h	Forsterite	80/20	-4.84	-	-	6.57	0.38	0.54	0.47	1.26	12	11
HAB2FS5-86[c]	1.5	1500	2 h	Forsterite	80/20	-2.95	-	-	6.27	0.12	0.81	0.06	1.61	8	1

Sample codes refer to the starting mixture of the silicate melt (PB or HAB) and the starting mixture of the metal melt (F, FN or FS) as shown in Table 4.1, followed by the actual run number.

[a] Non-ideal fO_2, which considers the interaction between the components in the metallic and silicate melt (γ_{Fe} determined by the online calculator *MetalAct* (http://www.earth.ox.ac.uk/~expet/metalact/, Wood, BJ; Wade, J; Norris, A, last accessed on October 18th 2017), and $\gamma FeO = 1$ after Médard et al. (2008), respectively). Carbon saturation was computed in the activity calculation for experiments showing excess carbon that precipitated from the metal melt (labelled with [c] in the table).

[b] NBO refers to 2*(ΣO - 4T) with T = Si + Ti + Al.

[c] Metal melt precipitated excess carbon.

Experiments in italics are re-reported from Fichtner et al. (2018a).

Errors are given in 1 σ standard deviation based on replicate measurements using EPMA or SIMS.

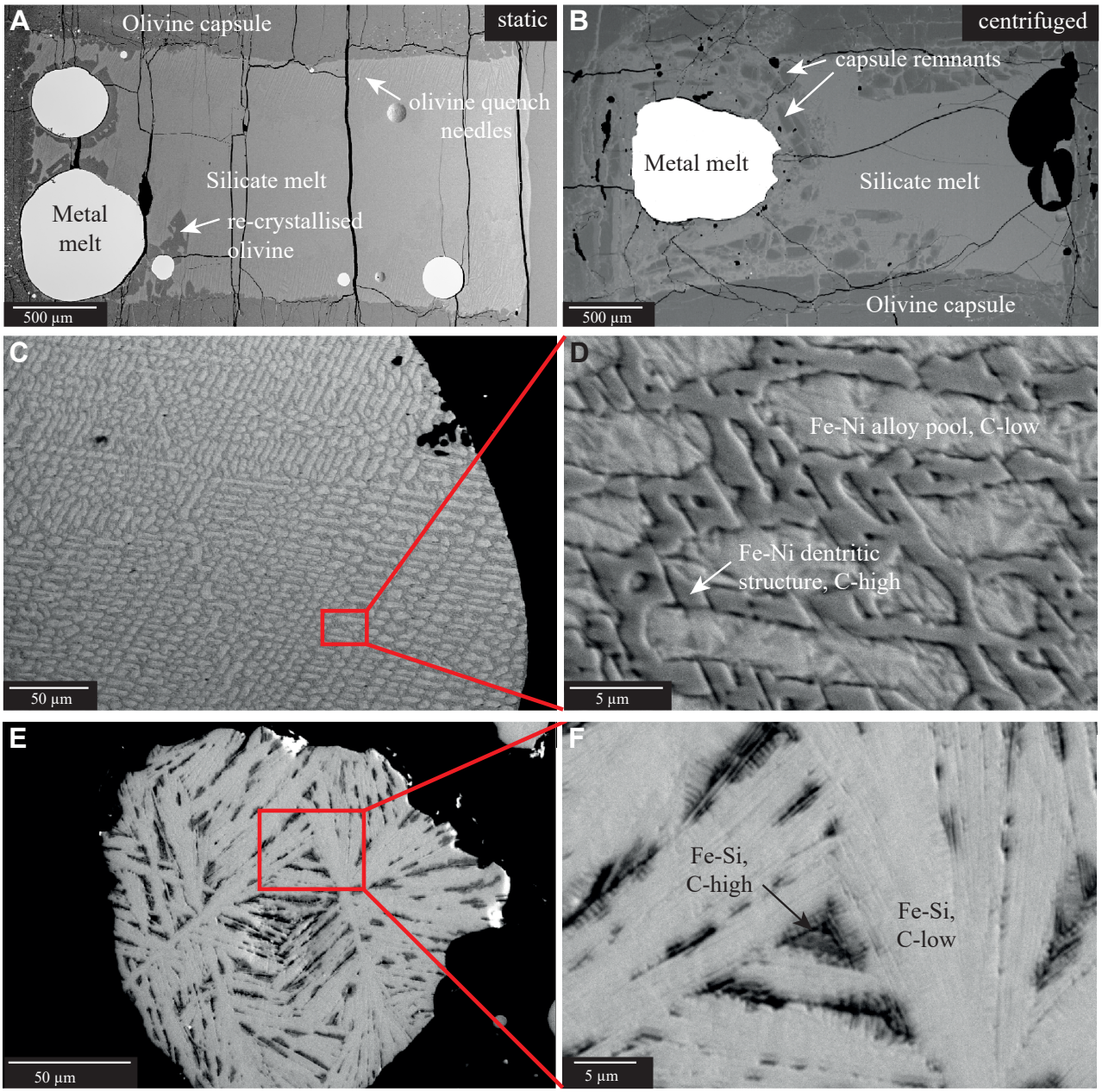

Fig. 4.1. *Back-scattered electron images of selected samples.* ***A and B:*** *silicate and metal melt pairs of a static (HAB2F1-92) and a centrifuged (PB1FN1-37) piston cylinder experiment, respectively.* ***C:*** *Detailed image of the Fe-C-Ni metal droplet in (A).* ***D:*** *Detailed quench texture of metal droplet in (C).* ***E:*** *Detailed image of a Fe-C-Si bearing metal droplet surrounded by homogeneous silicate glass (run HAB2FS4-85).* ***F:*** *Detailed quench texture of metal droplet in (E).*

4.2.2 Analytical methods

4.2.2.1 Electron probe microanalysis (EPMA)

Quantitative major and minor element concentrations of the experimental silicate glasses and metallic alloys were determined using a JEOL electron microprobe JXA 8900 equipped with five spectrometers at the Goethe University of Frankfurt. All samples were carbon-coated and 10 – 15 points per glass were analysed. Analytical conditions used for silicate glasses (Si, Ti, Al, Fe, Mg,

Ca, Ni, Na, K) were 15 kV accelerating voltage, 20 nA beam current, and a peak and background counting time of 20 s. For metal alloys (Fe ± Ni ± Si) the conditions were 20 kV, 30 nA and 30 s, respectively. A 30 µm diameter beam was used to obtain the most homogeneous analyses possible, especially in the heterogeneous quench textures of the metal melts. In addition to SIMS analyses (described below), the metal alloys of 11 samples were analysed for carbon by electron microprobe. For these, the previous carbon coat of the samples was removed by re-polishing the samples with 1 µm corundum polishing paste. Conductive silver paint was then applied to ground the metal sample surface to the sample holder. Dissolved carbon in the metal alloy was quantitatively measured with 10 kV accelerating voltage, 120 nA beam current and 20 s peak and background counting time. To minimise carbon blanks, a decontaminant device ("cold finger") was installed, which improves the vacuum and removes organic hydrocarbon molecules in the probe vacuum chamber by condensation. For the silicate melt, a NIST mineral glass (NBS K-412) was used as analytical standard. For the metal melt, pure Fe, Ni and Si metal standards from NIST were used. For carbon measurements an experimentally synthesised stoichiometric cohenite ($(Fe,Ni)_3C$) was employed as standard.

4.2.2.2 Secondary ionisation mass spectrometry (SIMS)

Carbon concentrations in silicate glasses and the quenched metallic alloy were measured using the IMS 1280HR ion probe at the SwissSIMS laboratory at the University of Lausanne. Samples were re-polished to remove previous C coating, and surrounding epoxy was cut off using a diamond saw. Subsequently, a 300 µm diamond wire saw was used to cut the samples at the contact between the platinum outer capsule and the olivine inner capsule. After removing all four sides of the capsule, the inner part was recovered and mounted in indium. Usually 4 to 6 samples were embedded with the standards in one single indium mount and coated with ~ 40 nm gold.

As ion source, a primary beam of $^{133}Cs^+$ was employed with intensities of ~ 2 and ~ 0.2 nA for metal and silicate melts, respectively. A lower intensity for silicate melts was chosen to enable the analysis of all samples with identical analytical conditions (regardless of their C content) using an electron multiplier (EM) with a field aperture of 4000 µm and an energy slit of 50 µm. Entrance slits were closed to 122 µm width and exit slits to 405 µm, resulting in a mass resolving power of ~ 3000 ($M / \Delta M$).

Prior to each analysis, pre-sputtering times of 180 s for metal and of 130 s for glass were applied, using a raster beam of 50 µm diameter to avoid any surface contamination during analyses. Automatic centring of secondary deflectors after pre-sputtering was achieved on ^{12}C and ^{28}Si for metal and glass,

respectively. For the actual measurements, a raster of 30 × 30 microns was chosen to homogenise the signal from heterogeneous quench structures, which particularly occurred in the metal melt.

Each analysis was performed in mono-collection mode and consisted of 20 cycles of the peak-stepping sequence mass 11.8 (background: 2 s), $^{12}C^+$ (3 s, FC), $^{28}Si^+$ (1.6 s, EM), $^{56}Fe^+$ (1.8 s, EM) for metal, and 11.8 (2 s), $^{12}C^+$ (5 s, EM), $^{28}Si^+$ (3 s, FC), $^{56}Fe^+$ (1 s, FC) for silicate glasses. In order to minimise the effect of primary intensity variations, $^{28}Si^+$ and $^{56}Fe^+$ were used to normalise $^{12}C^+$ intensities in glasses and metals, respectively. Both elements were consecutively analysed during the measurements of both metals and glasses to enable a reasonable magnet stability over successive sessions of these two materials.

Carbon standards for silicate glasses were experimentally synthesised in order to produce matrix-matching glasses (piston cylinder apparatus, 1500°C, 1.5 GPa, San Carlos olivine capsules) and synthetic cohenite ($(Fe,Ni)_3C$) (piston cylinder apparatus, 1100°C, 3 GPa, crushable MgO capsules). All standards were analysed with independent methods, i.e., X-ray powder diffraction for identifying stoichiometric cohenite, and a conventional elemental analyser (LECO CS844) to determine the bulk carbon content of the standard glasses by non-dispersive infrared cells. To verify the bulk analyses, some standard glasses were additionally analysed by EPMA for C contents. The results agree very well within uncertainties as shown in Fig. B1 (Appendix B).

Typical standard reproducibility was 1 − 6 % (standard deviation (1SD) relative) for glasses and 1 − 3 % (1SD relative) for metals. For SIMS measurements, internal errors (standard error of the mean (1SE) over the 20 cycles) were usually < 2 % for glasses and < 1 % for metals. Internal errors were larger (~ 8 %) for glasses with lower C contents, typically below 0.5 wt.%. The final uncertainty on the C content for each individual point of the analyses was computed with equation (2.1) as presented in section 2.2.2.

4.2.2.3 Elemental analyser (EA)

Bulk carbon contents of glass standards used for SIMS measurements were determined by a CS844 LECO elemental carbon analyser (at ETH Zurich), which employs non-dispersive infrared cells. Sample fragments of glass ranging from 1 to 10 mg were inserted into low carbon and low sulphur ceramic crucibles (LECO Part No. 529-018), together with 1 g of copper flux to enable homogeneous combustion of the non-conducting glass samples in the induction furnace. Depending on the available amount of sample material, measurements were repeated two or three times. Prior to each session,

crucibles were annealed at 1000°C for at least 2 h to minimise the carbon blank signal. The latter is determined by the combustion of 5 to 6 sintered crucibles filled with 1 g of copper flux, defining a carbon detection limit of 0.5 µg. For each analysis, the combustion volume was purged with oxygen for 20 s to eliminate any atmospheric impurities. After purging, a delay time of 25 s was given to the instrument to establish a stable baseline for detection. The actual duration of analysis, when sample carbon peaks were collected, was set to 60 s for glass analyses. A sample cooling time of 5 to 10 s was applied when the analysis had completed to avoid splashing of hot material while the furnace pedestal was lowered. As shown in Fig. 2.10 in section 2.2.3, calibration was made for each carbon mass range using a synthetic carbon standard (0.12 ± 0.01 wt.% C) and a high purity iron standard (0.0062 ± 0.0008 wt.% C), both LECO reference materials (Part No. 502-632 and 501-950, respectively).

4.2.2.4 Raman spectroscopy

Raman spectra of all glass samples were collected to determine the carbon speciation of the silicate melt. A Labram Dilor Raman spectroscope equipped with a 532 nm laser at ETH Zurich was used at an output power of 25 mW yielding a power on the sample surface of 5 mW. Some glass samples could not be analysed with a 532 nm laser due to excessive luminescence. Spectra were obtained in the wave number range of 400 - 3800 cm^{-1} with 3 cm^{-1} resolution, using a ×100 objective lens. At each point, a spectrum was accumulated three times with an exposure time of 200 s.

4.2.3 Redox work in the experimental charges

The Ni-NiO, Fe-FeO, and Si-SiO_2 ratios in the starting materials were chosen such that the range of oxygen fugacities proposed for Earth's accretion was covered. The actual oxygen fugacity of the experimental charges depended on (1) the chemical interaction between the silicate melt and the capsule material, and (2) the equilibration of metallic and silicate melts. In this context, oxygen fugacity is not a free variable but a resultant from temperature and bulk composition, which control the resulting metal-silicate ratio and compositions. Redox reactions that took place in our charges are

$$Fe^{metal} + {}^{1}/_{2}\, O_2 \leftrightarrow FeO^{silicate\ melt}, \tag{4.2}$$

$$Si^{metal} + O_2 \rightarrow {SiO_2}^{silicate\ melt}, \tag{4.3}$$

$$NiO^{silicate\ melt} \rightarrow Ni^{metal} + {}^{1}/_{2}\, O_2, \text{ and} \tag{4.4}$$

$$2Fe^{metal} + O_2 + {SiO_2}^{silicate\ melt} \leftrightarrow Fe_2SiO_4^{olivine\ capsule} \tag{4.5}$$

for the non-carbon part, and

$$C^{metal} + O_2 \leftrightarrow {CO_2}^{silicate\ melt} \quad (4.6)$$

$${CO_2}^{silicate\ melt} + 2H_2O \leftrightarrow {CH_4}^{silicate\ melt} + 2O_2 \quad (4.7)$$

involving the target element. While oxygen fugacity can be calculated from any of these reactions, it is effectively controlled by the equilibrium that can achieve the highest redox-work. For oxygen fugacities > IW, the added Ni and hence equilibrium (4.4) has the highest redox capacity. For experiments at < IW, equilibria (4.2) and (4.5) have the by far the highest redox capacity in the San Carlos olivine capsule experiments, and any Si present in the metal starting material will be oxidised. For the most reducing conditions with wt.% of Si in the metal melt, equilibrium (4.3) controls oxygen fugacity. The silicate melt then results almost FeO-free and hence requires a (synthetic) forsterite capsule.

Calculated oxygen fugacities in our charges relative to the iron-wüstite buffer (ΔIW) were at -1.4 ± 0.4 ΔIW in San Carlos olivine capsules. More reducing conditions could not be attained with olivine of X_{Mg} = 0.90 due to reaction (4.5), which buffered the oxygen fugacity within the San Carlos olivine capsule, any excess Si^{metal} being readily oxidised by $FeO^{San\ Carlos\ olivine}$. Therefore, we had to use synthetic forsterite capsules, which enables more reducing conditions in the experimental charges down to ΔIW -4.8.

4.3 Results

Experimental conditions, carbon concentrations, and carbon partition coefficients are summarised in Table 4.2. Silicate and metal melt compositions in terms of major elements are presented in Table 4.3.

4.3.1 Sample description and phase equilibrium

Experiments with all starting materials produced glassy silicate melt pools, in which several metal droplets (static experiments) or one large metal melt pool (centrifuged experiments) were embedded (Fig. 4.1A,B). The sample material is surrounded by a slightly dissolved San Carlos olivine capsule or a synthetic forsterite capsule. Some experiments with the HAB1/-2 starting material in San Carlos olivine capsules generated olivine quench needles along the interface between the silicate melt pool and the capsule walls. Further, re-crystallisation of olivine occurred next to the metal droplets (Fig. 4.1A). These domains were carefully avoided by in-situ measurements.

Table 4.3
Major element compositions of silicate and metallic melts in wt.%.

Sample No.	SiO_2	TiO_2	Al_2O_3	FeO	MgO	CaO	NiO	Na_2O	K_2O	Total	Fe	Ni	Si	Total
PB1FN1-31	45.46	1.95	6.30	11.51	14.77	6.58	0.63	6.70	3.00	96.89	4.98	93.79	0.0	98.77
1 σ	0.27	0.05	0.08	0.11	0.19	0.08	0.04	0.07	0.04	0.92	0.05	0.16	0.0	0.21
PB1FN1-32	45.37	1.97	6.39	12.00	14.33	6.45	1.80	6.89	3.08	98.28	3.61	96.11	0.0	99.72
1 σ	0.20	0.02	0.05	0.09	0.12	0.06	0.06	0.08	0.03	0.71	0.10	0.20	0.0	0.29
PB1FN1-37	45.97	1.92	5.72	12.33	15.97	6.60	0.72	6.20	2.74	98.17	5.52	93.73	0.0	99.26
1 σ	0.14	0.03	0.06	0.11	0.05	0.06	0.03	0.09	0.03	0.60	0.12	0.24	0.0	0.36
PB1FN2-95	43.23	1.94	6.61	17.63	12.40	7.07	0.34	6.82	2.33	98.35	19.34	76.49	0.0	95.83
1 σ	0.15	0.04	0.04	0.09	0.09	0.04	0.03	0.07	0.03	0.58	0.27	0.77	0.0	1.04
PB2F2-40	45.43	2.04	6.61	16.16	11.90	6.75	0.02	7.36	3.10	99.37	92.97	1.25	0.0	94.21
1 σ	0.25	0.07	0.12	0.14	0.11	0.08	0.03	0.17	0.07	1.04	0.46	0.13	0.0	0.59
PB2F2-44	43.11	1.91	6.23	18.81	13.65	6.17	0.03	7.20	2.86	99.97	94.08	0.93	0.0	95.00
1 σ	0.14	0.02	0.08	0.43	0.10	0.06	0.01	0.07	0.03	0.94	0.35	0.07	0.0	0.42
PB2F2-72	41.18	1.71	5.94	20.51	13.91	6.12	0.04	6.61	2.64	98.65	89.54	3.90	0.0	93.44
1 σ	0.07	0.03	0.05	0.23	0.10	0.06	0.02	0.08	0.04	0.69	0.03	0.39	0.0	0.42
HAB1F2-46	44.05	0.35	11.19	14.19	21.68	7.42	0.09	1.35	0.01	100.34	94.79	0.57	0.0	95.36
1 σ	0.22	0.02	0.04	0.11	0.18	0.05	0.03	0.04	0.01	0.68	0.31	0.07	0.0	0.38
HAB2F1-92	46.39	0.41	12.32	10.36	21.87	7.97	0.01	1.43	0.01	100.76	93.01	0.56	0.0	93.57
1 σ	0.10	0.04	0.10	0.02	0.14	0.06	0.01	0.03	0.01	0.51	3.70	0.51	0.0	4.20
HAB2F2-49	46.74	0.42	12.49	9.28	21.32	8.38	0.00	1.49	0.01	100.12	95.01	0.21	0.0	95.22
1 σ	0.19	0.02	0.10	0.08	0.14	0.10	0.01	0.02	0.01	0.67	0.29	0.01	0.0	0.31
HABF2-52	46.44	0.48	13.97	12.68	15.17	9.30	0.02	1.65	0.01	99.70	94.62	0.75	0.0	95.37
1 σ	0.27	0.03	0.64	0.37	1.59	0.53	0.01	0.07	0.01	3.52	0.45	0.19	0.0	0.63
HAB2F2-54	46.95	0.43	12.81	11.18	18.49	8.35	0.02	1.51	0.02	99.74	93.78	0.56	0.0	94.35
1 σ	0.29	0.05	0.12	0.15	0.21	0.14	0.02	0.07	0.02	1.07	0.43	0.05	0.0	0.48
HAB2FS1-97	52.43	0.40	12.14	0.89	23.43	8.16	0.01	1.38	0.02	98.85	93.28	0.0	1.70	94.98
1 σ	0.40	0.03	0.14	0.38	0.27	0.12	0.01	0.04	0.00	1.39	1.13	0.0	1.40	2.53
HAB2FS1-96	51.06	0.35	10.82	0.46	27.21	7.80	0.01	1.16	0.08	98.95	92.71	0.0	2.83	95.54
1 σ	0.85	0.00	0.11	0.01	0.68	0.14	0.00	0.02	0.00	1.80	0.47	0.0	0.04	0.51
HAB2FS3-83	52.79	0.37	12.25	0.39	24.93	8.57	0.00	1.29	0.06	100.66	91.18	0.0	2.19	93.37
1 σ	0.11	0.02	0.08	0.05	0.14	0.07	0.00	0.04	0.01	0.52	1.37	0.0	1.19	2.56
HAB2FS3-88	48.08	0.23	7.75	0.68	39.17	5.02	0.01	0.76	0.01	101.72	91.95	0.0	1.48	93.43
1 σ	2.26	0.09	2.83	0.07	7.38	1.97	0.01	0.32	0.01	14.95	0.31	0.0	0.28	0.59
HAB2FS4-85	54.36	0.39	12.25	0.25	22.92	8.77	0.01	1.41	0.08	100.42	91.40	0.0	1.46	92.86
1 σ	0.32	0.02	0.14	0.03	0.48	0.10	0.01	0.06	0.01	1.17	0.57	0.0	0.09	0.66
HAB2FS5-86	50.19	0.37	12.11	2.43	26.01	8.59	0.01	1.30	0.08	101.09	93.69	0.0	0.018	93.71
1 σ	0.12	0.02	0.04	0.08	0.20	0.09	0.01	0.03	0.01	0.61	0.24	0.0	0.004	0.25

Sample codes refer to the starting mixture of the silicate melt (PB or HAB) and the starting mixture of the metal melt (F, FN or FS) as shown in Table 4.1, followed by the actual run number. For each sample, typically 10 - 15 spots were analysed. The standard deviation (1 σ) is based on the replicate analyses.

In Ni-rich experiments (starting mix PB1FN1/-2), metal droplets quenched into a fine, homogeneous mass of Fe-Ni alloy. Experiments with very low Ni contents in the metal melt (0.5 – 3.9 wt.% Ni, starting mixes HAB1/-2, PB2F1/-2) show low-carbon Fe-Ni alloy pools surrounded by high-C Fe-Ni dendritic structures (Fig. 4.1C,D). Experiments conducted in synthetic forsterite capsules with Si added to the metallic melt (HAB2FS1/-3/-4/-5) produced low-C Fe-Si skeleton structures with interstitial C-rich patches of Fe-Si alloy (Fig. 4.1E,F). Some of these experiments also show euhedral blades of graphite, which either intersperse the metal droplets or are present next to them. Dasgupta et al. (2013) argued that these graphite blades crystallised in equilibrium with the metallic and silicate melts, which would then demonstrate graphite-saturation.

4.3.2 Silicate melt: major element composition

The major element compositions of the silicate melts show variations depending on the starting material and the capsule material (Tables 4.1 and 4.2). Experiments with the NiO-bearing compositions PB1/-2 run in San Carlos olivine capsules at 1.5 GPa and 1400°C produced silicate glasses with 41.2 – 46.0 wt.% SiO_2, 5.7 – 6.6 wt.% Al_2O_3, 11.9 – 16.0 wt.% MgO, and 11.5 – 20.5 wt.% FeO. These experiments show a compositional shift towards higher FeO values with decreasing SiO_2 content owing to a redox-reaction of Fe^0 with NiO and to chemical reaction with the olivine capsule. High-alumina and FeO-free starting mixes (HAB1 and HAB2) run in San Carlos olivine capsules at 1.5 GPa and 1500°C resulted in silicate melt compositions with 44.0 – 47.0 wt.% SiO_2, 11.2 – 14.0 wt.% Al_2O_3, 15.2 – 21.9 wt.% MgO, and 9.3 – 14.2 wt.% FeO. Experiments of the same silicate starting mix (HAB2) performed in synthetic forsterite capsules at 1.5 GPa, 1500°C, and very reducing conditions (ΔIW -3.0 to ΔIW -4.8) produced liquids with 50.2 – 54.4 wt.% SiO_2, 10.8 – 12.3 wt.% Al_2O_3, 22.9 – 27.2 wt.% MgO, and very low FeO contents varying from 0.3 − 2.4 wt.%. A single experiment (HAB2FS3-88) was run at 3.5 GPa and 1900°C, leading to an increase of MgO content to 39.2 wt.% and a decrease of SiO_2 to 48.1 wt.%, due to enhanced dissolution of forsterite at higher temperatures. Further, a single experiment of the starting mix HAB2FS1 (run 97) was conducted for comparison in a San Carlos olivine capsule at 1.5 GPa and 1500°C, which resulted in a melt composition similar to that of the equivalent experiment in a synthetic forsterite capsule. The silicate melt of this particular experiment was not in equilibrium with the San Carlos olivine capsule, due to its low FeO content of 0.89 ± 0.38 wt.%, resulting in ΔIW -3.8.

The compositional variation of the silicate melts in the experiments results from (1) the different degrees of dissolution of the capsule material in the silicate melt, (2) the different metal compositions

of the starting mix combined with the silicate starting mix, and (3) the prevailing fO_2 during the experiment, which is induced by processes (1) and (2).

4.3.3 Metallic melt: major element composition

Starting compositions of the metallic melt were chosen in order to cover a large range of oxygen fugacity conditions. Most resulting metallic melts are Fe-rich (≥ 90 wt.% Fe), with variations in Fe content depending on the starting material (Table 4.1), capsule material, and the prevailing oxygen fugacity (Table 4.2). Some experiments were performed with an initial Fe/Ni ratio of 10/90 (starting mix FN1) or 50/50 (starting mix FN2) at 1.5 GPa and 1400°C in San Carlos olivine capsules. This resulted in metallic melt compositions with 76 – 96 wt.% Ni, but only 19 – 4 wt.% Fe, which yields fairly oxidising conditions (ΔIW +0.4 to ΔIW +2.2). Experiments with initially Ni-free metal compositions (starting mix F1/-2), run in San Carlos olivine capsules at 1.5 GPa and 1400 – 1500°C, produced metallic melts with 90 – 95 wt.% Fe and 0.2 – 3.9 wt.% Ni, due to the reduction of NiO to metallic Ni. For experiments performed in synthetic forsterite capsules, metallic Si was added to the starting mix (FS1/-3/-4/-5) to obtain more reducing conditions. This resulted in metal melts with 91 – 94 wt.% Fe and 0.02 – 2.8 wt.% Si.

4.3.4 Calculation of oxygen fugacity

The equilibrium oxygen fugacity, fO_2, during the experiments was calculated from the Fe contents of the conjugate metal and silicate melts. Oxygen fugacity relative to the iron-wüstite buffer (ΔIW) is calculated through the following equations:

$$Fe^{metal} + {}^{1}/_{2}\, O_2 = FeO^{silicate\ melt} \tag{4.8}$$

$$\Delta \log fO_2\,[IW] = 2\log\left(\frac{a_{FeO}^{silicate}}{a_{Fe}^{metal}}\right) = 2\log\left(\frac{X_{FeO}^{silicate}}{X_{Fe}^{metal}}\right) + 2\,log\left(\frac{\gamma_{FeO}^{silicate}}{\gamma_{Fe}^{metal}}\right), \tag{4.9}$$

where a_{Fe}^{metal} and $a_{FeO}^{silicate}$ are the activities of Fe in the molten metal and FeO in the silicate melt, respectively. There is much debate about the activity coefficients in this equation, and both completely ideal and highly non-ideal activity models are used. Holzheid et al. (1997) argued that $\gamma_{FeO}^{silicate}$ would be constant at 1.7, which would increase any calculated oxygen fugacity by 0.46 log units (see functional form of equation 4.9), but more recently, Médard et al. (2008) argued that $\gamma_{FeO}^{silicate}$ is unity, which we are adopting in this study. The activity coefficients of Fe in metal melts were determined using the online calculator MetalAct (http://www.earth.ox.ac.uk/~expet/metalact/, Wood, BJ; Wade,

J; Norris, A, last accessed on October 18th 2017), which accounts for the non-ideal interactions between all components in liquid Fe melt (Wade & Wood, 2005). Carbon saturation was computed in the activity calculation for experiments showing excess carbon that precipitated from the metal melt (see Table 4.2). This calculation results in γ_{Fe}^{metal} ranging from 0.66 to 0.73 except for the Ni-rich melts, and contributes hence < 0.1 log units to the calculated value. The covered oxygen fugacity of our experiments ranges from ΔIW +2.2 to -4.8.

4.3.5 Carbon in metallic melts

Carbon contents of metallic melts show little variability and amount to 5.6 ± 0.7 wt.% over most of the investigated parameter range. Nevertheless, there is a marked decrease to 0.034 ± 0.004 wt.% C when fO_2 increases to > IW (Fig. 4.2A). The low C content at these relatively oxidising conditions (> IW) may result from high Ni concentrations of such melts (> 90 wt.% Ni), Ni possibly diminishing the C solubility in the metallic melt (Gordon & Breach, 1988; Dasgupta & Walker, 2008; Dasgupta et al., 2013; Chi et al. 2014). On the other end of the fO_2 range, increasing metal Si concentrations from 1.46 ± 0.09 wt.% to 2.83 ± 0.04 wt.% cause C to decrease from 6.6 ± 0.4 wt.% to 4.5 ± 0.3 wt.% in the metal melt (Fig. 4.3), a trend consistent with what is known from the steel metallurgy literature and what was found by Li et al. (2015) and Li et al. (2016).

4.3.6 Carbon in silicate melts

The carbon content of the silicate melts correlates positively with the degree of depolymerisation (NBO/T) and with increasing fO_2 for the silicate melts equilibrated in San Carlos olivine capsules with FeO- and NiO-bearing starting compositions PB1 and PB2. For example, C concentration increases from 0.0224 ± 0.0004 wt.% to 0.97 ± 0.01 wt.% with increasing fO_2 from ΔIW -0.75 to +1.68 (Fig. 4.2B), while NBO/T also slightly increases. These observations are similar to those reported by Chi et al. (2014).

The experiments presented in this study were performed over the widest range of temperature, fO_2 and NBO/T, compared to other studies. This parameter range and also the instrumental conditions overlap with previous studies. Yet, the carbon concentrations of our silicate glasses are mostly 1 to 2 orders of magnitude larger than those reported by Dasgupta et al. (2013), Chi et al. (2014), Stanley et al. (2014), Li et al. (2015), Li et al. (2016), and Dalou et al. (2017). All of these authors measured C concentrations << 0.05 wt.% in silicate melt, irrespective of P-, T-, fO_2-conditions, or melt compositions.

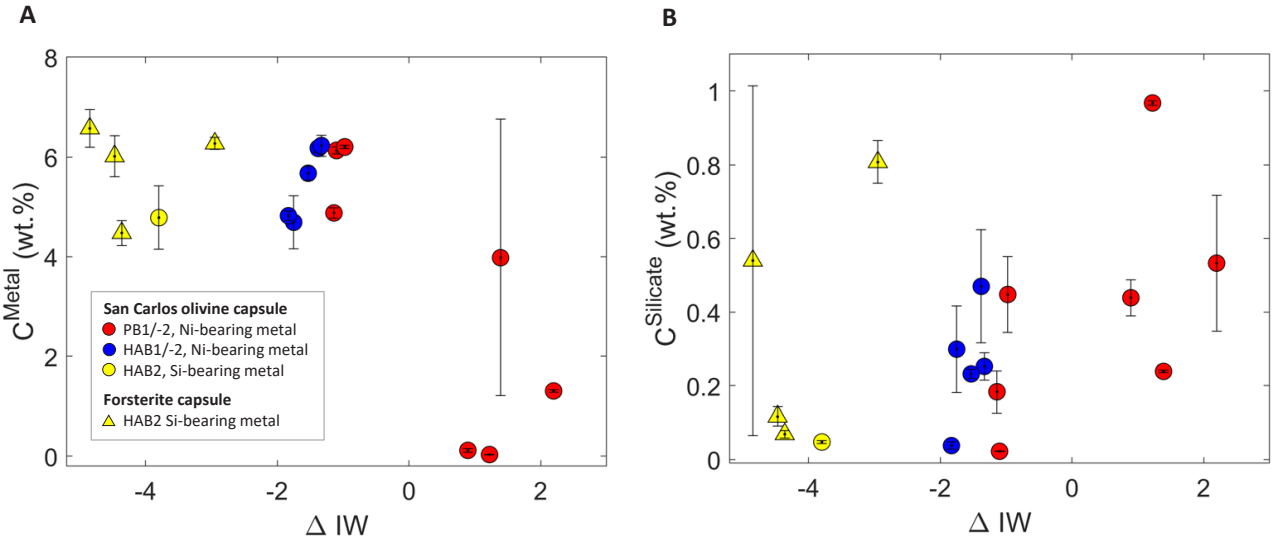

Fig. 4.2. *Carbon content of the metal melt (A) and silicate melt (B) as a function of oxygen fugacity (ΔIW).* ***A:*** *Metal melt C concentration decreases with oxygen fugacity, which might result to some extent from the high Ni content of the oxidised samples.* ***B:*** *Silicate melt C content correlates positively with oxygen fugacity for experiments with FeO- and NiO-bearing starting compositions (PB1/-2). This correlation is less distinct for experiments with high-alumina, Fe-free starting mixes (HAB1/-2).*

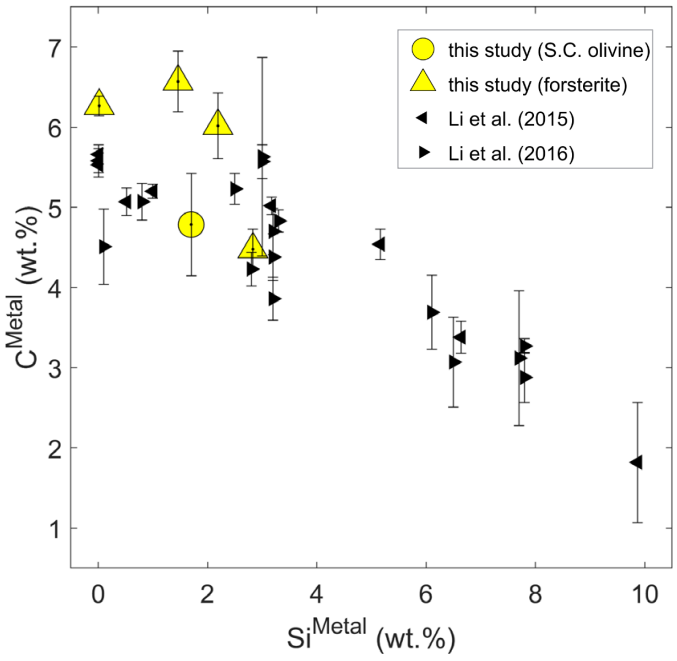

Fig. 4.3. *Carbon concentration of the metal melt as a function of the Si concentration of the metal melt.* C^{Metal} *correlates negatively with* Si^{Metal}*. Our results are in agreement with those of Li et al.(2015) and Li et al. (2016), which are also plotted for comparison.*

4.3.7 Speciation of C-H-O volatiles in silicate melt

Raman spectra (Fig. 4.4) were obtained for all silicate glasses in order to detect the speciation of carbon. Most spectra of quenched glasses from synthetic forsterite capsules were strongly affected by luminescence, and C speciations in these samples could not be constrained. All Raman spectra show the three broad peaks in the low wave number range (400 - 1150 cm^{-1}) characteristic for aluminosilicate glasses (Kadik et al., 2004). In one spectrum (HABF2-52) two sharp peaks at 820 and 835 cm^{-1} are additionally present. These result from quench-olivine in the silicate glass (e.g., Weber et al., 2014). The carbon-bearing volatile species in basaltic melts are mostly related to the prevailing oxygen fugacity. At oxidising conditions (ΔIW +1 or higher) the silicate glasses with compositions PB1FN1/-2 show a pronounced peak at ~1080 cm^{-1} assigned to carbonate groups (Brooker et al., 1999). For intermediately reduced silicate glasses (~ΔIW -1), the dominant carbon species appears to contain C ≡ O groups with a characteristic peak at ~ 2115 cm^{-1}, also observed in previous studies. It has been attributed to (1) iron carbonyls associated with isolated C ≡ O groups as part of more complex C-bearing or organometallic clusters (Bley et al., 1997; Wetzel et al., 2013; Stanley et al., 2014; Armstrong et al., 2015), (2) C ≡ C stretching vibrations in alkynes (Socrates, 2002), or (3) molecular carbon monoxide (Brooker et al., 1999). There is no evidence for molecular CO_2 being dissolved in the silicate glasses due to the absence of its characteristic peaks at 1284 and 1388 cm^{-1}. At highly reducing conditions (ΔIW ≤ -2), carbon seems to be predominantly present as CH_4, CH_3, or CH_2, referring to the observed C-H stretch vibrations at ~ 2870 and ~ 2930 cm^{-1} (Socrates, 2002; Mysen et al., 2009). The observation of the broad doublet peak suggests weak C-H bonding in dissolved methane molecules that interact with the silicate melt and may not only depend on fO_2 but also on the total availability of hydrogen. For example, the oxidised silicate glass of run PB1FN1-31 (ΔIW +2.2) shows the methane doublet peak in addition to the carbonate peak. Further evidence for the presence of hydrogen arises from the broad, asymmetric band at ~ 3590 cm^{-1}, which is either attributed to OH^- groups bonded to cations in the silicate framework, or to molecular H_2O (Mysen & Virgo, 1986; Kadik et al., 2004).

4.3.8 Carbon partitioning between metallic and silicate melt

The experiments of this study aim at the effect of oxygen fugacity and different compositional parameters on carbon partitioning at 1.5 GPa and 1400 – 1500°C. Experimental $D_C^{metal/silicate}$ range over 5 orders of magnitude from 0.035 ± 0.004 (PB1FN1-32, 1400°C, 1.5 GPa, ΔIW +1.68) to 274 ± 6 (PB2F2-40, 1400°C, 1.5 GPa, ΔIW -0.75). Concerning oxygen fugacity, three classes of experiments can be distinguished: (1) high fO_2 (> IW), where Ni is the dominant metal component, (2) intermediate

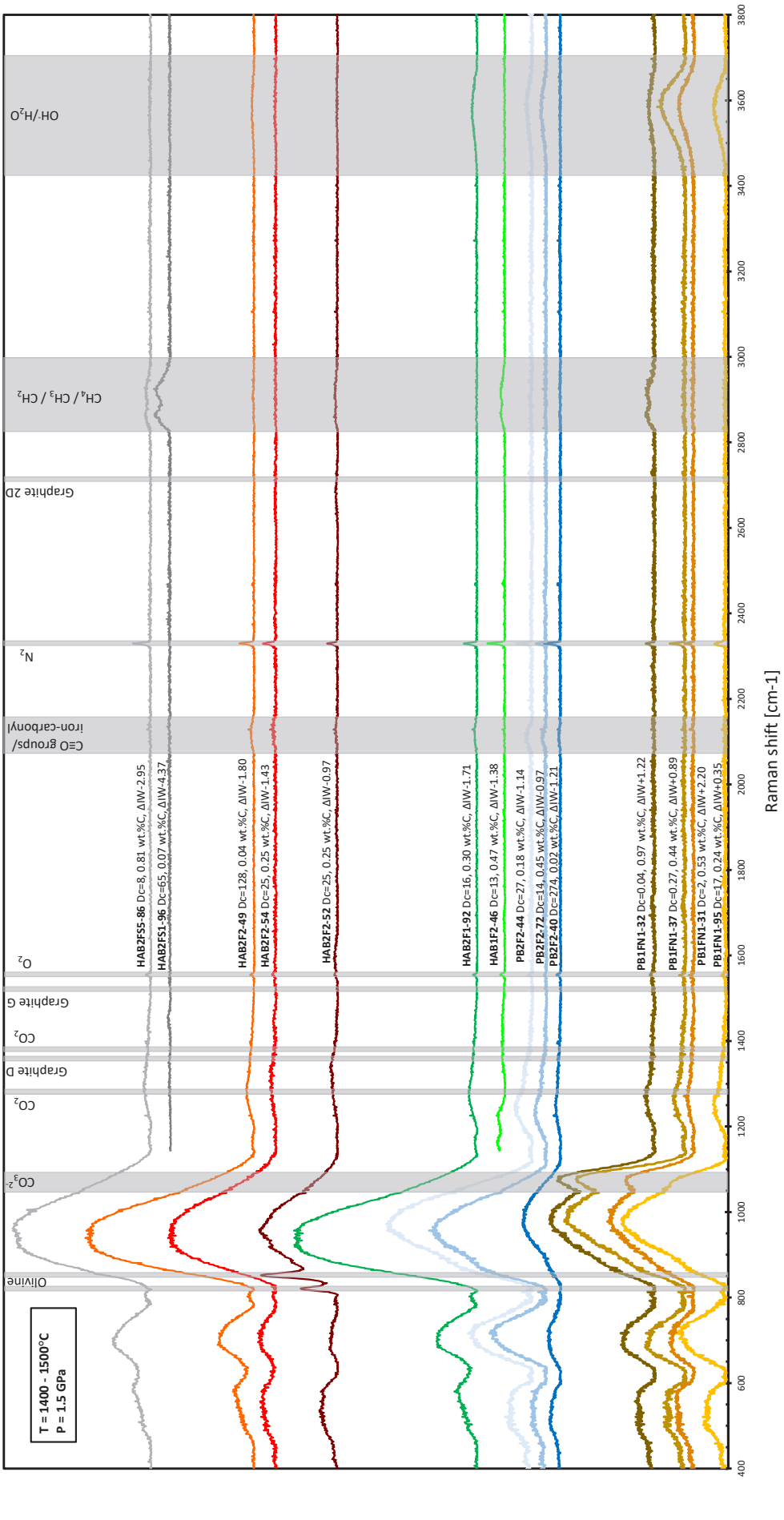

Fig. 4.4. *Raman spectra of silicate glasses. Intensities are shifted to avoid overlapping spectra. The prevailing carbon speciation is mainly controlled by the oxygen fugacity and the availability of hydrogen. With decreasing fO_2, the carbon speciation changes from carbonate to $C \equiv O$ groups, and at very reducing conditions to CH_4 or methyl groups. Further, OH^- groups are present in some glasses at moderately reduced to oxidised fO_2 conditions.*

fO_2 (between IW and ΔIW -1.8), where Si is absent in the metal, and (3) low fO_2 (< ΔIW -3), where appreciable quantities of Si are dissolved in the metal. Except for the oxidising experiments at fO_2 > IW, $D_C^{metal/silicate}$ practically results from variations in the C content of the silicate melt which in turn is a function of fO_2 and silicate melt NBO/T (Fig. 4.5). In fact, with the exception of the Ni-rich and Si-rich metals, there is no systematic variation of C^{metal} with fO_2 across all datasets (Appendix B, Fig. B2) (Dasgupta et al., 2013; Chi et al., 2014; Li et al., 2015).

$D_C^{metal/silicate}$, however, shows a positive correlation with Si content in metallic melt, which is not in agreement with the studies of Li et al. (2015) and Li et al. (2016), at least at Si^{metal} contents < 4 wt.% (Fig. 4.6A). The effect of Ni on carbon partitioning is less distinct and does hardly show a particular correlation as demonstrated in Fig. 4.6B. This is not the case for the very oxidising experiments (ΔIW ≥ + 1), where the metal melt is very rich in Ni (> 76 wt.%) and very low in C (< 4 wt.%). Here, $D_C^{metal/silicate}$ appears to correlate negatively with Ni content and positively with C content in the metallic melt (Appendix B, Fig. B3).

The above correlations reflect mostly changes in the oxygen fugacity, which causes metal compositions and speciations of C in the silicate melt to change. It is not possible to vary, e.g., Ni or Si contents in the melt independent of temperature and oxygen fugacity, consequently individual effects on carbon partitioning cannot be determined. Therefore, we developed a parameterisation that is applicable to a broad range of conditions.

4.4 Discussion

The experimentally determined carbon partion coefficients, $D_C^{metal/silicate}$, were implemented in a parameterisation and combined with core formation scenarios from the literature, allowing the extrapolation to conditions of core-mantle segregation and consequently, placing constrains on the initial C distribution between magma ocean and Earth's core.

4.4.1 Determining the C content of metallic alloy and silicate glass: SIMS and EPMA

The carbon content of most metallic melts was analysed by SIMS, as summarised in Table 4.2. For some experiments, SIMS measurements were not possible due to too small metal droplets (< 50 µm), or due to the lack of an appropriate (high Ni) metal standard. The C content of these metals was analysed by EPMA, similar to previous studies (e.g., Dasgupta & Walker, 2008; Buono et al., 2013; Li et al., 2015). To evaluate the precision of both methods, several experiments were analysed

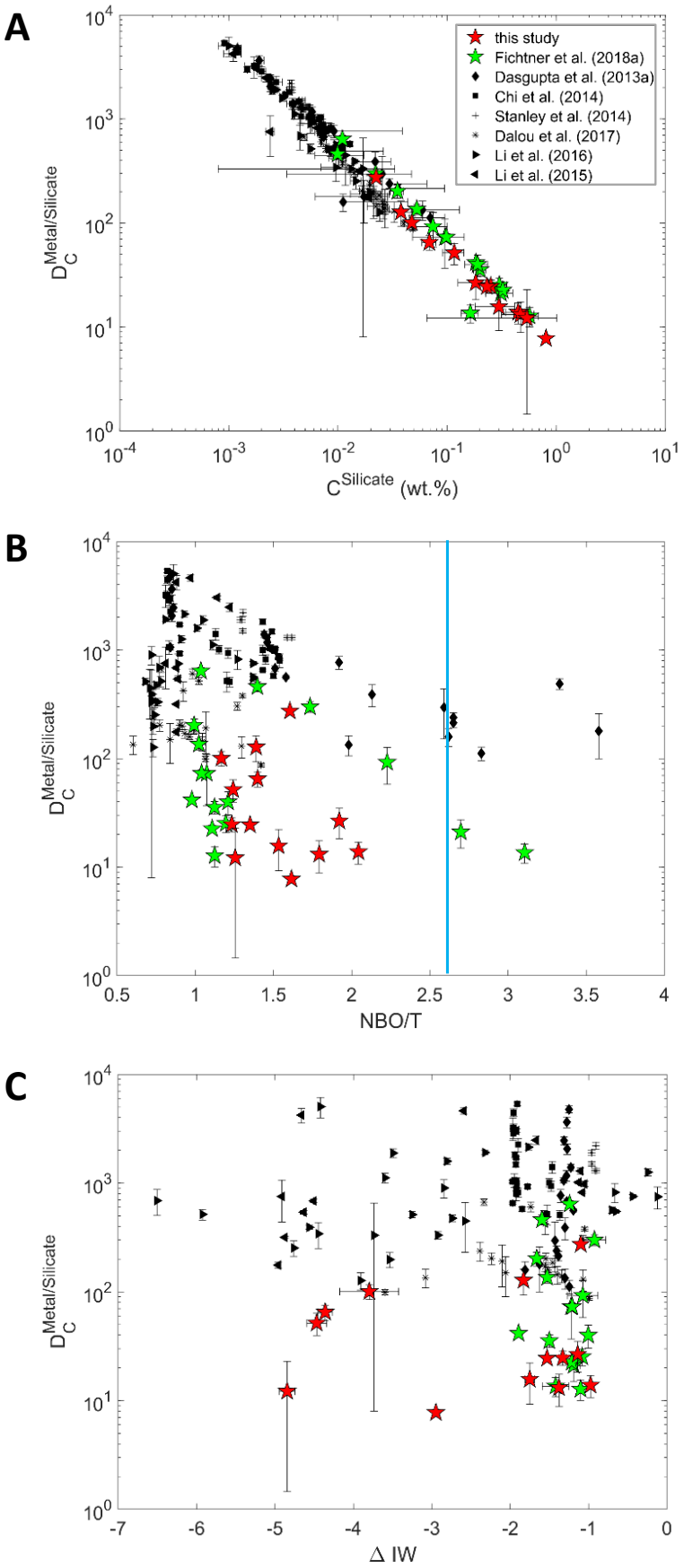

Fig. 4.5. *$D_C^{metal/silicate}$ correlates negatively with increasing C concentration of the silicate glass (A), and the silicate melt depolymerisation index (NBO/T) (B). The solid blue line represents the NBO/T value of the Earth's mantle calculated from the Earth's mantle composition suggested by McDonough & Sun (1995). The correlation between $D_C^{metal/silicate}$ and oxygen fugacity (ΔIW) appears less distinct (C).*

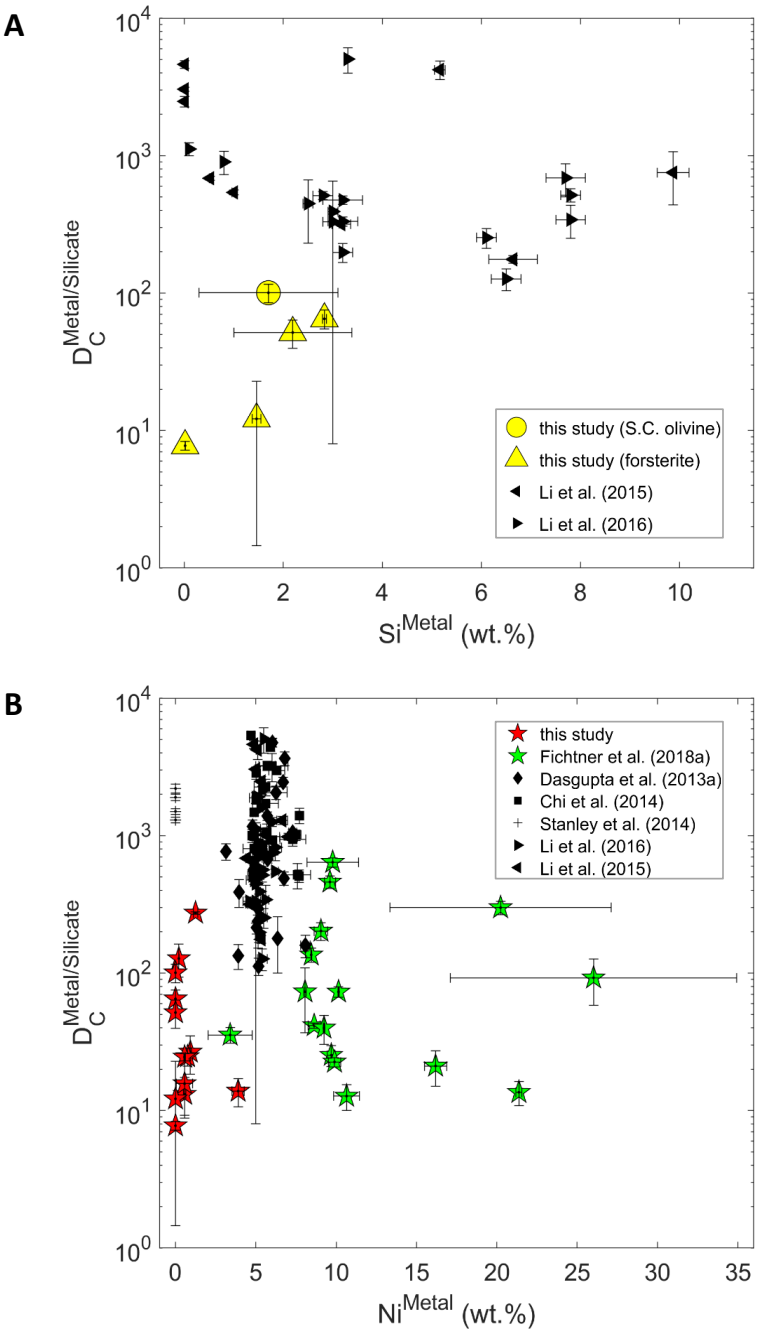

Fig. 4.6. *$D_C^{metal/silicate}$ as a function of Si content of the metallic melt (A), and Ni content of the metallic melt (B).* ***A:*** *$D_C^{metal/silicate}$ appears to correlate positively with increasing metallic Si content, whereas previous studies by Li et al. (2015) and Li et al. (2016) reported an inverse correlation.* ***B:*** *The effect of metallic Ni on carbon partitioning is less distinct and hardly shows a particular correlation.*

with both EPMA and SIMS. Fig. 4.7 shows root-mean-square deviations of < 1 wt.% C between the methods. This relatively large deviation may occur for two reasons: (1) metal melts with very low C content (≤ 0.8 wt.%) were relatively close to the EPMA detection limit of 0.05 wt.% C, and (2) over- or under-sampling of some graphite inclusions or quenched graphite within the metal droplets may have occurred for metal melts with high C content (> 5 wt.%). This phenomenon could have been avoided by EPMA analyses, but was inevitable for SIMS measurements, because of its larger raster

of 50 × 50 µm and its worse optical resolution. Nevertheless, due to higher accuracy and consistency, SIMS data were preferentially used for further considerations in this study, wherever available.

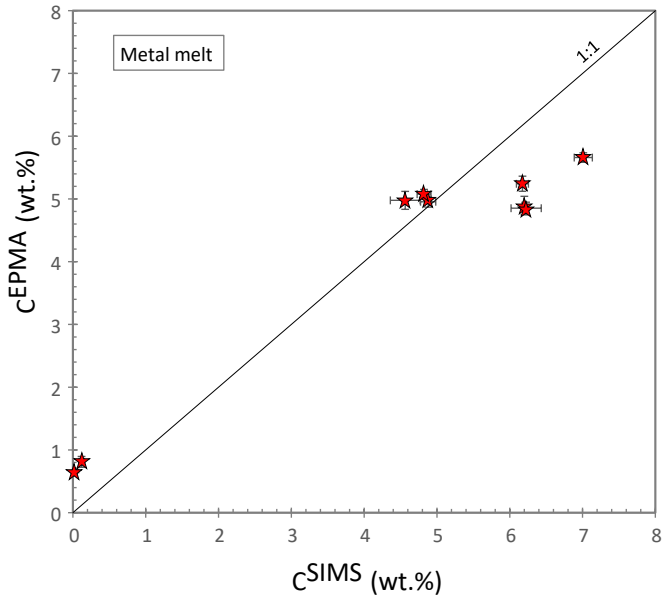

Fig. 4.7. *Comparison of metal C concentrations analysed by SIMS and EPMA. The solid line is the 1:1 line. Errorbars represent the standard deviation (1σ) based on replicate measurements.*

4.4.2 Carbon solubility in silicate melts and its implications for carbon partitioning

Partition coefficients are calculated from the concentrations in both phases under consideration, but for most of the experiments, the carbon partition coefficient depends predominantly on the concentration of carbon in the silicate melt. The C contents of the metallic melts are relatively similar (5.3 ± 1.5 wt.% C) within all experimental studies without extreme Ni or Si contents in the metal (Dasgupta et al., 2013; Chi et al., 2014; Stanley et al., 2014; Li et al., 2015; Li et al., 2016; Dalou et al. 2017; Fichtner et al., 2018a), regardless of experimental conditions. The silicate melts, however, vary substantially in carbon content (over 4 orders of magnitude) and also between this study and previous studies by 1 – 2 orders of magnitude (see section 4.3.6).

The large difference in silicate melt C contents between this and previous studies is most likely rooted in the principally different starting materials. All other studies used C-free oxide/silicate and metallic material and assumed that the silicate melt would saturate with C species by dissolution of the graphite capsule material. Instead, this study added carbon in the form of carbonate to the silicate starting mix, and in the form of graphite powder to the metallic starting mix. Thus, a C species principally soluble in each of the melts is initially available.

The question arises whether our experiments are carbon oversaturated or experiments based on the graphite capsule as carbon source remain undersaturated. In general, reactions involving volatiles such as CO_2 and CH_4, and most likely their dissolved equivalents in silicate melts, progress fast. Even

though all components of our starting material and all assembly parts were carefully dried, a truly dry experiment is almost impossible as several thousands of ppm H_2O may well be gained during the experiment due to hydrogen diffusion through the capsule walls. In fact, most experimental high pressure studies on carbon partitioning between metal and silicate melt are nominally dry but those who searched after H-species all report some and up to half a wt.% H_2O in their nominally dry melts (Dasgupta et al., 2013; Chi et al., 2014). Depending on the prevailing oxygen fugacity conditions and the availability of hydrogen, carbon is dissolved either as carbonate species, forms other C ≡ O species, or reduces to CH_4, CH_3 or CH_2, all of them relatively soluble in silicate melts (e.g., Holloway et al., 1992; King & Holloway, 2002; Mysen et al., 2009; Ardia et al., 2013), while there is no known solubility of C^0 in silicate melts.

Any excess carbon present in the starting material should precipitate as C^0, either in an amorphous form or as variably crystalline graphite. Our Raman spectra do not show any indication for C^0, i.e., the characteristic D, G, and 2D bands at 1360, 1560, and 2710 cm^{-1}, respectively (Ferrari, 2007), are absent. Hence, we do not measure finely dispersed C^0 that does not correspond to a true solubility. Some of the experiments, where the bulk carbon content exceeds what is soluble in the silicate and metal melts, form large graphite flakes. These are easily identifiable in BSE images and avoidable when measuring carbon. We therefore argue that any excess carbon present in the starting material would precipitate, and that our elevated concentrations in the silicate melt correspond to true solubilities.

Apparently, these solubilities are mostly not reached when graphite capsules are used. Graphite is one of the most refractory materials with one of the lowest diffusion constants for Earth materials (0.4 cm^2/s; Kanter, 1957). Because C^0 is not soluble in silicate melts, all of the melts are graphite saturated but not automatically saturated in oxidised or reduced carbon species. Carbon dissolution requires redox reactions, e.g., oxidation of C to a CO_3^{2-} species or to C ≡ O species (e.g., Ni & Keppler, 2013). Such reactions may be hindered by the high chemical inertness of graphite.

In any experiment, that has all graphite on the capsule walls and no carbon in the metal melt, carbon has to migrate from the wall to metal droplets enclosed by silicate melt. This process requires two redox reactions (at the wall/silicate melt interface and at the silicate melt/metal droplet interface) and diffusion of CO or CH species through the silicate melt, which may be kinetically hindered. Direct contact of metal to graphite should however lead to fast dissolution of graphite in the iron melt, in this case the metallic melt would saturate much faster in carbon than the silicate melt. This, in turn, results in very high carbon partition coefficients, as observed in previous studies (Dasgupta et al.,

2013; Chi et al., 2014; Stanley et al., 2014; Li et al., 2015; Li et al., 2016; Dalou et al. 2017), which may be overestimated.

4.4.3 The parameterisation of $D_C^{metal/silicate}$

The last years have seen a wave of published studies determining $D_C^{metal/silicate}$, all with the goal to better understand the early distribution of carbon in the Earth. There is agreement that the principal parameters are temperature, pressure, silicate melt polymerisation, metal melt composition and oxygen fugacity, which are, however, not independent variables. We have hence formulated a parameterisation model that incorporates our own and previous results with the aim to predict $D_C^{metal/silicate}$ for the variable conditions that prevailed during Earth's accretion.

In order to constrain a model for extrapolation to conditions of core formation, the equation developed by Chi et al. (2014) has been applied as basis for a (probabilistic) Monte Carlo coefficient estimation. To account for the effect of Si content in metallic melt on $D_C^{metal/silicate}$, the additional term $f \times ln\,(1–X_{Si})$ was added to the equation of Chi et al. (2014), such that the final equation is as follows:

$$\ln\left[D_C^{metal/silicate}\right] = \frac{a}{T} + \frac{b \times P}{T} + c \times \ln(fO_2) + d \times (NBO/T) + e \times \ln(1 - X_{Ni}) + f \times \ln(1 - X_{Si}), \quad (4.10)$$

where temperature is given in K, pressure in GPa, fO_2 in ΔIW, and X_{Ni} and X_{Si} are the mole fractions of Ni and Si in metallic melt, respectively. The coefficients of Chi et al. (2014) were adopted as prior mean values, and then varied randomly in a standard Metropolis-Hastings sampler (e.g. Sambridge & Mosegaard, 2002; Tarantola, 2005) with a robust likelihood (misfit) function defined as:

$$misfit = \frac{1}{n}\sum_{i=1}^{n}\left|\frac{D_{C_i}^{initial} - D_{C_i}^{measured}}{D_{C_i}^{1\sigma}}\right|, \quad (4.11)$$

where $D_{Ci}^{initial}$ is the carbon partitioning coefficient calculated with the initial coefficients of Chi et al. (2014), $D_{Ci}^{measured}$ is the measured carbon partitioning coefficient of experiment *i*, $D_{Ci}^{1\sigma}$ is the standard deviation (1σ) of the measured carbon partitioning coefficient of experiment *i*, and *n* is the total number of experiments. To extend the temperature, pressure and NBO/T range, the recent results of Fichtner et al. (2018a) were included in our parameterisation. More details concerning the motivation for and the implementation of the Metropolis-Hastings algorithm can be found in Appendix C.

The outstanding benefit of the Metropolis-Hastings sampler, in contrast to deterministic estimation methods (e.g., Chi et al., 2014; Li et al., 2015), is its ability to provide complete probability densities

for the coefficients, which allows us to quantify in detail their uncertainties and inter-dependencies. Furthermore, the use of a robust misfit functional avoids the notorious dominance of outliers in the standard least-squares method. To ensure proper convergence of the sampler, 5 million random sets of test coefficients were used. For evaluation of the maximum-likelihood coefficients and their uncertainties (Table 4.4), probability densities of all coefficients are shown in Fig. 4.8. Trade-offs between pairs of coefficients are displayed in the form of 2D probability densities in Fig. 4.9. Most pronounced inter-dependencies exist between coefficients of temperature and NBO/T (negatively correlated), fO_2 and NBO/T (positively correlated), NBO/T and X_{Ni} (positively correlated), fO_2 and X_{Ni} (positively correlated), and fO_2 and X_{Si} (negatively correlated). This for example means, that a temperature variation by a certain amount can be compensated by a variation of NBO/T in such a way that the resulting $D_C^{metal/silicate}$ is unchanged within the measurement uncertainties. The correlation between a pair of coefficients does not necessarily imply that these parameters have a dominant effect on carbon partitioning. It, however, demonstrates a co-variation, i.e., an unavoidable trade-off. All other parameter pairs appear to be mainly independent from each other.

Table 4.4
Coefficients of parameterisations for $D_C^{metal/silicate}$ after equations (4.10).

	Coefficient	Coefficient uncertainty
a	11795 K	561 K
b	198 K/GPa	78 K/GPa
c	0.24	0.08
d	-2.1	0.4
e	2.5	0.7
f	-50	14

Coefficients of parameterisation using equation (4.10) as given in the text. Uncertainties are determined by the probability densities shown in Fig. 4.8.

To compare the relative contributions of the different terms in the parameterisation of equation (4.10), we consider their approximate order of magnitude. The term bP/T has order of magnitude 9, and is by far the largest. This implies that P/T has the strongest effect on carbon partitioning. (Note that this is independent of the units used for P and T, because a change in units would be compensated by a change in the numerical value of b. The term bP/T is followed by NBO/T (order of magnitude 4) and temperature (order of magnitude 3). This is in agreement with the results of Chi et al. (2014), who argued that the depth of the magma ocean seems to be the key variable for metal-silicate fractionation of carbon. Still, the coefficient related with pressure has a large uncertainty (b = 198 ± 78, Fig. 4.8),

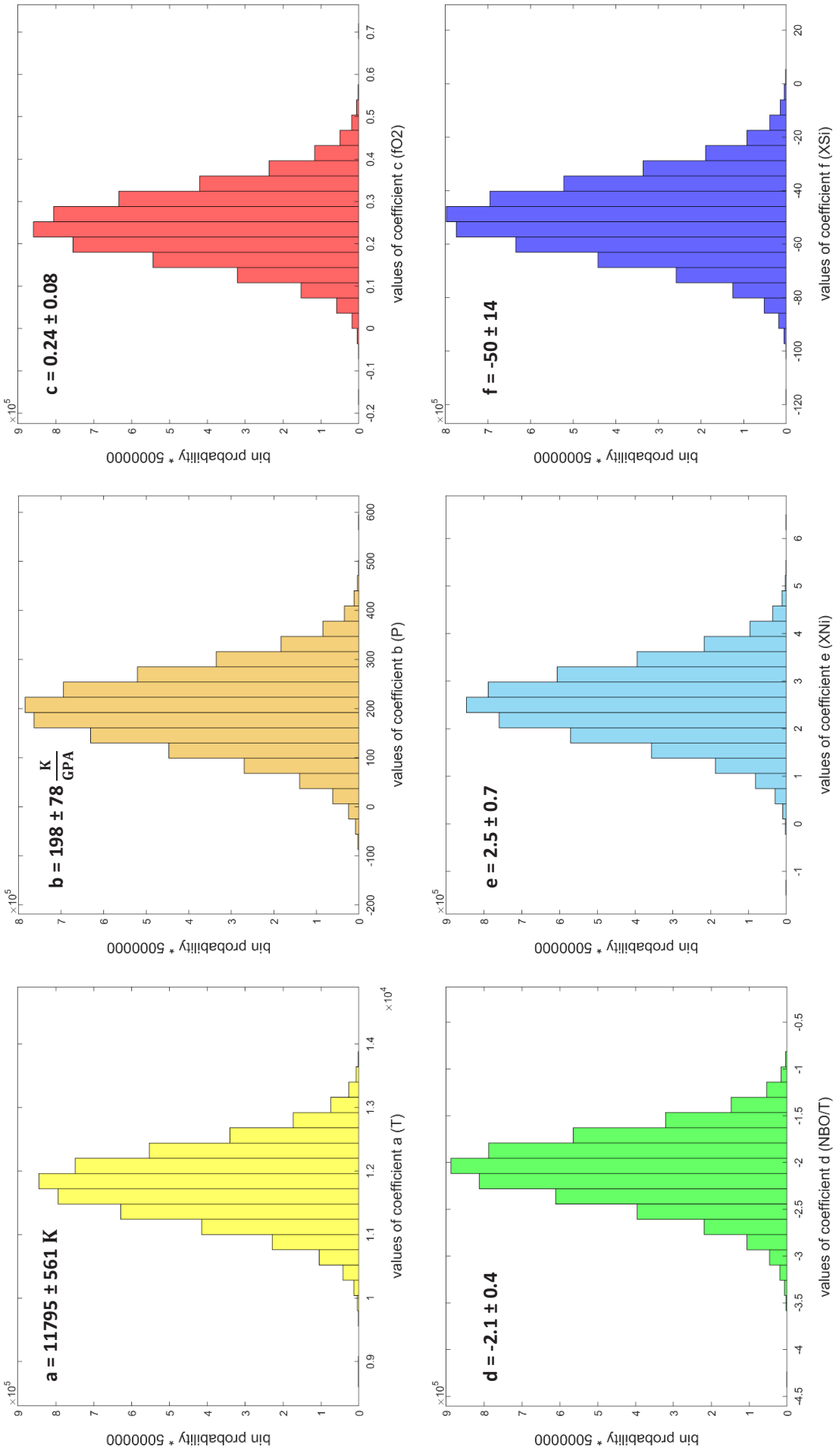

Fig. 4.8. *Probability densities for all coefficients found in equation (4.10), which show the maximum-likelihood of the coefficients and their uncertainties.*

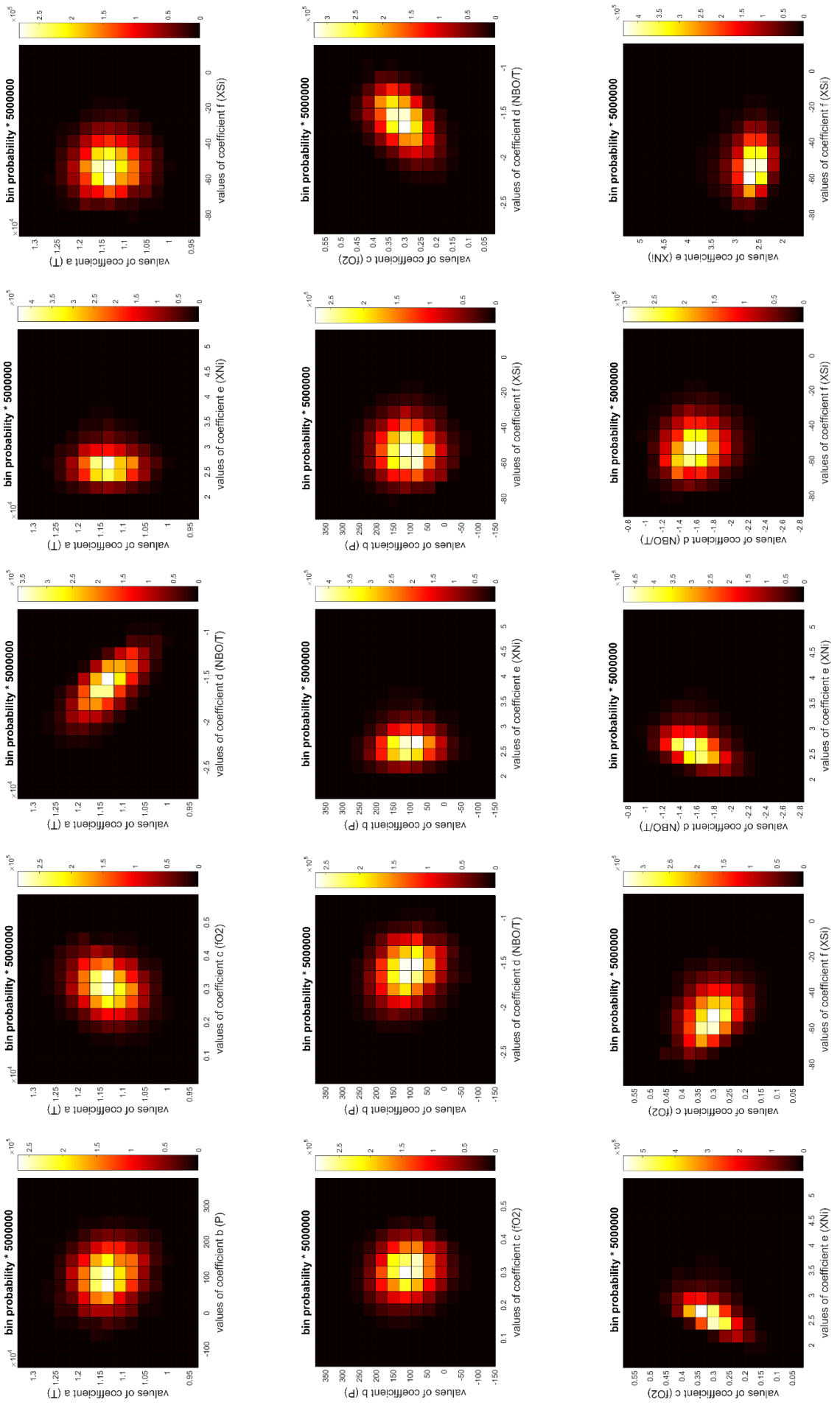

Fig. 4.9. *2D probability densities between pairs of coefficients of equation (4.10) to demonstrate their trade-offs..*

implying that a variety of coefficients can be applied without significantly changing the resulting partition coefficient.

A key question concerns the possibility to find alternative coefficients that may explain individual observations of $D_C^{metal/silicate}$ better than the optimal set of coefficients described above. Testing carefully different sets of coefficients yields that alternative sets of coefficients may explain individual observations of $D_C^{metal/silicate}$ very well, yet the remaining observations only very poorly. This attests indeed to the uniqueness of the optimal coefficients described above. Still, the minimum misfit of the optimal set of coefficients is 4.5. This indicates, assuming that the functional form of our parameterisation is correct, that the standard deviation (1 σ) of the measured $D_C^{metal/silicate}$ values is underestimated by at least a factor of 4. Therefore, the standard deviation has been corrected, i.e., multiplied by a factor of 4. Fig. 4.10 shows that, when applying the parameterisation to our data, the difference between the measured and the calculated $D_C^{metal/silicate}$ divided by its standard deviation is close to or below 1. This suggests that the distance between the measured and the calculated $D_C^{metal/silicate}$ is as large or smaller than its uncertainty.

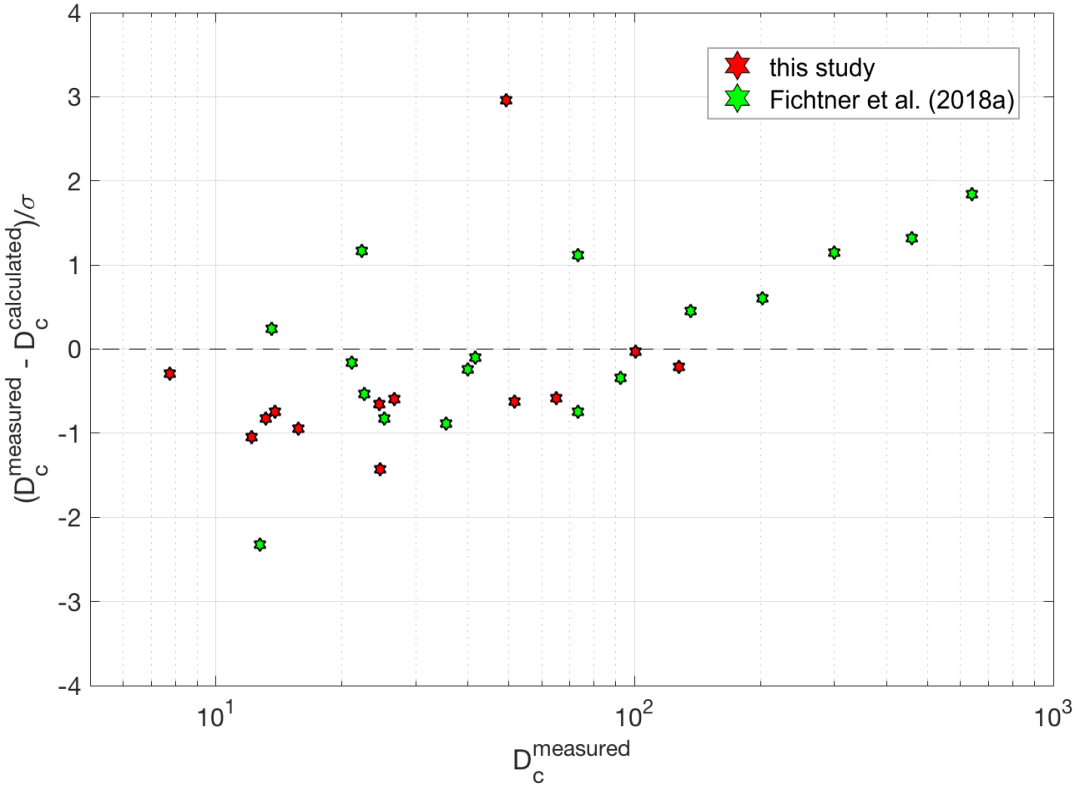

Fig. 4.10. *Measured $D_C^{metal/silicate}$ values plotted against the difference between the measured and the calculated $D_C^{metal/silicate}$ divided by its standard deviation (σ). The calculated $D_C^{metal/silicate}$ is based on equation (4.10) and coefficients are shown in Table 4.4. Note that the standard deviation has been corrected (multiplied by a factor of 4), such that the average distance between the measured and the calculated $D_C^{metal/silicate}$ is close to the standard deviation.*

While optimal coefficients explain our measurements well within uncertainties, applying our parameterisation to literature data (Dasgupta et al., 2013; Chi et al., 2014; Stanley et al., 2014; Li et al., 2015; Li et al., 2016; Dalou et al. 2017), reveals that in particular the higher $D_C^{metal/silicate}$ values cannot be explained very well with the model based on our data. This may be caused by a possible overestimation of the accuracy of C concentration measurements of the literature data and may also ultimately reflect the higher carbon solubilities in the silicate melt of our data.

As an alternative approach, all available experiments are used as the data basis for the Monte Carlo estimation of coefficients. Furthermore, the model was extended with a range of additional effects by newly incorporating coefficients and various functional forms for, e.g., sulfur content of the metallic melt, and the magnesium number. Excluding all other options by extensive trial and error, this suggests that the C content of the silicate glass is the only remaining influence factor.

4.4.4 Carbon partitioning between Earth's core and magma ocean

Based on the parameterisation of $D_C^{metal/silicate}$ developed from our experiments, carbon partitioning between a segregating core and a magma ocean may be constrained. To achieve this, the prevailing T-, P- and fO_2-conditions during Earth accretion need to be estimated. Since recent studies argue for a multi-stage core formation process (e.g., O'Brien et al., 2006, Rubie et al., 2015; Bourdon et al., 2018) rather than a single-stage process, T-, P- and fO_2-conditions have changed over time as accretion progressed. Further complication arises from the amount of impacting material that has fully or partially equilibrated with the terrestrial magma ocean. This is especially of importance if the impacting body has already segregated a core. Thus, in case that the impactor's core has failed to equilibrate with the magma ocean, which likely happened for larger and later impactors (Rubie et al., 2011), the initial C inventory of the impactor and, for already differentiated impactors, the carbon partition coefficient at the conditions of differentiation of the impactor are decisive for the Earth's core carbon content.

In general, metal-silicate equilibration occurred at the base of the magma ocean where the temperature of equilibrium is assumed to be a function of pressure based on the liquidus of mantle peridotite (e.g., Rudge et al., 2010; Bourdon et al., 2018). Pressure (and hence temperature) at the base of the magma ocean increases as the Earth grows and is estimated to correspond to 30 % (Wood et al., 2006) to 70 % (Rubie et al., 2015) of the pressure at the core-mantle boundary in the growing planet at the time of each impact. Assuming that accretion started with a Moon-size proto-Earth (e.g., Wood et al., 2006), this would lead to magma ocean depths ranging from 290 to 2230 km with corresponding P-T

conditions of 3 – 90 GPa and 1800 – 4200°C. The prevailing oxygen fugacity conditions are thought to increase over time from ΔIW -5 to ΔIW -2 due to (1) impactors delivering more oxidised material at a later stage of accretion (Rubie et al., 2011; Nimmo & Kleine, 2015) and/or (2) the crystallisation of silicate perovskite in the lower mantle as the Earth attained the size of Mars (Frost et al., 2004, Wade & Wood, 2005). The silicate melt depolymerisation NBO/T, however, is estimated to be at a constant value of 2.6 during the entire accretion process, calculated from the Earth's mantle composition suggested by McDonough & Sun (1995). Constraining $D_C^{metal/silicate}$ at the base of a terrestrial magma ocean is found to be highly dependent on the Si content of the Earth's core. For example, if a core Si content of 8 wt.% is assumed as proposed by Rubie et al. (2011), the resulting $D_C^{metal/silicate}$ values would be > 200, and thus lead to relatively low silicate Earth C contents of < 200 ppm and very high C concentrations of > 5 wt.% in the core. This is clearly implausible, since this would exceed the core density deficit of 10 %, especially when the established core value of ~ 2 wt.% S (Allègre et al., 1995; McDonough & Sun, 1995; Dreibus & Palme, 1996) is also taken into account. Since several authors suggested a lower Si concentration in the core of ~ 4 wt.% (e.g., Chakrabarti & Jacobsen, 2010; Badro et al., 2014), we implemented the estimate of 4.5 wt.% Si content of Badro et al. (2014) in our model, as well as 5 wt.% Ni.

Since the estimated P-T conditions at the base of the magma ocean, where metal-silicate equilibration took place, are significantly higher than our experimental P-T conditions, extrapolations from 6 GPa to 90 GPa and from 2000°C to 4200°C have to be made. This extrapolation may not be appropriate in terms of linear pressure- and temperature-dependence on $D_C^{metal/silicate}$. In contrast, the estimated oxygen fugacity conditions and the NBO/T value are inside our calibration range. However, the aim of our parameterisation is to constrain the partitioning of carbon between the core and the magma ocean, in case the effects of the investigated parameters on $D_C^{metal/silicate}$ remain valid at extrapolations to higher P-T conditions. Finally, with the above-described estimations, this study constrains the carbon partitioning at the base of a terrestrial magma ocean to range from ~ 3 to ~ 30 as accretion proceeds, depending on the core formation scenario (Fig. 4.11).

4.4.5 Implications for the carbon inventory of the Earth's mantle and core

The range of $D_C^{metal/silicate}$ modelled for various accretion scenarios constrains the initial distribution of carbon between the Earth's core and mantle and hence the bulk Earth carbon content for a given mantle carbon content at the completion of core segregation. The results, however, are highly dependent on the initial C inventory of the accreted impactors. Details about the calculations, on which the core formation scenarios are based on, can be found in Appendix D.

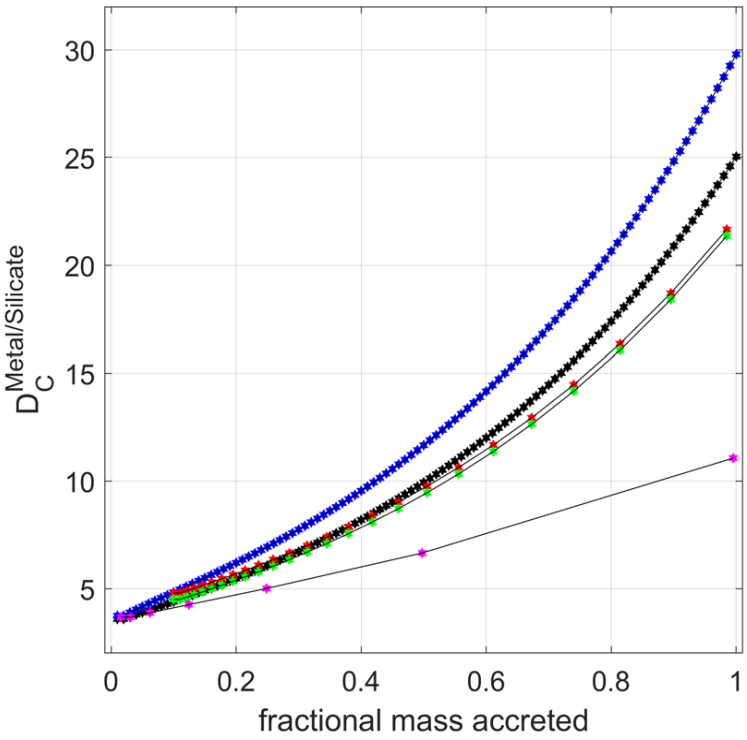

Fig. 4.11. *$D_C^{metal/silicate}$ values are in the range of ~ 3 to ~ 30 at the base of a terrestrial magma ocean as accretion proceeds. See section 4.4.5 and Appendix D for the description of the individual scenarios represented by the different lines.*

The bulk composition of the silicate Earth (BSE) is often approximated by the composition of C1 carbonaceous chondrites that match well the Earth's volatile depletion trend (Allègre et al., 2001; Palme & O'Neill, 2003). These carbonaceous chondrites represent pristine material from the early state of the solar system and are thought to be essential building blocks of the Earth (Allègre et al., 1995; McDonough & Sun, 1995; O'Neill & Palme, 1998). In recent years, however, several observations like the superchondritic abundances of some element ratios (e.g., H/C; Mg/Si, Ca/Al) and the different isotopic signature of the Earth in comparison to C1 chondrites (e.g., ^{48}Ca, ^{50}Ti, ^{62}Ni) give reason to assume a non-C1-chondritic composition of the bulk Earth (O'Neill & Palme, 2008; Dauphas, 2017). Possible explanations include (1) a loss of crust during accretion caused by large impactor collisions that modified the original chondritic composition (Caro et al., 2008; Bonsor et al., 2015; Carter et al., 2015), (2) a "hidden" reservoir in the deep Earth (Boyet & Carlson, 2005; Labrosse et al., 2007; Hirschmann & Dasgupta, 2009), (3) a large fraction of the accreting material being composed of enstatite chondrites (Javoy, 1995; Dauphas, 2017; Liebske & Khan, 2018) or (4) a fractionation process like mantle differentiation of ultra-high pressure mantle phases such as perovskite and ferropericlase (Walter et al., 2004; Walter, 2014), which would then require a stratified

mantle. Still, assuming CI chondritic bulk Earth carbon concentrations of 3.5 wt.% C (Anders & Grevesse, 1989; Lodders, 2003), the BSE C content could have reached a saturation value of up to 4500 ppm. These high chondritic C values for the bulk silicate Earth would result in a maximum Earth core C content of 9.5 wt.%. However, a C1 chondritic bulk Earth composition is very unlikely, due to the potential loss of crust (and atmosphere) caused by collisions during Earth accretion (Caro et al., 2008; O'Neill & Palme, 2008).

Direct measurements of the mantle carbon inventory are difficult, because samples might not represent the original C concentrations of the primary magma due to CO_2 degassing (e.g., Wallace, 2005). The majority of existing studies estimate the mantle C content based on (1) measurements of incompatible element concentration ratios (e.g., Trull et al., 1993; Saal et al., 2002; Salters & Stracke, 2004; Cartigny, 2008; Hirschmann & Dasgupta, 2009), (2) fluxes of a modern CO_2 cycle (Sleep & Zahnle, 2001), (3) stable isotope ratios (Marty, 2012), or (4) the relative abundances of non-lithophile and non-refractory elements in the Earth (McDonough & Sun, 1995). The above studies vary by an order of magnitude in their results, leading to a range for the bulk silicate Earth C content of 42 − 75 ppm C (Sleep & Zahnle, 2001) to 765 ± 300 ppm C (Marty, 2012).

Applying our parameterisation of $D_C^{metal/silicate}$ to the above-described core-formation scenarios, it is remarkable that all scenarios yield very similar results of more than 2000 ppm C in the bulk silicate Earth and 4 – 5 wt.% C in the Earth's core. Consequently, the C distribution and inventory does not primarily depend on the number and size of impacting bodies, nor the depth of the magma ocean, nor wether the impactors equilibrate with the entire magma ocean or wether the impactor's cores (if any) merge directly with the Earth's core without equilibration with the silicate Earth. The most important factor controlling the Earth's carbon inventory, however, is the initial C concentration of the accreting bodies. This means that, to match present-day BSE C concentrations of ~ 100 to ~ 500 ppm, either severe carbon loss may have occurred (e.g., due to evaporation of carbon during the impact) or most of the impacting bodies were highly reduced enstatite chondrites with low C concentrations of 0.42 wt.% (Jarosewich, 1990) as suggested, e.g., by Javoy (1995). The latter scenario would result in ~ 550 ppm C concentration for the BSE and ~ 1.15 wt.% C for the Earth's core, that corresponds well with the present-day BSE C concentration.

Fig. 4.12 shows five core formation scenarios, in which the estimated BSE C concentrations are normalised to 100 (Fig. 4.12A) and 500 ppm (Fig. 4.12B), respectively. The first two scenarios involve 99 Moon-size impactors (0.01 present-day Earth masses) that accrete to a proto-Earth of the

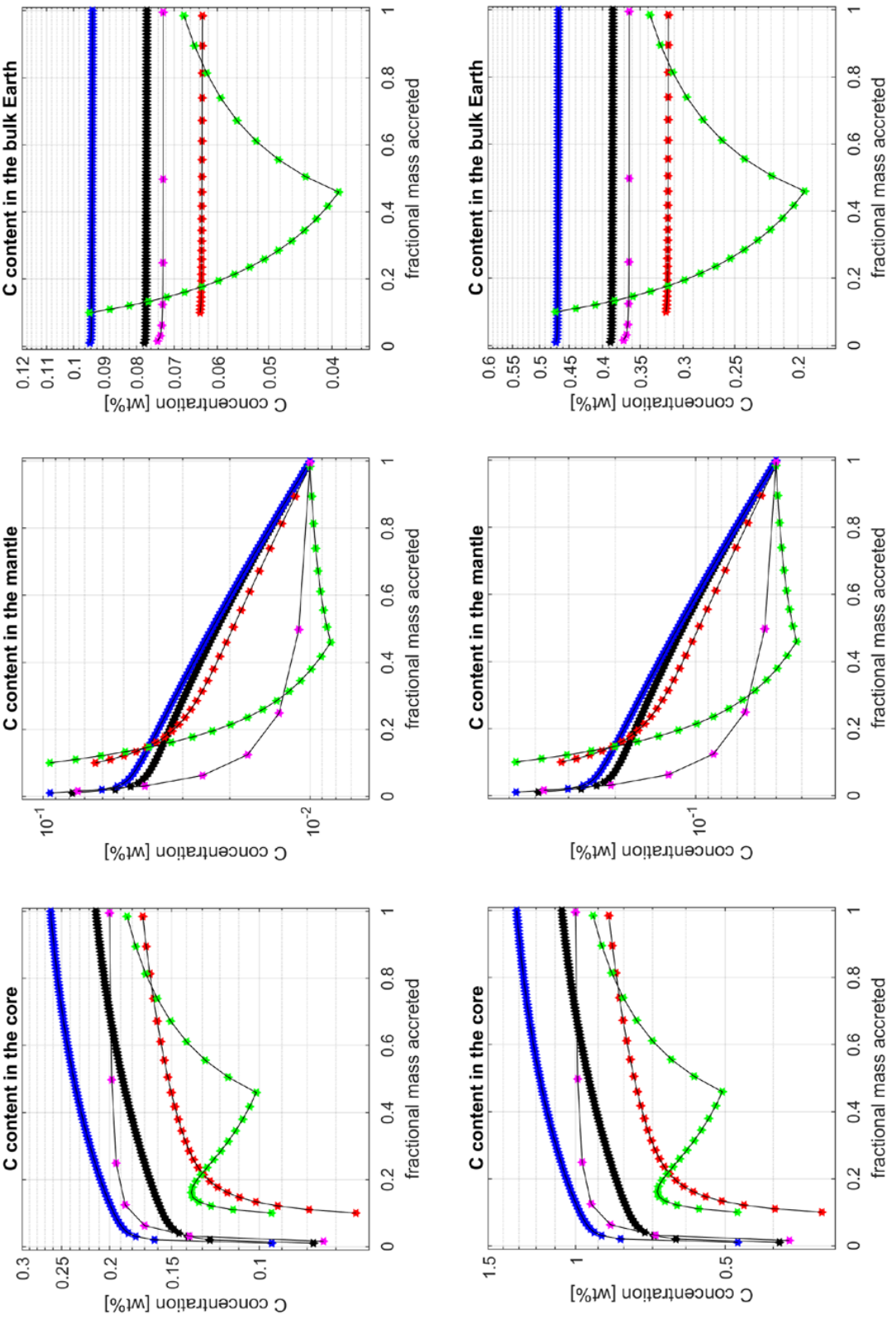

Fig. 4.12. *Carbon inventory of the Earth as accretion proceeds of core, mantle and bulk Earth normalised to 100 ppm (A) and 500 ppm (B) BSE carbon content. Core concentrations are in the range of 0.17 – 0.27 and 0.85 – 1.30 wt.%, respectively, independent of the applied core formation scenario. The resulting bulk Earth C concentration ranges from ~ 630 ppm to ~ 0.47 wt.%, respectively. See text and Appendix D for the description of the individual scenarios represented by the different lines.*

size of the Moon. All impactors equilibrate entirely with the magma ocean at its base, corresponding to 30 % (Wood et al., 2006) and to 70 % (Rubie et al., 2015) of the depth of the core-mantle boundary at the time of the impact. These two scenarios are presented in Fig. 4.12 as black and blue symbols, respectively. The third scenario (red symbols in Fig. 4.12) is the same as the first one but assumes a Mars-size starting Earth (0.1 present-day Earth masses). The mass of each impactor is 10 % of the Earth's mass at the time of the impact (Rubie et al., 2011), summing up to 24 impactors in total. The fourth scenario (green symbols in Fig. 4.12) is based on the third one but assumes that 70 % of the Earth's mass accretes from highly reduced enstatite chondrites, and the last 30 % of more oxidised chondrites. Further, only the first 16 impactors equilibrate with the magma ocean, whereas the last 8 impactors merge directly with the Earth's core (Rubie et al., 2011). The last scenario (pink symbols in Fig. 4.12) involves 6 impactors in total, which have a comparable size to the Earth at the time of the impact and none of the impactors equilibrates with the magma ocean (Nimmo & Kleine, 2015). All impactors that fail to equilibrate are assumed to have already segregated a core, whereas for the fully equilibrating impactors it is irrelevant wether they are differentiated or not. In general, normalising the estimated BSE C concentrations to 100 and 500 ppm yields core concentrations of 0.17 – 0.27 and 0.85 – 1.30 wt.%, respectively, independent of the applied core formation scenario (Fig. 4.12). The resulting bulk Earth C concentration ranges from ~ 630 ppm to ~ 0.47 wt.%, respectively.

4.5 Conclusions

Experimental determinations of $D_C^{metal/silicate}$ between a metallic and a silicate melt vary from 0.035 ± 0.004 to 274 ± 6 over a large range of fO_2 (ΔIW +2.2 to ΔIW -4.8). This suggests that C is lithophile for oxidising fO_2 conditions and evolves to be more siderophile as oxygen fugacity decreases towards highly reducing conditions. Similarly, NBO/T correlates negatively with $D_C^{metal/silicate}$, which is expressed by the fact that C becomes strongly siderophile in polymerised silicate melts. Both effects mainly result from the strong control of fO_2 and NBO/T on the amount of C dissolved in the silicate melt. For instance, the C speciation changes from carbon being chiefly dissolved as carbonate complexes to being dissolved mainly as methyl groups, while fO_2 decreases. Thereby, the amount of C dissolved in the silicate melt is reduced from 0.97 ± 0.01 to 0.07 ± 0.01 wt.%. At the same time, the C content of the silicate melt decreases from 0.97 ± 0.01 wt.% to 0.0224 ± 0.0004, as NBO/T decreases. Dissolved carbon in Fe-rich metallic melt, however, is hardly affected by fO_2 and shows similar values in all experiments (5.6 ± 0.7 wt.% C), clearly suggesting that $D_C^{metal/silicate}$ mainly depends on the C content of the silicate melt.

The parameterisation developed in this study indicates that the carbon partitioning at the base of a terrestrial magma ocean is in the range of 3 – 30 for core-forming conditions, i.e., 3 – 90 GPa, 1800 – 4200°C, and ΔIW -5 to ΔIW -2 with a fixed NBO/T of 2.6, Ni and Si content of 5 and 4.5 wt.%, respectively. Combining our parameterisation with core formation scenarios from the literature, the C inventory of the Earth's mantle and core during Earth's accretion can be constrained. Normalising the estimated silicate Earth C concentrations to present-day BSE values of ~ 100 to ~ 500 ppm, the Earth's core is estimated to store 0.17 – 1.30 wt.% C. The resulting bulk Earth C content ranges from ~ 0.06 to ~ 0.47 wt.% C. These results are mostly independent of the applied core formation scenario (e.g., homogeneous vs. heterogeneous accretion, number and size of impactors, depth of magma ocean) but strongly depend on the initial C concentration of the accreting impactors. Assuming, for instance, that later impactors were more oxidising and thus similar to carbonaceous chondrites (Rubie et al., 2011; Nimmo & Kleine, 2015), the silicate Earth C concentration would result in > 2000 ppm. Therefore, to explain present-day BSE concentrations, either a loss of carbon may have occurred, e.g., due to the escape of an early atmosphere (Caro et al., 2008; O'Neill & Palme, 2008), or the Earth may have accreted mainly from highly reduced enstatite chondrites with initial low C concentrations (Javoy, 1995). In conclusion, the Earth's C inventory may have been set during accretion rather than through a post-core formation C-delivery event like a "late veneer". Still, if significant amounts of carbon have been brought to the Earth after core formation has completed, accordingly less carbon would be stored in the core.

5. Conclusions and Outlook

The aim of this doctoral project was to experimentally constrain the carbon partitioning between silicate melt and metal melt at conditions that might have prevailed during Earth's accretion and differentiation. The results of this study contribute to a better understanding of the parameters determining the carbon partitioning, and they lead to important implications on the origin of carbon and its distribution between the Earth's core and mantle. In this chapter, a brief summary of the main conclusions is given, followed by an outlook about other light elements that might be present in the Earth's core and may contribute to the core's density deficit.

5.1 Summary of the main conclusions

In this doctoral thesis, the carbon partitioning between a mantle-forming silicate melt and a core-forming metal melt has been investigated in a range of conditions that are thought to have prevailed during Earth's accretion. The results demonstrate that carbon partitioning is mainly controlled by the composition of the silicate melt (NBO/T) and the oxygen fugacity (fO_2). Experimentally determined carbon partition coefficients ($D_C^{metal/silicate}$) vary within our experiments from 0.035 ± 0.004 to 640 ± 49, as NBO/T increases and fO_2 decreases. This can be explained by two effects: First, highly depolymerised silicate melts dissolve carbon more effectively than less depolymerised melts. Second, the C speciation changes from carbon being mainly dissolved as carbonate complexes to being dissolved as methyl groups, while the C content of the silicate melt decreases. Since the amount of carbon dissolved in Fe-rich metallic melt is hardly affected by fO_2 and shows similar values in all experiments (5.6 ± 0.7 wt.% C), our results clearly suggest that $D_C^{metal/silicate}$ mainly depends on the C content of the silicate melt.

It is suggested in Chapter 3 of this thesis that the C concentration of the silicate melt mainly depends on the degree of silicate melt depolymerisation (NBO/T). This correlation is then used to determine the carbon partition coefficients for Earth, Mars and the Moon, as their NBO/T values are well known and thought to be constant over the period of accretion. The resulting $D_C^{metal/silicate}$ values for Earth, Mars and the Moon are in the ranges of 25 − 43, 28 − 48, and 35 − 57 for NBO/T values of 2.6 (McDonough & Sun, 1995), 2.55 (Lodders & Fegley, 1997), and 2.46 (Rai & van Westrenen, 2014), respectively. Applying a homogeneous core formation scenario to the partition coefficients of Earth and Mars, the terrestrial and martian core, and bulk carbon contents can be estimated for a given C content of the

respective mantle. For a BSE C content of 120 to 765 ppm (McDonough & Sun, 1995; Marty, 2012), this yields a C content of 0.4 ± 0.1 to 2.6 ± 0.7 wt.% for the core and 0.14 ± 3 to 0.9 ± 0.2 wt.% for the bulk Earth, respectively. Due to unknown bulk silicate Mars C concentrations, we assume that Mars was built from the same building blocks as the Earth, which results in core concentrations of 0.4 ± 0.1 to 2.7 ± 0.7 wt.% C and inferred bulk Mars C contents of 0.15 ± 0.03 – 0.9 ± 0.2 wt.%.

In Chapter 4 the experimental set is extended to a wider range of conditions, in particular to a large range of fO_2 from ΔIW +2.2 to ΔIW -4.8. This is needed for the development of a parameterisation that enables the estimation of the carbon partitioning during core formation. The results indicate that the carbon partitioning at the base of a terrestrial magma ocean is in the range of 3 – 30 for core-forming conditions, i.e., 3 – 90 GPa, 1800 – 4200°C, and ΔIW -5 to ΔIW -2 with a fixed NBO/T of 2.6, Ni and Si content of 5 and 4.5 wt.%, respectively. Combining our parameterisation with core formation scenarios from the literature, the C inventory of the Earth's mantle and core during Earth's accretion can be constrained. Normalising the estimated silicate Earth C concentrations to present-day BSE values of ~ 100 to ~ 500 ppm, the Earth's core is estimated to store 0.17 – 1.30 wt.% C. The resulting bulk Earth C content ranges from ~ 630 ppm to ~ 0.47 wt.% C. These results are mostly independent of the applied core formation scenario (e.g., homogeneous vs. heterogeneous accretion, number and size of impactors, depth of magma ocean), but they highly depend on the initial C concentration of the accreting impactors. Assuming, for instance, that later impactors were more oxidising and thus similar to carbonaceous chondrites (Rubie et al., 2011; Nimmo & Kleine, 2015), the silicate Earth C concentration would result in > 2000 ppm. Therefore, to explain present-day BSE concentrations, either a loss of carbon may have occurred, e.g., due to the escape of an early atmosphere (Caro et al., 2008; O'Neill & Palme, 2008), or the Earth may have accreted mainly from highly reduced enstatite chondrites with initial low C concentrations (Javoy, 1995).

In summary, the approaches described in Chapters 3 and 4 deliver consistent results and lead to the general conclusion that the Earth's C inventory may have been set through equilibrium core formation in the early Earth's history rather than through a post-core formation C-delivery event like a "late veneer". Still, if significant amounts of carbon have been brought to the Earth after core formation has completed, accordingly less carbon would be stored in the core. Finally, C is likely to be present in the core and may contribute ~ 0.2 to ~ 3 wt. C to the core's density deficit.

5.2 Outlook

It is well established that the core comprises 32 % of the mass of the Earth and has a diameter of 6942 km, roughly the size of Mars. Seismically determined density and sound velocity estimates have shown that the core is less dense than molten iron-nickel alloy at corresponding P-T conditions, concluding that the core's density deficit is about 10 % (Birch, 1964). This leads to the assumption that "light elements" such as carbon, hydrogen (Birch, 1952), sulphur, silicon, oxygen (Birch, 1964), phosphorous or nitrogen (McDonough, 2003) may exist in the core.

This doctoral study focusses on carbon as potential light element present in the core. Carbon is likely to contribute to the density deficit because of its ability to lower the density of molten iron (Ogino et al., 1984) and because of its high cosmic abundance. In addition, carbon shows a chemical affinity to iron, even at low pressure (Benz and Elliott, 1961), and it is present as graphite, diamond and metal carbides in iron meteorites, that may have carried carbon to the Earth (Deines and Wickman, 1973). The results of this thesis constrain the carbon content of the Earth's core to be in the range of 0.2 to 3 wt.%, depending on the estimate of the bulk silicate Earth carbon content (120 – 765 ppm, McDonough & Sun (1995), Marty (2012)). Consequently, carbon may at most account for 30 % of the core's density deficit. This naturally raises questions concerning the identity and abundance of the other light element(s).

Generally, the composition of the Earth's core in terms of its light element abundances depends mainly on the devolatisation and redox history, as well as the bulk composition of the Earth (e.g. Fischer et al., 2017). In fact, an extrapolation of the volatility trend (McDonough, 2003; Wood et al., 2006) shown in Fig. 5.1 provides an initial estimate of the depletion of volatile elements in the silicate Earth compared to chondrites. This depletion may have been caused either by massive blow-off of the Earth's atmosphere, the formation of mantle phases during differentiation that are now "hidden" in the deep mantle, or by trapping these elements in the core (e.g. Wood et al., 2006; Marty, 2012; Chi et al., 2014; Dalou et al., 2017). The efficiency of the latter process mainly depends on the degree of interaction and equilibration between mantle-forming silicate melt and core-forming metallic liquid during Earth's accretion and differentiation (Williams & Hemley, 2001; Dalou et al., 2017). Assuming that the depletion of the light elements is due to sequestration into the core, abundances of 1.5 – 2 wt.% S (McDonough & Sun, 1995; Allègre et al., 1995; Dreibus & Palme, 1996), 0.1 wt.% H (McDonough, 2003), 0.2 wt.% C (McDonough, 2003), 0.2 wt.% P (McDonough, 2003), 75 ppm N (McDonough, 2003) and 4 – 8 wt.% Si (Allègre et al., 1995; McDonough, 2003; Rubie et al., 2011;

Badro et al., 2014) in the core may be inferred. Consequently, silicon appears to be the major light element in the core.

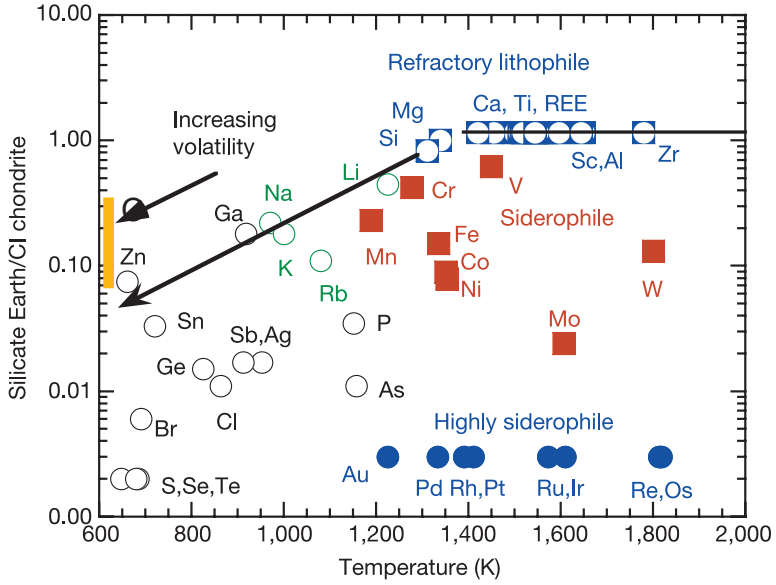

Fig. 5.1. *Volatility trend after Wood et al. (2006). The relative elemental abundances in the silicate Earth are plotted against the 50 % condensation temperature (K) at 10^{-4} bar. This temperature reflects the point at which 50 % of the element would have condensed from the solar nebula.The depletion of siderophile (refractory) and highly siderophile elements relative to C1 chondrites is thought to be due to the sequestration of these elements into the core. The orange bar represents the 50 % condensation temperature for graphite at 626 K (Lodders, 2003) for the BSE C content range of 100 to 500 ppm and a C1 chondrite composition of 3.5 wt.% (Anders & Grevesse, 1989).*

While the above-mentioned arguments based on depletion are attractive because of their simplicity, they are not always in accord with geochemical constraints. For instance, such high Si concentrations in the core would require unrealistically reducing conditions (fO_2 << ΔIW -3) during core formation that are not consistent with the current FeO content of the mantle (Kilburn & Wood, 1997). Therefore, a more moderate concentration of 4 – 5 wt.% Si in the core is more likely (Wood et al., 2006, Tsuno et al., 2013; Badro et al., 2014). The volatility trend does not provide estimates of the abundance of oxygen in the core, because the trend is not extended to systems, where oxygen is the dominant element as it is in terrestrial rocks. Also, available experimental data do not provide a consistent and explicit indication about the solubility behavior of oxygen in Fe-rich melts at high pressure and temperature conditions (Ohtani & Ringwood, 1984; O'Neill et al., 1988; Rubie et al., 2004). A recent experimental study of Tsuno et al. (2013), however, reported very little pressure dependence but a strong temperature dependence for oxygen and silicon partitioning. They found that the presence of

oxygen in metallic Fe influences the partitioning behaviour of Si such that more Si partitions into the liquid metal with increasing temperature. Still, an oxygen-dominant core would involve mostly oxidising conditions during core formation, which are thought to be unrealistic (e.g., Wade & Wood, 2005). Consequently, there is evidence that silicon and oxygen are mutually exclusive candidates for light elements in core-forming melts (O'Neill et al., 1988; Hillgren et al., 2000; Li & Fei, 2003), whereas the study of Tsuno et al., (2013) proposes that at high temperatures (> 3000 K) liquid metal could store more than 1 wt.% of both elements.

Further requirements for light elements in the core are that both their constrained abundances and properties have to match the density and sound velocity observations throughout the core provided by seismic data (e.g. Kennett et al., 1995). Therefore, ab initio calculations (Badro et al., 2014) and accretion simulations (Fischer et al., 2017) have been used to find the best matching light element composition for the Earth's core. Both studies strongly favour at least several wt.% of oxygen and/or silicon as major light elements stored in the core. Badro et al. (2014) argue that oxygen is the only light element that is always required in order to find a composition that fits the seismological data and suggested oxygen as major light element in the core with a likely concentration of 5.4 ± 0.4 wt.%. These authors further suggested a core composition with a silicon concentration below 4.5 wt.% and a sulphur concentration below 2.4 wt.%. Fischer et al. (2017), however, found in their simulations that Si is the dominant light element in the core, followed by oxygen. They allowed only for 1 – 2 wt.% of other light elements.

In recent years, nitrogen has also been suspected of being one of these other light elements present in the Earth's core (Marty, 2012). Therefore, several experimental studies have investigated the behaviour of nitrogen at high temperature and pressure conditions (Kadik et al., 2011; 2013; Roskosz et al., 2013; Dalou et al., 2017). Kadik et al. (2011), and Roskosz et al. (2013) found that nitrogen is siderophile at high pressures and could have sequestered into the core, assuming that nitrogen was delivered to the Earth through wet planetesimals, and was present during Earth's accretion (Marty, 2012). Dalou et al. (2017), however, argued that this pressure effect is actually owing to a simultaneous increase of oxygen fugacity with pressure, which is positively correlated with the solubility of nitrogen in an iron-rich liquid. Further confusion arises, when the effect of several light elements on their metal affinity behaviour is taken into account. For example, the N solubility decreases with increasing Si and C content in the metal, whereas S and H seem to have no effect on the solubility of N (Roskosz et al., 2013).

In conclusion, many different experimental and theoretical approaches of modelling the core's light element composition can be found in the literature. The fact that these models propose a large range of plausible core compositions, illustrates that the issue is still a matter of considerable debate. Furthermore, it is not well constrained to which extent various light elements in core-forming metals influence each other in terms of their own partitioning behaviour and also the partitioning behaviour of major and trace elements. Further experimental and numerical research on the interaction of C, N, Si, O, and S in liquid metal is clearly needed to constrain these effects independently, and to implement them into improved models of core formation.

APPENDIX A

Experimental conditions and back-scattered images of all experiments

A.1. Silicate melt experiments

In this section, the experimental conditions, phase assemblages and back-scattered electron (BSE) images of all silicate melt experiments are presented in Table A.1 and Fig. A.1. The aim of these experiments was to synthesise homogeneous silicate glasses of various chemical compositions and carbon contents that can be used as analytical standards for SIMS analyses. Therefore, different starting compositions were tested. These are shown in Table 2.1 in Chapter 2. The experiments displayed in italic in Table A.1 refer to successful experiments that were used as analytical standards for SIMS analyses (see section 2.1.5).

Most difficulties occurred due to the crystallisation of olivine, garnet, ortho- or clinopyroxene, and occasionally garnet that prevented the formation of larger volumes of glass. Further, excessive iron loss took place in experiments conducted in metallic capsule material owing to alloy formation. To circumvent this problem, most experiments were performed in olivine capsules.

Table A.1
List of silicate melt experiments.

Run #	T (°C)	P (GPa)	Duration (h)	Capsule	Starting Mix	Ol	Opx	Cpx	Grt	Comment
1-S-2	1350	2	72	Olivine-$Au_{80}Pd_{20}$	PB1S					Homogeneous, carbon-free glass.
2-S-6	1400	3	70	Olivine-$Au_{80}Pd_{20}$	PB2S		X	X		Homogeneous glass with idiomorphic opx and cpx crystals. Not useful for centrifugation.
3-S-7	1400	3	28	Olivine-$Au_{80}Pd_{20}$	PB3	X	X			Large areas of quench and idiomorphic opx and olivine crystals. Not useful for C analysis.
4-S-9	1400	3	27.5	Olivine-$Au_{80}Pd_{20}$	PB4	X		X		Olivine equilibrium crystals and cpx within homogeneous glass. Not useful for C analysis.
4-S-13	1450	3	24	Olivine-Pt	PB4	X		X		Large areas of quench. Cpx and olivine crystals. Not useful for C analysis.
6-S-16	1400	3	2	$Au_{50}Pd_{50}$	PB6		X			Large areas of quench and idiomorphic opx crystals. Very low FeO content. Not useful for C analysis.
8-S-19	1450	3	5.5	$Au_{50}Pd_{50}$	PB8	X				Olivine equilibrium crystals within homogeneous glass. One olivine grain was added to the experimental charge, which was partly dissolved. Very low FeO content of the silicate. Not useful for C analysis.
9-S-21	1450	3	3	Ir-Pt	PB9					Homogeneous, carbon-bearing glass. Material tested as SIMS standard, but C content is not homogeneous.
9-S-34	1450	3	2	Pt	PB9					Homogeneous, carbon-bearing glass. Material used to test reproducibility of the elemental carbon analyser (LECO).
1-B-35	1500	3.5	1.5	Pt	HAB1				X	Homogeneous, Fe-free glass with garnet crystals. Not useful for centrifugation.
1-B-38	1650	3.5	0.5	Pt	HAB1					Gas bubbles within the silicate melt, which probably formed during quenching. Not considered further.
1-B-50	1650	3.5	0.5	Pt	HAB1					Homogeneous, carbon-bearing glass. Material used to test reproducibility of the elemental carbon analyser (LECO).
2-B-51	1500	3	2	Pt	HAB2			X	X	Homogeneous, Fe-free glass with idiomorphic garnet and cpx crystals. Not useful for centrifugation.
2-B-53	1500	1.5	2	Pt	HAB2					Homogeneous, carbon-bearing, Fe-free glass. C content determined by LECO.
9-S-56	1450	3	3	Ir-Pt	PB9					Homogeneous, carbon-bearing glass. Material used to test reproducibility of the elemental carbon analyser (LECO).
1-B-58	1650	3.5	0.5	Pt	HAB1					Homogeneous, carbon-bearing glass. Material used to test reproducibility of the elemental carbon analyser (LECO).
2-B-59	1500	1.5	2	Pt	HAB2					Homogeneous, carbon-bearing glass. Material used to test reproducibility of the elemental carbon analyser (LECO).
1-1-B-63	1650	3.5	0.5	Pt	HAB1-1					Homogeneous, carbon-bearing glass. Fe added through Fe_2O_3 to avoid iron loss due to the Pt capsule. C content determined by LECO.
12-S-64	1500	1.5	2	Pt	PB12					Homogeneous, carbon-bearing glass. Fe added through Fe_2O_3 to avoid iron loss due to the Pt capsule. C content determined by LECO.
11-S-70	1400	1.5	1.5	Olivine-Pt	PB2					Homogeneous, carbon-bearing glass. C content determined by LECO.
2-B-71	1500	1.5	2.25	Olivine-Pt	HAB2					Homogeneous, carbon-bearing glass. C content determined by LECO.
2-B-73	1500	1.5	1.5	Pt	HAB2					Homogeneous, carbon-bearing glass. C content determined by LECO.
2-B-74	1500	1.5	2.5	Olivine-Pt	HAB2					Homogeneous, carbon-bearing glass. C content determined by LECO.
9-S-76	1450	3	3	Ir-Pt	PB9					Homogeneous, carbon-bearing glass. C content determined by LECO.

Abbreviations: Ol = olivine, Opx = orthopyroxene, Cpx = clinopyroxene, Grt = garnet. Composition of the starting mixtures is displayed in Table 2.1.

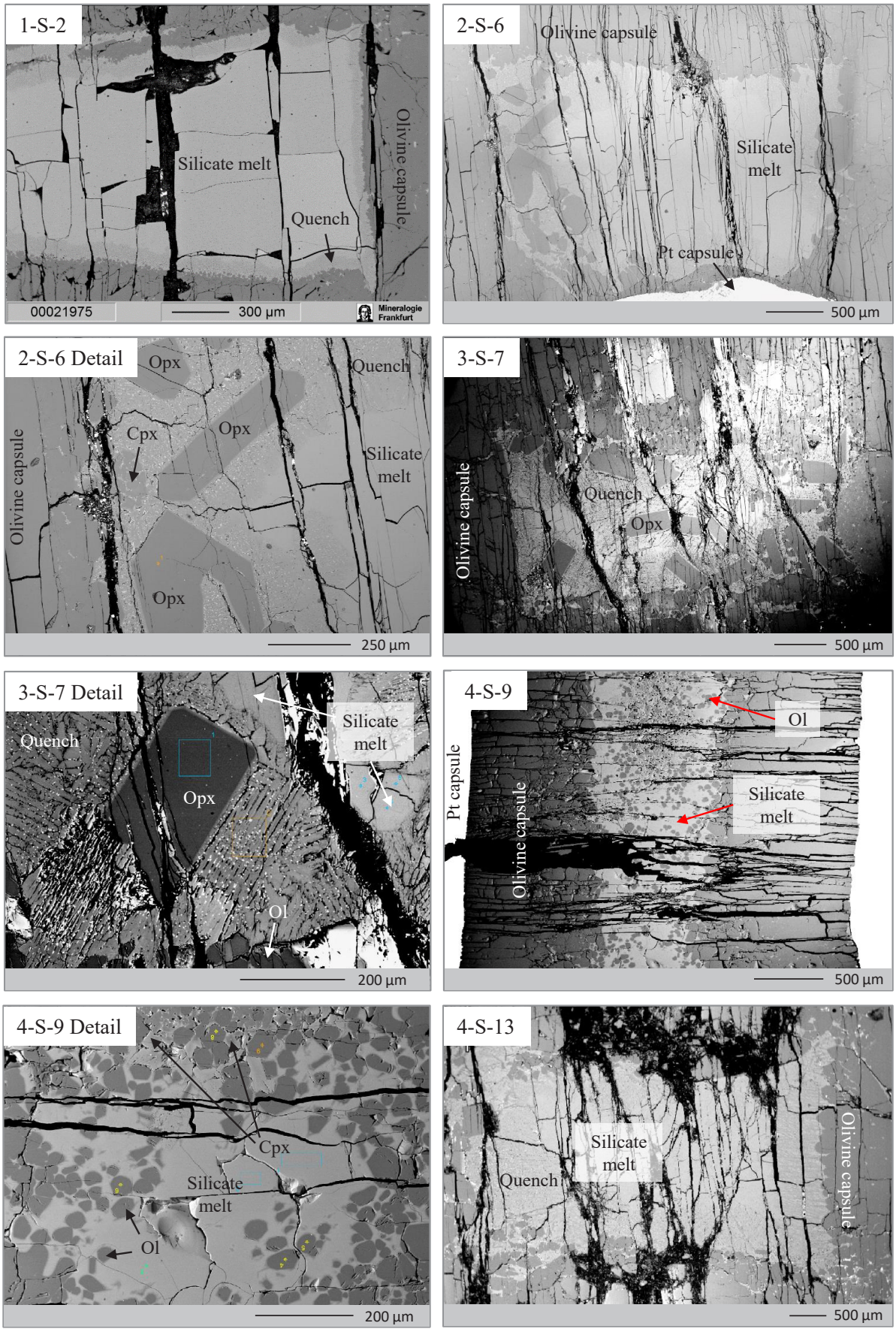

Fig. A.1. *Back-scattered electron images of silicate melt experiments presented in Table A.1. Abbreviations: Ol = olivine, Opx = orthopyroxene, Cpx = clinopyroxene.*

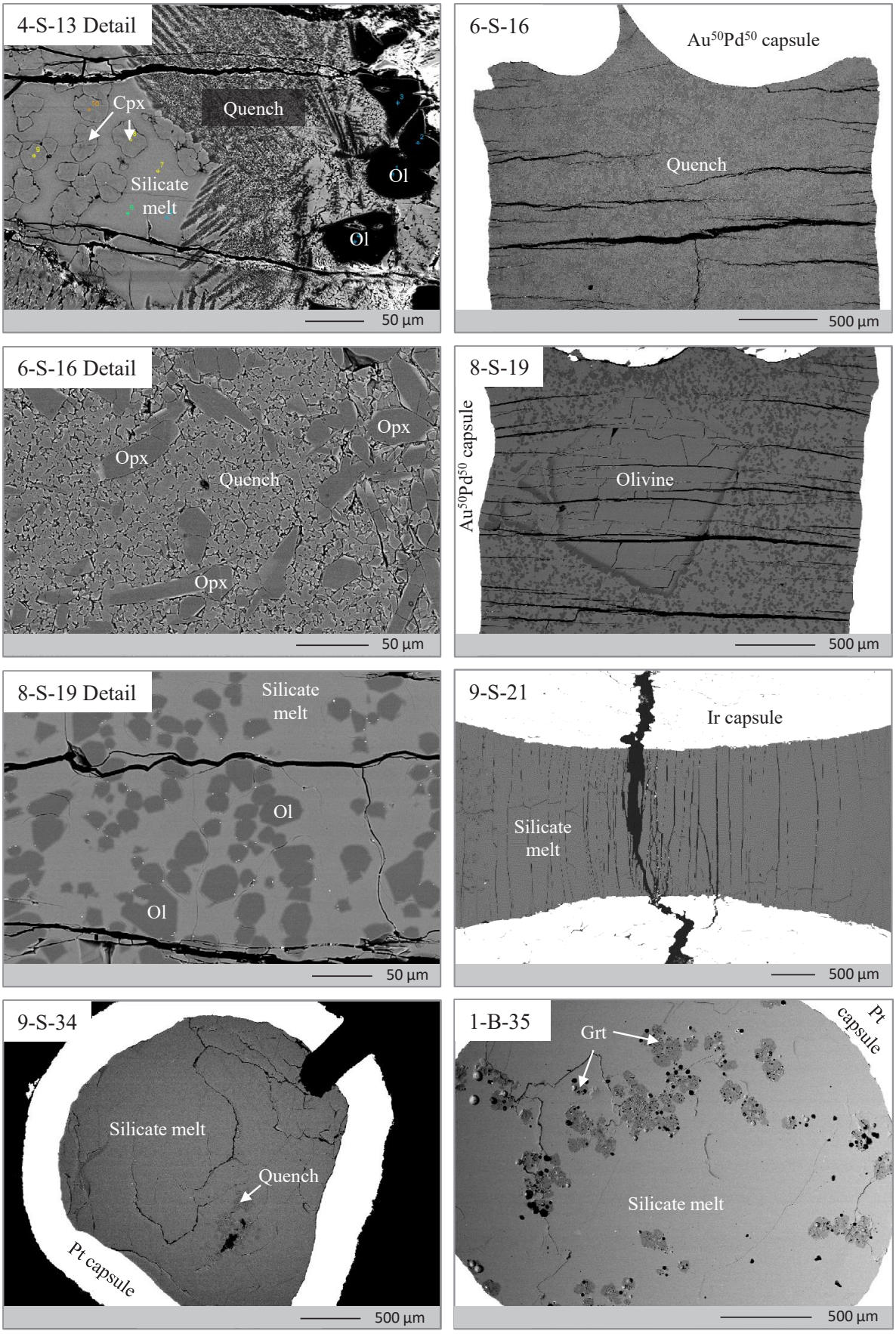

Fig. A.1 (continued). *Back-scattered electron images of silicate melt experiments presented in Table A.1. Abbreviations: Ol = olivine, Opx = orthopyroxene, Cpx = clinopyroxene, Grt = garnet.*

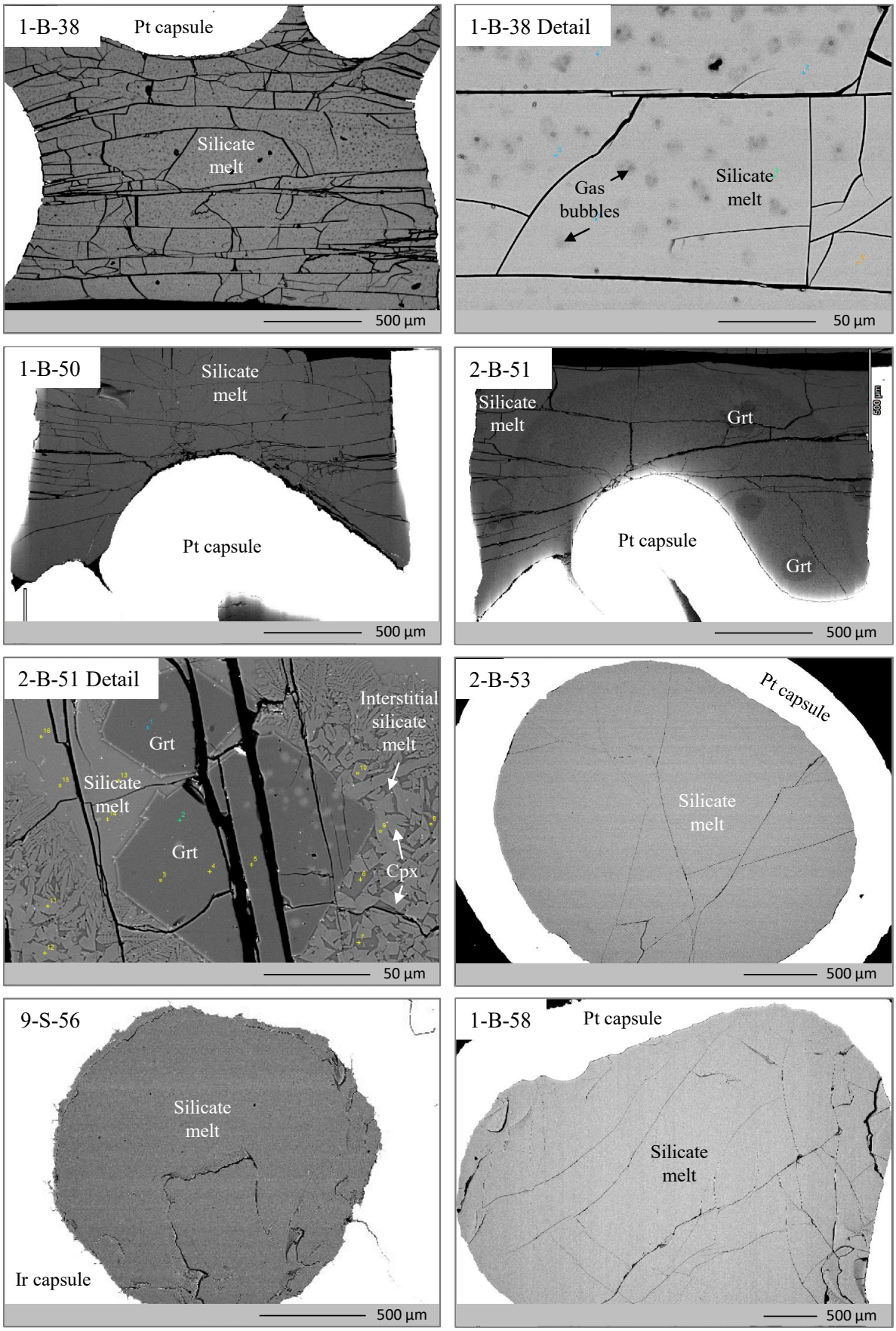

Fig. A.1 (continued). *Back-scattered electron images of silicate melt experiments presented in Table A.1. Abbreviations: Ol = olivine, Opx = orthopyroxene, Cpx = clinopyroxene, Grt = garnet.*

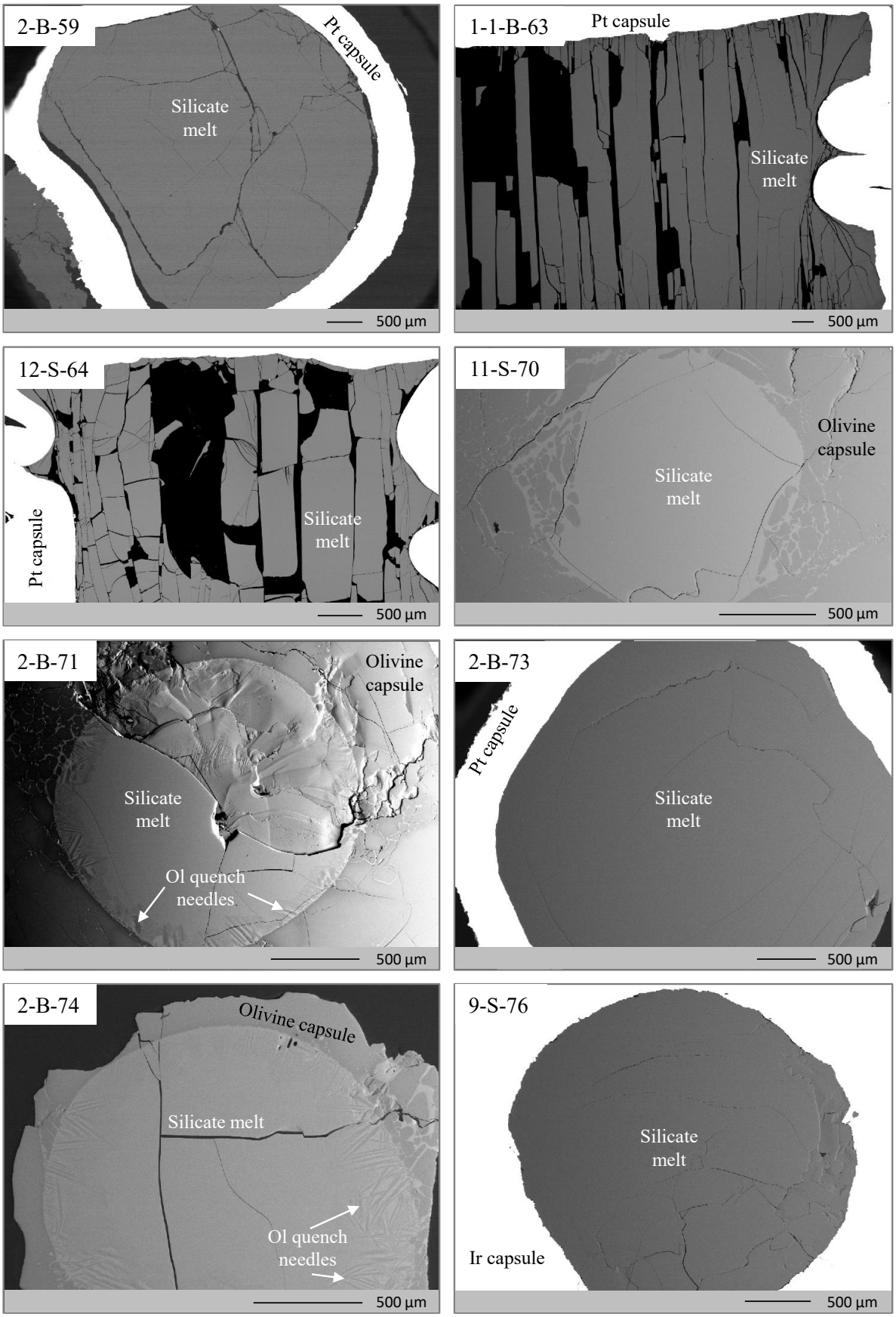

Fig. A.1 (continued). *Back-scattered electron images of silicate melt experiments presented in Table A.1. Abbreviations: Ol = olivine, Opx = orthopyroxene, Cpx = clinopyroxene.*

A.2. Metallic melt experiments

This section presents the experimental conditions, phase assemblages and back-scattered electron images of all metallic melt experiments (Table A.2 and Fig. A.2). The aim of these experiments was to synthesise homogeneous metallic alloys of various Fe-Ni ratios and carbon contents that can be used as analytical standards for SIMS analyses. The different starting compositions tested are shown in Table A.3. The experiments displayed in italic in Table A.2 refer to successful experiments that were used as analytical standards for SIMS analyses (see section 2.1.5).

As described in section 2.1.5, only stoichiometric Fe-Ni carbide could be synthesised successfully and used as SIMS standard. All other attempts failed due to iron loss, formation of heterogeneous dentritic quench structures, and the formation of wüstite and graphite pockets within the metallic alloy.

Table A.2
List of metallic melt experiments.

Run #	T (°C)	P (GPa)	Duration	Capsule	Starting Mix	Press	Comment
Fe3C-1	1050	2	121.5 h	$Au_{80}Pd_{20}$	Fe_3C-1	PC	Fe loss due to alloy formation with the capsule material. Large graphite flakes, Fe pieces and wüstite within the metallic melt. Not useful as SIMS standard.
Fe7C3-4	1400	10	48 h	crushable Al_2O_3	Fe_7C_3-1	MA	3 different metal phases, representing either disequilibrium caused by incomplete chemical reaction or a shift in stoichiometry of the starting material due to e.g. oxidation of iron.
Fe3C-5	1350	2	146.5 h	crushable Al_2O_3-Au	Fe_3C-1	PC	Fe and Au penetrated through the Al_2O_3 capsule. Wüstite, Au pieces and graphite flakes within the metallic melt. Not useful as SIMS standard.
Fe3C-8	1400	1atm	15 min	graphite	Fe_3C-1	1atm-oven	Fe melted and formed a blubb, inside the blubb is graphite (powder). Experiment not considered further.
Fe3C-12	1650	2	10 min	dense Al_2O_3	Fe_3C-1	PC	Al_2O_3 capsule material reacted with Fe and formed 2 different Fe-Al phases. Carbide probably oxidised and CO_2 was lost leaving behind a large hole.
Fe3C-26	1100	2	24 h	crushable Al_2O_3	Fe_3C-1	PC	Large graphite flakes and wüstite within the metallic melt. Excess C was added to the starting mix. Not useful as SIMS standard.
FeNi-33	1400	10	48 h	crushable Al_2O_3	FeNi-1	MA	2 metallic quench phases with graphite pockets and FeO inclusions. C content not homogeneously distributed (tested by SIMS). Not useful as SIMS standard.
Fe3C-39	1100	2	70.5 h	MgO	Fe_3C-1	PC	Large graphite flakes, wüstite and nitride within the metallic melt. Carbon was added through diamond powder to the starting mix. Not useful as SIMS standard.
Cohenite-41	1150	3	24 h	MgO	Cohenite-1	PC	Fe-Ni carbide in a S-rich metallic melt. Fe-Mg silicates within the metal melt. Carbon was added through diamond powder to the starting mix.
Fe3C-42	1200	2	72 h	MgO	Fe_3C+Fe	PC	Carbide needles in heterogeneous metallic melt. Excess Fe and C was added to the starting mix. Not useful as SIMS standard.
Cohenite-43	1150	3	24 h	MgO	Cohenite-1	PC	Fe-Ni carbide in heterogeneous S-bearing metallic melt. Carbon was added through diamond powder to the starting mix. Not useful as SIMS standard.
Cohenite-45	1150	3	24 h	MgO-Pt	Cohenite-1	PC	Heterogeneous, S-bearing, dendritic Fe-Ni quench textures. Fe-silicates within the quench textures. Carbon was added through diamond powder to the starting mix.
Fe3C-47	1100	2	72 h	MgO	Fe_3C-1	PC	Carbide with graphite flakes. Excess C was added to the starting mix. Not useful as SIMS standard.
Cohenite-48	1100	3	48 h	MgO-Pt	Cohenite-1	PC	Fe-Ni carbide (left part) and Fe-Ni-C dendrites embedded in a S-rich liquid (right part). Fe-Ni carbide is successfully tested as carbon standard for SIMS analyses.
Cohenite-55	*1100*	*3*	*48 h*	*MgO-Pt*	*Cohenite-1*	*PC*	*Repetition of run Cohenite-48. Used as carbon standard for SIMS analyses.*
Cohenite-62	1100	3	48 h	MgO-Pt	Cohenite-2	PC	Fe-Ni carbide in Ni-rich metallic melt (left part), Fe-Ni carbide (middle part) and Fe-Ni-C dendrites embedded in a S-rich liquid (right part). Fe-Ni carbide is successfully tested as carbon standard for SIMS analyses.
FeNi-65	1450	3	2.5 h	MgO-Pt	FeNi-2	PC	Pt outer capsule reacted with sample material to form homogeneous Fe-Ni-Pt-carbides (right part) and quench (left part). Not useful as SIMS standard.
FeNi-66	1450	3	2 h	MgO-Pt	FeNi-3	PC	Pt outer capsule reacted with sample material to form a Fe-Ni-Pt-C quench pattern. Not useful as SIMS standard, due to Pt contamination.
FeNi-67	1450	3	1.5 h	MgO-Pt	FeNi-4	PC	Quench pattern of Fe-Ni carbides. Not homogeneous in terms of C content in a scale of 50 µm (tested by SIMS). Not useful as SIMS standard.
Cohenite-75	*1100*	*3*	*48 h*	*MgO-Pt*	*Cohenite-1*	*PC*	*Repetition of run Cohenite-48. Used as carbon standard for SIMS analyses.*
Cohenite-105	*1100*	*3*	*48 h*	*MgO-Pt*	*Cohenite-1*	*PC*	*Repetition of run Cohenite-48. Used as carbon standard for SIMS analyses. No BSE image available.*

Abbreviations: PC = piston cylinder apparatus, MA = multi anvil apparatus, C = graphite. Composition of the starting mixtures is displayed in Table A.3.

Table A.3

Starting compositions of the metallic melt experiments (wt.%).

Metal mix	Fe3C-1*	Fe7C3-1	FeNi-1	FeNi-2	FeNi-3	FeNi-4	Cohenite-1*	Cohenite-2
Fe	93.3	91.6	76.6	9.9	34.5	34.7	85.3	87.3
Ni	-	-	19.1	89.5	64.0	64.4	5.3	5.4
S	-	-	-	-	-	-	4.7	4.9
C	6.7	8.4	4.3	0.6	1.5	1.0	4.7	2.4
Total	100	100	100	100	100	100	100	100

Carbon was added through graphite powder to the starting mix. *Mixtures are additionally prepared with diamond powder instead of graphite powder.

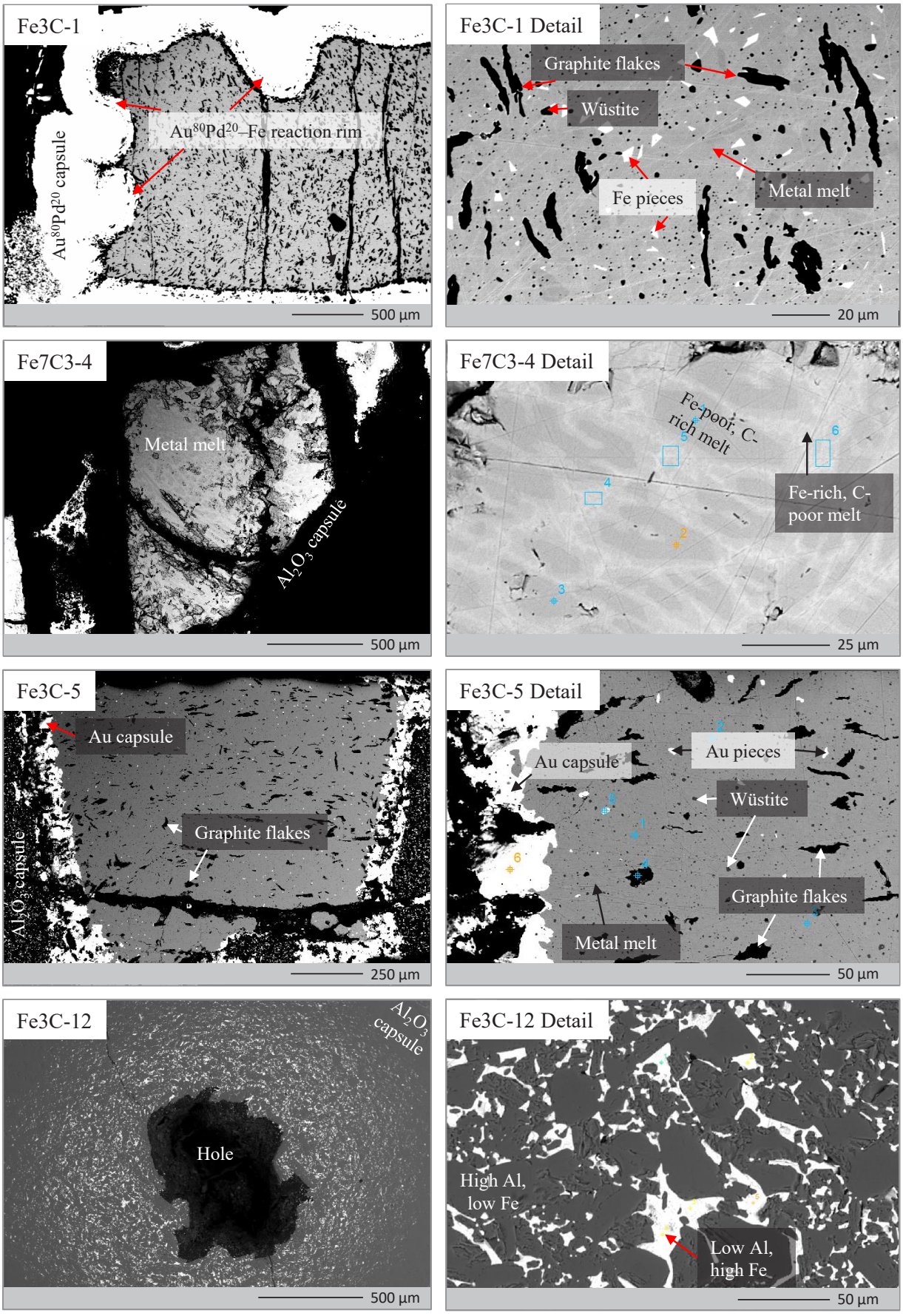

Fig. A.2. *Back-scattered electron images of metal melt experiments presented in Table A.2.*

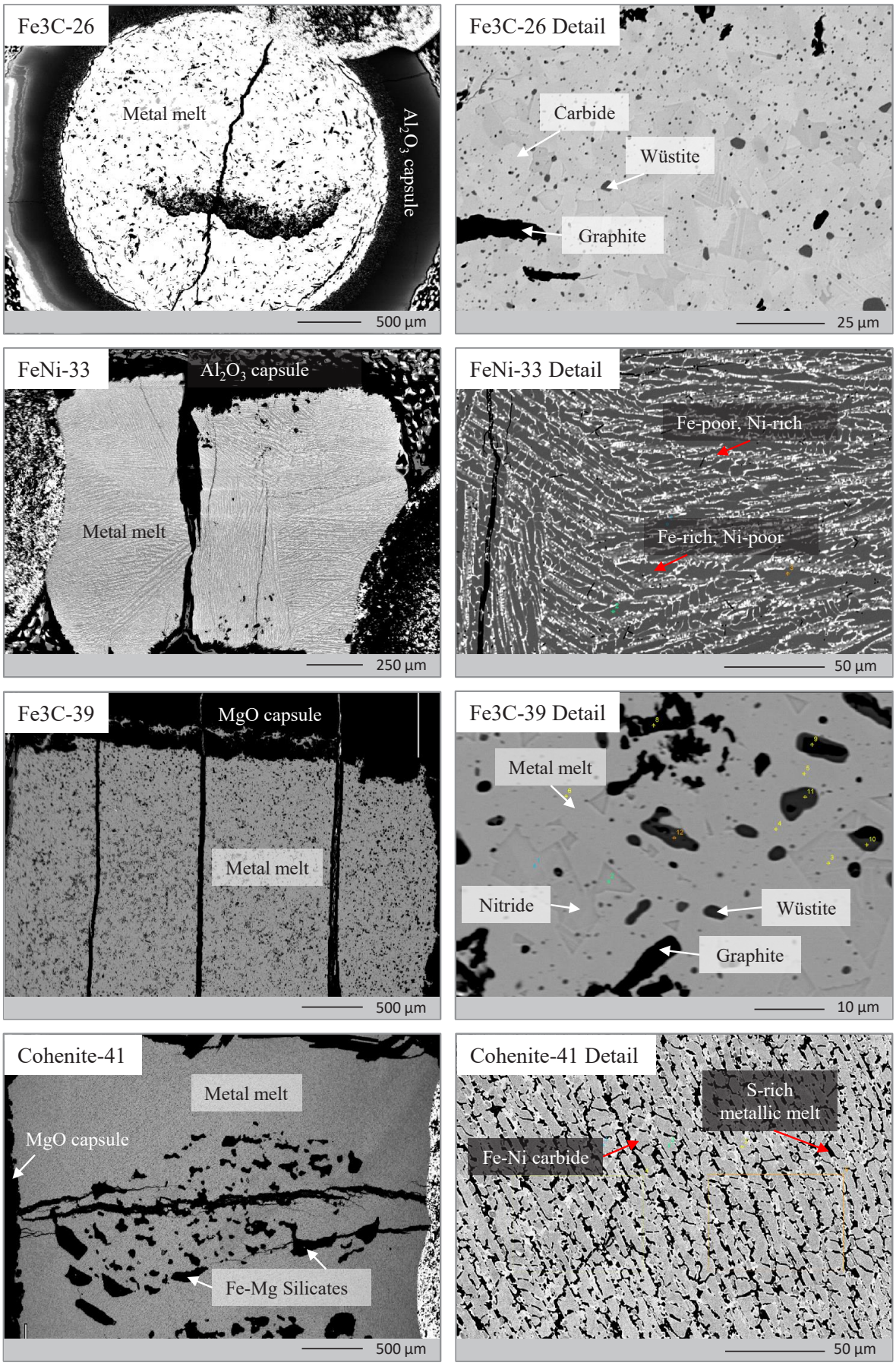

Fig. A.2 (continued). *Back-scattered electron images of metal melt experiments presented in Table A.2.*

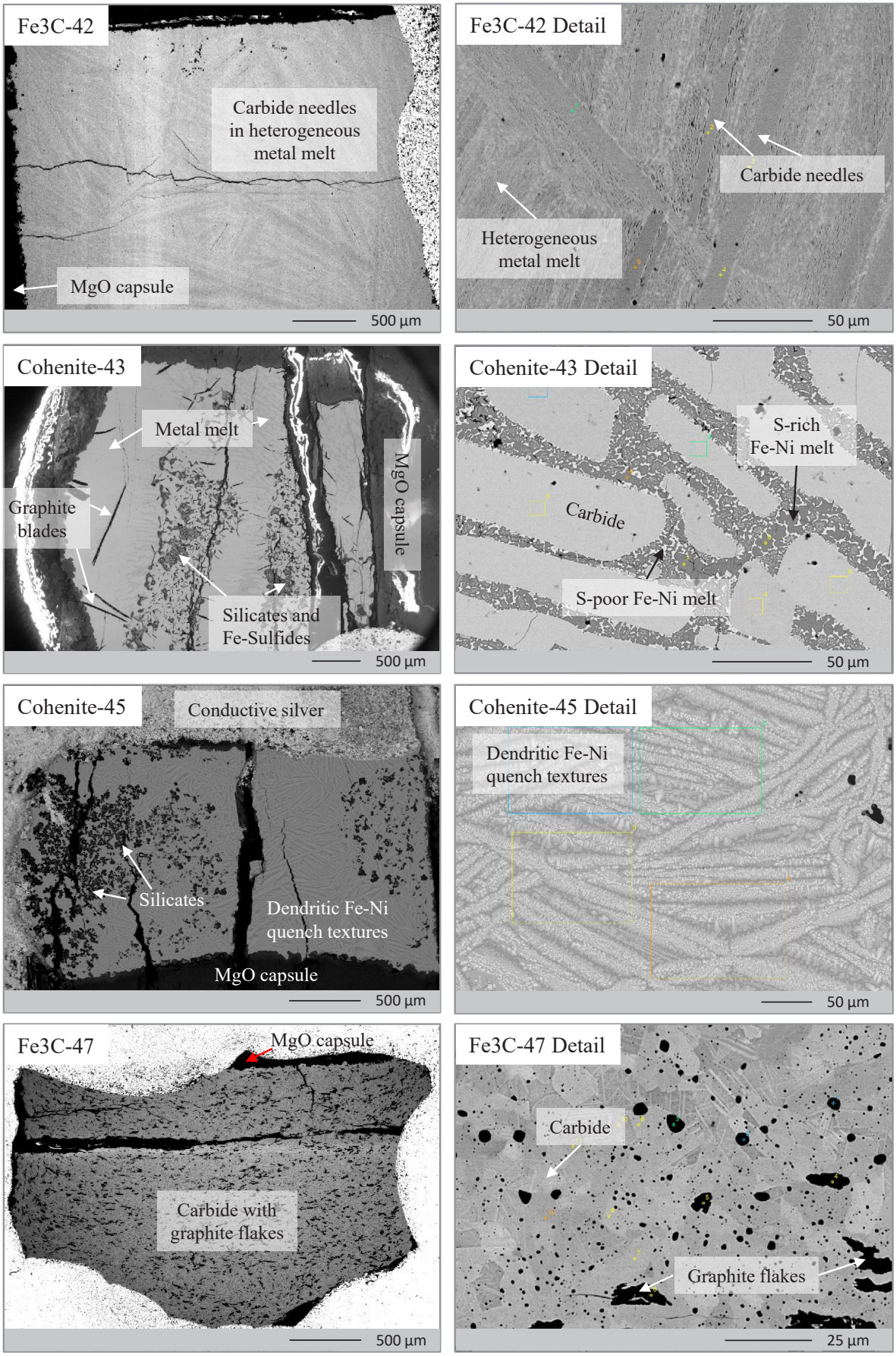

Fig. A.2 (continued). *Back-scattered electron images of metal melt experiments presented in Table A.2.*

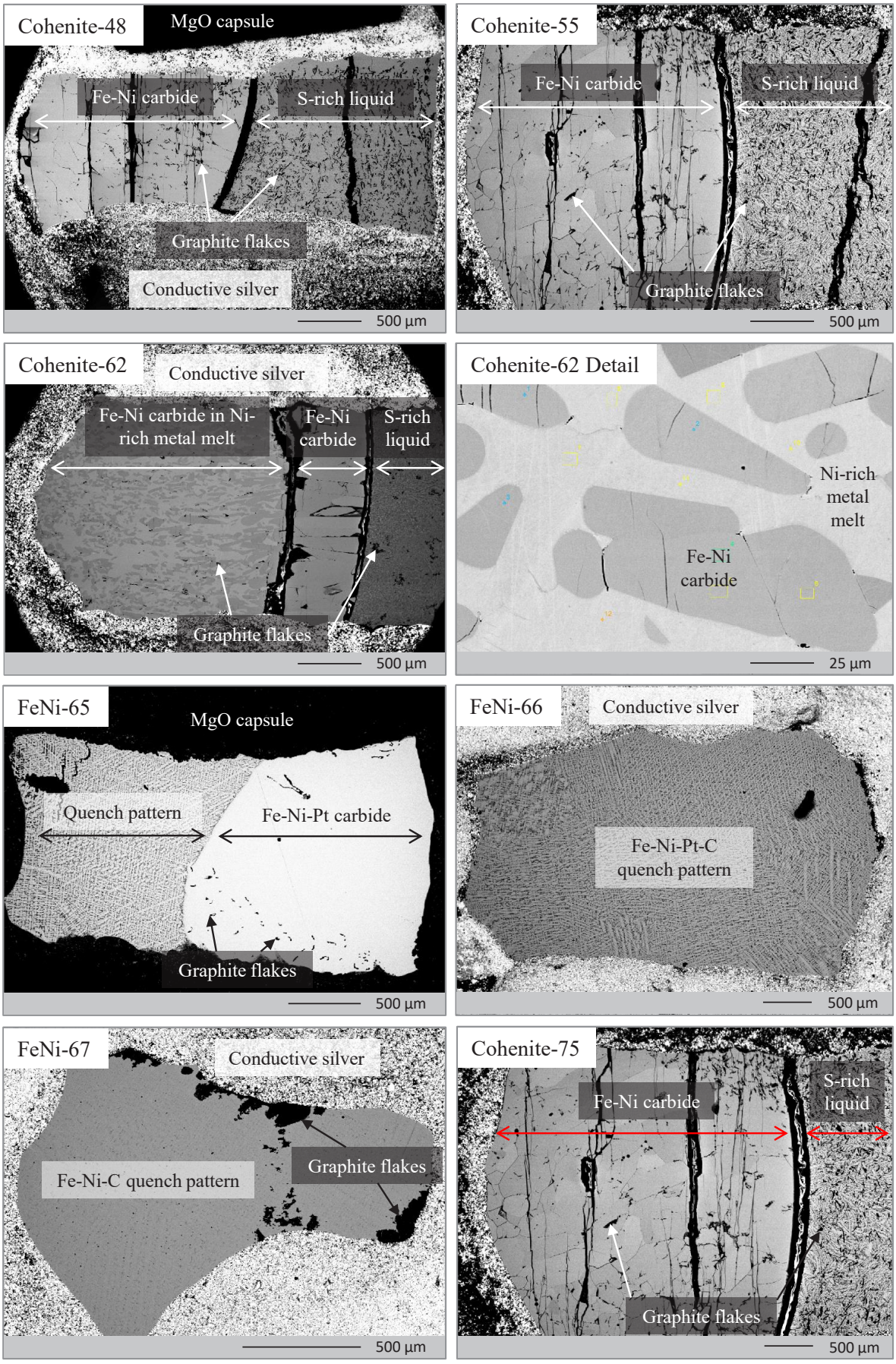

Fig. A.2 (continued). *Back-scattered electron images of metal melt experiments presented in Table A.2.*

A.3. Silicate melt - metallic melt equilibrium experiments

In this section, the experimental conditions, phase assemblages and BSE images of all silicate melt - metal melt experiments are presented in Table A.4 and Fig. A.3. The aim of these experiments was to equilibrate C-bearing silicate melt with C-bearing metallic melt to determine carbon partition coefficients between these two melts. In order to investigate the effect of temperature, pressure, oxygen fugacity, and melt depolymerisation on carbon partitioning, experiments were performed in a wide range of conditions (see Tables 3.2, 4.2 and A.4). The starting compositions are shown in Tables 2.1 and 2.2 in Chapter 2. The experiments displayed in italic in Table A.4 refer to successful experiments that were used to investigate the carbon partitioning and are further discussed in Chapters 3 and 4 of this thesis.

Most difficulties occurred due to the dissolution of the capsule material (i.e., San Carlos olivine), leading to a compositional shift so that olivine, ortho- or clinopyroxene crystallised. These crystals prevented the formation of large areas of glass and large metal droplets (> 50 μm), which are required for SIMS and bulk analyses. After adjusting the silicate melt compositions iteratively, homogeneous silicate glass in equilibrium with one or several metal droplets could be synthesised. Using other capsule materials like iridium or rhenium resulted in excessive iron loss owing to alloy formation. Therefore, San Carlos olivine, synthetic forsterite and graphite were found to be the most successful capsule materials for this kind of experiments. Further problems occurred in higher temperature experiments (≥ 1500°C) due to the formation of olivine quench needles within the silicate melt. These experiments could be analysed by SIMS across a raster of 50 × 50 μm to determine the C content of the silicate melt. Some experiments performed in graphite capsules at 6 GPa delivered euhedral graphite blades of ≤ 300 μm length. These graphite blades were carefully omitted during SIMS analyses.

Table A.4
List of silicate melt - metal melt equilibrium experiments.

Run #	T (°C)	P (GPa)	Duration	Capsule type	Starting Mix	Silicate/metal ratio	Centrifuge (C)/ static (S)	Ol	Opx	Cpx	Comment
5-SM-14	1450	3	12 h	Olivine-Pt	PB5+FN5	80/20	S	X			Not successful, because of too small FeNi-droplets for SIMS analyses (< 20 µm). Further, the crystallisation of olivine prevents the formation of large glassy areas.
5-SM-15	1450	3	2.5 h	Olivine-Pt	PB5+FN4	80/20	S	X		X	Not successful, because the crystallisation of olivine and cpx prevents the formation of large glassy areas that are required for SIMS analyses. Further, most FeNi-droplets are too small for SIMS analyses (< 20 µm).
6-SM-17	1450	3	2 h	Olivine-Pt	PB6+FS1	80/20	S			X	Not successful, because the crystallisation of cpx prevents the formation of large glassy areas that are required for SIMS analyses. Further, most FeSi-droplets are too small for SIMS analyses (< 20
7-SM-18	1450	3	2 h	Olivine-Pt	PB7+FN4	80/20	S	X			Not successful, because of too small FeNi-droplets for SIMS analyses (< 20 µm). Further, the crystallisation of olivine prevents the formation of large glassy areas.
7-SM-20	1450	3	2 h	Ir-Pt	PB7+FN4	80/20	S	X			Not successful, because of too small FeNi-droplets for SIMS analyses (< 20 µm). Outer part of the run product consists of homogeneous silicate melt. In the inner part, crystallisation of olivine prevents the formation of large glassy areas.
9-SM-22	1450	3	3 h	Ir-Pt	PB9+FN3	80/20	S			X	Not successful, because of too small FeNi-droplets for SIMS analyses (< 20 µm). Outer part of the run product consists of homogeneous silicate melt and quench. In the inner part, crystallisation of cpx prevents the formation of large glassy areas.
9-SM-23	1450	3	4 h	Ir-Pt	PB9+FN3	80/20	S				Not successful, because all metal was absorbed by the iridium capsule.
9-SM-24	1450	3	2 h	Re-Pt	PB9+FN3	80/20	S				Not successful, because all metal was absorbed by the Re foil and the Pt capsule.
9-SM-25	1450	3	2.5 h	dense Al_2O_3	PB9+FN3	80/20	S			X	Not successful, because the dissolution of the capsule material led to > 20 wt.% Al_2O_3 content of the silicate melt, which is no representative for magma ocean compositions.
10-SM-27	1450	3	2 h	Olivine-Pt	PB1+FN1	80/20	S				Successful, but the large FeNi-droplet was lost during polishing and the remaining droplets were too small to be analysed by SIMS.
9-SM-28	1450	3	2.5 h	Graphite	PB9+FN3	80/20	S			X	Successful, but finally not used for SIMS analyses due to the formation of cpx in the inner part of the capsule.
10-SM-29	1450	3	2 h	Ir-Pt	PB1+FN1	80/20	S				Not successful, because all metal was absorbed by the iridium capsule.
9-SM-30	1450	3	2.5 h	Graphite	PB9+FN3	80/20	S			X	Not successful, because the crystallisation of cpx prevents the formation of large glassy areas that are required for SIMS analyses.
10-SM-31	*1400*	*1.5*	*1.5 h*	*Olivine-Pt*	*PB1+FN1*	*80/20*	*S*				*Successful.*
10-SM-32	*1400*	*1.5*	*2 h*	*Olivine-Pt*	*PB1+FN1*	*80/20*	*C*				*Successful, repetition of run 10-SM-31 in centrifuge. Metal melt did not form a single metal droplet, but metal fragmemts were large enough to fit a 50 x 50 µm raster for SIMS analyses.*
10-SM-36	1400	1.5	4 h	Olivine-Pt	PB1+FN1	80/20	C	X			Not successful, because metal melt did not form a single metal droplet and metal fragmemts were too small to fit a 50 x 50 µm raster for SIMS analyses.
10-SM-37	*1400*	*1.5*	*1.5 h*	*Olivine-Pt*	*PB1+FN1*	*80/20*	*C*				*Successful, repetition of run 10-SM-32 but experiment was pre-equilibrated in a static piston*

Abbreviations: Ol = olivine, Opx = orthopyroxene, Cpx = clinopyroxene, Grt = garnet. Composition of the starting mixtures is displayed in Tables 2.1 and 2.2.

Table A.4 (continued)
List of silicate melt - metal melt equilibrium experiments.

Run #	T (°C)	P (GPa)	Duration	Capsule type	Starting Mix	Silicate/metal ratio	Centrifuge (C)/ static (S)	Ol	Opx	Cpx	Comment
11-SM-40	*1400*	*1.5*	*1.5 h*	*Olivine-Pt*	*PB2+F2*	*80/20*	*S*				*Successful. BSE image looks like the one of run 10-SM-31.*
11-SM-44	*1400*	*1.5*	*40 min*	*Olivine-Pt*	*PB2+F2*	*70/30*	*C*				*Successful. BSE image looks like the one of run 10-SM-31.*
1-BM-46	*1500*	*1.5*	*2 h*	*Olivine-Pt*	*HAB1+F2*	*70/30*	*S*				*Successful. BSE image looks like the one of run 10-SM-31.*
2-BM-49	*1500*	*1.5*	*2 h*	*Olivine-Pt*	*HAB2+F2*	*70/30*	*S*				*Successful. BSE image looks like the one of run 10-SM-31.*
2-BM-52	*1500*	*1.5*	*2 h*	*Olivine-Pt*	*HAB2+F2*	*70/30*	*C*	*X*			*Successful. Several metal droplets formed and olivine quench needles are present within the silicate melt, but melt pools are large enough (> 50 µm) for SIMS analyses.*
2-BM-54	*1500*	*1.5*	*2 h*	*Olivine-Pt*	*HAB2+F2*	*70/30*	*C*				*Successful. BSE image looks like the one of run 10-SM-31. Experiment was analysed for C content by SIMS and bulk method (LECO).*
10-SM-57	*1400*	*1.5*	*2 h*	*Olivine-Pt*	*PB1+FS2*	*80/20*	*S*				*Successful. BSE image looks like the one of run 10-SM-31.*
10-SM-60	1400	1.5	2 h	Olivine-Pt	PB1+FS2	80/20	C				Experiment fell apart while cutting the capsule with the diamond wire saw and was lost.
9-SM-61	1400	1.5	2 h	Olivine-Pt	PB9+FN1	70/30	S				Not successful. BSE image looks like the one of run 10-SM-31, but metallic and silicate melt were highly heterogeneous in composition.
11-SM-72	*1400*	*1.5*	*0.5 h*	*Olivine-Pt*	*PB2+F2*	*70/30*	*C*				*Successful. Experiment was analysed for C content by SIMS and bulk method (LECO).*
10-SM-77	*1500*	*1.5*	*1.75 h*	*Olivine-Pt*	*PB1+FS2*	*80/20*	*S*				*Successful. Several metal droplets formed and olivine quench needles are present within the silicate melt. 50 x 50 µm raster across the quench needles were analysed by SIMS.*
10-SM-78	*1600*	*1.5*	*0.5 h*	*Olivine-Pt*	*PB1+FS2*	*80/20*	*S*				*Successful. Several metal droplets formed and olivine quench needles are present within the silicate melt. 50 x 50 µm raster across the quench needles were analysed by SIMS. BSE image looks like the one of run 10-SM-77.*
10-SM-79	~1550	1.5	15 min	Olivine-Pt	PB1+FS2	80/20	S				Successful, but thermocouple broke during the experiment such that this experiment was excluded from further considerations. BSE image looks like the one of run 10-SM-77.
10-SM-80	*1700*	*1.5*	*20 min*	*Olivine-Pt*	*PB1+FS2*	*80/20*	*S*				*Successful. Olivine quench needles are present within the silicate melt. 50 x 50 µm raster across the quench needles were analysed by SIMS. BSE image looks like the one of run 10-SM-77.*
10-SM-81	1800	1.5	15 min	Olivine-Pt	PB1+FS2	80/20	S				Not successful, because Pt capsule was molten and formed an alloy with the metallic melt. Olivine capsule was mostly dissolved. No silicate glass, just olivine needles.
2-BM-83	*1500*	*1.5*	*2 h*	*Forsterite-Pt*	*HAB2+FS3*	*80/20*	*S*				*Successful.*
10-SM-84	*1300*	*1.5*	*3 h*	*Olivine-Pt*	*PB1+FS2*	*80/20*	*S*			*X*	*Successful. Several metal droplets formed together with some clusters of cpx crystals, but melt pools are large enough (> 50 µm) for SIMS analyses.*
2-BM-85	*1500*	*1.5*	*2 h*	*Forsterite-Pt*	*HAB2+FS4*	*80/20*	*S*				*Successful. BSE image looks like the one of run 2-BM-83.*
2-BM-86	*1500*	*1.5*	*2 h*	*Forsterite-Pt*	*HAB2+FS5*	*80/20*	*S*				*Successful. BSE image looks like the one of run 2-BM-83.*
10-SM-87	*1750*	*1.5*	*2 min*	*Olivine-Pt*	*PB1+FS2*	*80/20*	*S*				*Successful. Several metal droplets formed and olivine quench needles are present within the silicate melt. 50 x 50 µm raster across the quench needles were analysed by SIMS. BSE image looks like the one of run 10-SM-77.*

Abbreviations: Ol = olivine, Opx = orthopyroxene, Cpx = clinopyroxene, Grt = garnet. Composition of the starting mixtures is displayed in Tables 2.1 and 2.2.

Table A.4 (continued)
List of silicate melt - metal melt equilibrium experiments.

Run #	T (°C)	P (GPa)	Duration	Capsule type	Starting Mix	Silicate/metal ratio	Centrifuge (C)/ static (S)	Ol	Opx	Cpx	Comment
2-BM-88	*1900*	*3.5*	*2 min*	*Forsterite-Pt*	*HAB2+FS3*	*80/20*	*S*				*Successful. Several metal droplets formed and olivine quench needles are present within the silicate melt. 50 x 50 µm raster across the quench needles were analysed by SIMS. BSE image looks like the one of run 10-SM-77.*
10-SM-89	*1900*	*3.5*	*2 min*	*Graphite-Pt*	*PB1+FS2*	*80/20*	*S*				*Successful.*
10-SM-90	1500	1.5	2 h	Forsterite-Pt	PB1+FS2	80/20	S	X			Not succesful. Olivine crystallised and no larger glassy areas were present.
10-SM-91	*1500*	*1.5*	*2 h*	*Graphite-Pt*	*PB1+FS2*	*80/20*	*S*				*Successful. BSE image looks like the one of run 10-SM-89.*
2-BM-92	*1500*	*1.5*	*2 h*	*Olivine-Pt*	*HAB2+F1*	*70/30*	*S*				*Successful. BSE image looks like the one of run 10-SM-31.*
2-BM-93	~1200	1.5	2 h	Forsterite-Pt	HAB2+FS1	80/20	S		X	X	Not successful, because the thermocouple broke during the experiment. Temperature was probably not high enough and cpx and opx crystallised.
2-BM-94	<1500	1.5	0.5 h	Olivine-Pt	HAB2+FS1	80/20	S		X	X	Not successful, because the thermocouple broke during the experiment. Temperature was probably not high enough and cpx and opx crystallised. BSE image looks like the one of run 2-BM-93.
10-SM-95	*1400*	*1.5*	*1.5*	*Olivine-Pt*	*PB1+FN2*	*80/20*	*S*				*Successful. BSE image looks like the one of run 10-SM-31.*
2-BM-96	*1500*	*1.5*	*2 h*	*Forsterite-Pt*	*HAB2+FS1*	*80/20*	*S*				*Successful. BSE image looks like the one of run 2-BM-83.*
2-BM-97	*1500*	*1.5*	*2 h*	*Olivine-Pt*	*HAB2+FS1*	*80/20*	*S*				*Successful. BSE image looks like the one of run 10-SM-31.*
10-SM-98	~1850	10	15 min	Olivine-Pt	PB1+FS2	80/20	S			X	Not successful, because the thermocouple broke during the experiment. Composition of the silicate melt was too SiO_2-undersaturated to form a glass => olivine-normative melts are not quenchable.
10-SM-100	*1800*	*6*	*0.5 h*	*Graphite-Pt*	*PB1+FS2*	*80/20*	*S*				*Successful. BSE image looks like the one of run 10-SM-89.*
10-SM-101	1500	6	2 h	Graphite-Pt	PB1+FS2	80/20	S				Not successful, because the temperature was below the liquidus. No BSE image available.
10-SM-102	*1600*	*6*	*1 h*	*Graphite-Pt*	*PB1+FS2*	*80/20*	*S*				*Successful. Graphite blades were present which were carefully avoided during SIMS analyses.*
10-SM-103	*1750*	*1.5*	*20 min*	*Olivine-Pt*	*PB1+FS2*	*80/20*	*S*				*Successful. Olivine quench needles are present within the silicate melt. 50 x 50 µm raster across the quench needles were analysed by SIMS. BSE image looks like the one of run 10-SM-77. Pt capsule started to melt and migrated through the sample, which resulted in a contamination of the metal droplet by 18.14 ± 0.69 wt.% Pt.*
10-SM-107	*1720*	*6*	*0.5 h*	*Graphite*	*PB1+FS2*	*80/20*	*S*				*Successful. BSE image looks like the one of run 10-SM-89.*
10-SM-108	*1810*	*6*	*0.5 h*	*Graphite*	*PB1+FS2*	*80/20*	*S*				*Successful. BSE image looks like the one of run 10-SM-89.*
10-SM-109	*2000*	*6*	*12 min*	*Graphite*	*PB1+FS2*	*80/20*	*S*				*Successful. BSE image looks like the one of run 10-SM-89.*
10-SM-110	*1700*	*6*	*50 min*	*Graphite*	*PB1+FS2*	*80/20*	*S*				*Successful. Large areas of quench are present, but glassy areas were large enough (> 50 µm) for SIMS analyses.*
10-SM-111	*1865*	*6*	*20 min*	*Graphite*	*PB1+FS2*	*80/20*	*S*				*Successful. Large areas of quench are present, but glassy areas were large enough (> 50 µm) for SIMS analyses. BSE image looks like the one of run 10-SM-110.*
10-SM-112	*1600*	*6*	*1 h*	*Graphite*	*PB1+FS2*	*80/20*	*S*				*Successful. BSE image looks like the one of run 10-SM-89.*
10-SM-113	*1650*	*6*	*1 h*	*Graphite*	*PB1+FS2*	*80/20*	*S*				*Successful. Sample broke apart during polishing. Recovered fragments were large enough (> 50 µm) for SIMS analyses. No BSE image available.*

Abbreviations: Ol = olivine, Opx = orthopyroxene, Cpx = clinopyroxene, Grt = garnet. Composition of the starting mixtures is displayed in Tables 2.1 and 2.2.

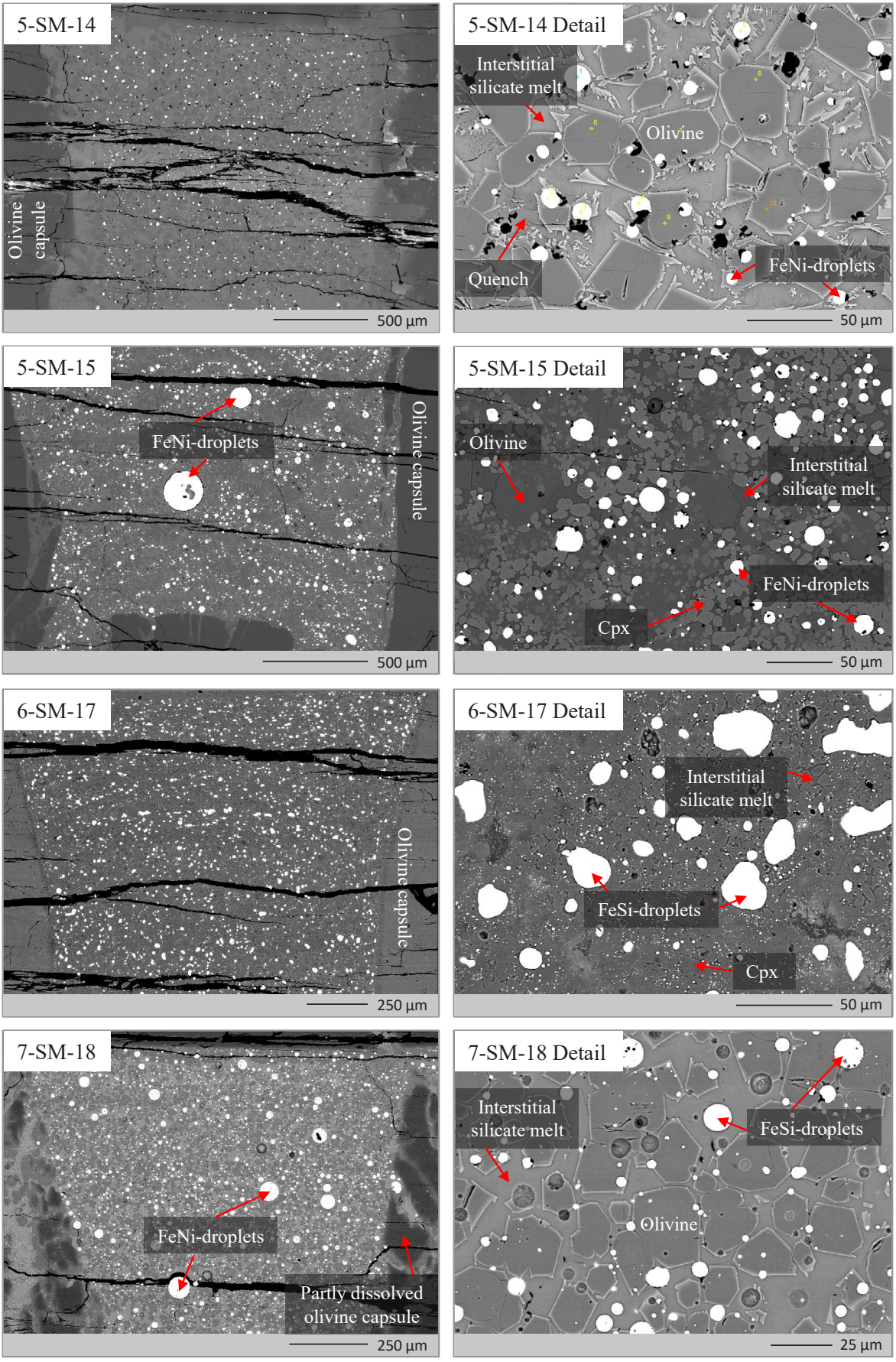

Fig. A.3. *Back-scattered electron images of silicate melt - metal melt experiments presented in Table A.4. Abbreviation: Cpx = clinopyroxene.*

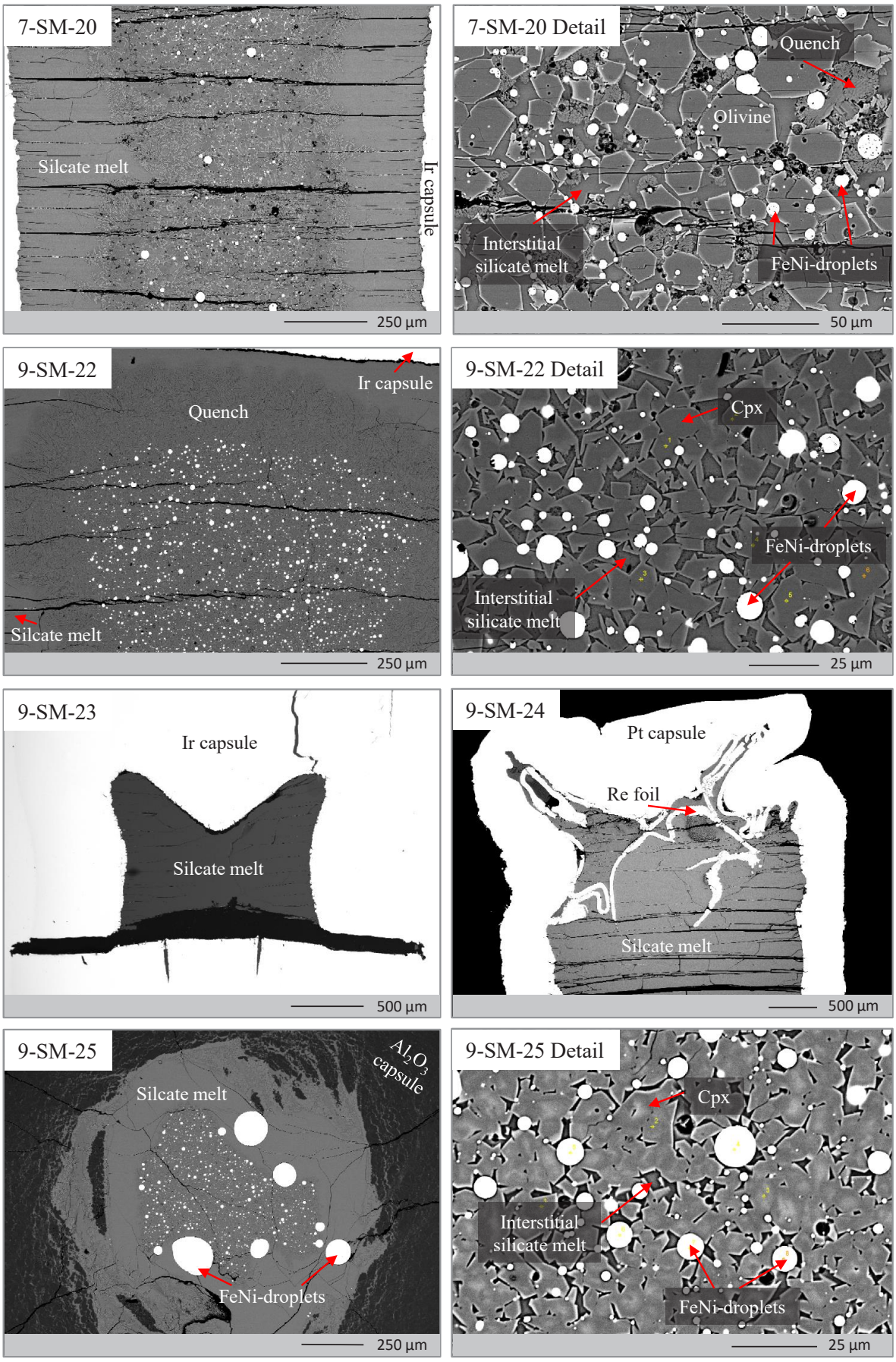

Fig. A.3 (continued). *Back-scattered electron images of silicate melt - metal melt experiments presented in Table A.4. Abbreviation: Cpx = clinopyroxene.*

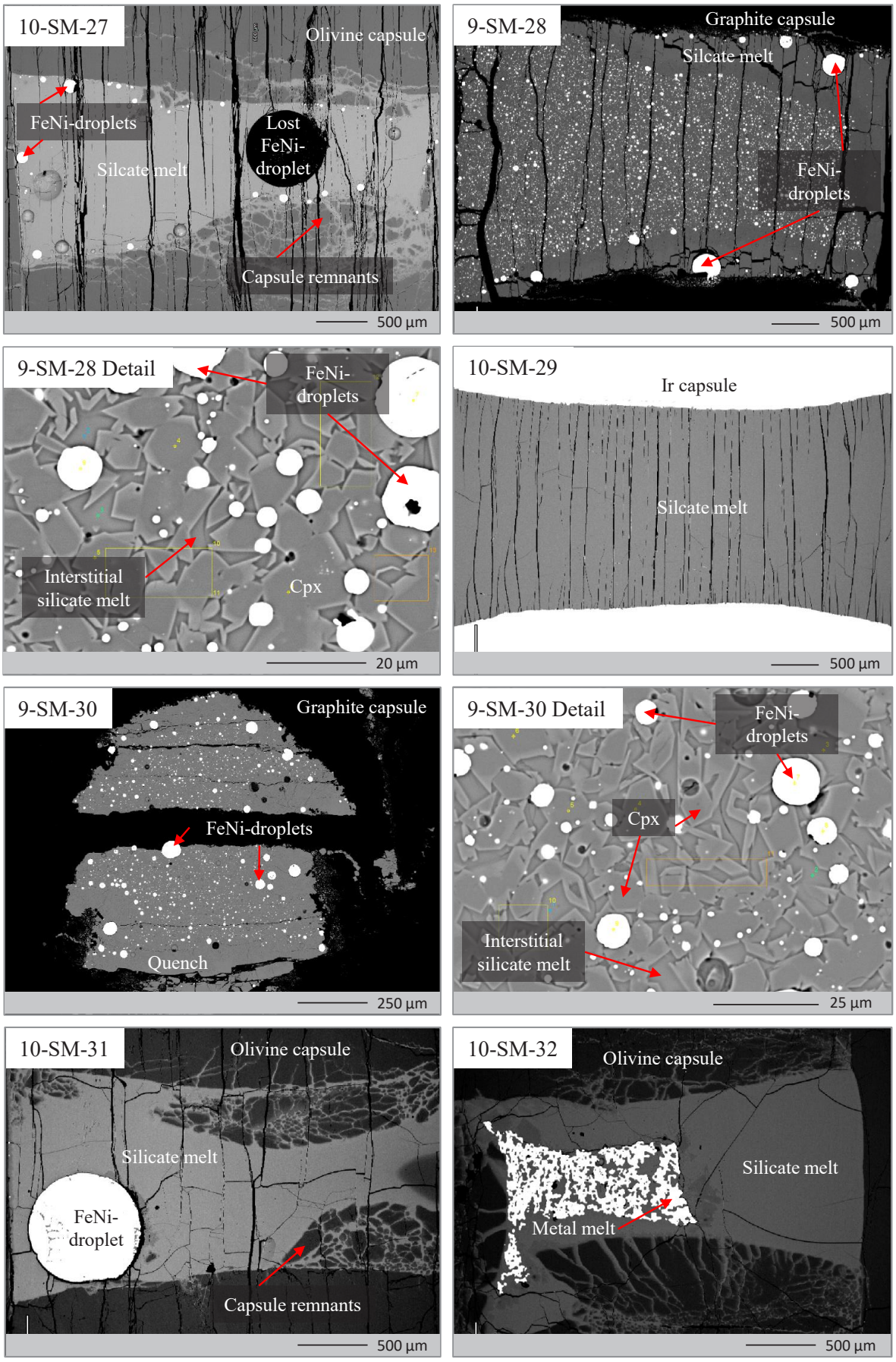

Fig. A.3 (continued). *Back-scattered electron images of silicate melt - metal melt experiments presented in Table A.4. Abbreviation: Cpx = clinopyroxene.*

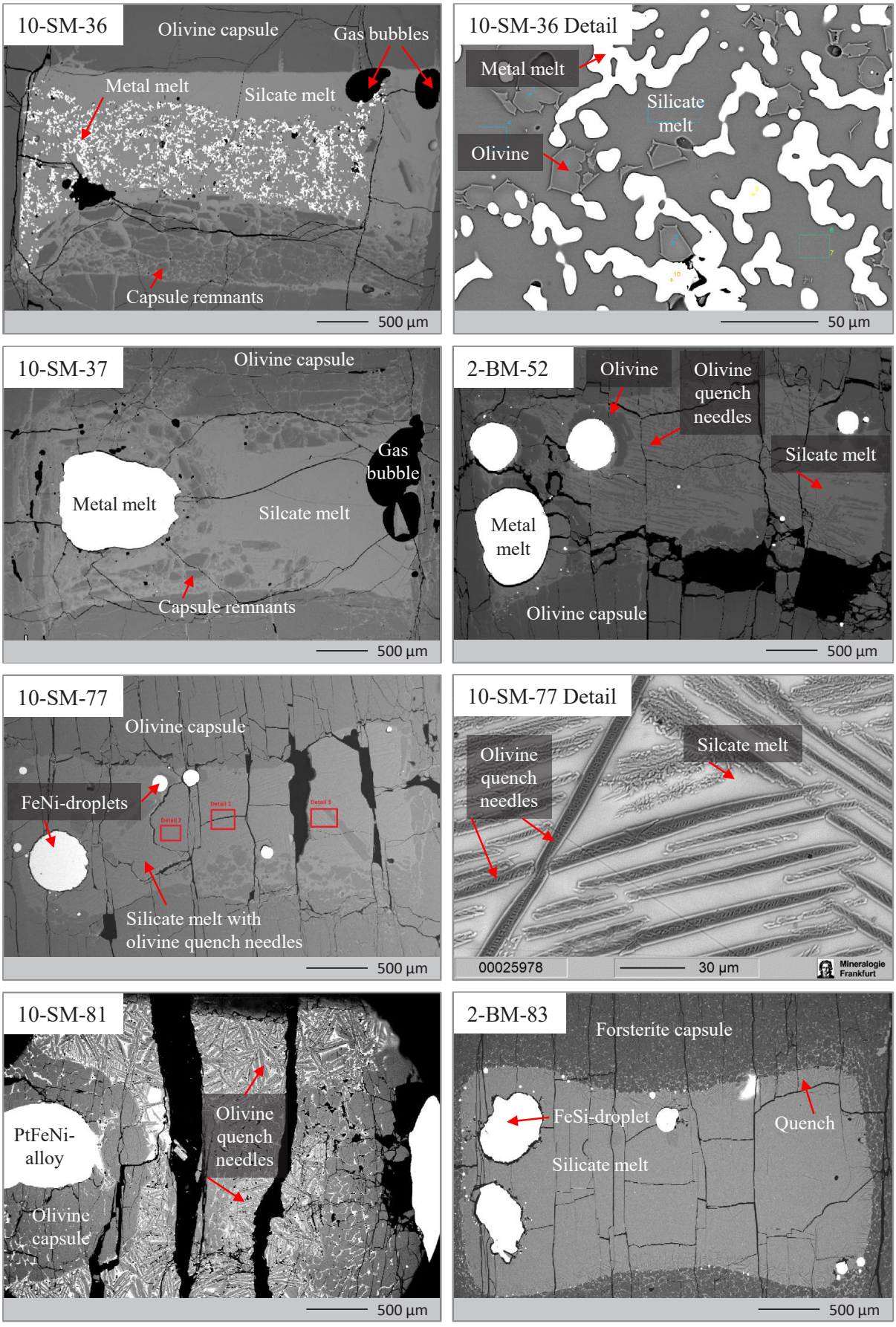

Fig. A.3 (continued). *Back-scattered electron images of silicate melt - metal melt experiments presented in Table A.4.*

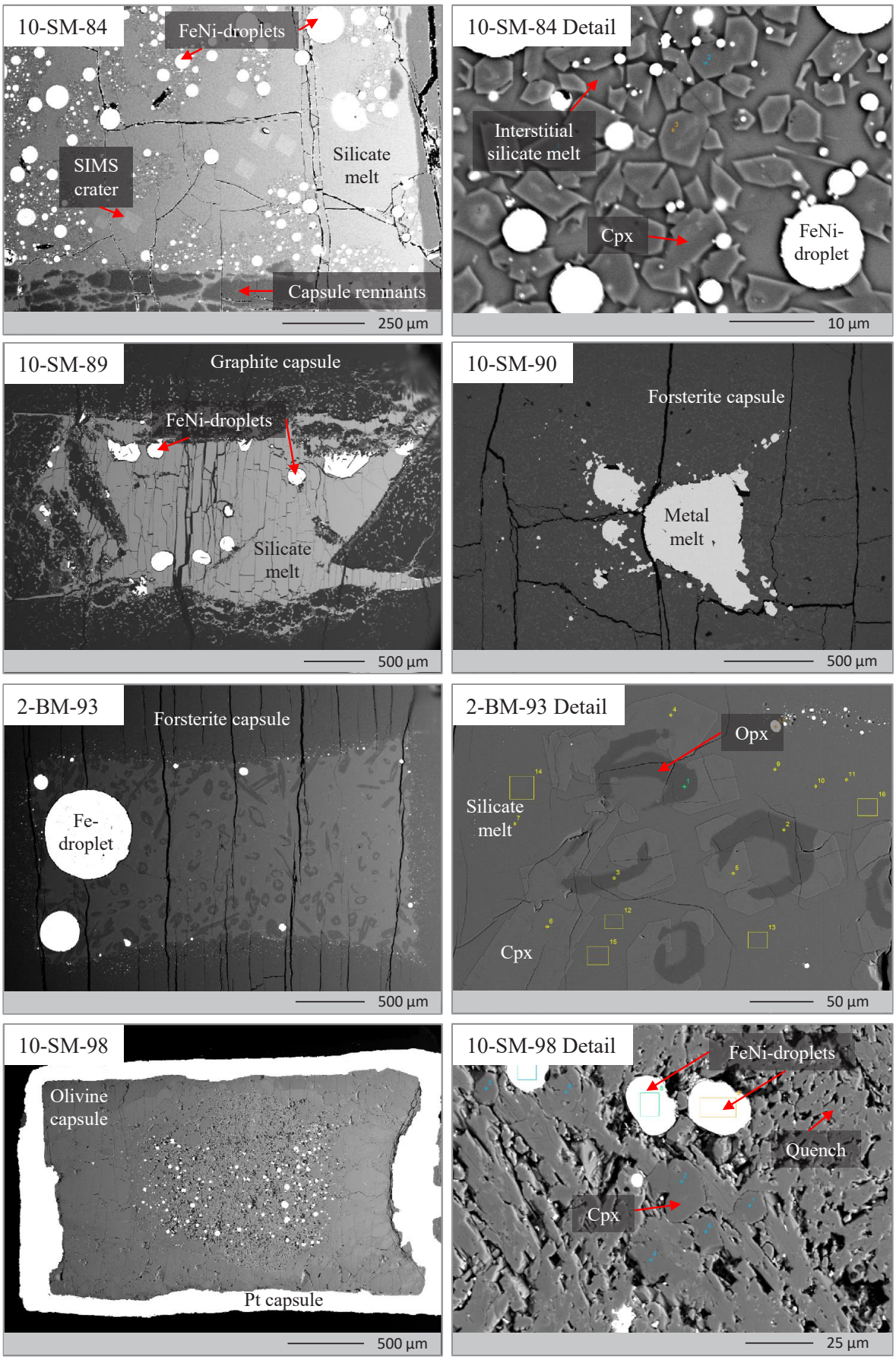

Fig. A.3 (continued). *Back-scattered electron images of silicate melt - metal melt experiments presented in Table A.4. Abbreviations: Opx = orthopyroxene, Cpx = clinopyroxene.*

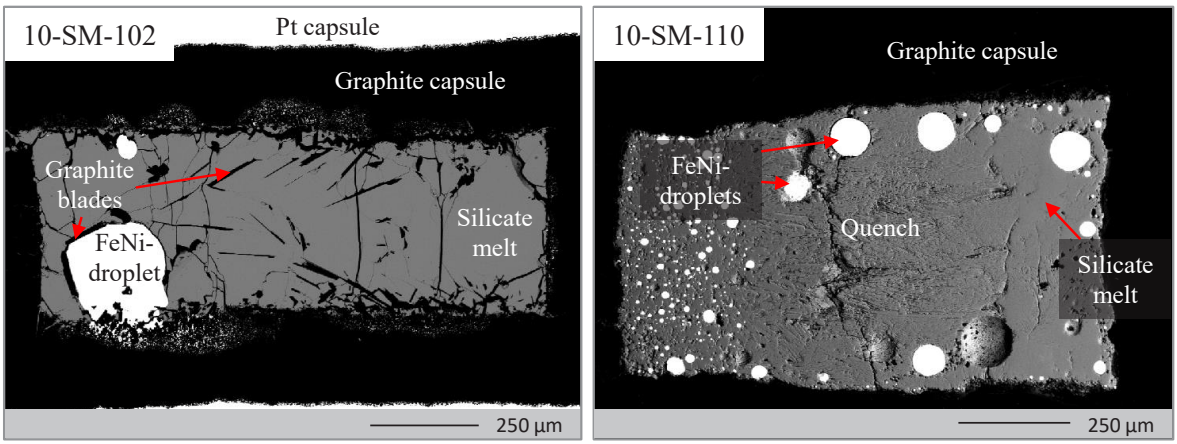

Fig. A.3 (continued). *Back-scattered electron images of silicate melt - metal melt experiments presented in Table A.4.*

APPENDIX B

Supplementary figures to Chapter 4

This Appendix consists of supplementary figures that are mentioned in Chapter 4. Please refer to the text in Chapter 4 for the context of the figures.

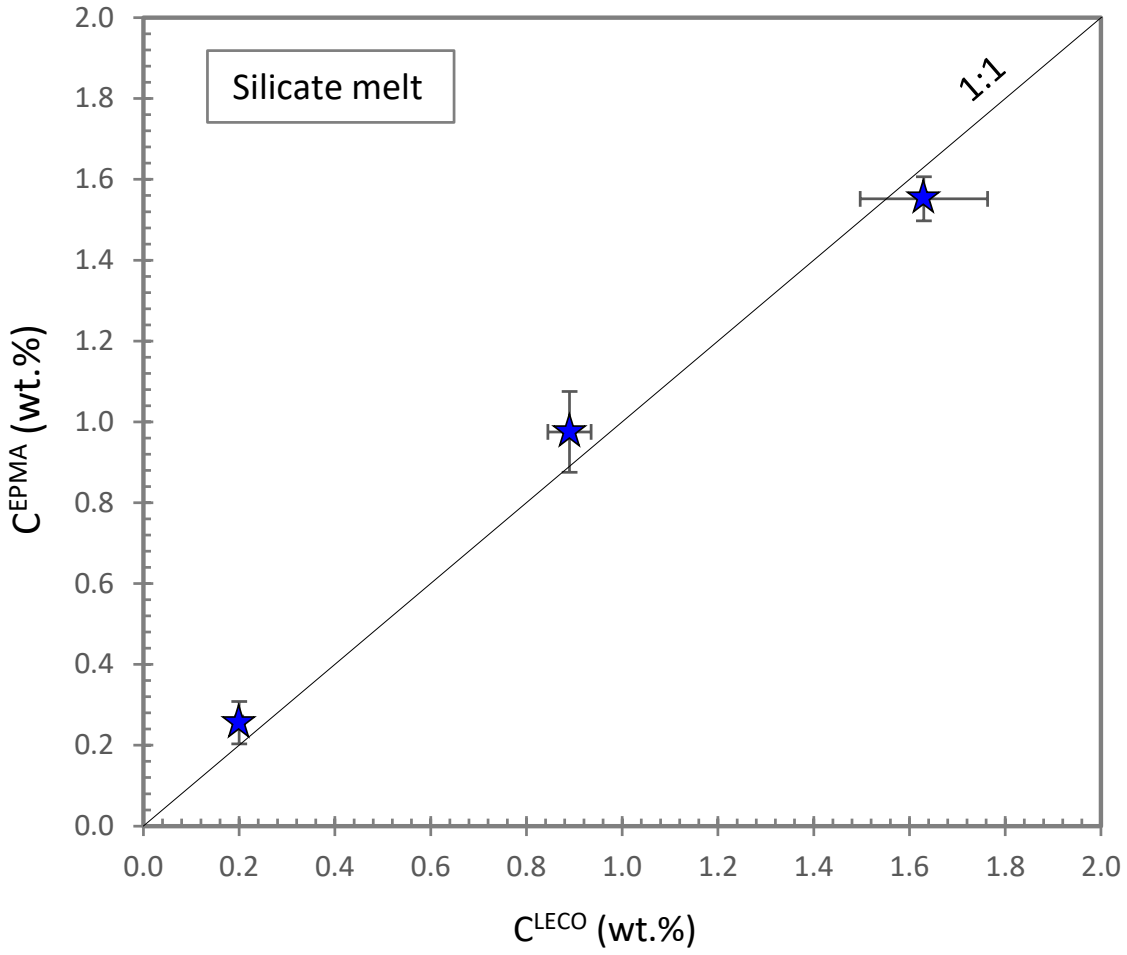

Fig. B.1. *Carbon contents of standard glasses used for SIMS analyses detemined by EPMA vs. C contents determined by a bulk elemental C analyser (LECO). For EPMA analyses, samples were coated with an 8 nm thick layer of aluminium. Analytical conditions were 20 nA beam current and 15 kV acceleration voltage. Analytical conditions for the bulk analyses is described in detail in section 2.2.3. The solid line represents the 1:1 line. Errorbars represent the standard deviation (1σ) based on replicate measurements.*

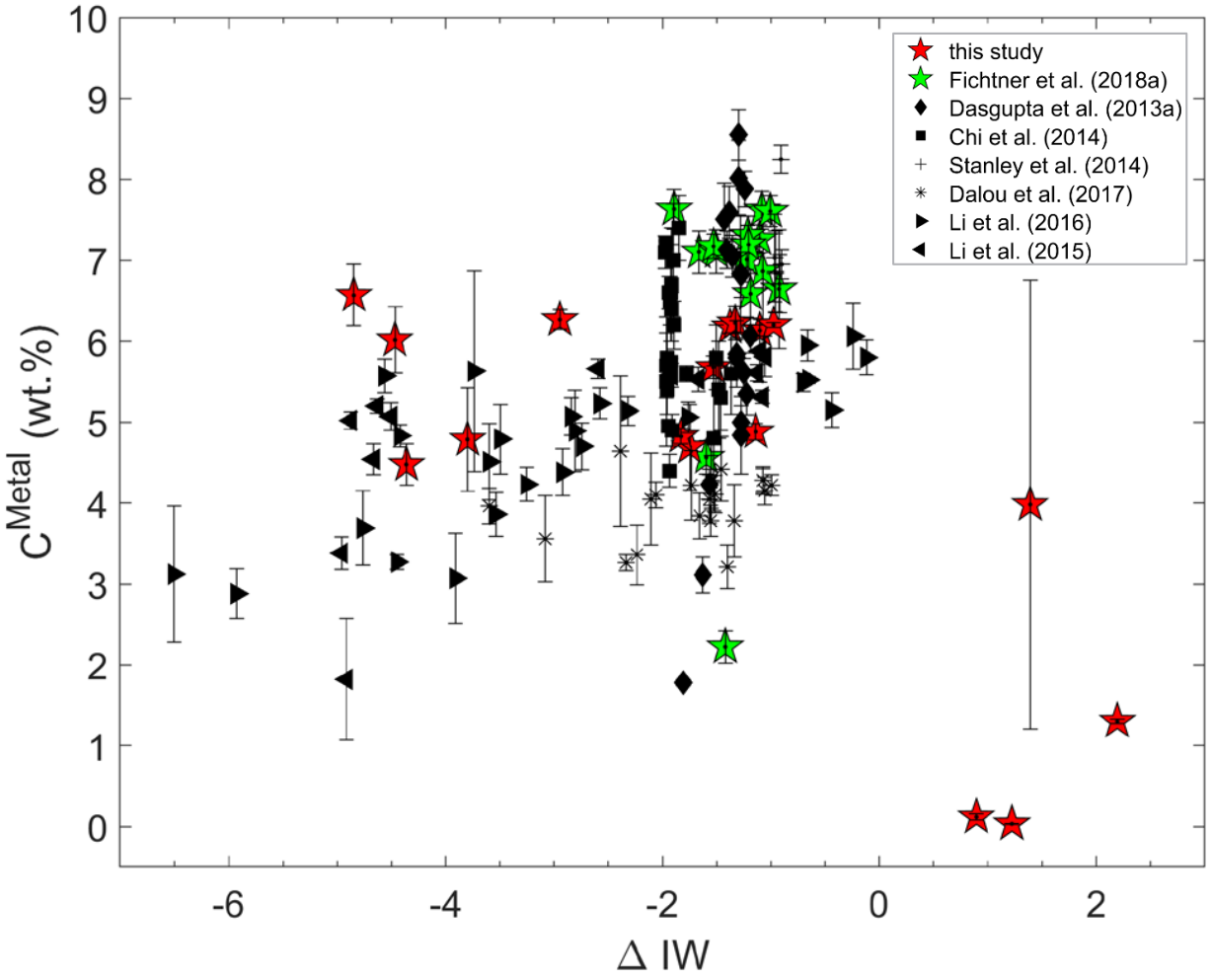

Fig. B.2. *Carbon concentrations of the metal melt vs. oxygen fugacity (ΔIW). There is no systematic variation of* C^{metal} *with* fO_2 *across all datasets with the exception of the Ni-rich (ΔIW > 0) and Si-rich metals (ΔIW < -3).*

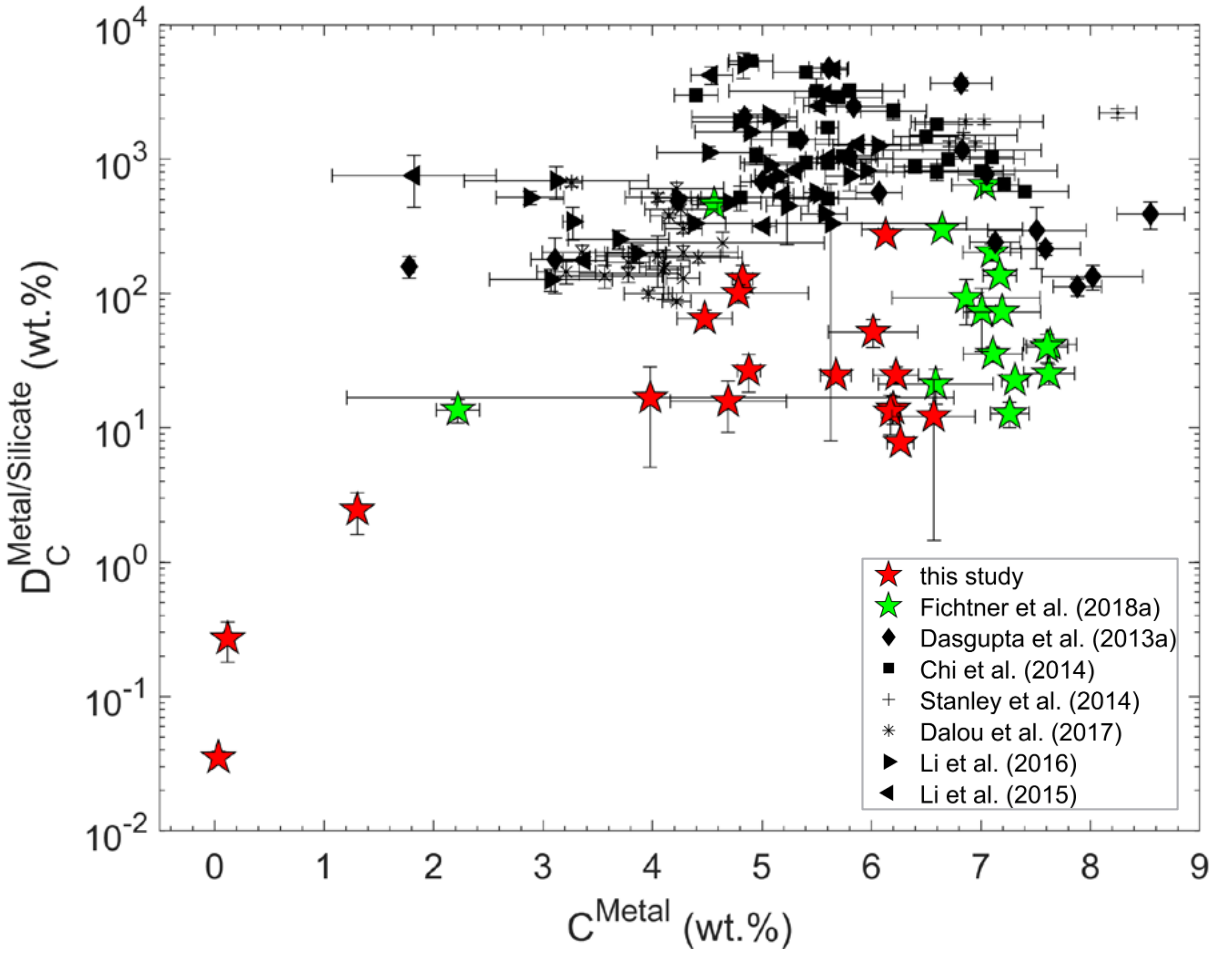

Fig. B.3. *$D_C^{metal/silicate}$ as a function of C content of the metal melt. $D_C^{metal/silicate}$ is little affected by C^{Metal}, except for the Ni-rich experiments, where $D_C^{metal/silicate}$ appears to correlate negatively with Ni content and positively with C^{Metal}.*

APPENDIX C

Constraining parameterisation coefficients by Monte Carlo sampling

C.1. Problem statement: Constraining uncertain coefficients

In this Appendix, a Monte Carlo method to constrain the coefficients *a* to *f* in the parameterisation

$$\ln\left[D_C^{\frac{metal}{silicate}}\right] = \frac{a}{T} + \frac{b \times P}{T} + c \times \ln(fO_2) + d \times \left(\frac{NBO}{T}\right) + e \times \ln(1 - X_{Ni}) + f \times \ln(1 - X_{Si}) \qquad \text{(C.1)}$$

is described. In addition to finding a set of coefficients, that fits the observed data optimally, it is required to quantify uncertainties. This is intended to provide answers to key questions concerning the reliability of our parameterisation and the extrapolation to P-T-conditions not covered in the experiments: How well constrained are the coefficients? Can the coefficients be constrained independently from each other, or does the choice of one coefficient affect the choice of another one? Is there potentially a completely different set of coefficients that explain the observations equally well but may lead to a very different extrapolation and subsequent alternative interpretation of the experimental data?

By trying to quantify uncertainties, we significantly expand the method of Chi et al. (2014), while still using their coefficients as a first guess. Contrary to Chi et al. (2014), we do not search deterministically for one optimal solution. Instead, we employ a probabilistic search, accounting for the fact that coefficients are inherently uncertain, and that multiple near-optimal solutions may exist.

C.2. Probability densities

Our task fits ideally into the well-established framework of probabilistic or Bayesian inference (e.g. Tarantola, 2005). Instead of finding one (possibly non-unique) set of coefficients, we aim to express all our knowledge about the coefficients in terms of probability densities *p*. Assuming, for instance, that *p(a)* is the probability density for coefficient *a*, then the probability *P* of *a* being between some values a_1 and a_2 is given by

$$P(a_1 < a < a_2) = \int_{a_1}^{a_2} p(a)\, da. \qquad \text{(C.2)}$$

The coefficient *a* is well constrained, when *p(a)* is rather peaked around a specific value. Otherwise, when *p(a)* is rather broad, the coefficient *a* is poorly constrained by the observations, meaning that its probability is similar for potentially very different values (Fig. C.1).

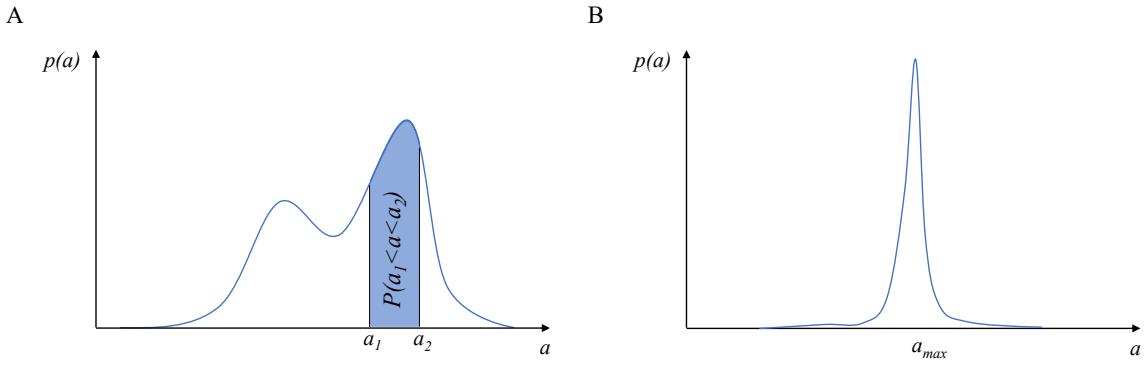

Fig. C.1. *Schematic illustration of probabilities and probability densities.* ***A:*** *Probability density* p(a) *for the parameter* a*. The probability of a being located between some values* a_1 *and* a_2 *is equal to the integral of* p(a) *from* a_1 *to* a_2*, that is, the shaded area under the curve.* ***B:*** *While the probability density shown in (A) indicates that* a *may plausibly vary over a rather wide range, this probability density is more peaked, suggesting that plausible values of* a *are confined to a narrow interval around* a_{max}.

C.3. Monte Carlo sampling - The Metropolis-Hastings algorithm

An expression for the probability density *p* cannot be derived analytically, i.e., in the form of a closed mathematical formula. Instead, it needs to be approximated by Monte Carlo sampling, where many sets of coefficients (a^i, ..., f^i), with *i=1, ..., N*, are drawn randomly and then tested against the observations.

The family of Monte Carlo methods that is suitable for our task is large, including algorithms with variable levels of sophistication and speed of convergence. Here, in the interest of simplicity and robustness, we employ the classical Metropolis-Hastings algorithm in the variant described by Sambridge & Mosegaard (2002). For completeness, we restate their algorithm in the context of our specific problem.

1. Initialisation

We use the coefficients (a^0, ..., f^0) proposed by Chi et al. (2014), and $f^0=0$ in order to compute a first set of partition coefficients $D_{c_k}^0$ via modelling equation (C.1) for all observations *k=1, ..., n*. This is then used to compute the initial misfit χ_0 by evaluating the equation

$$\chi_0 = \frac{1}{n}\sum_{k=1}^{n}\left|\frac{D_{C_k}^0 - D_{ck}^{measured}}{D_{C_k}^{1\sigma}}\right| \tag{C.3}$$

2. Random test models

Following the initialisation, we compute a random set of coefficients (a^1, ..., f^1), using a random number generator that produces normally distributed coefficients. As mean values for the normal (Gaussian) distribution, we use the coefficients proposed by Chi et al. (2014), and *0* for coefficient *f* that we added to Chi et al.'s original equation. As standard deviations, we choose very large values in order to ensure that the algorithm does not miss any plausible set of coefficients that may be far from the ones proposed by Chi et al. (2014).

3. Metropolis rule

Using the randomly generated set of coefficients, we compute a new set of partition coefficients $D_{c_k}^1$ via equation (C.1) and the corresponding misfit χ_1 via equation (C.3). At this point, we distinguish two cases:

a) If $\chi_1 < \chi_0$, i.e., when the newly proposed misfit is smaller than the initial one, the new set of coefficients (a^1, ..., f^1) is accepted.

b) Otherwise, i.e., when the newly proposed misfit is larger than the initial one, the new set of coefficients is accepted with probability χ_0 / χ_1 only. Thus, if the new misfit χ_1 is just slightly larger than the initial one, χ_0, the probability of accepting the test coefficients is still rather large (close to 1). Otherwise, if the misfit is much larger, it is unlikely to be accepted. Computationally, this probabilistic acceptance of a set of coefficients is again implemented using a random number generator[1].

[1] This can be imagined like a computer programme throwing dice. Assume, for illustration that $\chi_0 / \chi_1 = 0.9$, meaning that the new misfit is indeed larger than the initial one. The random number generator producing uniformly distributed random numbers between 0 and 1 act like a dice with many faces, not numbered 1 to 6, but numbered from 0 to 1 in many small steps. When throwing the dice produces a number between 0 and 0.9 - which statistically happens with 90 % probability - the new set of coefficients is accepted. Otherwise, i.e., when the dice produces a number between 0.9 and 1, the new coefficients are rejected.

[2] In practice, convergence means that adding new iterations does not change the histograms significantly. In more sophisticated implementations of Monte Carlo algorithms, convergence could be checked automatically. Here, in the interest of simplicity, we decided to manually test how many iterations are needed in order to obtain stable results, i.e. histograms that are the same, no matter if many more iterations are added or not.

4. Iteration

If a set of coefficients has been accepted, then it is treated as the new initial set of coefficients, and we go back to step 2 of the algorithm. Otherwise, if the proposed model is not accepted (rejected), the original initial model is re-used, and we also proceed again from step 2. This iteration is repeated until the set of test models has converged[2] to a sufficiently stable distribution. Finding a suitable number of test models that ensures convergence requires some unavoidable trial and error.

C.4. Histograms

The Metropolis-Hastings algorithm approximates the probability densities *p* with histograms. For instance, the probability density of coefficient *a* within a range from a_1 to a_2 can simply be obtained by counting the number of test coefficients that fell into this interval during the Metropolis-Hastings sampling (Fig. C.2).

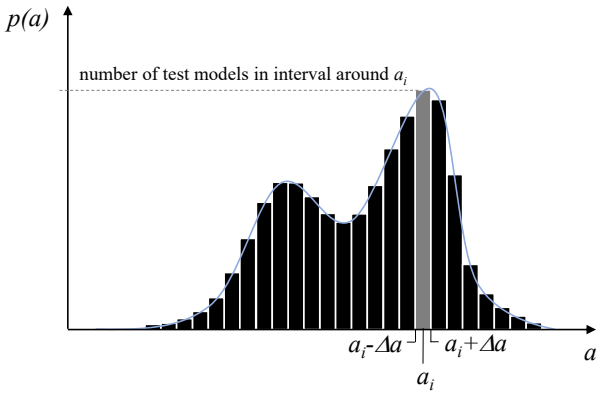

Fig. C.2. *Schematic illustration of the result of Monte Carlo sampling. The probability density* p(a) *is approximated by a histogram that counts the number of test models (randomly drawn sets of coefficients) that fall within predefined interval bins. For instance, the probability density* $p(a_i)$ *is approximated by the number of test models falling into the interval from* a_i-Δa *to* a_i+Δa*, shown as grey bar.*

Similarly, one may compute joint probability densities for a pair of coefficients, e.g., *p(a,b)* for the pair of coefficients *a* and *b*. From the ensemble of test coefficients, the joint probability density is again obtained by simply counting how many test coefficients a^i and b^i are positioned inside a certain two-dimensional domain $[a_1, a_2]\times[b_1, b_2]$.

The two-dimensional probability densities contain information about the dependence of a pair of coefficients. For instance, when *p(a,b)* is nearly circular in shape, the two coefficients are said to be independent. This means, that a plausible value for *a* is independent of how a plausible value for *b* has been chosen. This specific case can be exemplarily seen in Fig. C.2A, coefficient pair *a (T)* and $f(X_{Si})$.

Conversely, when *p(a,b)* is strongly skewed, choosing a plausible value for a pre-determines plausible values for *b*. The coefficients are then said to be dependent. This specific case is exemplarily shown in Fig. C.3B, coefficient pair *a (T)* and *d (NBO/T)*.

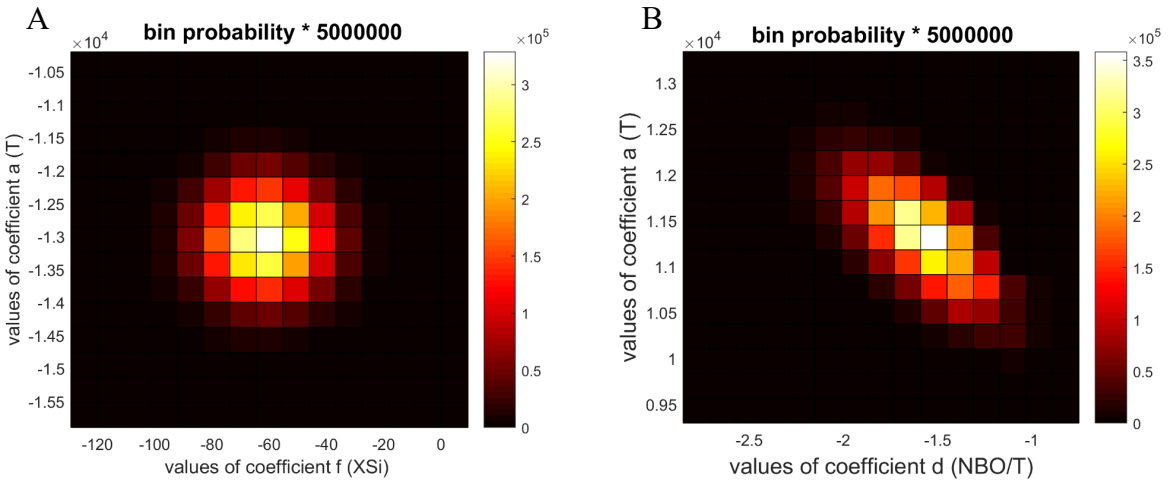

Fig. C.3. *Two-dimensional probability densities between pairs of coefficients of equation (C.1) to demonstrate their trade-offs.* ***A:*** *coefficient pair* a (t) *and* f (X_{Si}) *and* ***B:*** *coefficient pair* a (T) *and* d (NBO/T).

One generally needs to be careful with the interpretation of dependence. Fundamentally, it means that coefficients in the parameterisation cannot be determined independently, i.e., that they always have to be considered in pairs. The dependence of two coefficients, i.e., *a* for *T* and *d* for *NBO/T* as in the example above, provides an indication that also the two corresponding parameters, *T* and *NBO/T* may be dependent. However, this is merely an indication that should not be over-interpreted, but that may deserve further investigation.

APPENDIX D

Core formation scenarios

These notes describe scenarios for the evolution of the carbon content of the Earth's core. They are based on a sequence of impacts where the impactor either equilibrates with a magma ocean or directly transfers its core into the core of the current Earth. In our description, we proceed as follows: First, we summarise the two basic scenarios in words, already introducing some of the basic symbols. Subsequently, we provide a mathematical description of the scenarios.

D.1. Scenarios

For simplicity, we start with a single impact, before later considering a sequence of them. The impactor of mass Δm hits the Earth at some point in time when the Earth has a mass m. Lacking more detailed knowledge, we assume that the mass of the Earth's core is $^1/_3\, m$, and the mass of its mantle is $^2/_3\, m$. For the impactor, we assume the same ratio, meaning that the mass of its core is $^1/_3\,\Delta m$, and the mass of its mantle is $^2/_3\,\Delta m$. Obviously, this distinction only matters in those scenarios where the core of the impactor remains intact, without being assimilated into the magma ocean.

The current Earth of mass m has a C concentration of C_{Si} (in kg/kg) in its mantle, averaged over the solid and fluid parts. The C concentration in the current core is C_{Fe}. Similarly, we denote the C contents of the impactor's mantle and core by C_{Si} and C_{Fe}, respectively. Based on our previous assumption that the mass distributions between core and mantle are 1 : 2, we find that the average C concentrations of the Earth and the impactor are

$$C = \frac{1}{3} C_{\mathrm{Fe}} + \frac{2}{3} C_{\mathrm{Si}}\,, \tag{D.1}$$

and

$$\Delta C = \frac{1}{3} \Delta C_{\mathrm{Fe}} + \frac{2}{3} \Delta C_{\mathrm{Si}}\,, \tag{D.2}$$

respectively. With this notation established, we now introduce the two basic scenarios:

D.1.1 No equilibration between impactor and magma ocean

In this scenario we assume that the core of the impactor directly joins the Earth's core, not leaving enough time to establish an equilibrium between the magma ocean and the impactor's core. This means that the carbon of the impactor's core is added directly to the carbon of the current Earth, and

the two cores then mix perfectly. Similarly, we assume that the mantles of Earth and the impactor mix directly after the impact.

D.1.2 Full equilibration between impactor and magma ocean

At the other end of the spectrum, we consider a scenario where the impactor's core melts and sinks to the base of the magma ocean. There it has sufficient time to establish an equilibrium with the surrounding magma ocean before it sinks through the solid mantle of the Earth into its core. Following this process, we assume that there is enough time for the magma ocean and the solid mantle to mix, so as to establish a nearly homogeneous carbon concentration.

D.2. Mathematical description

The basic idea of the mathematical formulation of these scenarios is to first consider only one impact that follows one of the two basic scenarios. What we need to find is a set of equations that translate the current mass of the Earth, m, the current C concentration of the mantle, C_{Si}, and the current C concentration of the core, C_{Fe}, into the new mass of the Earth m', the new C concentration of the mantle, C'_{Si}, and the new C concentration of the core, C'_{Fe}.

D.2.1 No equilibration between impactor and magma ocean

The case where no equilibration takes place at all is arguably the simplest one. The total mass of carbon contained in the new mantle is $^2/_3\, m\, C_{Si} + {}^2/_3\, \Delta m\, \Delta C_{Si}$. Dividing this by the new total mass of the mantle, $^2/_3\, m + {}^2/_3\, \Delta m$, we obtain the new concentration of carbon in the mantle,

$$C'_{\mathrm{Si}} = \frac{m C_{\mathrm{Si}} + \Delta m\, \Delta C_{\mathrm{Si}}}{m + \Delta m}\,. \tag{D.3}$$

Analogously, the new carbon concentration in the core is

$$C'_{\mathrm{Fe}} = \frac{m C_{\mathrm{Fe}} + \Delta m\, \Delta C_{\mathrm{Fe}}}{m + \Delta m}\,. \tag{D.4}$$

The new mass of the Earth is

$$m' = m + \Delta m\,. \tag{D.5}$$

With equations (D.3) to (D.5) we can define an iteration where the left-hand sides of the equations serve as initial state of the Earth prior to the next impact.

D.2.2 Full equilibration between impactor and magma ocean

Following the impact, the molten core of the impactor with mass $^1/_3\,\Delta m$ is in contact with the molten magma ocean with mass m_m. We can estimate m_m based on assumptions of the magma ocean depth and density, following the ideas in section D.3.2. Thus, the total mass of carbon that we can now distribute between the fluid metal (formerly the core of the impactor) and the magma ocean is given by

$$m_c = m_m C_{\mathrm{Si}} + \Delta m\, \Delta C\,. \tag{D.6}$$

Of the total mass available, a fraction x adds to the magma ocean, and the remaining fraction $(1 - x)$ enters the fluid metal. Taking into account that the total mass of the new magma ocean is now $m_m + {}^2/_3\,\Delta m$, we find that the new carbon concentration in the magma ocean is

$$C_m = \frac{x\, m_c}{m_m + \frac{2}{3}\Delta m}\,. \tag{D.7}$$

Similarly, we find the carbon concentration in the fluid metal that has accumulated at the base of the magma ocean,

$$C_c = \frac{(1-x)\, m_c}{\frac{1}{3}\Delta m}\,. \tag{D.8}$$

The two concentrations are assumed to be in equilibrium, described by the partition coefficient D_C, that is,

$$D_c = \frac{C_c}{C_m} = \frac{1-x}{x}\,\frac{3m_m + 2\Delta m}{\Delta m}\,. \tag{D.9}$$

Solving for x, we have

$$x = \frac{3m_m + 2\Delta m}{\Delta m\, D_c + 3m_m + 2\Delta m}\,. \tag{D.10}$$

The partition coefficient is a function of pressure, P, and temperature, T. A procedure to estimate P at the base of the magma ocean is described in section D.3.3. Assuming pressure in GPa, we estimate temperature in°C as (Bourdon et al., 2018)

$$T = 1700.0 + 28.57\, P\,. \tag{D.11}$$

From equations (D.6) to (D.10) we deduce that the total mass of carbon moving into the core is $(1 - x)$ m_c, with m_c from equation (D.6) and x from equation (D.10). Adding to this the total mass of carbon already present in the core, $^1/_3\, C_{Fe}\, m$ and dividing by the new mass of the core, $^1/_3\, m + {}^1/_3\, \Delta m$, we obtain the new carbon concentration of the core after the impact,

$$C'_{\mathrm{Fe}} = \frac{C_{\mathrm{Fe}} m + 3(1-x) m_c}{m + \Delta m} \,. \tag{D.12}$$

Follwing the same logic, we find the carbon concentration of the new mantle after the impact and after the magma ocean has re-equilibrated with the solid mantle. The total mass of carbon in the new magma ocean is xm_c, and the total mass of cabon in the remaining solid mantle is $(^2/_3\, m - m_m)\, C_{Si}$. Dividing this by the new total mass of the mantle, $^2/_3\, m + {}^2/_3\, \Delta m$, we find

$$C'_{\mathrm{Si}} = \frac{3x\, m_c + (2m - 3m_m) C_{\mathrm{Si}}}{2\,(m + \Delta m)} \,. \tag{D.13}$$

With equations (D.12) and (D.13) we can now iterate, meaning that we may take the new concentrations as initial concentrations prior to the next impact.

D.3. Little helper calculations

D.3.1 The radius of the current Earth

All our calculations only involve masses. However, we also need the radius r of the current Earth in order to compute, for instance, the volume of the magma ocean or the pressure at the base of the magma ocean. To compute a radius, we assume that the Earth at any stage of its evolution had the same average density that it has today, that is, $\rho = 5510$ kg/m^3. We then have for the volume of the Earth

$$V = \frac{m}{\rho} = \frac{4}{3}\pi r^3 \,. \tag{D.14}$$

Rearranging equation (D.14), we find an estimate for the radius of the Earth

$$r = \left(\frac{3m}{4\pi\rho}\right)^{\frac{1}{3}} \,. \tag{D.15}$$

D.3.2 The mass of the magma ocean

To compute the partitioning of carbon between the magma ocean and the impactor's core, we need the mass of the magma ocean. Assuming that the depth of the magma ocean is h, its volume, V, is given as the difference between the volume of the Earth with radius r and the volume of sphere with radius $r - h$, that is,

$$V = \frac{4}{3}\pi r^3 - \frac{4}{3}\pi (r-h)^3 \,. \tag{D.16}$$

Furthermore assuming that the depth of the magma ocean is always a constant fraction, γ, of the current Earth's radius, that is,

$$h = \gamma r \,, \tag{D.17}$$

we have

$$V = \frac{4}{3}\pi r^3[1-(1-\gamma)^3] \,. \tag{D.18}$$

With the average density of molten peridotite, ρ_m = 4000 kg/m^3, we find an estimate for the mass of the magma ocean,

$$m_m = \frac{4}{3}\pi \rho_m r^3[1-(1-\gamma)^3] \,. \tag{D.19}$$

D.3.3 Pressure at the base of the magma ocean

To compute pressure at the base of the magma ocean, we first estimate the radius, *r*, of the current Earth, following section D.3.1. Though we do not know the precise distribution of mass inside the current Earth, we can compute the gravitational acceleration, *g* at its surface by lumping all its mass, *m*, into a point at its centre using the universal law of gravitation,

$$g = G\frac{m}{r^2} \,, \tag{D.20}$$

where *G* is the gravitational constant. For the current Earth, *g* happens to be roughly constant throughout the mantle. Therefore, we can approximate the pressure at the base of the magma ocean, that is, at depth *h*, as

$$P = \rho_m g h \,. \tag{D.21}$$

Bibliography

Abe, Y. (1997) Thermal and chemical evolution of the terrestrial magma ocean. Physics of the Earth and Planetary Interiors 100, 27-39.

Allègre, C., Manhès, G. and Lewin, É. (2001) Chemical composition of the Earth and the volatility control on planetary genetics. Earth and Planetary Science Letters 185, 49-69.

Allègre, C.J., Poirier, J.-P., Humler, E. and Hofmann, A.W. (1995) The chemical composition of the Earth. Earth and Planetary Science Letters 134, 515-526.

Anders, E. (1968) Chemical processes in the early solar system, as inferred from meteorites. Accounts of Chemical Research 1, 289-298.

Anders, E. and Grevesse, N. (1989) Abundances of the elements: Meteoritic and solar. Geochimica et Cosmochimica Acta 53, 197-214.

Ardia, P., Hirschmann, M.M., Withers, A.C. and Stanley, B.D. (2013) Solubility of CH_4 in a synthetic basaltic melt, with applications to atmosphere–magma ocean–core partitioning of volatiles and to the evolution of the Martian atmosphere. Geochimica et Cosmochimica Acta 114, 52-71.

Armstrong, L.S., Hirschmann, M.M., Stanley, B.D., Falksen, E.G. and Jacobsen, S.D. (2015) Speciation and solubility of reduced C–O–H–N volatiles in mafic melt: Implications for volcanism, atmospheric evolution, and deep volatile cycles in the terrestrial planets. Geochimica et Cosmochimica Acta 171, 283-302.

Badro, J., Côté, A.S. and Brodholt, J.P. (2014) A seismologically consistent compositional model of Earth's core. Proceedings of the National Academy of Sciences 111, 7542-7545.

Benz, M.G. and Elliott, J.F. (1961) The austenite solidus and revised iron-carbon diagram. Trans. AIME 221, 323-331.

Beyssac, O., Rouzaud, J.-N., Goffé, B., Brunet, F. and Chopin, C. (2002) Graphitization in a high-pressure, low-temperature metamorphic gradient: a Raman microspectroscopy and HRTEM study. Contrib Mineral Petrol 143, 19-31.

Birch, F. (1952) Elasticity and constitution of the Earth's interior. Journal of Geophysical Research 57, 227-286.

Birch, F. (1964) Density and composition of mantle and core. Journal of Geophysical Research 69, 4377-4388.

Bley, B., Willner, H. and Aubke, F. (1997) Synthesis and Spectroscopic Characterization of Hexakis(carbonyl)iron(II) Undecafluorodiantimonate(V), $[Fe(CO)_6][Sb_2F_{11}]_2$. Inorganic Chemistry 36, 158-160.

Bose, K. and Ganguly, J. (1995) Quartz-coesite transition revisited: Reversed experimental determination at 500-1200ºC and retrieved thermochemical properties, American Mineralogist, p. 231.

Bourdon, B., Roskosz, M. and Hin, R.C. (2018) Isotope tracers of core formation. Earth-Science Reviews 181, 61-81.

Boyd, F.R. and England, J.L. (1960) Apparatus for phase-equilibrium measurements at pressures

up to 50 kilobars and temperatures up to 1750°C. Journal of Geophysical Research 65, 741-748.

Boyet, M. and Carlson, R.W. (2005) 142Nd Evidence for Early (> 4.53 Ga) Global Differentiation of the Silicate Earth. Science 309, 576-581.

Brooker, R.A., Kohn, S.C., Holloway, J.R., McMillan, P.F. and Carroll, M.R. (1999) Solubility, speciation and dissolution mechanisms for CO_2 in melts on the $NaAlO_2$–SiO_2 join. Geochimica et Cosmochimica Acta 63, 3549-3565.

Buono, A.S., Dasgupta, R., Lee, C.-T.A. and Walker, D. (2013) Siderophile element partitioning between cohenite and liquid in the Fe–Ni–S–C system and implications for geochemistry of planetary cores and mantles. Geochimica et Cosmochimica Acta 120, 239-250.

Cameron, A.G.W. (2000) Higher-resolution simulations of the giant impact. The University of Arizona Press, Tucson.

Canup, R.M. (2004) Simulations of a late lunar-forming impact. Icarus 168, 433-456.

Caro, G., Bourdon, B., Halliday, A.N. and Quitté, G. (2008) Super-chondritic Sm/Nd ratios in Mars, the Earth and the Moon. Nature 452, 336.

Carter, P.J., Leinhardt, Z.M., Elliott, T., Walter, M.J. and Stewart, S.T. (2015) Compositional Evolution during Rocky Protoplanet Accretion. The Astrophysical Journal 813, 72.

Cartigny, P., Pineau, F., Aubaud, C. and Javoy, M. (2008) Towards a consistent mantle carbon flux estimate: Insights from volatile systematics (H_2O/Ce, δD, CO_2/Nb) in the North Atlantic mantle (14° N and 34° N). Earth and Planetary Science Letters 265, 672-685.

Chakrabarti, R. and Jacobsen, S.B. (2010) Silicon isotopes in the inner Solar System: Implications for core formation, solar nebular processes and partial melting. Geochimica et Cosmochimica Acta 74, 6921-6933.

Chi, H., Dasgupta, R., Duncan, M.S. and Shimizu, N. (2014) Partitioning of carbon between Fe-rich alloy melt and silicate melt in a magma ocean – Implications for the abundance and origin of volatiles in Earth, Mars, and the Moon. Geochimica et Cosmochimica Acta 139, 447-471.

Chipman, J. (1972) Thermodynamics and phase diagram of the Fe-C system. Metallurgical and Materials Transactions B 3, 55-64.

Chou, C.-L. (1978) Fractionation of siderophile elements in the Earth's upper mantle. Proc. Lunar Planet. Sci. Conf 9th 1, 219-230.

Corgne, A., Keshav, S., Wood, B.J., McDonough, W.F. and Fei, Y. (2008) Metal–silicate partitioning and constraints on core composition and oxygen fugacity during Earth accretion. Geochimica et Cosmochimica Acta 72, 574-589.

Corgne, A., Siebert, J. and Badro, J. (2009) Oxygen as a light element: A solution to single-stage core formation. Earth and Planetary Science Letters 288, 108-114.

Cottrell, E., Walter, M.J. and Walker, D. (2009) Metal–silicate partitioning of tungsten at high pressure and temperature: Implications for equilibrium core formation in Earth. Earth and Planetary Science Letters 281, 275-287.

Couzi, M., Bruneel, J.-L., Talaga, D. and Bokobza, L. (2016) A multi wavelength Raman scattering study of defective graphitic carbon materials: The first order Raman spectra revisited. Carbon 107, 388-394.

Dalou, C., Hirschmann, M.M., von der Handt, A., Mosenfelder, J. and Armstrong, L.S. (2017) Nitrogen and carbon fractionation during core–mantle differentiation at shallow depth. Earth and Planetary Science Letters 458, 141-151.

Dasgupta, R., Buono, A., Whelan, G. and Walker, D. (2009) High-pressure melting relations in Fe–C–S systems: Implications for formation, evolution, and structure of metallic cores in planetary bodies. Geochimica et Cosmochimica Acta 73, 6678-6691.

Dasgupta, R., Chi, H., Shimizu, N., Buono, A.S. and Walker, D. (2013a) Carbon solution and partitioning between metallic and silicate melts in a shallow magma ocean: Implications for the origin and distribution of terrestrial carbon. Geochimica et Cosmochimica Acta 102, 191-212.

Dasgupta, R. and Hirschmann, M.M. (2006) Melting in the Earth's deep upper mantle caused by carbon dioxide. Nature 440, 659-662.

Dasgupta, R. and Hirschmann, M.M. (2010) The deep carbon cycle and melting in Earth's interior. Earth and Planetary Science Letters 298, 1-13.

Dasgupta, R. and Walker, D. (2008) Carbon solubility in core melts in a shallow magma ocean environment and distribution of carbon between the Earth's core and the mantle. Geochimica et Cosmochimica Acta 72, 4627-4641.

Dauphas, N. (2017) The isotopic nature of the Earth's accreting material through time. Nature 541, 521.

Davies, G.F. (1985) Heat deposition and retention in a solid planet growing by impacts. Icarus 63, 45-68.

Debernardi, A., Ulrich, C., Syassen, K. and Cardona, M. (1999) Raman linewidths of optical phonons in 3*C*-SiC under pressure: first principles calculations and experimental results. Physical Review B 59, 6774-6783.

Deines, P. and Wickman, F.E. (1973) The isotopic composition of 'graphitic' carbon from iron meteorites and some remarks on the troilitic sulfur of iron meteorites. Geochimica et Cosmochimica Acta 37, 1295-1319.

Dixon, J.E. (1997) Degassing of alkalic basalts, American Mineralogist, p. 368.

Donnelly-Nolan, J.M., Champion, D.E., Grove, T.L., Baker, M.B., Taggart, J.E. and Bruggman, P.E. (1991) The Giant Crater Lava Field: Geology and geochemistry of a compositionally zoned, high-alumina basalt to basaltic andesite eruption at Medicine Lake Volcano, California. Journal of Geophysical Research: Solid Earth 96, 21843-21863.

Dreibus, G. and Palme, H. (1996) Cosmochemical constraints on the sulfur content in the Earth's core. Geochimica et Cosmochimica Acta 60, 1125-1130.

Duncan, M.S., Dasgupta, R. and Tsuno, K. (2017) Experimental determination of CO_2 content at graphite saturation along a natural basalt-peridotite melt join: Implications for the fate of carbon in terrestrial magma oceans. Earth and Planetary Science Letters 466, 115-128.

Ertel, W., Walter, M.J., Drake, M.J. and Sylvester, P.J. (2006) Experimental study of platinum solubility in silicate melt to 14 GPa and 2273 K: Implications for accretion and core formation in Earth. Geochimica et Cosmochimica Acta 70, 2591-2602.

Falloon, T.J. and Green, D.H. (1989) The solidus of carbonated, fertile peridotite. Earth and Plan-

etary Science Letters 94, 364-370.

Ferrari, A.C. (2007) Raman spectroscopy of graphene and graphite: Disorder, electron–phonon coupling, doping and nonadiabatic effects. Solid State Communications 143, 47-57.

Fichtner, C.E., Schmidt, M.W., Liebske, C., Bouvier, A.-S. and Baumgartner, L. (2018a) Carbon partitioning between metal and silicate melts during Earth accretion (in preparation).

Fischer, R.A., Campbell, A.J. and Ciesla, F.J. (2017) Sensitivities of Earth's core and mantle compositions to accretion and differentiation processes. Earth and Planetary Science Letters 458, 252-262.

Frost, D.J., Liebske, C., Langenhorst, F., McCammon, C.A., Tronnes, R.G. and Rubie, D.C. (2004) Experimental evidence for the existence of iron-rich metal in the Earth's lower mantle. Nature 428, 409-412.

Gordon and Breach (1988) Steelmaking Data Sourcebook. Gordon and Breach Science Publishers.

Halliday, A.N. (2004) Mixing, volatile loss and compositional change during impact-driven accretion of the Earth. Nature 427, 505.

Halliday, A.N. (2008) A young Moon-forming giant impact at 70–110 million years accompanied by late-stage mixing, core formation and degassing of the Earth. Philosophical Transactions of the Royal Society A: Mathematical, Physical and Engineering Sciences 366, 4163-4181.

Hillgren, V.J., Gessmann, C.K. and Li, J. (2000) An Experimental Perspective on the Light Element in Earth's Core. University of Arizona Press, Tucson, Arizona.

Hirschmann, M.M. (2012) Magma ocean influence on early atmosphere mass and composition. Earth and Planetary Science Letters 341–344, 48-57.

Hirschmann, M.M. and Dasgupta, R. (2009) The H/C ratios of Earth's near-surface and deep reservoirs, and consequences for deep Earth volatile cycles. Chemical Geology 262, 4-16.

Holloway, J.R., Pan, V. and Gudmundsson, G. (1992) Highpressure fluid-absent melting experiments in the presence of graphite; oxygen fugacity, ferric/ferrous ratio and dissolved CO_2. Eur. J. Mineral. 4, 105-114.

Holzapfel, C., Rubie, D.C., Frost, D.J. and Langenhorst, F. (2005) Fe-Mg Interdiffusion in (Mg,Fe) SiO_3 Perovskite and Lower Mantle Reequilibration. Science 309, 1707-1710.

Holzheid, A. and Grove, T.L. (2005) The effect of metal composition on Fe–Ni partition behavior between olivine and FeNi-metal, FeNi-carbide, FeNi-sulfide at elevated pressure. Chemical Geology 221, 207-224.

Holzheid, A., Palme, H. and Chakraborty, S. (1997) The activities of NiO, CoO and FeO in silicate melts. Chemical Geology 139, 21-38.

Jagoutz, E., Palme, H., Baddenhausen, H., Blum, K., Cendales, M. and Dreibus, G. (1979) The abundances of major, minor and trace elements in the earth's mantle as derived from primitive ultramafic nodules. Lunar and Planetary Science Conference, 10th, Houston, Texas 2, 2031-2050.

Jana, D. and Walker, D. (1997) The impact of carbon on element distribution during core formation. Geochimica et Cosmochimica Acta 61, 2759-2763.

Jarosewich, E. (1990) Chemical analyses of meteorites: A compilation of stony and iron meteorite analyses. Meteoritics 25, 323-337.

Acta 73, 1696-1710.

Mysen, B.O. and Virgo, D. (1986) Volatiles in silicate melts at high pressure and temperature: 2. Water in melts along the join $NaAlO_2 - SiO_2$ and a comparison of solubility mechanisms of water and fluorine. Chemical Geology 57, 333-358.

Nakajima, Y., Takahashi, E., Suzuki, T. and Funakoshi, K.-i. (2009) “Carbon in the core” revisited. Physics of the Earth and Planetary Interiors 174, 202-211.

Neuville, D.R. and Mysen, B.O. (1996) Role of aluminium in the silicate network: In situ, high-temperature study of glasses and melts on the join SiO_2-$NaAlO_2$. Geochimica et Cosmochimica Acta 60, 1727-1737.

Newsom, H.E. (1990) Accretion and Core Formation in the Earth: Evidence from Siderophile Elements. Oxford Univ. Press, New York.

Newsom, H.E. and Sims, K.W.W. (1991) Core Formation During Early Accretion of the Earth. Science 252, 926-933.

Ni, H. and Keppler, H. (2013) Carbon in Silicate Melts. Reviews in Mineralogy and Geochemistry 75, 251-287.

Nimmo, F. and Kleine, T. (2015) Early Differentiation and Core Formation, The Early Earth. John Wiley & Sons, Inc, pp. 83-102.

O'Brien, D.P., Morbidelli, A. and Levison, H.F. (2006) Terrestrial planet formation with strong dynamical friction. Icarus 184, 39-58.

O'Neill, H.S.C. (1988) Systems Fe-O and Cu-O; thermodynamic data for the equilibria Fe-"FeO," Fe-Fe_3O_4 , "FeO"-Fe_3O_4 , Fe_3O_4 -Fe_2O_3 , Cu-Cu_2O, and Cu_2O-CuO from *emf* measurements. American Mineralogist 73, 470-486.

O'Neill, H.S.C. (1991) The origin of the moon and the early history of the earth—A chemical model. Part 2: The earth. Geochimica et Cosmochimica Acta 55, 1159-1172.

O'Neill, H.S.C. and Palme, H. (1998) Composition of the silicate Earth: implications for accretion and core formation. Cambridge University Press, Cambridge, UK.

O'Neill, H.S.C. and Palme, H. (2008) Collisional erosion and the non-chondritic composition of the terrestrial planets. Philosophical Transactions of the Royal Society A: Mathematical, Physical and Engineering Sciences 366, 4205-4238.

Ogino, K., Nishiwaki, A. and Hosotani, Y. (1984) Density of Molten Fe-C Alloys. J. Japan Inst. Metals 48, 1004-1010.

Ohtani, E. and Ringwood, A.E. (1984) Composition of the core, I. Solubility of oxygen in molten iron at high temperatures. Earth and Planetary Science Letters 71, 85-93.

Palme, H. and St. C. O'Neill, H. (2003) Cosmochemical Estimates of Mantle Composition. Elsevier-Pergamon, Oxford.

Parman, S.W., Dann, J.C., Grove, T.L. and de Wit, M.J. (1997) Emplacement conditions of komatiite magmas from the 3.49 Ga Komati Formation, Barberton Greenstone Belt, South Africa1. Earth and Planetary Science Letters 150, 303-323.

Pineau, F., Shilobreeva, S., Hekinian, R., Bideau, D. and Javoy, M. (2004) Deep-sea explosive activity on the Mid-Atlantic Ridge near 34°50′N: a stable isotope (C, H, O) study. Chemical Geology 211, 159-175.

Jarosewich, E., Nelen, J.A. and Norberg, J.A. (1980) Reference Samples for Electron Microprobe Analysis. Geostandards Newsletter 4, 43-47.

Javoy, M. and Pineau, F. (1991) The volatiles record of a "popping" rock from the Mid-Atlantic Ridge at 14°N: chemical and isotopic composition of gas trapped in the vesicles. Earth and Planetary Science Letters 107, 598-611.

Javoy, M. (1995) The integral enstatite chondrite model of the Earth. Geophysical Research Letters 22, 2219-2222.

Jones, J.H. and Drake, M.J. (1986) Constraints on the origin of the Moon. Geochimica et Cosmochimica Acta 50, 1827.

Kadik, A., Pineau, F., Litvin, Y., Jendrzejewski, N., Martinez, I. and Javoy, M. (2004) Formation of Carbon and Hydrogen Species in Magmas at Low Oxygen Fugacity. Journal of Petrology 45, 1297-1310.

Kadik, A.A., Kurovskaya, N.A., Ignat'ev, Y.A., Kononkova, N.N., Koltashev, V.V. and Plotnichenko, V.G. (2011) Influence of oxygen fugacity on the solubility of nitrogen, carbon, and hydrogen in FeO-Na_2O-SiO_2-Al_2O_3 melts in equilibrium with metallic iron at 1.5 GPa and 1400°C. Geochemistry International 49, 429.

Kanter, M.A. (1957) Diffusion of Carbon Atoms in Natural Graphite Crystals. Physical Review 107, 655-663.

Kennett, B.L.N., Engdahl, E.R. and Buland, R. (1995) Constraints on seismic velocities in the Earth from traveltimes. Geophysical Journal International 122, 108-124.

Kilburn, M.R. and Wood, B.J. (1997) Metal–silicate partitioning and the incompatibility of S and Si during core formation. Earth and Planetary Science Letters 152, 139-148.

King, P.L. and Holloway, J.R. (2002) CO_2 solubility and speciation in intermediate (andesitic) melts: the role of H_2O and composition. Geochimica et Cosmochimica Acta 66, 1627-1640.

Kleine, T., Münker, C., Mezger, K. and Palme, H. (2002) Rapid accretion and early core formation on asteroids and the terrestrial planets from Hf–W chronometry. Nature 418, 952.

Kleine, T., Palme, H., Mezger, K. and Halliday, A.N. (2005) Hf-W Chronometry of Lunar Metals and the Age and Early Differentiation of the Moon. Science 310, 1671-1674.

Kruijer, T.S., Touboul, M., Fischer-Gödde, M., Bermingham, K.R., Walker, R.J. and Kleine, T. (2014) Protracted core formation and rapid accretion of protoplanets. Science 344, 1150-1154.

Labrosse, S., Hernlund, J.W. and Coltice, N. (2007) A crystallizing dense magma ocean at the base of the Earth's mantle. Nature 450, 866.

Li, J. and Agee, C.B. (1996) Geochemistry of mantle–core differentiation at high pressure. Nature 381, 686.

Li, J. and Fei, Y. (2003) Experimental constraints on core composition. Elsevier-Pergamon, Oxford.

Li, Y., Dasgupta, R. and Tsuno, K. (2015) The effects of sulfur, silicon, water, and oxygen fugacity on carbon solubility and partitioning in Fe-rich alloy and silicate melt systems at 3 GPa and 1600 °C: Implications for core–mantle differentiation and degassing of magma oceans and reduced planetary mantles. Earth and Planetary Science Letters 415, 54-66.

Li, Y., Dasgupta, R., Tsuno, K., Monteleone, B. and Shimizu, N. (2016) Carbon and sulfur budget of

the silicate Earth explained by accretion of differentiated planetary embryos. Nature Geoscience 9, 781.

Liebske, C. and Khan, A. (2018) On the principle building blocks of Mars (submitted).

Lodders, K. (2003) Solar System Abundances and Condensation Temperatures of the Elements. The Astrophysical Journal 591, 1220.

Lodders, K. and Fegley, B. (1997) An Oxygen Isotope Model for the Composition of Mars. Icarus 126, 373-394.

Mandt, K.E., Mousis, O., Marty, B., Cavalié, T., Harris, W., Hartogh, P. and Willacy, K. (2015) Constraints from Comets on the Formation and Volatile Acquisition of the Planets and Satellites. Space Science Reviews 197, 297-342.

Mann, U., Frost, D.J. and Rubie, D.C. (2009) Evidence for high-pressure core-mantle differentiation from the metal–silicate partitioning of lithophile and weakly-siderophile elements. Geochimica et Cosmochimica Acta 73, 7360-7386.

Marty, B. (2012) The origins and concentrations of water, carbon, nitrogen and noble gases on Earth. Earth and Planetary Science Letters 313–314, 56-66.

Marty, B. and Zimmermann, L. (1999) Volatiles (He, C, N, Ar) in mid-ocean ridge basalts: assesment of shallow-level fractionation and characterization of source composition. Geochimica et Cosmochimica Acta 63, 3619-3633.

Matsui, T. and Abe, Y. (1986) Impact-induced atmospheres and oceans on Earth and Venus. Nature 322, 526-528.

McDonough, W.F. (2003) Compositional Model for the Earth's Core, in: Holland, H.D., Turekian, K.K. (Eds.), Treatise on Geochemistry. Pergamon, Oxford, pp. 547-568.

McDonough, W.F. and Sun, S.s. (1995) The composition of the Earth. Chemical Geology 120, 223-253.

Médard, E., McCammon, C.A., Barr, J.A. and Grove, T.L. (2008) Oxygen fugacity, temperature reproducibility, and H_2O contents of nominally anhydrous piston-cylinder experiments using graphite capsules. American Mineralogist 93, 1838-1844.

Melosh, H.J. (1990) Giant impacts and the thermal state of the early Earth. In Origin of the Earth (H. E. Newsom and J. H. Jones, Eds.), 69-84. Oxford Univ. Press, New York.

Melson, W.G., Vallier, T.L., Wright, T.L., Byerly, G. and Nelen, J. (1976) Chemical Diversity of Abyssal Volcanic Glass Erupted Along Pacific, Atlantic, and Indian Ocean Sea-Floor Spreading Centers. Geophysical Monograph Series 19, 351-367.

Morbidelli, A., Marchi, S., Bottke, W.F. and Kring, D.A. (2012) A sawtooth-like timeline for the first billion years of lunar bombardment. Earth and Planetary Science Letters 355-356, 144-151.

Morgan, J.W. and Anders, E. (1979) Chemical composition of Mars. Geochimica et Cosmochimica Acta 43, 1601-1610.

Mysen, B.O. (1998) Interaction between Aqueous Fluid and Silicate Melt in the Pressure and Temperatures Regime of the Earth's Crust and Upper Mantle.

Mysen, B.O., Fogel, M.L., Morrill, P.L. and Cody, G.D. (2009) Solution behavior of reduced COH volatiles in silicate melts at high pressure and temperature. Geochimica et Cosmochimica

Popper, K. (1935) Logik der Forschung. Julius Springer, Vienna, Austria.

Rai, N. and Van Westrenen, W. (2012) Constraints on the Formation of a Lunar Core from Metal-Silicate Partitioning of Siderophile Elements.

Rantitsch, G., Lämmerer, W., Fisslthaler, E., Mitsche, S. and Kaltenböck, H. (2016) On the discrimination of semi-graphite and graphite by Raman spectroscopy. International Journal of Coal Geology 159, 48-56.

Righter, K. (2011) Prediction of metal–silicate partition coefficients for siderophile elements: An update and assessment of P-T conditions for metal–silicate equilibrium during accretion of the Earth. Earth and Planetary Science Letters 304, 158-167.

Righter, K. and Chabot, N.L. (2011) Moderately and slightly siderophile element constraints on the depth and extent of melting in early Mars. Meteoritics & Planetary Science 46, 157-176.

Righter, K. and Drake, M.J. (1999) Effect of water on metal-silicate partitioning of siderophile elements: a high pressure and temperature terrestrial magma ocean and core formation. Earth and Planetary Science Letters 171, 383-399.

Righter, K., Drake, M.J. and Yaxley, G. (1997) Prediction of siderophile element metal-silicate partition coefficients to 20 GPa and 2800°C: the effects of pressure, temperature, oxygen fugacity, and silicate and metallic melt compositions. Physics of the Earth and Planetary Interiors 100, 115-134.

Righter, K. and Ghiorso, M.S. (2012) Redox systematics of a magma ocean with variable pressure-temperature gradients and composition. Proceedings of the National Academy of Sciences 109, 11955-11960.

Ringwood, A.E. (1966) Chemical evolution of the terrestrial planets. Geochimica et Cosmochimica Acta 30, 41-104.

Roskosz, M., Bouhifd, M.A., Jephcoat, A.P., Marty, B. and Mysen, B.O. (2013) Nitrogen solubility in molten metal and silicate at high pressure and temperature. Geochimica et Cosmochimica Acta 121, 15-28.

Rubie, D.C., Frost, D.J., Mann, U., Asahara, Y., Nimmo, F., Tsuno, K., Kegler, P., Holzheid, A. and Palme, H. (2011) Heterogeneous accretion, composition and core–mantle differentiation of the Earth. Earth and Planetary Science Letters 301, 31-42.

Rubie, D.C., Gessmann, C.K. and Frost, D.J. (2004) Partitioning of oxygen during core formation on the Earth and Mars. Nature 429, 58.

Rubie, D.C., Jacobson, S.A., Morbidelli, A., O'Brien, D.P., Young, E.D., de Vries, J., Nimmo, F., Palme, H. and Frost, D.J. (2015) Accretion and differentiation of the terrestrial planets with implications for the compositions of early-formed Solar System bodies and accretion of water. Icarus 248, 89-108.

Rubie, D.C., Melosh, H.J., Reid, J.E., Liebske, C. and Righter, K. (2003) Mechanisms of metal–silicate equilibration in the terrestrial magma ocean. Earth and Planetary Science Letters 205, 239-255.

Rubie, D.C., Nimmo, F. and Melosh, H.J. (2007) Formation of Earth's Core, in: Editor-in-Chief: Gerald, S. (Ed.), Treatise on Geophysics. Elsevier, Amsterdam, pp. 51-90.

Rudge, J.F., Kleine, T. and Bourdon, B. (2010) Broad bounds on Earth's accretion and core forma-

tion constrained by geochemical models. Nature Geoscience 3, 439-443.

Saal, A.E., Hauri, E.H., Langmuir, C.H. and Perfit, M.R. (2002) Vapour undersaturation in primitive mid-ocean-ridge basalt and the volatile content of Earth's upper mantle. Nature 419, 451.

Sambridge, M. and Mosegaard, K. (2002) Monte Carlo Methods in Geophysical inverse problems. Reviews of Geophysics 40, 3-1-3-29.

Scherstén, A., Elliott, T., Hawkesworth, C., Russell, S. and Masarik, J. (2006) Hf–W evidence for rapid differentiation of iron meteorite parent bodies. Earth and Planetary Science Letters 241, 530-542.

Schmidt, M.W., Connolly, J.A.D., Günther, D. and Bogaerts, M. (2006) Element Partitioning: The Role of Melt Structure and Composition. Science 312, 1646-1650.

Siebert, J., Corgne, A. and Ryerson, F.J. (2011) Systematics of metal–silicate partitioning for many siderophile elements applied to Earth's core formation. Geochimica et Cosmochimica Acta 75, 1451-1489.

Sleep, N.H. and Zahnle, K. (2001) Carbon dioxide cycling and implications for climate on ancient Earth. Journal of Geophysical Research: Planets 106, 1373-1399.

Socrates, G. (2002) Infrared and Raman Characteristic Group Frequencies: Tables and Charts. Journal of the American Chemical Society 124, 1830-1830.

Solomatov, V.S. (2000) Fluid dynamics of a terrestrial magma ocean. In Origin of the Earth and Moon, Canup R. M. and Righter K. (eds.), 323-338.

Spohn, T. and Schubert, G. (1991) Thermal equilibration of the Earth following a giant impact. Geophysical Journal International 107, 163-170.

Stanley, B.D., Hirschmann, M.M. and Withers, A.C. (2014) Solubility of C-O-H volatiles in graphite-saturated martian basalts. Geochimica et Cosmochimica Acta 129, 54-76.

Steenstra, E.S., Lin, Y., Rai, N., Jansen, M. and Westrenen, W. (2017) Carbon as the dominant light element in the lunar core. American Mineralogist 102, 92-97.

Stevenson, D.J. (1981) Models of the Earth's core. Science, 611-619.

Stevenson, D.J. (1990) Fluid dynamics of core formation. In Origin of the Earth, Newsom H.E. and Jones J.H. (eds.), 231-250, New York: Oxford University Press.

Stevenson, D.J. (2008) A planetary perspective on the deep Earth. Nature 451, 261-265.

Tarantola, A. (2005) Inverse problem theory and methods for model parameter estimation. Society for insdustrial and applied mathematics, Philadelphia.

Taylor, W.R. and Norman, S.R. (1990) Accretion of differentiated planetesimals to the Earth. Oxford University Press, New York.

Tonks, B.W. and Melosh, J.H. (1992) Core formation by giant impacts. Icarus 100, 326-346.

Tonks, W.B. and Melosh, H.J. (1993) Magma ocean formation due to giant impacts. Journal of Geophysical Research: Planets 98, 5319-5333.

Trull, T., Nadeau, S., Pineau, F., Polve´, M. and Javoy, M. (1993) C-He systematics in hotspot xenoliths: Implications for mantle carbon contents and carbon recycling. Earth and Planetary Science Letters 118, 43-64.

Tsuno, K., Frost, D.J. and Rubie, D.C. (2013) Simultaneous partitioning of silicon and oxygen into the Earth's core during early Earth differentiation. Geophysical Research Letters 40, 66-71.

Tuinstra, F. and Koenig, J.L. (1970) Raman Spectrum of Graphite. The Journal of Chemical Physics 53, 1126-1130.

Wade, J. and Wood, B.J. (2005) Core formation and the oxidation state of the Earth. Earth and Planetary Science Letters 236, 78-95.

Wallace, P.J. (2005) Volatiles in subduction zone magmas: concentrations and fluxes based on melt inclusion and volcanic gas data. Journal of Volcanology and Geothermal Research 140, 217-240.

Walter, M.J. (2000) A shear pathway to the core. Nature 403, 839.

Walter, M.J. (2014) Melt Extraction and Compositional Variability in Mantle Lithosphere A2 - Holland, Heinrich D, in: Turekian, K.K. (Ed.), Treatise on Geochemistry (Second Edition). Elsevier, Oxford, pp. 393-419.

Walter, M.J., Nakamura, E., Trønnes, R.G. and Frost, D.J. (2004) Experimental constraints on crystallization differentiation in a deep magma ocean. Geochimica et Cosmochimica Acta 68, 4267-4284.

Walter, M.J. and Trønnes, R.G. (2004) Early Earth differentiation. Earth and Planetary Science Letters 225, 253-269.

Wänke, H. (1981) Constitution of terrestrial planets. Philosophical Transactions of the Royal Society of London. Series A, Mathematical and Physical Sciences 303, 287-302.

Wänke, H., Baddenhausen, H., Palme, H. and Spettel, B. (1974) On the chemistry of the Allende inclusions and their origin as high temperature condensates. Earth and Planetary Science Letters 23, 1-7.

Weber, I., Böttger, U., Pavlov, S.G., Jessberger, E.K. and Hübers, H.W. (2014) Mineralogical and Raman spectroscopy studies of natural olivines exposed to different planetary environments. Planetary and Space Science 104, 163-172.

Wetzel, D.T., Hauri, E.H., Saal, A.E. and Rutherford, M.J. (2015) Carbon content and degassing history of the lunar volcanic glasses. Nature Geoscience 8, 755.

Wetzel, D.T., Rutherford, M.J., Jacobsen, S.D., Hauri, E.H. and Saal, A.E. (2013) Degassing of reduced carbon from planetary basalts. Proceedings of the National Academy of Sciences 110, 8010-8013.

Williams, Q. and Hemley, R.J. (2001) Hydrogen in the Deep Earth. Annual Review of Earth and Planetary Sciences 29, 365-418.

Wood, B.J. (1993) Carbon in the core. Earth and Planetary Science Letters 117, 593-607.

Wood, B.J., Wade, J. and Kilburn, M.R. (2008) Core formation and the oxidation state of the Earth: Additional constraints from Nb, V and Cr partitioning. Geochimica et Cosmochimica Acta 72, 1415-1426.

Wood, B.J., Walter, M.J. and Wade, J. (2006) Accretion of the Earth and segregation of its core. Nature 441, 825-833.

Wyllie, P.J. and Huang, W.-L. (1976) Carbonation and melting reactions in the system CaO–MgO–SiO_2–CO_2 at mantle pressures with geophysical and petrological applications. Contrib Mineral Petrol 54, 79-107.

Acknowledgements

First of all, I would like to thank my supervisor Prof. Dr. Max Schmidt for giving me the opportunity to do a doctorate at ETH Zurich, for providing the topic of this doctoral study, and for the constructive comments that helped to improve this thesis. I really appreciated the support and freedom I received, especially after the birth of my daughter. Also, I am very grateful to Dr. Christian Liebske for many fruitful discussions, feedback on my thesis, and assistance with experimental issues. Furthermore, I would like to thank Prof. Dr. Peter Ulmer, whose door was always open and who always had time to answer my questions. Also, I would like to acknowledge Prof. Dr. Jamie Connolly who provided much help in answering thermodynamic questions. In addition, many thanks to Prof. Dr. Mike Walter for being in my doctoral defense committee.

This doctoral project would not have been realised without the technical, instrumental, and analytical support of Dr. Eric Reusser, Dr. Lukas Martin, Lydia Zehnder, Dr. Claudio Madonna, Thomas Good, Urs Graber, Andreas Huber, and Remy Lüchinger. Special thanks to Andreas Jallas who prepared most of my olivine capsules and who even took apart the wastewater pipe once, in order to search for a sample that I lost. Also, many thanks to Claudia Büchel for administrative support.

Furthermore, I would like to thank Prof. Dr. Lukas Baumgartner, Dr. Anne-Sophie Bouvier, Dr. Guillaume Siron, and Dr. Florence Bégué for their assistance with the SIMS analyses, sample preparation, and data processing. I really much appreciated the constructive and friendly working atmosphere at the SwissSIMS Lab and always had a great time in Lausanne.

I would also like to take this opportunity to thank my office mates Lotta, Nico, Dawid, Iris, Michaël and all other members of our institute, especially Jule, Jakub, Alina, Ben, Max, Giuliano, Felix, Basti, Kathi, Julia, Nadia, Paul, Julien, Julian, Jörn, Matthieu, Fabio, and Ozge for sharing coffee breaks, lunch times, sports classes and life. In this sense, I would also like to include my former ETH fellows Francesca, Anna, Shahrzad, Moni, Nastia, Sasha, Steffi, Sonja, Rohit, Sujoy, Rita, Natalia, Stéphane, Simon and Matthias.

Many special thanks to Maren, Annina, Susanne, Lotta and my friends back in Germany and elsewhere in the world, Chrischi, Sina, Katharina, Nazanin, Lea, Kristi, and Fernando. You were always there for me and made the past five years so much more pleasant.

From the bottom of my heart I would like to thank my parents Drs. Heidi and Hans Höfer for their unconditional support in everything I decided to do in my life. I am especially thankful for the great help with the EPMA measurements in Frankfurt, and the constructive and thoughtful comments on my manuscripts and thesis, which helped to improve them significantly.

With my final words, I would like to give heartfelt thanks to my husband Prof. Dr. Andreas Fichtner for his endless encouragement, guidance, help and support. Heartfelt thanks also to my little Helena for filling my life with happiness.